

FLUID-DYNAMICS OF EXPLOSIONS IN MULTI-CHAMBER SYSTEMS PHENOMENOLOGY TEST PROGRAM

Approved for public release; distribution is unlimited.

July 2000



Prepared for:
Defense Threat Reduction Agency
45045 Aviation Drive
Dulles, VA 20166-7517

DNA001-94-C-0078

Heinz Reichenbach
Peter Neuwald

Prepared by: Ernst-Mach Institut
Fraunhofer Institut für Kurzzeitdynamik
Eckerstraße 4
79104 Freiburg i. Br.
Germany

20001124 128

Technical Report

DESTRUCTION NOTICE:

Destroy this report when it is no longer needed. Do not return to sender.

PLEASE NOTIFY THE DEFENSE THREAT REDUCTION AGENCY, ATTN: ADM, 45045 AVIATION DRIVE, DULLES, VA 20166-7517, IF YOUR ADDRESS IS INCORRECT, IF YOU WISH IT DELETED FROM THE DISTRIBUTION LIST, OR IF THE ADDRESSEE IS NO LONGER EMPLOYED BY YOUR ORGANIZATION.

REPORT DOCUMENTATION PAGE			Form Approved OMB No. 0704-0188	
Public reporting burden for this collection of information is estimated to average 1 hour per response, including the time for reviewing instructions, searching existing data sources, gathering and maintaining the data needed, and completing and reviewing the collection of information. Send comments regarding this burden, estimate or any other aspect of this collection of information, including suggestions for reducing this burden, to Washington Headquarters Services, Directorate for Information Operations and Reports, 1215 Jefferson Davis Highway, Suite 1204, Arlington, VA 22202-4302, and to the Office of Management and Budget, Paperwork Reduction Project (0704-0188), Washington, DC 20503.				
1. AGENCY USE ONLY (Leave blank)		2. REPORT DATE JULY 2000		3. REPORT TYPE AND DATES COVERED Technical 940901-971231
4. TITLE AND SUBTITLE Fluid-Dynamics of Explosions in Multi-Chamber Systems Phenomenology Test Program			5. FUNDING NUMBERS C - DNA 001-94-C-0078 PE - 62715H PR - AC TA - AK WU - DH50079	
6. AUTHOR(S) Heinz Reichenback and Peter Neuwald				
7. PERFORMING ORGANIZATION NAME(S) AND ADDRESS(ES) Ernst-Mach Institute - Fraunhofer Institut für Kurzzeiddynamik Ecker Strausse, 4 79104 Freiburg i. Br. Federal Republic of Germany			8. PERFORMING ORGANIZATION REPORT	
9. SPONSORING/MONITORING AGENCY NAME(S) AND ADDRESS(ES) Defense Threat Reduction Agency 45045 Aviation Drive Dulles, VA 20166-7517 CPWT/Giltrud			10. SPONSORING/MONITORING AGENCY REPORT NUMBER DSWA-TR-98-21	
11. SUPPLEMENTARY NOTES This work was sponsored by the Defense Threat Reduction Agency under RDT&E RMC code B 4662 D AC AK 50079 4300 AC 25904D.				
12a. DISTRIBUTION/AVAILABILITY STATEMENT Approved for public release; distribution is unlimited			12b. DISTRIBUTION CODE	
13. ABSTRACT (Maximum 200 words) The report focuses on the topic of indoor detonations in multi-chamber structures. The central part of the presented project investigated a generic model of a single-story building. By means of PETN-charges in the range of 0.5g model scales of about 1:70 were feasible. Main diagnostic were pressure measurements at the model walls and high-speed visualization of the flow field. The tests are well reproducible and easily repeated; thus a number of parametric changes was feasible (e.g., variation of the charge location, size of a venting hole in the chamber, where the detonation occurs). In addition, experiments on selected typical components of a multi-chamber structure (e.g., corridors, connecting doors, staircases) were also performed in a shock tube, in order to investigate the typical flow field phenomena in dependence from the Mach number.				
14. SUBJECT TERMS Indoor Detonation Charge Location Cylindrical Charge Confined Detonation Venting Shock Tube Test Multi-Chamber-System Khobar Towers Small-Scale Experiment			15. NUMBER OF PAGES 261	
			16. PRICE CODE	
17. SECURITY CLASSIFICATION OF THIS PAGE UNCLASSIFIED	18. SECURITY CLASSIFICATION OF REPORT UNCLASSIFIED	19. SECURITY CLASSIFICATION OF ABSTRACT UNCLASSIFIED	20. LIMITATION OF ABSTRACT SAR	

UNCLASSIFIED

SECURITY CLASSIFICATION OF THIS PAGE

CLASSIFIED BY:

N/A since Unclassified

DECLASSIFY ON:

N/A since Unclassified

13. ABSTRACT (Maximum 200 words) (Continued)

On the topic of detonations in the vicinity of a building exploratory experiments were performed; with the focus on a small-scale simulation of the bomb attack at Khobar Towers, Saudi Arabia. The feasibility of manufacturing cylindrical small-scale charges was shown. Flow field visualization and pressure measurements indicate characteristic differences between cylindrical charges (unconfined or confined) and spherical ones.

14. SUBJECT TERMS (Continued)

Shadow Photography

Pressure Measurement

SECURITY CLASSIFICATION OF THIS PAGE

UNCLASSIFIED

Summary

This report describes investigations of flow phenomena by small-scale laboratory experiments. In an extended manner optical and photographic methods were applied in this research program that contains three main tasks.

Shock propagation in component systems. For a better understanding of shock induced flows in complex multi-chamber buildings five different typical component systems were investigated in 2-D shock tube tests. Single-room, room-corridor, single story, stairwells and duct configuration were taken into consideration. Results of different versions of the individual configurations are represented in sequences of shadowgraphs, partly in schlieren and color-schlieren photographs. Pressure-time and impulse-time histories mediate quantitative data of the complex flow behavior.

Airblast propagation in a scaled chamber system. A small-scale multi-chamber system with transparent floor and ceiling was developed for the visualization of the flow behavior inside the system after an indoor detonation. Results in form of shadowgraph sequences and pressure and impulse records are given for different charge positions in the detonation room. Also the influence of openings in the detonation room on the flow behavior and the loading of the walls was taken into account. Some data of feasibility tests to the problem of the energy release by afterburning processes are given.

Developments and experiments on special request of DSWA. In a first subtask cylindrical charges for laboratory-scale experiments were developed. Results are reported of axial and face ignited unconfined HE-cylinders as well as of confined versions. The latter simulate the charge used at the Khobar Towers Building event.

In the second subtasks the bomb attack onto the Khobar Towers Building was simulated in a scale of 1 : 200. The results are summarized in sequences of shadowgraphs and pressure records.

Table of Contents

Section		Page
	Summary.....	iii
	Figures	v
	Tables	xv
1	Introduction	1
2	Shock Propagation in Component Systems	3
	2.1 Experiment Design.....	3
	2.2 Results of Component System Tests.....	4
3	Airblast Propagation in a Scaled Chamber System	15
	3.1 Experimental Setup.....	15
	3.2 Charges.....	15
	3.3 Diagnostics.....	16
	3.4 Experimental Results for the Standard Configuration.....	16
	3.5 Influence of the Charge Location.....	19
	3.6 Variation of the Charge Weight.....	20
	3.7 Influence of a Venting Hole.....	21
	3.8 Flow Field in the Detonation Chamber.....	24
	3.9 Summary.....	25
4	Developments and Experiments on Special Request of DSWA	26
	4.1 Evaluation of Former EMI-Tests.....	26
	4.2 Development of Small Cylindrical Charges.....	27
	4.3 Simulation of the Bomb Attack onto the Khobar Towers Building.....	31
5	Tables and Figures	36
6	References.....	243
	Distribution List	245

Figures

Figure		Page
1	Single room configuration; A = Area of the opening, V = Volume of the room.	51
2	Single room models according to the dimensions, given in Figure 1. At tests, pressure gages will be placed in the bore holes of the back wall.	52
3	Single room configuration, model 1; (test 14 783) shadow pictures; $M_s = 1,41$.	53
4	Single room configuration, model 1; (test 14 783) schlieren pictures; $M_s = 1,41$.	55
5	Single room configuration, model 1; (test 15 174) shadow pictures; $M_s = 2,05$.	57
6	Single room configuration, model 2, (test 14 860) shadow pictures; $M_s = 1,31$.	61
7	Single room configuration, model 2, color-schlieren pictures; $M_s = 1,31$	63
8	Pressure-time and overpressure impulse histories of single room configuration, model 1, $M_s = 1,41$ (test: 14 783).	64
9	Pressure-time histories in a single room configuration, model 1 $M_s = 2.05$; (test: 15 175).	65
10	Impulse-rise at $t = 1$ ms vs shock Mach number single room configuration; models 2 and 3	66
11	Scaled impulse-rise at $t = 1$ ms vs shock Mach number single room configuration; models 2 and 3	66
12	Time of arrival vs range of test 14 783. Single room configuration, model 1. (see Figures 3 and 4)	67
13	Room corridor configurations. A = area of the opening, V = volume of the room.	68
14	Room corridor models according to the dimensions given in Figure 13	69
15	Room corridor configuration, model 6; shadow pictures, shock Mach number: $M_s = 1.41$; (test: 14 769).	70
16	Room corridor configuration, model 6; schlieren pictures, shock Mach number: $M_s = 1.41$; (test: 14 769).	72
17	Room corridor configuration, model 5; shadow pictures, early times.	74

Figures (Continued)

Figure		Page
18	Room corridor configuration, model 4; shadow pictures, later times.	76
19	Room corridor configuration, model 4; color schlieren pictures; shock Mach number: $M_s = 1.31$.	78
20	Pressure-time record at the end wall of a room corridor configuration, model 6. $M_s = 1.67$. An additional scale is included for comparisons with the shadowgraph sequence of Figure 21.	79
21	Shock- and flow visualization, room corridor model 6, $M_s = 1.67$ (test 15 105) . Exposure time is related to the first peak of the pressure record (Figure 20).	80
22	Shock Tube tests. Average pressure p at the end-walls of single room (models 1 - 3) and room corridor configurations (models 4 - 6) for an averaging interval of $t_0 = 0.5$ ms (except model 1; $t_0 = 0.25$ ms).	82
23	Sketch of the two versions of single story system for shock tube tests.	83
24	Flow in the single story system. Version A. $M_s = 1.63$; (test 15 153).	84
25	Flow in the single story system. Version B. $M_s = 1.61$; (test 15 223).	86
26	Pressure-time and impulse-time histories at different gage locations of the single story system, version A. $M_s = 1.63$; (test 15 153).	88
27	Pressure-time and impulse-time histories at different gage locations of the single story system, version B, $M_s = 1.61$; (test 15 223).	89
28	Mean overpressure vs shock Mach number M_s for single story systems version A and B.	90
29	Stairwells configuration.	91
30	Stairwell models.	92
31	2-D version of the stairwells configuration. Comparison of color schlieren (top) and shadow pictures (below).	93
32	3-D version of the stairwells configuration. Comparison of color schlieren and shadow pictures.	96
33	Duct systems for shock tube tests.	98
34	Shock wave propagation in a straight duct; $M_s = 1.22$.	100

Figures (Continued)

Figure		Page
35	Shock wave propagation in a straight duct, $M_s = 1.53$; (test 15 373).	102
36	Shock wave propagation in a straight duct; $M_s = 2.20$; (test 15379).	104
37	Shock wave propagation in a T-shaped duct, $M_s = 1.21$; (test 15 325).	106
38	Shock wave propagation in a T-shaped duct, $M_s = 2.18$.	108
39	Inflow into a T-shaped duct at different Mach numbers.	110
40	Shock wave propagation in a L-shaped duct; $M_s = 1.22$; (test 15 382).	112
41	Shock wave propagation in a L-shaped duct, $M_s = 2.16$; (test 15 390).	114
42	Shock wave propagation in a double L-shaped duct, $M_s = 1.22$; (test 15 392).	116
43	Shock wave propagation in a double L-shaped duct, $M_s = 2.18$; (test 15 401).	118
44	Pressure records at the end wall of the straight duct; gage position 3 in version A of Figure 33.	120
45	Overpressure of the first peak vs shock Mach number at the three gage positions in the straight duct. Given is also the normal reflected pressure of a planar shock wave (black line).	121
46	Pressure-time histories at gages 1 to 5 of the T-shaped duct. $M_s = 1.21$; (test 15 325)	122
47	Pressure-time histories at gages 1 to 5 of the T-shaped duct. $M_s = 2.18$; (test 15 334)	123
48	Pressure records at the end wall of the L-shaped duct.	124
49	Pressure records at the end wall of the double L-shaped duct.	125
50	Schematic sketch of the multi-chamber configuration used for small-scale detonation experiments(dimensions in mm).	126
51	Photograph of the scaled chamber system.	127
52	Self-luminous plasma cloud after the detonation in the chamber system.	127
53	Blast propagation in the scaled chamber system. Time difference between ignition and exposure: $\Delta t = 450\mu s$ (test 15134).	128
54	Blast propagation in the scaled chamber system, $\Delta t = 750\mu s$ (test 15136).	128

Figures (Continued)

Figure		Page
55	Blast propagation in the scaled chamber system, $\Delta t = 900 \mu s$ (test 15128).	129
56	Blast propagation in the scaled chamber system, $\Delta t = 1500 \mu s$ (test 15132).	129
57	Pressure time history at gages 1 to 10 for a test in standard configuration (spherical 0.5-g NP-charge centered in detonation chamber).	130
58	Overpressure impulses versus time for a test in standard configuration. $t = 0$ denotes detonation. Origin: test 0015.MC / 15236.	135
59	Average overpressure in terms of $I(t) / t$ for the records from Figure 58. Here $t = 0$ denotes the time of arrival.	136
60	Ensemble-averaged overpressure and corresponding confidence bandwidth at gage 1 for the standard configuration. Ensemble of eight tests.	137
61	Ensemble-averaged overpressure and corresponding confidence bandwidth at gage 9 for the standard configuration. Ensemble of eight tests.	137
62	Ensemble-averaged overpressure impulse and corresponding confidence bandwidth at gage 1 for the standard configuration. Ensemble of eight tests.	138
63	Ensemble-averaged overpressure impulse and corresponding confidence bandwidth at gage 9 for the standard configuration. Ensemble of eight tests.	138
64	Ensemble-averaged mean overpressure in terms of $I(t)/t$ and corresponding confidence bandwidth at gage 1 for the standard configuration. Ensemble of eight tests.	139
65	Ensemble-averaged mean overpressure in terms of $I(t)/t$ and corresponding confidence bandwidth at gage 9 for the standard configuration. Ensemble of eight tests.	139
66	Schematic of the different charge locations in the detonation chamber.	140
67	Blast propagation in a scaled chamber system for different charge locations, $\Delta t = 450 \mu s$.	141
68	Blast propagation in a scaled chamber system for different charge locations, $\Delta t = 1200 \mu s$.	142
69	Comparison of the time-averaged pressure $I(t)/t$ at gage 1 for three different charge positions.	143

Figures (Continued)

Figure		Page
70	Comparison of the time-averaged pressure $I(t)/t$ at gage 9 for three different charge positions.	143
71	Ensembled-averaged pressure at gage 1 for three different charge locations.	144
72	Ensemble-averaged overpressure impulse at gage 1 for three different charge positions (yellow: confidence band of standard experiments).	145
73	Ensemble-averaged pressure at gage 9 for three different charge positions.	146
74	Ensemble-averaged overpressure impulse at gage 9 for three different charge positions. (yellow: confidence bandwidth of standard experiments).	147
75	Ensemble-averaged pressure-time histories. Comparison of gage 8,9 and 10 for different charge locations.	148
76	Ensemble-averaged overpressure impulse histories. Comparison of gage 8,9 and 10.	149
77	Influence of the charge weight on the wave propagation; $\Delta t = 900 \mu s$.	150
78	Influence of an Al-admixture to the NP-charge; $\Delta t = 900 \mu s$.	152
79	Peak values of the overpressure records at gage 1 as a function of charge weight (squares denote values from the three charges containing aluminum).	154
80	Impulse-time histories for different charge weights. Results for charges with an Al admixture are shown in red.	155
81	Impulse-time histories for different charge weights. Results for charges with an Al admixture are shown in red.	157
82	Impulses as function of the charge weight after 1ms, 2ms, 3ms and 4ms resp., gage position 4.	159
83	Impulses as function of the charge weight after 2ms, 4ms and 8ms resp.	160
84	Time-averaged overpressure $I(t)/t$ at gage 4 for different charge weights.	161
85	Time-averaged overpressure $I(t)/t$ at gage 9 for different charge weights.	162
86	Schematic sketch of the bore hole arrangement used in the test series on the influence of venting holes.	163
87	Influence of a venting hole; $\Delta t = 450 \mu s$.	164

Figures (Continued)

Figure		Page
88	Wave diagram for the multi-chamber system (distance of the gages from the center of detonation in terms of a pathlength along room and corridor axes). Results from tests with different venting holes are overlaid without signifying any relevant influence of the hole onto the incident blast.	165
89	Time-of-arrival values for the incident blast as a function of the venting hole diameter (note that symmetrically positioned gages have nearly identical ToA-values).	166
90	Comparison of two test at gage 1. Both tests in standard configuration without venting hole.	167
91	Comparison of a test in standard configuration to a test with 25-mm venting hole.	167
92	Time-averaged overpressure $I(t)/t$.	169
93	3-D diagram of the average pressure-time histories at gage 9 for different venting holes.	171
94	Average pressure load $I(t)/t$ at $t = 3$ ms versus the area of the venting hole.	172
95	Average pressure loads $I(t)/t$ at gage 9. Comparison of the curves for different charge weights to those with different venting holes and a 0.5-g NP-charge (colored). The parameter labeling the colored curves is the venting hole diameter in mm.	173
96	Shadowgraph sequence of a detonation in a closed room. Charge: HX2; (test: 15479).	174
97	Shadowgraph sequence of a detonation in a closed room. Charge: 0.18 g NP; (test: 15460).	176
98	Detonation of an HX2-ignitor inside a closed chamber (test 15 459). Overpressure and impulse versus time.	177
99	Detonation of a 0.18-g NP charge inside a closed chamber (test 15 460). Overpressure and impulse versus time.	178
100	Peak overpressure for a TNT surface burst as a function of the charge geometry. Included are hemispherical, spherical and cylindrical charges, lying ($L/D = 1$; $L/D = 5$) and standing upright ($L/D = 1$ to 3).	179
101	Peak overpressure vs distance for a bare cylindrical charge with $L/D = 5$ at a surface tangent burst.	180
102	Positive Impulse vs distance for a bare cylindrical charge with $L/D = 5$ at a surface tangent burst.	181

Figures (Continued)

Figure		Page
103	Time of arrival vs distance for a bare cylindrical charge with $L/D = 5$ at a surface tangent burst.	182
104	Double peaked blast wave domains for the 90° - and 180° -directions of a bare cylindrical charge with $L/D = 5$.	183
105	Isobars of a bare cylindrical charge with $L/D = 5$ at a surface tangent burst.	184
106	Iso-impulse curves of a bare cylindrical charge with $L/D = 5$.	185
107	Constant time-of-arrival for a bare cylindrical charge with $L/D = 5$.	186
108	Different bare cylindrical charges	187
109	Detonation of an axial ignited bare cylindrical charge in top view. $W = 1.29$ -g Nitropenta; $L = 28$ mm; $D = 7$ mm; $HOB = 2D$; t = time after ignition. (test 15 558)	188
110	Distance-time curves for face (0° -direction) and jacket wave (90° -direction) of two tests with axial ignited bare cylindrical charges. $HOB = 2D$; $L = 28$ mm; $D = 7$ mm; $L:D = 4:1$.	190
111	Estimated overpressure-range behavior for face and jacket waves from the fit-functions in Figure 110; (tests 15 556 and 15 558)	191
112	Detonation of a face ignited bare cylindrical charge in top view. $W = 1.31$ -g Nitropenta; $L = 28$ mm; $D = 7$ mm; $HOB = 2D$; t = time after ignition.	192
113	Wave diagrams of the face waves in 0° and 180° direction of a face ignited unconfined cylindrical charge. (test 15 559).	195
114	Wave diagrams of the jacket waves in 90° and 270° direction of a face ignited unconfined cylindrical charge. (test 15 559).	196
115	Estimated overpressure-range behavior for face and jacket waves from the fit functions in Figure 113 and 114.	197
116	Manufacturing procedure of a blasting composition to simulate the WES experiment. Instead of water the tube is filled with a gelatin solution	198
117	Detonation of an axial ignited confined cylindrical charge in top view. $W = 1.28$ g Nitropenta, $L = 28$ mm, $D = 7$ mm, tube diameter: $D_i = 11$ mm, $HOB = 2 D_i$, t = time after ignition.	199

Figures (Continued)

Figure		Page
118	Detonation of a face ignited confined cylindrical charge in top view. $W = 1.32\text{-g}$ Nitropenta, $L = 28\text{ mm}$, $D = 7\text{ mm}$, Tube diameter $D_t = 11\text{ mm}$, $HOB = 2 D_t$, $t = \text{time after ignition}$.	201
119	Wave diagrams of the face waves in 0° - and 180° - direction of an axial ignited confined cylindrical charge. (test 15 563 and 15 564)	203
120	Wave diagrams of the jacket waves in 90° and 270° direction of an axial ignited confined cylindrical charge. (test 15 563 and 15 564)	204
121	Estimated overpressure-range behavior for face and jacket waves from the fit functions in Figure 119 and 120.	205
122	Wave diagrams of the face waves in 0° - and 180° - direction of a face ignited confined cylindrical charge. (test 15 561)	206
123	Wave diagrams of the jacket waves in 90° and 270° direction of a face ignited confined cylindrical charge. (test 15 561)	207
124	Estimated overpressure-range behavior for face and jacket waves from the fit functions in Figure 122 and 123.	208
125	Side view of the Kohbar Towers building. The blue Figures correspond to the original dimensions. The measures of the small-scale model are given in black. Charge position is drawn in red.	209
126	Top view of the Khobar Towers building.	210
127	Schematic scenario of the Khobar Towers building.	211
128	Model of the Khobar Towers building in a scale of 1 : 200. The ground surface is transparent, allowing top view shadowgraphs. Visible are also the position of the pressure gages in the front wall.	212
129	Sketch of the 2-D Khobar Towers model for shock tube tests.	212
130	Sequence of shadowgraphs. $M_s = 1.7$. (test 15 503)	213
131	Sequence of shadowgraphs of a detonation test in the shock tube. The windows of the observation chamber were removed. As charge a HX2 igniter was used. (test: 15 517).	215

Figures (Continued)

Figure		Page
132	Open-shutter picture of a test with a bare spherical charge of 0.98-g Nitropenta, corresponding in full-scale to 20 700 lb. TNT. (test 15 545)	217
133	Sequence of shadowgraphs in side view of the loading of the Khobar Towers building by the blastwave generated by a bare spherical charge of 0.98-g Nitropenta.(test 15 545).	218
134	Shadowgraph of the flow field around the building.	222
135	Sequence of shadowgraphs in top view of a test with a spherical charge. Scaling factor of the model is 1 : 350. Charge weight: $W = 0.19\text{-g}$.	223
136	Peak overpressure at the front wall vs weight of the spherical charge.	225
137	Overpressure-impulse at the front wall vs weight of the spherical charge	227
138	Loading of the Khobar Towers model by an axial ignited unconfined cylindrical charge. Single frame shadowgraph in top view. $HOB = 14\text{ mm} = 2D$; $L : D = 4 : 1$. time after ignition: $t = 0.110\text{ ms}$; $W = 1.34\text{-g}$; (test 0055 KT)	229
139	Loading of the Khobar Towers model by a face ignited unconfined cylindrical charge. Single frame shadowgraph in top view. $HOB = 14\text{ mm} = 2D$; $L : D = 4 : 1$. time after ignition: $t = 0.140\text{ ms}$; $W = 1.12\text{-g}$; (test 0058 KT)	230
140	Loading of the Khobar Towers model by an axial ignited unconfined cylindrical charge. Shadowgraph sequence in side view. $HOB = 14\text{ mm} = 2D$; $L : D = 4 : 1$; $W = 1.27\text{-g}$.	231
141	Loading of the Khobar Towers model by a face ignited unconfined cylindrical charge. Shadowgraph sequence in side view. $HOB = 14\text{ mm} = 2D$; $L : D = 4 : 1$; $W = 0.984\text{-g}$.	233
142	Loading of the Khobar Towers model by an axial ignited confined cylindrical charge. Single frame shadowgraph in top view. Time after ignition $t = 0.160\text{ ms}$; $W = 1.46\text{-g}$ (test 0061 KT)	235
143	Loading of the Khobar Towers model by a face ignited confined cylindrical charge. Single frame shadowgraph in top view. Time after ignition $t = 0.160\text{ ms}$; $W = 1.11\text{ g}$ (test 0060 KT)	236

Figures (Continued)

Figure		Page
144	Loading of the Khobar Towers model by an axial ignited confined cylindrical charge. Single frame shadowgraph in side view. $W = 1.22\text{-g}$ (test 15 598)	237
145	Loading of the Khobar Towers model by a face ignited confined cylindrical charge. Single frame shadowgraph in side view. $W = 1.32\text{-g}$ (test 15 575)	239
146	Location of the pressure gages in the front wall of the model. A photograph of the destroyed facade of the original edifice is underlaid.	241
147	Pressure-time histories at 4 different locations of the front wall. The charge was confined and face ignited. Shadowgraphs of the same test are given in Figure 145. $W = 1.32\text{-g}$; (test 15 575).	242

Tables

Table		Page
1	Survey of the performed experiments for the Single Room Configuration, Model 1.	36
2	Survey of performed experiments for the Single Room Configuration, Model 2.	37
3	Survey of performed experiments for the Single Room Configuration, Model 3.	38
4	Survey of performed experiments for the Room Corridor Configuration, Model 4	39
5	Survey of the performed experiments for the Room Corridor Configuration, Model 5	40
6	Survey of the performed experiments for the Room Corridor Configuration, Model 6	41
7	Survey of the performed experiments for the Single - Story System, Version A	42
8	Survey of the performed experiments for the Single - Story System, Version B	43
9	Survey of the performed experiments for the Stairwells, 2 - D Version	44
10	Survey of the performed experiments for the Stairwells, 3 - D Version	45
11	Survey of the performed experiments for the Straight Duct	46
12	Survey of the performed experiments for the T-shaped Duct	46
13	Survey of the performed experiments for the L-shaped Duct	47
14	Survey of the performed experiments for the Double L-shaped Duct	47
15	Survey of the available data from the small-scale experiments in the scaled multi-chamber system	48
16	Survey of the available data from the small-scale experiments in the closed detonation chamber.	50
17	Gage positions and gage-charge distances for the small-scale model of the Khobar Towers building.	50

Section 1

Introduction

The main objectives of this research was to use advanced flow visualization techniques for a better understanding of the blast propagation through multi-chamber systems and to develop high fidelity experimental data for computer and code validation, This data is essential to validate advanced airblast codes which DSWA (formerly DNA) has developed for Nuclear Weapons Effects (NWE) and is using to determine the airblast propagation from a modern conventional weapon within and throughout complex structures from an internal detonation.

The ability to visualize the entire flow field as well as to measure the pressure at specific locations is absolutely essential to thoroughly validate the codes. The flow visualization techniques were conducted on small scale precise tests of flow through complex multi-room structures because it is impossible to visualize the flow field by advanced optical methods on large and even intermediate scale tests.

The laboratory scale phenomenology experiments were performed in two different test apparatus. The first series was conducted in a shock tube which allowed 2-D studies of various geometries. The optical measurement facilities are used to examine the interaction of planar square-wave shocks with different geometric details of the chamber system. The second series are HE explosion tests in multi-chamber models. These tests allowed 3-D studies of complex blast waves inside multi-room structures.

At DSWA request the original statement of work was modified. Some new tasks were added concerning the simulation of the bomb attack onto the Khobar Towers Building. Of special interest was the flow field in plan- and side-view as well as the pressure and impulse distribution at the front wall of the edifice.

The modified research program contains now the following main tasks:

Task 1: Shock propagation in component systems

- 1.1 Single room configuration with a door opening.
The shock wave enters the room by the opening.
Shock Mach number variation: $1.1 < M_s < 1.5$.
- 1.2 Room-corridor configuration.
The shock wave propagates along a straight corridor
and enters the room by the door. Same parameter variation as before.
- 1.3 Single-story system.
The shock wave propagates along a corridor with junctions
and enters different rooms. Same parameter variation as before.

- 1.4 Stairwells configuration.
The shock wave propagates in a stairwell model.
Same parameter variation as before.
- 1.5 Duct systems.
The shock wave propagates in ducts of different shape.
Four different geometries. Same parameter variation as before.

Task 2: Airblast propagation in a scaled chamber system.

- 2.1 Develop a 7 room model which is suited for optical visualization.
The details of the design will be provided by the government at contract award. The rooms will have door openings to study the blast propagation inside the system depending on the charge location.
- 2.2 Conduct 20 laboratory tests at a scale factor of approximately 1 : 77 using a 0.5 g spherical bare charge. All tests include optical visualization and pressure time records.

Task 3: Developments and experiments on special request of DSWA.

- 3.1 Development of small cylindrical charges.
 - 3.1.1 Bare charges , face ignited
 - 3.1.2 Bare charges, axial ignited
 - 3.1.3 Confined charges, face and axial ignited
(for simulation of the Khobar Towers bomb attack)
- 3.2 Simulation of the bomb attack onto the Khobar Towers Building
 - 3.2.1 Develop a laboratory scale model
 - 3.2.2 Visualization in side view
 - 3.2.3 Visualization in plan view
 - 3.2.4 Pressure measurement at different locations of the front wall

Section 2

Shock Propagation in Component Systems

A shock tube is a versatile device to investigate shock wave effects, unsteady flow phenomena and many other features of two-dimensional fluid dynamics. It is especially suited for flow visualization. Together with optical measurements and photographic methods, a shock tube represents a powerful tool for fluid dynamic experiments. Therefore it was used to study the propagation of shock waves in component systems.

2.1 Experiment Design.

Since the EMI shock tube and the optical and photographic methods were described in several earlier reports [e.g. 1, 2, 3], only an over-view summary is presented in the following paragraphs.

2.1.1 Shock Tube.

The physical characteristics of the EMI shock tube are:

Length of the driver section:	180 cm
Length of the driven section:	890 cm
Diameter of the tube:	20 cm
Optical test section (rectangular)	
inner dimensions:	4 cm x 11 cm
view field dimensions:	11 cm x 20 cm
Shock Mach number range:	$1 < M_s < 5$

2.1.2 Visualization Methods.

The visualization of complex flow phenomena is one of the essential tasks within the present DSWA project. For optical investigations in the shock tube, a Cranz-Schardin camera can be used advantageously because it produces several high-quality pictures of the same event at different times and can easily be combined with schlieren and shadow visualization methods. Our camera consists of 24 point-spark sources focused by a concave mirror on 24 lenses. At the instant of ignition, a spark is projected on the film through the very objective lens on which the image of the spark was copied.

2.1.2.1 Shadow Photography. In our shadow method arrangement, the point light source has a diameter of 0.5 mm. Furthermore, the lenses are not focussed in the middle of the test chamber, but on a reference plane at a distance in the range of 40 to 80 cm from the center of the chamber. Because the shadow method makes visible the second derivative of the gas density with respect to a length dimension, $\partial^2 \rho / \partial x^2$, this method is eminently suited for the visualization of shock fronts.

2.1.2.2 Schlieren Photography. In our schlieren method arrangement the same point light sources are used as before. A sharp knife edge is placed in the image plane of the light source. Instead of focusing the middle of the test chamber on the film - as is normally done - the reference plane is copied. In this case, schlieren and shadow methods are combined. As is known, schlieren methods make visible the density gradients, $\partial\rho/\partial r$, in a flow field, where r denotes the direction perpendicular to the knife edge. Therefore schlieren systems are suited to visualize spatial density changes. In combination with the shadow effect, shock fronts in the flow are visualized much more sharply.

2.1.2.3 Color Schlieren Photography. The schlieren arrangement with a knife edge (Toepler method) can be modified by applying a circular aperture for both the (virtual) light source and the schlieren cut-off. Then, it visualizes density gradients without any respect to their direction. In rather complex fields this can cause an ambiguity in the interpretation of the schlieren photographs.

This ambiguity can be resolved if the information about the density gradients is coded into different colors instead of into the local brightness of a schlieren photograph. Such a coding is fairly easily accomplished when a mask of colored filter segments is used as a virtual light source (or instead of the schlieren cut-off). To realize a setup of a single pass color schlieren system, a short-duration light source of high intensity and large radiation area is needed, as well as selected color masks. A detailed description is given in [4].

2.1.3 Pressure Measurement Equipment.

In addition to high-speed photography, also pressure measurements were performed. Shock- and blast wave experiments require a pressure recording system with a high time resolution and also a large gain capacity. Therefore a computer-operated transient recorder system (LeCroy type T.R. 8837 F) is in use as described in earlier reports (e.g. [3]). In maximum 16 channels can be operated simultaneously. Kistler gages (type 603B) with charge amplifiers (type 5001) serve as pressure transducers. The signals are stored in digital form and can be plotted channel by channel (Plotter: Epson type 800).

2.2 Results of Component System Tests.

This chapter presents a condensed description of numerous shock tube experiments. More detailed information can be found in the Quarterly Letter Reports [5] and in symposium papers [e.g. 6 to 8], prepared during the running time of the contract.

According to the original statement of work, all component systems experiments were intended for a shock Mach number range of $1.1 < M_s < 1.5$. In this case the flow Mach number behind the shock front is smaller than $M < 1$. In order to also include the case of supersonic flow speed, *additional* tests were performed with $M_s < \approx 2$.

2.2.1 Single Room Configuration.

Three different room configurations were investigated. Figure 1 sketches the models and gives the main dimensions. Since the ratio of inlet-area A to volume V is an impor-

tant parameter for the pressure history inside the room, the dimensions have been selected in such a way that this parameter takes on the values $A/V = 0.01 \text{ cm}^{-1}$, and $A/V = 0.02 \text{ cm}^{-1}$, respectively. The design of the models is shown in Figure 2. Tables 1 to 3 give a survey of the test numbers and the shock Mach numbers of the different performed experiments with the three models of the single room configuration.

2.2.1.1 Visualization of the Shock Wave Propagation. For the visualization the 24-spark Cranz-Schardin camera has been used. 12 light paths were adjusted for schlieren photographs and the remaining 12 for shadow photographs. Shadow photographs as well as schlieren pictures are therefore available for the *same* experiment. In some special cases, also individual color schlieren photographs have been made.

Figure 3 shows an extract from a picture series of a shock wave, penetrating into a single-room (model 1). The shock Mach number is $M_s = 1.41$. *Shadow* photographs have been chosen from the test series 14 783. As a contrast, Figure 4 shows *schlieren* pictures of the *same* test series. The time instants of the individual photographs are given in the figure captions. The time scale is based on the arrival of the shock front at the entrance of the room.

Both picture series show clearly the development and separation of vortices at the edges and the later formation of slip lines. The delayed formation of a secondary shock is typical. It causes the adaptation of the nozzle flow in the inlet to the flow behind the primary shock front. The inflow jet forms a mushroom shaped turbulent mixing zone (see e.g. Figure 3e).

As mentioned earlier, additional tests for Task 1 were performed in the Mach number range $1.5 < M_s < 2.2$. A series of shadowgraphs at $M_s = 2.05$ for model 1 is shown in Figure 5. The inflow differs significantly from the situation at $M_s = 1.41$ as demonstrated in Figures 3 and 4. Clearly visible at the edges of the inlet is a Prandtl-Meyer expansion fan. The interaction between reflected shock waves at the wall and the inflow jet entail a highly turbulent flow field as can be seen at later time instants.

Figure 6 shows a shock wave penetrating into model 2 of a single room. The dimensions are listed in Figure 1. The shock Mach number is $M_s = 1.31$. In contrast to the Figures 3, 4 and 5 a more extended space and time interval has been visualized. The most interesting event is shown in Figure 6 d, where the reflected shock interacts with the mushroom-shaped turbulent mixing zone of the inflow jet. The reflected shock is significantly deformed and dispersed by the inhomogeneous flow field and the three-dimensional mixing process. The following pictures demonstrate the important influence of the turbulent mixing. The different waves become dispersed in a short time-period.

In Figure 7 the same interaction between reflected shock and mixing zone of the inflow jet is visualized by using the method of color-schlieren photography. The different colors indicate the direction of the density gradient and allow easily to decide the face direction of the shock waves.

2.2.1.2 Pressure Measurements. In Figure 8, different pressure-time curves are presented that were measured in the experiments with the single room model 1. Figure 8 a shows the pressure history in the shock tube at a measuring point 540 mm in front of the model entrance. The side-on overpressure of the incident shock front is $\Delta p = 1.0$

bar. It has to be taken into consideration that the ambient pressure was reduced to $p_0 = 0.845$ bar.

Figure 8b shows the pressure history at the back wall center (see Figure 1). The first shock wave arriving at the measuring point causes a pressure jump of $\Delta p_r = 0.90$ bar as a result of a normal reflection. Due to the waves reflected at the floor and the ceiling, arriving about $110 \mu s$ later at the measuring station, a peak overpressure of about 3.35 bar is reached. After different reflections, this pressure is measured again about 400 - 600 μs after the arrival of the first shock front.

In the first 600 μs , an almost identical curve is found at the measuring point 30 mm above (Figure 8 c) and 30 mm below (Figure 8 d) the middle of the back wall. It is significantly different from the one in the middle (Figure 8b). These differences are caused by the various reflections leading to high pressure values in the symmetry axis of the model by head-on collisions. The differences of the pressure histories at later times can be attributed to the repeated interactions of the shocks with the turbulent flow field of the inflow jet. The shadowgraphs (e.g. Figure 5) convey a vivid idea of this process.

Obviously pressure-time histories depend sensitively on the model geometry and the location of the pressure gages. For the interpretation of the first peaks in the curves, a cinematographic sequence of the visualized flow field is very helpful. An example is shown in Figure 9. The shock Mach number was $M_s = 2.05$. The pressure curves are measured in the single room configuration of model 1 at the middle of the back wall (location 3) and at the lower gage position (location 4) respectively.

In the first phase, several peaks appear in the pressure-time histories. However, these peaks differ significantly in the given records a and b of Figure 9. To explain that, we have to analyze the flow field. In the records of Figure 9, an additional horizontal scale indicates the time instants where the individual shadowgraphs of Figure 5 were taken. The incident shock wave hits the wall at the location of gage 3 shortly after the exposure of Figure 5 c. It is evident that the first peak in Figure 9 a indicates the peak pressure of the reflected incident wave with a value of $p = 0.85$ bar. But it is also evident that there is a delay of the first peak at the location of gage 4 (see Figure 9 b) because the shock front is curved. The second peak in the pressure records is caused by waves reflected at the upper and lower horizontal walls (see Figure 5 d). Because the distance for the wave from the lower wall to location 4 is shorter than to location 3, the second peak in Figure 9 b is recorded earlier than in Figure 9 a. Whereas the pressure of the first peak at location 4, $p = 0.85$ bar, is the same as at location 3, significant differences are found at the second peaks, $p = 1.80$ bar and $p = 2.90$ bar, respectively. The reason is that the waves, reflected at the upper and lower walls, meet just at gage position 3. The pressure jump at this head collision is of course much higher than the pressure jump when only one wave front hits the pressure gage at location 4 at that time. It should be mentioned that the given pressure values are based on a pressure in the driven section of the shock tube of only $p_1 = 0.168$ bar absolute. To convert the curves in Figure 9 to sea level ambient pressure, the scale for the pressure and impulse must be multiplied by a factor of $K = 5.95$. (The pressure reduction in the shock tube was needed to achieve the desired Mach number $M_s = 2.05$).

As shown in Figures 5 f to 5 m in the shadowgraph sequence, the flow in the single room becomes more and more turbulent. Therefore the shock fronts are more and more dispersed. It is no longer possible to visualize them. However, even under these circumstances, several peaks are recorded in the pressure-time histories. The slopes are not so steep any longer and the amplitudes are reduced at later times.

In contrast to the pressure records the impulse curves are much smoother. This is the reason why we prefer the impulse data to evaluate mean overpressure values, p_a , at a given time t .

$$p_{\text{average}} = p_a = \Delta J / \Delta t = 1 / \Delta t \int_0^{\Delta t} p(t) dt \quad (1)$$

As an example the impulse-rise, $\Delta J / \Delta t$ at a time $t = 1$ ms is shown in Figure 10 for the single room model 2 and 3, respectively, as function of the shock Mach number of the incident wave. $\Delta J / \Delta t$ represents the mean overpressure, averaged in an time interval Δt . The two models differ only in the size of the entrance opening. (see Figure 1). the opening in model 3 is two times larger, the $\Delta J / \Delta t$ value at a given Mach number is higher than that for model 2. If $\Delta J / \Delta t$ is scaled with $1/A^{1/2}$, where A denotes the opening area, both curves coincide as shown in Figure 11.

2.2.1.3 Comparison between Pressure Measurements and Optically Obtained

Results. On the basis of cinematographic picture sequences, obtained with the Cranz-Schardin camera, range-time curves can be established of the primary shock front. From this, the shock-front velocity can be calculated. With the known sound of the ambient air one receives the shock Mach number. Using the Rankine-Hugoniot relation, the pressure jump at the shock front can be then found. It is compared to the directly measured pressure jump to check the consistency of the independent measuring methods.

Figure 12 shows the distance-time diagram for test 14 783, single room model 1, with $M_s = 1.41$. A front velocity of 483 m/s is determined for the incident shock wave. This leads to a shock Mach number of $M_s = 1.405$, which corresponds very well with the electronically measured value of $M_s = 1.41$. The corresponding overpressure is $p = 0.96$ bar, taking into account that the ambient pressure in the shock tube was $p_0 = 0.845$ bar. The direct measurement was $p = 1.0$ bar (compare Figure 8 a).

For the transmitted shock wave a velocity of $W = 404.5$ m/s is found before the reflection at the back wall, which corresponds to a shock Mach number of $M_s = 1.176$. Taking into consideration that this wave is normal reflected and that $p_0 = 0.845$ bar, the peak overpressure amounts to $p_r = 0.89$ bar. Again, there is an excellent agreement between the measured peak overpressure, $p_r = 0.90$ bar, and the value determined from the diagram (Figure 12). We can conclude that the optical results and the independent pressure measurements are consistent.

2.2.2 Room Corridor Configurations.

Three different models were investigated. They are sketched in Figure 13 where also the dimensions are given. The design is shown in Figure 14. Tables 4 to 6 give a survey of

the test numbers and the shock Mach numbers of the different performed experiments with the three models of the room corridor configuration.

2.2.2.1 Visualization of the Shock Wave Propagation. Figure 15 demonstrates the shock wave penetration into the room of a room corridor configuration. The dimensions correspond to those of model 6 (see Figure 13). The shock Mach number is $M_s = 1.41$. Shadow photographs of test 14 769 were selected. Schlieren photographs of the same experiment are shown in Figure 16. In these sequences can clearly be seen that the inflow happens under an angle to the symmetry line of the entrance opening. As especially shown by the schlieren photographs, the turbulent mixing volume hit the opposite wall as a jet where it will produce a high stagnation pressure. Also the flow behavior in the corridor near the entrance region is very complex. Here, immobile shocks can be found.

Figures 17 and 18 demonstrate the change of the inflow behavior in a room corridor system due to shock Mach number variation. Two different time instants were chosen, where the shock shapes show about the same pattern. The flow behavior in the entrance region differs significantly when the flow velocity changes from subsonic to supersonic speed. Secondary shocks appear. As a consequence, the strength of the incident shock entering the room changes also. This fact is of course well known from nozzle flow behavior.

The color schlieren photographs, Figure 19, show clearly that the inflow jet with the mushroom-shaped turbulent mixing region enters the room in a relatively small volume until it hits the opposite wall. After reflection, the inflow and the mixing region are dispersed. After a short time period turbulent mixing occurs in the whole room.

2.2.2.2 Pressure Measurements. A typical pressure-time curve measured in a room corridor configuration, model 6, is shown in Figure 20. The shock Mach number was $M_s = 1.67$. The gage was located at the vertical end wall as can be seen in Figure 14. In the first phase several peak appear due to the different reflections of the incident shock wave at the upper and lower side walls of the room. Besides the pressure-time history (green) the impulse-time curve (red) is also given. An additional scale (blue) indicates the time instants where the individual shadowgraphs of Figure 21 were taken. This scale is based on the first peak of the pressure record. The incident shock wave hits the wall at the location of the pressure gage between the exposure of Figures 21 a and 21 b. It is evident that the first peak indicates the peak pressure of the reflected wave. The second peak - at a time instant between Figure 21 c and 21 d - is caused by a repeated reflected wave. The third peak - very close to the time instant of Figure 21 e - comes from an upward and downward running wave system. The same system causes also the fourth peak just at the time instant of Figure 21 f. The ambient pressure at the experiment shown in Figure 21 was $p_o = 400$ mb. To convert the curves of Figure 20 to an ambient pressure at sea level, the scale for pressure and impulse must be multiplied by a factor of $K = 2.48$. Figures 20 and 21 demonstrate the eminent advantage of having both, pressure measurements and flow field visualization of the same event at one's disposal.

2.2.3 Summarized Results for Single-Room and Room-Corridor Configurations.

The results for single room and room corridor configurations are summarized in Figure 22. The average pressures are given in the first 0.5 ms (except for model 1, where the averaging interval was 0.25 ms) as function of the shock Mach number, M_s . These pressure values are valid for the central part of the end-walls. The dimensions of the six configurations can be found in Figures 1 and 13, respectively.

As a reference, the overpressure of a planar shock wave and the reflected overpressure are also included in Figure 22 (black lines) as function of M_s . Length b in the single room model 1 differs from model 2 by a factor of 0.5 (see Figure 1). All other dimension are unchanged. This fact was the reason for reducing the time interval for pressure averaging by the same factor. If doing so, both curves come very close together.

The room opening in model 3 is twice as big as in model 1 and 2. So it is not surprising that greater mean overpressure values were found here. It is noteworthy that the average pressure values are greater than those for planar shock waves but smaller than for reflected planar shocks.

The average pressures in the first 0.5 ms for the room corridor configurations are smaller than the overpressure of a planar shock at the corresponding shock Mach number M_s . Near $M_s \approx 1.4$ a kink in the curves of model 4 and 5 indicates a change in the flow behavior. As detected in the shadowgraphs, there is a change from subsonic to supersonic inflow. The opening acts like a nozzle. The situation of configuration 6 is different. The width of the corridor is smaller than the opening to the room. Above $M_s = 1.8$ the curves for model 4 and 6 coincide with each other.

2.2.4 Single-Story System.

A sketch of the two versions of single story systems used in our experiments is shown in Figure 23. Originally only version A was listed in the statement of work. In order to obtain a geometrical configuration that is more similar to the scaled multi-chamber system (see section 3) a second version was additionally tested. In the end-wall of the last room three pressure gages were installed. One of them in the symmetry line, the two others in the quarter points.

For experiments these models will be inserted into the measuring section of the shock tube. A „cookie-cutter“-tube punches out a part of the shock wave propagating in the shock tube. The inflow of this part of the shock wave into the different rooms is then investigated. Tables 7 and 8 give a survey of the test numbers and the shock Mach numbers of the different performed experiments with the two versions of the single story system.

2.2.4.1 Visualization of the Shock Wave Propagation. Figures 24 and 25 present sequences of shadow photographs of the two single story versions. The tests were carried out with a shock Mach number of $M_s = 1.63$ and $M_s = 1.61$, respectively.

The typical feature of the flow is the vortex formation at each corner of the room entrances. Clearly visible are the inflow jets into the rooms with the mushroom-shaped mixing zones. The propagation of the turbulence within the rooms can be observed especially in the last room. The flow pattern is quite similar to those seen in the single room experiments. In both versions of the single story system a secondary shock is formed near the symmetrical room entrances indicating a transition from subsonic to supersonic flow speed. The upwards directed secondary shock stands nearly still in the corridor.

2.2.4.2 Pressure Measurements. Some of the pressure records are given in Figures 26 and 27. As expected from tests with the single room and room corridor tests, the pressure-time histories of the three gages not only depend on the geometry but also on the gage positions. The pressure records at location 4 and 5 are nearly identical in the same version but differ by comparing with the curve at location 3. Differences are found also in the measured overpressure values in the two different systems.

However, if we average the time histories in accordance with

$$p = 1/t_0 \int_0^{t_0} p(t) dt \quad (2)$$

the differences turn out to be smaller than originally presumed. The result of a comparison is shown in Figure 28, where $t_0 = 0.5$ ms was chosen. The results for gage location 3 (center of the wall) and for 4 and 5 were given separately. The latter are in a symmetrical position to gage location 3 and show almost identical pressure-time histories, so that we used the averaged values in the diagram. There, in addition also curves were included, which refer to the undisturbed propagation of a planar shock wave in the shock tube, and to the normal reflection of such a shock wave. Also registered were the experimentally determined maximum pressures, p_{max} , in the time interval 0 - 10 ms. Starting with shock Mach number $M_s > 1.7$, an enlarged data scatter can be found. This might mainly be caused by the fact that the values were taken directly from the plots of the recordings, which can lead to errors in reading. Experiments with shock Mach number $M_s > 1.5$ must be performed in our shock tube under reduced ambient pressure in the expansion chamber. To scale them to sea level values the pressure data have to be multiplied by scaling factors up to 10. Small errors in reading become then noticeable at higher Mach numbers.

As result in the comparison of the two single story versions under the described experimental conditions can be stated, that:

- the maximum pressure, p_{max} , which appears in the first 10 ms at gage location 3 and 4 and 5, respectively, is the same in the two versions. It corresponds to the reflection pressure of a planar shock wave,
- the average pressure, $\bar{p}_{0.5}$, (averaged for the first 0.5 ms) at gage location 4 and 5 is the same as expected. However, it is smaller in version A than in version B,

- the average pressure, $\bar{p}_{0.5}$, at gage position 3 (center of the end wall) is practically the same in the two versions. It is of the same order of magnitude as in the case of the undisturbed planar shock wave.

2.2.5 Stairwells Configuration.

Two different stairwells configurations were investigated as sketched in Figure 29. They represent a 2-D and a 3-D version. The design of the models is shown in Figure 30. Tables 9 and 10 give a survey of the test numbers and the shock Mach numbers of the different performed experiments with the 2-D and 3-D versions of stairwells.

Color schlieren and shadow photographs are compared in Figure 31. The shock Mach number is $M_s = 1.33$. The difference in the two visualization methods become evident in this comparison. While the *shadow* photographs mainly visualize the wave fronts and the vortices at the individual stair, the *color schlieren* photographs also indicate the direction of the density gradient. Especially in the vortices at the stair-steps it can be seen that all possible colors appear. This means that the direction of the density gradient in small areas changes steadily, i.e. there is a rotational velocity. In the center of the vortex a density minimum is to be found.

As shown by the picture sequence the loading of the downstream located stairs must be obviously higher than of the opposite being stairs. The incident shock wave is at first diffracted by rarefaction waves which are created at each step by flow expansion. The curved shock front is then reflected nearly normal at the downstream located stairs. The reflections lead to a higher loading of this part of the stairwells.

Figure 32 demonstrates the shock wave propagation in the 3-D stairwells configuration by color-schlieren pictures as well as by shadowgraphs, taken at nearly the same time instants. The shock wave with $M_s = 1.33$ enters the stairwells from above. Whereas one part of the wave is reflected at the first stairs, the rest keeps on moving forward (Figure 32 a). In the sequel now a complicated three dimensional turbulent flow field develops where waves, partly reflected and partly transmitted are mixed together. The picture sequence conveys an impression of the complex interaction processes.

2.2.6 Duct Systems. Visualization of the Flow Field.

The geometry and the gage position of the four different duct systems used for shock tube tests are shown in Figure 33. We distinguish between *straight* duct (version A), *T-shaped* duct (version B), *L-shaped* duct (version c) and *double L-shaped* duct, respectively. The tests were performed in the shock Mach number range $1.1 < M_s < 2.2$. Tables 11 to 14 give a survey of the test numbers and the shock Mach numbers of the different performed experiments with the four duct systems.

2.2.6.1 Straight Duct. Shadowgraph sequences of the straight duct system (version A in Figure 33) are presented in Figures 34 to 36 for different Mach numbers.

At time $t = 0$ the shock front hits the front wall of the duct system. In the first moment the central part of the shock front enters the duct without any disturbance whereas the rest of the front is reflected at the front wall. The pressure behind the reflected wave is

much higher than behind the entering shock wave. Therefore, gas from the high pressure region is accelerated toward the duct entrance. Depending from the shock Mach number characteristic patterns develop at the sharp corners of the entrance.

The flow field at Mach number $M_s = 1.22$ is shown in Figure 34 (test 15 369). It is visualized by shadowgraphs taken with the 24-spark Cranz-Schardin camera. The inflow at this Mach number is subsonic. Spiral vortices are formed at the entrance corners. Between Figure 34 c and 34 d the shock front is reflected at the end wall and propagates now upstream. In Figures 34 e to 34 h the interaction of the reflected shock wave is visualized. The outflow of the reflected wave at the duct entrance is to see in Figures 34 g and 34 h.

At $M_s = 1.53$, Figure 35 (test 15 373), no significant difference can be detected in the first 10 μs in comparison to Figure 34. The same mechanism is acting at the beginning of the entering process. But later on a secondary shock is created (Figure 35 d), indicating a transformation from supersonic to subsonic flow speed. In Figure 35 e the entering shock has just arrived the end wall and is reflected. The rest of the picture sequence makes visible the interaction between the reflected shock wave and the wall boundary layer and the turbulent regions of the inflow.

The flow behavior at $M_s = 2.20$ is visualized in Figure 36 (test 15 379). Remarkable are the diagonal running waves (see Figures 36 c and 36d). This type of waves are typical for supersonic expansion flows.

The flow behavior at the entrance corners in all of our examples indicates an additional gas flow into the duct. This flow transports additional mass into the channel. Therefore the reflected pressure at the end wall must be expected greater than the normal reflected pressure of a planar shock wave of the same Mach number at an extended plane wall.

It is remarkable that even in such a simple geometric system like a straight duct such a complicated flow field develops.

2.2.6.2 T-shaped Duct. Shadowgraph sequences are shown in Figures 37 and 38. At an incident shock Mach number of $M_s = 1.21$ (Figure 37; test 15 325), the inflow into the two branches of the T-shaped duct is subsonic. It is supersonic at $M_s = 2.18$ (Figure 38; test 15 334). In the first case spiral vortices are formed at the corners of the branches. By interaction with the reflected shock waves at the walls, the vortices were split in some much smaller vortex centers and turbulence starts. In the supersonic case, rarefaction fans appear and a secondary shock is formed.

The variation of the flow pattern at different shock Mach numbers, M_s , is given in Figure 39. The shadowgraphs are selected according comparable states of the flow.

2.2.6.3 L-shaped Duct. Figures 40 (test 15 382) and 41 (test 15 390) demonstrate the flow behavior at low and high shock Mach numbers for a shock entering a L-shaped duct.

In Figure 40 a the shock front with $M_s = 1.22$ (subsonic case) just hits the front wall of the duct system. Vortices are created at the sharp entrance corners as known e.g. from

the shadowgraphs of the straight tunnel. By interacting with the reflected waves (Figures 40 c and 40 d) they are destroyed and transferred into a turbulent regime. As a consequence of the numerous shock wave reflections at the duct walls, a lot of wave fronts arrive in a very short time at the end wall of the channel (Figures 40d and 40 e).

The wave propagation in case of a supersonic inflow into the tunnel at $M_s = 2.16$ is given in Figure 41. Instead of a spiral vortex at the second corner a rarefaction fan is formed with a secondary shock. The same behavior can be seen at the inner corner of the horizontal part of the duct (Figure 41d). Several waves hit the end-wall at nearly the same time (Figure 41 f). The curvature of the reflected wave in Figure 41g indicates a nonuniform flow in this part of the tunnel.

2.2.6.4 Double L-shaped Duct. The subsonic and supersonic inflow behavior of a shock wave into a double L-shaped duct is visualized in the shadowgraph sequences of Figures 42 (test 15 392) and 43 (test 15 401). As long as the entering shock wave propagates in the first L-shaped part of the channel, the flow field does not differ from that found for the corresponding L-shaped duct (see Figures 40 and 41) at the same Mach number. Later on of course significant changes can be observed.

At $M_s = 1.22$ (Figure 42) a lot of reflected waves are created (see Figure 42 d and 42 e). Therefore we have to expect a finite rise-time to a first pressure maximum instead of a sudden jump in the pressure records of gages 1 and 2. Remarkable is the stability of the vortex in the end part of the duct (see Figure 42 e to 42 h).

In the supersonic case, $M_s = 2.18$, (Figure 43), expansion fans develop at the sharp corners as expected and also seen at the other duct systems. Several slowly moving secondary shocks can be detected in the nonuniform turbulent flow in the tunnel.

2.2.7 Duct Systems. Pressure Measurements.

2.2.7.1 Straight Duct. The position of the three pressure gages are marked in Figure 33, version A. Typical pressure records at the end wall of the duct (gage 3) are represented in Figure 44 for Mach numbers $M_s = 1.22$ and $M_s = 2.20$. After the pressure jump due to the reflection of the entering shock wave, the pressure in both cases holds at first a nearly constant level. This period lasts about 0.8 ms at $M_s = 1.22$ and about 0.65 ms at $M_s = 2.20$ before the pressure drops down due to the arrival of a rarefaction wave. This wave starts at the duct entrance when the incident wave, reflected at the rear wall arrives there and starts to expand.

It should be noted that the pressure scale in Figure 44 b must be multiplied by a factor of 8 to get the sea level value. The supersonic test was performed at an ambient pressure in the shock tube of only 125 mbar. It should be taken into account also that time zero in the plots is not identical with time zero of the corresponding picture sequences.

The overpressure of the first peaks in the records of the three gage positions (see Figure 33) are given in Figure 45 as function of the shock Mach number of the incident shock wave. Included in this diagram is also the curve of a normal reflected planar shock wave, $p_{refl} = f(M_s)$ (black line).

As expected, the measured first peak values at gage position 1 and 2 agree very well with this theoretical relation. But significant deviations are found for the first peak at gage 3 (end of the duct). The peak pressures exceed the theoretical values for normal reflection by a factor of about 1.5. The reason for that is the additional inflow into the duct as a result of the wave reflection at the entrance wall as explained by the discussion of the corresponding shadowgraphs.

2.2.7.2 T-shaped Duct. Pressure measurements were performed at five different locations as marked in Figure 33 (version B). Pressure-time histories at these positions are summarized in Figure 46 for $M_s = 1.21$ and in Figure 47 for $M_s = 2.18$, respectively. The data is corrected for an ambient pressure of 1 000 mbar..

At gage position 4, the first peak of the reflected shock wave at $M_s = 1.21$ is more than a factor of 2 greater than at gage position 3 and 5. A factor of more than 3.5 is found at $M_s = 2.18$. This was to expect from tests with the single story configurations (see Figure 28). But after a while, the average pressure at gage 4 reaches more and more the same pressure level found at gages 3 and 5. The signals of the corresponding gages (e.g. 1 and 2; 3 and 5) are nearly identical. This indicates that the flow field is symmetrical in respect to the centerline of the duct.

2.2.7.3 L-shaped Duct. As marked in Figure 33, version C, two pressure gages are installed in this duct system. Two pressure-time records from the rear wall (gage 2) at $M_s = 1.22$ and $M_s = 2.16$, respectively, are represented in Figure 48. As observed in the shadowgraphs of Figure 40 at $M_s = 1.22$ not only one but several wave fronts arrive in a quick sequence after first signal at the rear wall of the channel. That is the reason why a pressure rise with finite slope is found in the pressure record of Figure 48 a. Altogether the pressure time history is more complex than that of the straight tunnel.

In the case of $M_s = 2.16$, Figure 48 b, the first arriving wave jumps to a first peak value before other reflected waves reach the rear wall. This behavior was to be expected according to the shadowgraphs of Figure 41. Due to the reduced ambient pressure in the shock tube at this test, the pressure scale in Figure 48 b must be multiplied by a factor of 8 to get the right values for normal ambient pressure.

2.2.7.4 Double L-shaped Duct. The locations of the two installed pressure gages are given in Figure 33, version D. Two pressure-time records of gage 2 in the rear Wall are shown in Figure 49 for $M_s = 1.22$ and $M_s = 2.18$, respectively. At the low Mach number, Figure 49 a, the sloped pressure rise at the beginning of the record is even more pronounced than in the L-shaped duct. This is not surprising after having seen the corresponding shadowgraphs, especially Figure 42 e.

The pressure signal at gage 2 in the case of $M_s = 2.18$ starts with a jump to the first peak. Then some more intense shocks arrive at the rear wall within a short time. In the shadowgraphs of Figure 43 this behavior is visualized. Remember that the pressure scale in Figure 49 b must be multiplied by a factor of 8.

Section 3

Airblast Propagation in a Scaled Chamber System

3.1 Experimental Setup.

The objective of this test series was to provide detailed information on the flow phenomena in a generic multi-chamber system exposed to an indoor explosion. Since the most essential information is obtained by the visualization of the flow features it was decided to study a closed single-story system with transparent floor and ceiling. The final design of the model was based on a scale of 1:77 and consists of 2 rows of 3 identical rooms separated by a corridor leading to a larger chamber. A schematic sketch is shown in Figure 50, a photograph of the assembled setup in Figure 51. Based on the chosen scale the dimensions of the 6 rooms correspond to 10 m x 9 m x 3 m in a realistic scenario, the width of the corridor to 2m and the large chamber at the end to 10 m x 21.56 m.

The walls of the model are realized in form of 39-mm high steel rails, the inner ones having a thickness of 10 mm. Thin sheets of rubber glued onto the rails as sealing added another millimeter to the height. The connecting doors of the room system are substituted by 20-mm wide slots centered in the corridor walls which keeps the model essentially 2-dimensional. 10 mm thick panes of a transparent polycarbonate material (tradename Makrolon) are bolted onto the top and bottom of the model.

For all experiments of the present study the source of the detonation was located in the lower left room which accordingly will be termed detonation chamber in the following. In this room the Makrolon panes are subjected to very high dynamic stresses. To avoid hazardous damage of the panes they were reinforced by additional aluminum plates bolted onto the floor and ceiling of this chamber.

The indoor explosions in these model experiments were generated by the means of custom-made spherical Nitropenta-charges which have already been successfully applied in a number of previous studies (see below). The standard configuration for the present study was that of a 0.5-g charge located at the center of the detonation room. This corresponds to a charge density γ of approximately 0.822 kg / m³.

3.2 Charges.

In order to resume some facts about our small-scale He-charges: they essentially consist of very fine grained Nitropenta powder (pentaerythritol tetranitrate $C_5H_8N_4O_{12}$, PETN). The powder is dissolved in acetone with a small volume percentage of gun-cotton admixed so that it forms a highly viscous paste. Two electrodes connected by a fine wire are fixed in a centered holder that is repeatedly dipped into the paste. By the repetitive dipping and drying a droplet of the explosive is grown around the central wire. When the droplet size is sufficient, an ideal spherical charge can be turned on a lathe before the holder is removed. The finished charge has a diameter of 10 mm. From previous tests the TNT equivalent value of these spherical charges was determined to be approximately 1.2. The charges can be quite reliably ignited by applying a high voltage

discharge (in the order of 8 to 10 kV) to the electrodes which vaporizes the central ignition wire thus driving the detonation of the Nitropenta charge.

3.3 Diagnostics.

In the design of the test setup emphasis was put upon the feasibility of flow visualization. It does not only help in the interpretation of more quantitative measurements which are typically only possible for a limited number of measurement points but is also a valuable means for the comparison with numerical simulations.

Nevertheless, the comparatively large dimensions of the model of about 320 mm x 590 mm call for some compromises. E.g., they are too large for the field of view of our 24-spark Cranz-Schardin camera. Thus single shot photography in a setup with a larger field of view (diameter approximately 600 mm) had to be applied. In addition, the quality of the Makrolon panes is not comparable to that of optical glass, thus schlieren- or color-schlieren techniques would yield only poor results. However, quality shadow photographs of the flow field are feasible.

The flow visualization was supplemented by pressure measurements. In the smaller rooms 1 to 5 a piezoelectric pressure gage type Kistler 603B was installed directly opposite to the door opening. Room 6, the larger end chamber was equipped with another five of these gages. The natural frequency of these gages is larger than 400 kHz, low pass filtering of the input to the charge amplifier at 180 kHz guarantees a linear frequency response and a signal rise time of approximately 2 μ s. Since the output of the charge amplifiers is digitized into a transient recorder with 8 kWords per channel, the sampling rate and length of the monitored time window are directly connected. The typical settings for the different gages are listed below.

gages	sample rate	window length
1	0.25 μ s	2 ms
2 - 5	0.50 μ s	4 ms
6 - 10	1.00 μ s	8 ms

3.4 Experimental Results for the Standard Configuration.

3.4.1 Results of the Flow Visualization.

Figure 52 shows a photograph obtained during the detonation of the charge by means of the Cranz-Schardin optics, though no shadow photograph. The visible exposure is due to the self luminous plasma cloud generated by the explosion. The photograph cannot reveal any time-resolved information about the propagation and decay of this plasma cloud; the exposure reflects a time-integration over the whole period of self-luminosity since the Cranz-Schardin camera is operated in an open-shutter technique. The same mode of operation is used for shadowgraphy, only that the test setup is additionally illuminated by a short duration spark that is exploited to visualize the density field. The time of exposure for the shadowgraph is determined by the duration of the

spark facilitating time-resolved photography. Nevertheless the self-luminous structure is superposed to all shadow photographs thus causing an overexposure and degradation of the contrast in certain areas like room 1 and the corridor.

Figures 52 to 56 show a sequence of shadowgraphs from individual tests, taken at different time instants after the ignition of the charge. The flow phenomena are similar to those seen in the shock tube tests of single components and component system. Room 1 directly opposite the detonation chamber is very rapidly filled by a turbulent jet of hot detonation products. The initial blast front is propagating along the corridor. Whenever it reaches one of the doors, it is deflected at the left corner of the corridor wall where a vortex rolls up. The further development is essentially the same as in the single-chamber and room-corridor configurations of the shock tube tests. The incident blast wave enters the rooms as a nearly cylindrical front. Then it is first reflected at the side walls, later on at the wall opposite from the door and sets up a number of multiple retro-reflections. The afterflow of the blast wave enters the rooms in form of jet-like structures with a turbulent head which is formed from the vortices which separate from the edges of the entrance. The turbulent plumes grow until they finally fill the whole chamber. In the intermediate state instabilities of the plume boundaries are quite obvious. Additional pressure waves are emanated from a multitude of reverberations within the detonation chamber.

3.4.2 Pressure Measurements.

To present an example of the pressure measurements, Figure 57 shows the recorded pressure-time histories for test 0015.MC (15136) with the exception of gage 5 originating from test 0014.MC (15134). The highest pressure peaks are found at gage 1 which is closest to the detonation and directly subjected to the strong jet from the detonation chamber. The room is pressurized to a average pressure of about 5 bar within a few hundred microseconds. Pressure peaks due to reflections are higher than for the initial blast front, because they can superpose at points of symmetry (the gage location is such a point) in a chamber. At gage 2 and 3 we find a different picture. The pressure peak of the incident blast front is already significantly reduced and the average pressure of during the first 4 ms attains only a value of about 1 bar. Within this period only a slight increase can be noticed, in contrast to the behavior at gages 4 and 5. Here the average pressure stays below 1 bar for the period below 2ms, but than starts to increase almost linearly to a value of 2 bar at $t = 4\text{ms}$. The end chamber (gages 6 to 10) again is pressurized much faster, the average pressure begins to rise immediately after the arrival of the incident blast front and obtains a maximum of about 2.7 bar after approximately 3 ms. In the further development it slowly decreases to 1.7 bar after 8 ms. The highest pressure peaks are found at gage 9 which is centered in the right wall of the chamber and thus again subjected directly to the jet-like inflow from the corridor. Again also the superposition of reflections can lead to high pressure peaks at this point of symmetry.

The pressure signatures are rather complex due to the multifold reflections and reverberations both in the detonation chamber and the other rooms. Even after 8 ms significant pressure waves can be detected. In addition, a field of turbulent fluctuations rapidly covers large area of the chamber system. The pressurization of the whole complex to some equilibrium value is non-uniformly distributed in time and space. As to be ex-

pected, the greatest impact of the detonation is found in room 1. Since a large amount of the detonation products is channeled into the corridor and directed into the end-chamber (room 6), this room is pressurized faster than the rooms branching from the corridor where the additional deflection diminishes the effects.

3.4.3 Impulse-Time Histories

From the pressure-time histories the values for the time-of-arrival (ToA) at a gage can easily be deduced. A time-integration of the pressure starting at the time-of-arrival yields the time-histories of the overpressure impulse. A few examples are shown in Figure 58, again for test 0015.MC (15136). The overpressure impulse can be a more appropriate way to rate the load onto a wall, especially if the time-scale of the pressure fluctuations is very small compared to the typical response time of the wall. Since the overpressure impulse curves often obscure differences in the initial time period we sometimes represent them by the way of an time-averaged overpressure:

The value of this variable at a time instant t equals the average overpressure during the time interval between the arrival of the blast front and the instant t ; i.e., at any given moment after the time of arrival one looks for the height of an equivalent step function that yields the same momentaneous overpressure impulse $I(t)$.

Figure 59 shows this time-averaged overpressure versus the time since blast arrival for the same gages and the same test as in Figure 58. Essentially the curves reflect the discussed effects on the pressurization of the individual chambers.

3.4.4 Repeatability of the Tests

We started the investigation with a series to establish some limits of reproducibility. We chose the standard configuration of a 0.5-g Nitropenta charge located in the center of the detonation chamber and repeated the test eight times. For the analysis we formed an ensemble average from the individual pressure recordings at each gage. As a means to define the confidence bandwidth of this average we inspected each ensemble *pointwise* for the minimum and maximum values. The same we did with the individual histories of the overpressure impulse at each gage. Figures 60 to 65 exemplify some of the results, Figures 60 and 61 for the overpressure at gage 1 and gage 9, Figures 62 to 65 for the corresponding overpressure impulses.

The typical bandwidth of the overpressure recordings for gage 1 and gage 9 is about $\pm 15\%$ of the average value. The definition of the bandwidth by the pointwise minima and maxima is quite strict; assuming that the differences between the tests follow a gaussian distribution, it amounts to about three times the standard deviation of the ensemble.

The results for the overpressure impulse curves are not only given directly, but also in the form of the time-averaged overpressure that was defined as the overpressure impulse $I(t)$ at a given instant divided by the period t since the arrival of the primary shock. The bandwidth for these curves is about 10 %.

In summary the reproducibility of the experiments is excellent, especially when we take into account the complex flow field with large turbulent areas. Some of the scatter can also be attributed to small deviations of the charge weight from the nominal value of 0.5 g.

3.5 Influence of the Charge Location.

Since the position of the charge in the center of the detonation room is quite arbitrary the question rises how relevant is the exact position of the charge in the detonation chamber. Thus we expanded the experiment from the standard configuration to tests where the charge was positioned on the room diagonal down at the lower left or at the upper right (see Figure 66).

Figures 67 and 68 show shadow photographs for the various charge locations at two different instants after the detonation. The general features in all configurations are very similar especially at the later time of 1200 μ s. At the earlier time small differences can be found for the arrival times of the primary blast front, in the direction of the inflow into room 1 opposite the detonation chamber and in the shape and size of the mushroom-like jets entering the rooms 2 and 3.

Upon the inspection of the pressure measurements the largest effects of the charge locations are found for room 1 opposite the detonation chamber. Figure 69 shows the time-averaged overpressure histories $I(t)/t$ for the three different cases. Again the data are derived from multiple tests by pointwise averaging, the ensemble being 8 tests for the standard configuration and 4 tests for both the case of charge located at the lower left or the upper right.

The differences in the start-off phase are obvious, but also at later times still significant, since the curves do not fall within the 10 % margin around the curve for the charge in center position. The differences have a number of reasons: The distance to gage 1 is different for the three charge positions and the superposition of the multiple reflections in the detonation chamber and in room 1 have a different timing. In addition the jetlike outflow from the detonation chamber attains a different preferred direction and is also afflicted in different ways by the shock reverberation in the room.

In the end chamber, room 6, the effects are much smaller (refer to Figure 70). In fact they are even smaller than the confidence interval of the reference case with the charge at the center position. To summarize things, the exact charge position essentially has a significant influence on the average loading of the walls only in the vicinity of the detonation chamber, further away it is justified to neglect it.

For completeness of the graphical information plots of the ensemble-averaged pressure and the overpressure impulses are included in Figures 71 to 74.

Figure 75 compares the pressure records at the gages 8, 9 and 10 in the end chamber for the three charge locations. Again we see that the influence of the charge position is comparatively low. But we see pronounced differences in the loads on gages 8 and 10 compared to that on gage 9. This highly non-uniform loading of the rear wall is even more obvious in Figure 76 showing the corresponding overpressure impulses.

3.6 Variation of the Charge Weight.

Another topic we investigated was that of a parametric study on the charge density in the detonation chamber. For this study we had to diversify our choice of Nitropenta-charges. Before, our institute has manufactured two types: spherical 1-g and spherical 0.5-g charges. Following the same process a number of specimens were manufactured ranging from around 0.06 g to 0.5 g. The test series thus covers approximately one decade of values for the charge density.

Whereas the larger charges can be turned on a lace as a final step of the production to give them a smooth spherical surface, this procedure is rather difficult and time-consuming. Since we were not sure whether we could detonate the smaller charges we skipped this final step in the production of the samples used for this parametric test series. Thus their shape is not exactly spherical and the surface is not really smooth.

We also included three further charges with an additional variation: these consisted of a core of pure Nitropenta and an outer layer of Nitropenta which had a certain amount of very fine aluminum powder admixed to it. The weights of these three charges were ranged between 0.46 g to 0.52 g Nitropenta and an additional content of aluminum powder ranging from 0.06 g to 0.10 g. The charges were meant to investigate the feasibility of experiments on afterburning effects in indoor explosions.

In Figure 77 some shadowgraphs from this test series are assembled. The photographs are all taken at a time $\Delta t = 900 \mu s$ after the detonation. The propagation speed of the blast wave inside the chamber system depends of course on the charge weight. Also the amount of overexposure due to the luminescence of the plasma cloud varies with the energy released in the detonation.

Figure 78 shows that the luminescence is significantly more intense for the charges which contain the Al-admixture. Though the total charge weight is not exactly identical for the shown cases and the digital reproduction of the shadowgraphs cannot cope with the quality of the negatives, it is evident that the light emission increases with the amount of aluminum in the charge.

Figure 79 shows the peak values of the initial blast wave at gage 1 in the room opposite the detonation chamber. Essentially one finds – within the scatter of the data points – a linear dependence of the peak pressure from the charge weight. The three aluminum containing charges do not show any peculiarities, within the limits of data scatter they are consistent with the data set from the pure Nitropenta charges (in Figure 79 the values from pure Nitropenta charge are shown as circles, the values from the Al-containing charges as squares). A second set of data points is also given in Figure 79, it depicts the highest peak occurring within the 2-ms time record of the overpressures at gage 1. This highest peak occurs typically within the first quarter of a millisecond after the arrival of the initial blast wave, but is not necessarily the same peak of the pressure signature in all cases. Again the data for pure Nitropenta charges can be fitted approximately by a straight line. Possibly due to the fast pressurization of the chamber the fit curve does not cross point zero. For the three Al-containing charges we find values well above the regression line. The highest value can be attributed to the charge containing about 0.1 g aluminum.

Since the detailed pressure-time histories with the multifold and intense peaks do not convey too clear a picture of the essential findings, we restrict the presentation to graphs of the overpressure impulse shown in Figures 80 and 81 for different gage positions. They depict the impulse versus time with the charge weight as an additional parameter. Given is the total charge weight; for the charges with aluminum admixture the content of Al is added in brackets.

The impulses increase both with time and charge weight, which is only naturally. At a fixed location all curves are essentially similar, but they differ from gage to gage and especially from room to room. For example, the absolute values of the impulses in the two side chambers 4 and 5 (Figure 80) 4 ms after the blast arrival differ only slightly. But they deviate by a factor of approximately 2 from the impulse at gage 9 in the end chamber (Figure 81). The impulse at this gage in the center of the rear wall is in all cases noticeably larger than at gage 6 or 7 in the same chamber. The diagram also indicates a different curvature of the impulse histories in room 4 and 5 compared to that of the histories in the end-chamber, room 6. In the latter case it is convex whereas it is essentially concave for room 4 and 5. A possible reason for these differences is that the inflow direction into the end chamber is identical to that of the afterflow behind the incident blast wave in the corridor. In contrast, the inflow into the side chambers branches off from this main direction at an angle of nearly 90°. In addition, in the first phase the inflow into the side chambers is only driven by the overpressure behind the initial blast front. At later times the pressure in the corridor increases due to reflected waves in the different rooms which causes the inflow rates into the side chambers to rise.

The impulses attained after 1 ms, 2 ms, 3 ms and 4 ms at gage 4 and 5 are shown in Figure 82. The data for the pure Nitropenta charges can be approximated by linear functions which confirms the similarity of the impulse-time histories. The three data points for a charge weight larger than 0.55 g originate from the aluminum-containing charges. At gage 4 and 5 these points deviate noticeably from the straight line fits thus indicating that the aluminum content contributes more to the impulse than an identical quantity of Nitropenta.

The similar effect, but less pronounced is found in Figure 83 which gives a similar diagram of the impulses at the gages 7 and 9. For the better comparison to previous result Figure 84 and 3-36 show the same analysis for the time-averaged overpressure $I(t)/t$. Also this representation signifies no specific instant where the curves for aluminum-containing charges starts to deviate from those for pure Nitropenta charges.

In conclusion we can say that – in the covered range of charge densities from 0.1 to 0.85 kg/m³ and within the reliability of single test results – the overpressure impulses essentially scale with the charge weight. Aluminum contents in the charge seem to increase the released energy. The number of tests though is too small to be too conclusive about the time-scale of this additional energy release.

3.7 Influence of a Venting Hole.

As far as described until now the setup reflects a situation where a charge is deposited in the detonation chamber and explodes there. In a more realistic scenario a bomb might have penetrated the ceiling of the room before the detonation occurs. Thus we

decided to investigate the changes that a hole in the detonation chamber imposes onto the fluid-dynamics of the explosion and the pressure loads of the walls. For this purpose we modeled the penetrated ceiling by a bore hole through the steel and Makrolon cover of the chamber (see Figure 86). The axis of the bore hole was directed onto the center of the charge. Since the detonation causes a jetlike outflow from the chamber which we did not want to show up in the shadow photographs we inclined the axis of the hole 45° against the ceiling in direction to the outer corner of the model. The diameter d of the bore hole was varied from 8 to 25 mm (in comparison: the 0.5 g charge has a diameter of 10 mm). In full scale this corresponds to hole diameters varying from 0.6 to 2 m.

The inspection of the shadow photographs from the test series was somewhat disappointing. Figure 87 compares three shadowgraphs, each one taken 0.45 ms after the ignition of the charge. In Figure 87 a the charge detonates in the closed chamber, Figure 87 b originates from a test with a 8-mm bore hole and Figure 87 c from a test with a 20-mm bore hole. The primary blast has propagated just beyond the entrances of rooms 4 and 5, its location and wave pattern being virtually identical in all three cases. Also the wave pattern in rooms 2 and 3 and the shape of the jet inflow there reveal no significant differences.

Obviously the propagation of the primary blast in the corridor and the adjacent rooms depends – for the specific geometry chosen – only on the portion of the incident blast cut out by the door of the detonation chamber, i.e., the solid angle spanned by the center of the charge and the area of the door opening. This solid angle has a value of about 0.228 sterad, which is equivalent to an aperture angle α of approximately 15.5°. This value is of the same order of magnitude as the aperture angles for the larger venting holes (for the definition of this angle α refer to Figure 86), which are about 17° for the 25-mm hole, 15° for the 20-mm hole, 12° for the 15-mm hole and 7° for the 8-mm hole.

3.7.1 Time-of-Arrival Analysis.

From the pressure records the time-of-arrival of the incident blast front at the 10 gages can easily be derived. Figure 88 shows a sort of wave diagram for the primary blast based on a series of 11 tests. The distance of the gage locations from the center of the charge is expressed in terms of a pathlength following room and corridor axes. Since the results of all 11 tests – done at different diameters of the venting hole – virtually coincide, Figure 89 shows the time-of-arrival values as a function of the venting hole diameter. Again we find no significant influence of the venting onto the propagation of the primary blast, the typical scatter of the values is 0.6 %. In addition it becomes obvious that the ToA-values for pairs of corresponding gages, i.e., for gages 2 and 3, 4 and 5, 6 and 7 and 8 and 10, are nearly identical, which shows that the blast propagation throughout the chamber system is symmetrical.

3.7.2 Detailed Pressure-Time Histories.

It is the inspection of the detailed pressure recordings that reveals differences caused by the venting hole. For better comparison the repeatability of the experiments is again

shown in Figure 90 which presents two tests without venting hole at gage 1. Figure 91 a compares the time-histories of the overpressure at gage 1 for a test with closed detonation chamber versus a test with a 25-mm venting hole. For the first 0.3 ms after the arrival of the primary blast both curves are in acceptable agreement and the differences are within the limits of reproducibility of the individual tests. For $t > 0.5$ ms the curve for the test with venting starts to deviate, exhibiting a lower level of overpressure than the test without venting. In addition the pressure signature shows a comparable structure but with peak locations increasingly shifted against the corresponding ones in the test without venting. This indicates a propagation of the pressure waves at slightly slower velocities. In the same comparison for the overpressure at gage 4, Figure 91 b, an even longer period of acceptable agreement between both tests can be found. It is again followed by a decrease of the average pressure level for the test with venting though it lacks the similarity in the structure of the signature. The decrease of the pressure level is most obvious in Figure 91 c showing the comparison for gage 9. Also quite prominent in this plot are a number of pressure peaks nearly equidistant in the late time history of the overpressure ($t > 3$ ms). The chamber system acts like a system of coupled resonators causing large oscillations in the wake of the initial excitation. The period of these oscillations is about 10% larger for the vented case. The same result can be found for the smaller venting holes but with less increase of the period.

To estimate the effect of venting in a more general way we again analyzed the time-averaged overpressure $I(t)/t$. For the following figures this quantity was evaluated only for a number of instants $t = n\Delta t$, where $t = 0$ denotes the time of arrival of the primary blast at the gage location. The increment Δt was chosen as 0.5 ms. Figures 92 a and b show the time histories of this average pressure at gage 9 and gage 6. Here in the last room of the chamber system the influence of venting is most obvious, the curves for the different values of the venting hole diameter are clearly set apart from each other. At gage 9 they attain a maximum at about 2 ms after the arrival of the primary blast, at gage 6 approximately 1 ms later. During the following decay the curves for different diameters stay virtually parallel. In the other rooms we have not extended the monitoring of the pressure up to 8 ms. Thus Figures 92 c and d show the average pressures for gage 4 and gage 2 only in the time range from 0.5 ms to 3 ms. Here the influence of venting is much less pronounced.

Figure 93 shows a 3-D diagram for the average pressure load $I(t)/t$ showing both the dependency from time and venting hole diameter. To give a better comparison of the results at the different gage locations Figure 94 a shows the average pressure 3 ms after the arrival of the primary blast as a function of the area of the venting hole. Figure 94 b represents the same data set but the values are scaled with the corresponding average pressure in the case of no venting. Here it becomes obvious that the effects depend on the room under consideration; for the specific geometry chosen they are the larger the further it is away from the detonation.

3.7.3 Venting Versus Reducing the Charge Density.

In order to give a further impression of the effects of venting we will compare it to the effects caused by a reduction of the charge density in the detonation chamber. Figure 95 shows the time histories of the average pressure load $I(t)/t$ at gage 9 from the test series where we did the variation of the charge weight. Included are the time histories

for the tests with a 0.5 g charge and the different venting holes. In the initial phase – approximately the first 1.5 ms – the curves are quite comparable to those of the unvented case. The effect of the largest venting hole corresponds here to charge reduction of about 20 %. But for larger times the time averaged overpressure decreases faster than for the tests with a closed detonation chamber. So 7 ms after the blast arrival a charge of 0.5 g and a venting hole 25 mm in diameter cause about the same value as a charge of 0.3 g in the unvented case.

3.7.4 Conclusions.

The results of our small-scale experiments indicate that the kind of venting hole scrutinized here has to be rather large to become effective in the initial phase of blast propagation through the chamber system. This result cannot be transferred to the effect of venting in general since it depends on the specific geometry. We have tried to model the effects due to the penetration of the ceiling, a case that differs in many respects to venting holes deliberately introduced into a system in order to reduce the destructive power of a blast. Located, for instance, in the corridor above the entrance to the detonation chamber such a venting hole might be more effective for the rest of the chamber system. Nevertheless, if longer time-scales are of interest venting has to be taken into account anyway, since it significantly lowers the average pressure levels during an intermediate time range where the flow fills up and pressurizes the rooms but still strong reverberations and pressure waves can be found throughout the system.

3.8 Flow Field in the Detonation Chamber.

The multi-chamber system experiments did not facilitate the visualization of effects inside the detonation chamber. Thus we did an additional investigation with a closed chamber. The dimensions of 130 mm x 170 mm x 40 mm corresponded to those of the detonation chamber in the previous experiment. Floor and ceiling were again manufactured from Makrolon, at least for the visualization experiments. The charge was located – in correspondence to the multi-chamber tests – in the center of this chamber.

The dimensions of the model allowed us to use the 24-spark Crazz-Schardin camera for cinematographic shadow photography. Figure 96 shows a sequence from a test with an HX2-ignitor as charge. The commercially available HX2 is an layered igniter system containing less than 50 mg Nitropenta with non-spherical geometry. The deviation from spherical geometry already becomes obvious in the distribution of the detonation products shown in Figure 96 a obtained some microseconds after the detonation. Nevertheless, the next frame shows a nearly spherical initial wave front which is first reflected at floor and ceiling and later on at the side walls of the chamber. The reflected and rereflected waves traverse several times the turbulent detonation cloud. By dissipation processes the wave strength is reduced more and more until the volume reaches a uniform equilibrium state.

If a larger charge is used the visualization of the wave structure becomes more difficult due to the luminosity of the hot detonation products. An example is presented in Figure 97 originating from a test with a 0.18-g NP charge. Again we observe a very symmetri-

cal wave pattern, but the turbulent detonation cloud rapidly fills the whole chamber thus blurring the shadowgraphs.

Figure 98 shows a pressure-time history obtained by a piezoresistive pressure gage, type Kistler 4075A100, which was located in the center of one side wall. Also included is the overpressure impulse (red curves). For the test with the HX2-ignitor we find a number of oscillations due to the wave reflection, but at about 6 ms after the detonation an average pressure of 0.56 bar is attained.

Figure 99 give the corresponding pressure-time history for the test with the 0.18-g NP charge. It is remarkable that the amplitudes of the reflected waves are stronger attenuated than in the case of the HX2 which indicates a higher dissipation probably due to the stronger turbulence in the detonation cloud. After approximately 2ms the long term pressure record shows an average pressure of about 5.5 bar with a slight tendency to decrease with time.

3.9 Summary.

This report can only summarize the essential phenomenological findings of our work and exemplify the data sets obtained in the contract period. Tables 15 and 16 give a survey of the performed test and the data available at EMI from this project.

In conclusion one can say that small-scale experiments have two major merits: They can be repeated at a moderate expense in time and money and thus allow to obtain a comparatively precise and reliable data base on the blast loads for a given geometry. And it is rather simple to introduce changes to the experiment, e.g., modify the geometry of a chamber system, for example the study on the influence of a venting hole in the detonation chamber. This makes small-scale experiments a versatile tool for parametric tests on a given parameter which is nearly prohibitive for large-scale tests. The trade-off for this is that information can only be obtained for a limited number of gage locations and that it would stretch the modeling technique to its limit when trying to incorporate shock-structure interactions. In spite of these trade-offs we think it worthwhile to continue the further development of our experimental techniques. One topic is to further diversify our choice of small-scale charges to different geometries, e.g., cylindrical charges, or to the simulation of afterburning effects. And since we monitor the blast environment over time spans that are continually increasing we also have to take into account effects that are negligible for the initial phases, e.g., heat transfer to the walls. This means that we possibly have to adopt our diagnostics to such problems. But with regard to its merits we feel that the work on small-scale blast experiments is a valuable supplement to large-scale testing and numerical simulation.

Section 4

Developments and Experiments on Special Request of DSWA

A discussion at DSWA in November 1996 resulted in the request to modify the working program. Due to the attack of terrorists onto the Khobar Towers Building there was the urgent desire for learning more about the physical effects of this event. So we concentrated after that our research effort primarily on the Khobar Towers problem and started by performing small-scale feasibility tests to visualize the wave propagation during the detonation of the charge. At first only our well proved small spherical charges were available for those tests. Small cylindrical charges of a weight in the range $0.2\text{-g} < W < 1.5\text{-g}$ had to be developed.

4.1 Evaluation of Former Emi-Tests.

One of the first questions at the inspection of the Khobar Towers event was how the pressure distribution looks like around cylindrical charges. To give a quick answer and not to wait for results of the new cylindrical charges who are to be in development corresponding publications and former EMI tests were evaluated.

Figure 100 summarizes the peak overpressures for surface bursts of TNT charges as a function of the range and the geometric arrangement, [12]. The diagram demonstrates that in the near field ($Z < 4 \text{ [m/kg}^{1/3}]$) the peak overpressure of a bare charge depends sensitively on the charge geometry.

At a scaled distance of $Z = 1 \text{ [m/kg}^{1/3}]$, for instance, the peak overpressure can vary from about 13 bar (hemispherical charge) to about 55 bar (cylindrical charge; $L/D = 5$), that means by a factor of 5. The important influence of the charge geometry is illustrated once again in a second example. A peak overpressure of $p_s = 50 \text{ bar}$ is found at $Z = 0.48 \text{ [m/kg}^{1/3}]$ for a bare hemispherical TNT charge and at $Z = 1.08 \text{ [m/kg}^{1/3}]$ for a cylinder with $L/D = 5$. To produce the same overpressure ($p_s = 50 \text{ bar}$) in a distance of $Z = 1.08 \text{ [m/kg}^{1/3}]$ with a bare hemispherical charge, the weight must be 11.4 times the weight of a bare cylindrical charge with $L/D = 5$.

In addition in Figure 100 are given former EMI results of a cylindrical charge ($L/D = 5$), where instead of Nitropenta a composition of 94% RDX, 4.5% wax and 1.0% graphite was applied. If a TNT equivalent factor of 1.27 is used, an excellent agreement exists in the range of $0.3 \text{ bar} < p_s < 20 \text{ bar}$ with the corresponding TNT curve.

4.1.1 Test Arrangement.

The cylindrical charges were surface tangent located on a thick steel plate. Pressure gages were arranged along radials. Test were performed in free field with three different charge weights, namely 16-g, 128-g and 1 024-g, receptively. As ignitor a precision microsecond fuse, PL 464, was used with a booster charge of RDX. The charge was ignited at one of the faces (0° -direction).

4.1.2 Some Previous Test Results.

The pressure distribution around a bare cylindrical charge at a surface tangent detonation is very complex, especially if fired asymmetrically. The 180°-direction is preferred in the near field. Blast waves of different strength start from the circular faces of the cylinder. From the jacketed surface starts another blast wave. Face waves and jacket wave interact in a complicated manner and form Mach waves. In some domains double peaked blast waves are found.

As expected the blast wave behavior and the peak pressure distribution depend sensitively from the propagation direction, especially in the near field. Figure 101 gives the peak overpressure of the first shock as a function of range for different propagation directions. For $Z < 1.75 \text{ [m/kg}^{1/3}]$ the greatest peak of the first shock at a given Z is found in the 180°-direction. But for $Z > 3.3 \text{ [m/kg}^{1/3}]$ the first peak is smallest compared to other directions.

The positive impulse vs. distance is given in Figure 102. In the near field the impulse in the 90°-direction is the dominant one. Differences of the time-of-arrival are represented in Figure 103 for different directions. It needs far distances before the dependency from the propagation direction disappears.

Figure 104 shows the domains of the double peaked pressure curves for the 90°- and 180°-directions, respectively. In the 90° situation (black curve) the second peak, p_2 , is caused by the diffracted face wave. The strength is smaller than the strength of the jacket wave, $p_2 < p_s$. The second peak in the 180°-direction (red curve) is generated by the more intense jacket wave. In this case $p_2 > p_s$ with a small exception close to $Z = 4 \text{ [m/kg}^{1/3}]$. At $Z = 12$ the two waves, represented by p_s and p_2 , merge and for $Z > 12$ only a single peaked blast wave remains. The same situation occurs in the 90°-direction at about $Z = 20$, but this is outside of the diagram.

Isobars for a bare cylindrical charge with $L/D = 5$ at a surface tangent burst are shown in Figure 105. At high pressure levels, 25 bar and 15 bar for instance, the isobars are asymmetrical concerning the propagation direction. The 180°- orientation is preferred, also the 90°-direction. At 157.5° exists a gap. As smaller the peak pressure or as greater the distance from the charge, the isobars show the trend to a more and more circular shape.

The iso-impulse curves, Figure 106, illustrate a quite similar behavior. Close to the charge at an impulse of $J = 1.0 \text{ [bar*ms/kg}^{1/3}]$ the iso-impulse curve is asymmetric with a gap at 157.5°. Further away from the charge the iso-curves correspond more and more to circles. The same tendency show the curves of constant time-of-arrival in Figure 107.

4.2 Development of Small Cylindrical Charges.

In the past our spherical Nitropenta charges have very well proved so we decided to use the same HE-mixture for manufacturing the new charge types. But we had to learn that it is more difficult to ignite small cylindrical charges than spherical ones. The smaller di-

ameter of the cylinder than of the sphere and the deviation from an ideal symmetry of a sphere might be the reasons for. Finally we found the appropriate HE mixture and handling for manufacturing the charges. In the course of time we developed three different types:

- a) bare cylindrical charge with an axial fuse wire,
- b) bare cylindrical charge with ignition on the face of one end of the cylinder,
- c) cylindrical charge, embedded in a water filled tube (on special request)

With the last type the „Half-Scaled Cylindrical Charge Experiments of WES“ should be simulated [11].

4.2.1 Bare Cylindrical Charge with Axial Ignition.

A picture of a bare charge with an axial fuse wire is shown in Figure 108 a. The dimensions of the cylindrical charge are: length $L = 28$ mm; diameter $D = 7$ mm.

4.2.1.1 Visualization of the flow field. A sequence of shadowgraphs in top view is represented in Figure 109. The axis of the cylindrical charge was horizontally oriented above a transparent surface (Makrolon) and was adjusted 14 mm above the ground. This corresponds to a height of burst of $HOB = 2 D$. The three marking lines represent a distance of 10 cm.

The first frames of Figure 109 show that the detonation cloud propagates at first in axial and in jacket direction before the corners are filled out due to Mach effects. At later times the blast front gets more and more a circular shape.

4.2.1.2 Evaluation of the Overpressure-Range Behavior. The shadowgraphs taken with the 24-spark Craz-Schardin camera allow to determine the distance-time curve of the blast front. The results of two experiments ($HOB = 2D$) is shown in Figure 110 in scaled dimensions. As propagation directions were chosen:

- a) along the axis of the cylinder (0° -direction), denoted as face wave and
- b) perpendicular to the axis (90° -direction), denoted as jacket wave.

Considering that the wave front in the near field is disturbed by small jets, the agreement of the data points of the two HOB-tests is quite acceptable. For both wave fronts approximation functions are given in polynomial form. The derivatives of these functions represent the propagation speed of the two wave fronts in the chosen directions. Under the assumption of ideal gas behavior the overpressure can be evaluated analytically. Figure 111 gives the result of this rough estimate. The overpressure are in the right order of magnitude as obtained from earlier tests performed with cylinders of RDX in tangent orientation to the ground (see paragraph 4.1.2). Not only by the different geometry but also due to other reasons a direct comparison is not possible. The present detonation tests were fired axially and not on one face of the HE-cylinder. Besides the estimated overpressures are valid (because of optical reasons) in a height of 14 mm above ground and not at the ground surface.

4.2.2 Bare Cylindrical Charge with Face Ignition.

A picture of the bare cylindrical charge is shown in Figure 108 b. The ignitor is inserted into a small cavity in one face side of the cylinder and fixed by a droplet of the HE-mixture. A drying process follows. The ignitor consists of a fine metal wire of about 3 mm in length at the end of the ignition cable. Ignition is started by a capacitor discharge at an operating voltage of about 8 kVolt.

4.2.2.1 Visualization of the Flow Field. A sequence of shadowgraphs in top view is given in Figure 112. The arrangement of the test was the same as described in paragraph 4.2.1. $HOB = 2D$. As expected the wave pattern is asymmetric. Opposite to the ignition point, the cloud of the detonation products is pushed forward with high speed and forms a jet like pattern. Inside the detonation cloud reflected waves are visible generated by reflection at the ground and interacting processes.

4.2.2.2 Wave diagrams from Shadowgraphs. To estimate the overpressure-range behavior of a face ignited bare cylindrical charge the same procedure was applied as mentioned in paragraph 4.2.1.2. For test 15 559 the position of the wave fronts in 0° - and 180° -directions (face waves) were plotted in a wave-diagram, as shown in Figure 113. For both curves fit function are given. The wave-diagram for the jacket waves in the 90° - and 270° - direction is represented in Figure 114.

The two face waves differ significantly as consequence of the jet formation in the 180° -direction. The wave-diagrams of the two jacket waves in the 90° and 180° propagation axis are nearly identical. The derivatives of the given fit functions represent the propagation speed and allow to estimate the overpressure as function of range, as mentioned earlier. The result of this estimate is shown in Figure 115. For $Z < 1.5 [m/kg^{1/3}]$, the face wave in forward direction ($=180^\circ$) has the highest pressure value, as expected. Afterwards ($Z > 1.5$) the pressures of both come close together, indicating that the combined wave fronts become more and more spherical.

4.2.3 Cylindrical Charge Embedded in a Water-filled Tube.

To simulate the WES experiments [11] where a charge is fired in a water filled steel tube a small scale blasting composition was developed. This charge is also applied in our simulation experiments to study the loading effects onto the front wall of the Khobar Towers building (see paragraph 4.3).

4.2.3.1 Manufacturing Procedure. The manufacturing of this blasting composition is demonstrated in Figure 116. A cylindrical axial ignited charge is embedded in a lacquered paper tube. This paper tube is then closed on one side before a gelatin solution is filled in. Due to experimental problems we decided to use a weak gelatin solution of about 4% gelatin mass instead of pure water. Finally the remaining is shut also.

According to the Cranz-Hopkinson scaling law we had to apply a factor of 1:100 to simulate the WES experiments and a factor of about 1 : 200 for the Khobar Towers test.

With this scaling factors it is impossible to use in the small scale blasting composition steel to manufacture a scaled steel tube. Therefore we used as material lacquered paper

and scaled the mass according to the scaling law. The difference in the strength of steel and paper has in this kind of test no significant influence.

Instead of using axial ignited cylindrical charges as high explosives in this blasting composition we employed also face ignited cylindrical charges. The manufacturing procedure is practically the same as described before.

4.2.3.2 Visualization of the Flow Field. The arrangement to visualize the flow field of the confined charge, where the confinement consists of a tube filled with a gelatin solution, is the same as described in paragraph 4.2.1.

For a blasting composition with axial ignition a sequence of shadowgraphs is shown in Figure 117. The detonation cloud looks quit similar to that of the axial ignited unconfined charge (Figure 109). However the cloud is much more opaque caused by the water portion in it and the shape is not so uniform as before.

Significant differences in the shape of the detonation cloud occur at a face ignited confined charge as demonstrated in Figure 118. The jet formation in forward direction (180°) is conspicuous.

4.2.3.3 Wave Diagrams from Shadowgraphs. The wave diagram for the axial ignited blasting composition is shown in Figure 119 in case of the face wave in 0° - and 180° -direction. The results are given for two different tests. Noticeable is the scatter of the measuring point. It indicates that the blasting composition is influenced by random effects. This is not astonishing by taking in account the complex construction of this special high explosive. A common fit function is given in the diagram.

For the jacket wave in 90° - and 270° -direction the corresponding wave diagram is represented in Figure 120. The scatter seems to be a little bit smaller in this plot. Also here a fit function is given in the diagram.

With the same procedure as described earlier the overpressure-range behavior can be evaluated. The result is represented in Figure 121. The data should not be overestimated, but it gives an idea of the order of magnitude of the strength of the first wave front.

Diagrams of the same type in case of the face ignited blasting composition are shown in the Figures 122 to 124. As expected, the wave diagrams for the face waves (Figure 122) are significant different in comparison to the axially ignited confined charge (Figure 119). The propagation speed in the 180° -direction is much larger than in the 0° -direction. However, for the jacket waves the diagrams for both directions are nearly identical. Also the fit functions for the jacket waves for axially or face ignited charges are practically the same (see Figure 120).

The estimated overpressure range behavior for a face ignited confined charge is represented in Figure 124. The pressure-range curves of the two face waves differ by nearly an order of magnitude. The course of the pressure-range curve is in good agreement with the corresponding curve for the axially ignited blasting composition (see Figure 121).

4.3 Simulation of the Bomb Attack onto the Khobar Towers Building

4.3.1 Laboratory Scale Model

According to the information given by DSWA a schematic scenario of the Khobar Towers Building attack is represented in Figures 125 to 127. For the simulation tests we decided to develop a model in a scale of 1 : 200. The original dimensions are given in blue figures. The measures of the model in the scale of 1 : 200 are marked in black. The position of the charge is drawn in red.

The design of the laboratory scale model was based on the following assumptions:

1. The test should be performed in the laboratory by using the well proved optical and electronic equipment of EMI
2. At first, the Nitropenta spherical charges, developed at EMI and immediately available for tests, should be used where a charge weight of not more than 1.4-g would be acceptable. Later on cylindrical charges of different types should be used (after their development)
3. In respect to the size of the Kistler pressure gages, intended to install in the front wall of the scaled building, the dimension of the model should not be too small, but due to the limited size of the available optical mirrors the model should not be too large. A compromise was found.
4. The ground surface should consist of an optical transparent material (tradename: Makrolon). This will allow the visualization of the blast wave also in a top view.
5. At the beginning it was not clear what the original weight of the explosive was at the event. (The assumptions varied between 4 000 lb TNT and 20 000 lb TNT). According to the Craz-Hopkinson scaling law, our Nitropenta-charges we intended to apply in the experiments at a scale of 1 : 200 correspond to the following full-scale charge weights of TNT. (The TNT equivalent factor for Nitropenta is assumed as 1.2)

small-scale

≅ 0.04-g (HX2)
0.50-g NP
0.95-g NP
1.20-g NP

full-scale

384 kg TNT = 846 lb TNT
4 800 kg TNT = 10 570 lb TNT
9 120 kg TNT = 20 090 lb TNT
11 520 kg TNT = 25 380 lb TNT

Small-scale charges of this size can be handled in our laboratory without any interference with the optical equipment.

In Figure 128 the model design of the Khobar Towers building is shown. The ground surface is transparent, allowing top view shadowgraphs. Visible are also the positions of the pressure gages in the front wall. In the first time only 5 gages were installed in one row. (At later times 16 gages were distributed over the front wall).

4.3.2 Test Results.

4.3.2.1 Shock Tube Tests. To visualize very quickly (before finishing the design and manufacturing) the fundamental influence of the ramp (embankment) and the Jersey barrier (see Figure 127) a 2-D model was manufactured and inserted in the EMI shock tube. The model was loaded by planar shock waves and the wave propagation was observed by photographic sequences. The range of the shock Mach number was $1.1 < M_s < 2.1$. In Figure 129 the dimensions of the 2-D model and the position of the four gages for pressure measurements are shown schematically.

As an example Figure 130 represents a sequence of shadowgraphs at $M_s = 1.7$. Due to the ramp a Mach wave is created. This wave is reflected at the Jersey barrier (Figure 130 b). Vortices are formed at the corners and the incident wave is diffracted. The curved wave reflects at the bottom (Figure 130 c) and generates a new Mach wave. Finally the modified incident wave impinges the front wall of the model (Figure 130 d). At this test the following peak pressures (corrected to 1000 mbar ambient pressure) were recorded at the different gage positions:

Position 1	6.8 bar	Position 2	9.1 bar
Position 3	9.1 bar	Position 4	9.1 bar

These data indicate a pressure decrease due to the influence of the ramp and the Jersey barrier. This trend was also observed at shocks with different Mach numbers.

Apart from experiments with planar shocks, a few tests were performed with explosion waves. Close to the ramp a HX2 ignitor was detonated and the flow visualized by shadowgraphs. The windows of the test chamber were removed. Therefore the flow could expand sideways. A sequence of shadowgraphs under these test conditions is given in Figure 131.

At the first frame the charge was just fired. The front of the blast wave hits then the Jersey barrier (Figure 131 b) and is partly reflected and partly diffracted. A spiral vortex is formed at the barrier and a Mach wave is visible as seen before in the 2-D tests with planar shocks. Because the charge weight of the HX2 is only about 40 mg, the full-scale charge weight corresponds only to about 384 kg TNT. Even if the charge was not confined as in the real event the sequence gives a qualitative impression of the first phase of the bomb attack.

4.3.2.2 Tests with the 3-D Model of Khobar Towers Building:

Spherical Charges, Flow Field Visualization. Figure 132 shows an open shutter picture in side view of a test with a bare spherical charge of $W = 0.98$ g Nitropenta, corresponding in full-scale to 20 700 lb. TNT. Under these test conditions the front wall of the Khobar Towers building is embedded in the fire ball. (In Figure 132 a picture just before the detonation is overlaid to make the contours better visible).

For optical investigations the fireball acts like a bright light source. Therefore shadowgraphs, taken with the 24-sparks Craz-Schardin camera, can be overexposed because this system is open-shutter operated. An appropriate geometrical arrangement, a suit-

able choice of the optical component and an adapted film sensitivity are to be selected to reduce the overexposure of the film.

Figure 133 represents a sequence of shadowgraphs under the same test parameters as in Figure 132. The position of the bare spherical charge was nearly surface tangent. As seen in the shock tube tests (Figure 130), the impinging wave front onto the wall is influenced by the embankment and the Jersey barriers. The shock front is curved and numerous reflections are visualized. Clearly visible is a Mach reflection at the ground surface just in front of the building see Figure 133 d. This frame indicates also that the blast front arrives earlier at gage 2 than at gage 1. As estimated from the shadowgraphs the time-of-arrival at gage 1 is about at $71 \mu\text{s}$ after ignition and $69 \mu\text{s}$ at gage 2.

For a better impression of the dynamics of the detonation event, a video was prepared for DSWA and delivered immediately after completion. The animated sequences consist of 24 frames obtained with the Cranz-Schardin camera in a single test. The apparent duration of the video sequences is enlarged by a multifold repetition of each frame.

To gain a better impression of the three-dimensional flow field also optical investigations in top view were performed. This was possible, because the ground plate consists of a transparent material (see Figure 128). In Figure 134 a the flow field is visualized in single-frame mode by a top view shadowgraph at $t = 110 \mu\text{s}$ after ignition of a spherical charge with $W = 1.00\text{-g}$ Nitropenta. The ramp and the Jersey barriers appear in this picture as black stripes. The height of burst was $\text{HOB} = 7 \text{ mm}$. The blast front is reflected at the front wall. Due to the asymmetrical location of the detonation point in respect to the model the reflected wave has reached only one corner and creates there a spiral vortex, whereas at the opposite side the wave is still approaching the other corner. For comparison a test with an observation in side view is given in Figure 134 b at nearly the same conditions ($t = 107.6 \mu\text{s}$; $W = 0.98 \text{ g}$).

To visualize the flow field in top view in multi-frame mode with the Cranz-Schardin camera a smaller model of the Khobar Towers building was manufactured with a scaling factor of $1 : 350$. The reason for that was that the view field of the camera in our arrangement is too small for a model of $1 : 200$. A sequence of shadowgraphs is shown in Figure 135. Due to the fact that the influence of the ramp is hardly visualized in top view observation, the ramp was not considered in this smaller model. Therefore only the Jersey barrier is visible as a thin black stripe.

Spherical Charges, Pressure Measurements. The positions of the different gages are given in Table 17, (see also Figure 128). A number of tests were performed with charge weights varying in the range of $0.2 \text{ g} < W < 1.2 \text{ g}$ Nitropenta (corresponding to $4\,200 \text{ lbm} < W < 25\,400 \text{ lbm}$ in full-scale).

Results for the peak overpressure at the different gage positions are given in Figure 136. Approximation curves are marked in red whereas the $\pm 10 \%$ deviation is indicated by blue lines. The fit functions of the curves are included in the different diagrams. The jitter of the measuring points can be caused by many factors e.g. formation of jets, reproducibility of the charge, precision of the gages. Nevertheless the results are very satisfactory. Nearly all measuring points are within the range given by the 10% deviation lines. If we assume that the deviation follow a Gaussian error function, then 99.7% of

the values are within the 3σ limit, where σ represents the standard deviation of the error distribution. If we equate 3σ with 10 % then we find a standard deviation of approximately $\sigma \cong 3.5$ %. This is an excellent value for pressure measurements at detonation processes. Quite similar are also the results for the overpressure-impulses as function of the charge weight as can be seen in Figure 137.

Cylindrical Charges, Flow Field Visualization. The wave pattern in *top view* is represented in Figure 138 when the Khobar Towers model is loaded by a detonation of an *axially ignited unconfined* cylindrical charge. The axis of the HE- cylinder was directed toward the front wall of the building. The position of the charge was 14 mm above ground (HOB = 2D) and the center of the charge 126 mm distant from the front wall.

In Figure 139 the wave pattern is shown in the case of a *face ignited unconfined* cylindrical charge under similar conditions. The shape of the wave looks in both cases quite similar. By comparing these shadowgraphs however with those where a spherical charge were used (e.g. Figure 134 a) it is obvious that the pattern of the wave fronts differs significantly. In Figure 138 and 139, respectively, the wave front hitting the front wall is more elliptical whereas in Figure 134 a a more circular shape is visualized.

For comparison the loading of the model in *side view* is represented in Figure 140 in the case of an *axially ignited unconfined* cylindrical charge. The flow field is visualized with the 24-spark Craz-Schardin camera. The same type of charge was used as before. Also the orientation of the HE-cylinder remained unchanged. The charge weight, $W = 1.27$ -g of Nitropenta is slightly smaller than in the corresponding test shown in Figure 138. In side view the front wall seems to be impacted by a nearly planar wave. But by comparing with the top view shadowgraph (Figure 138) it is evident that the loading is not uniform.

Differences are found if the wave pattern is visualized at a test with a *face ignited unconfined* cylindrical charge as shown in Figure 141. Clearly visible is a jet in 180° -direction propagating to the front wall of the building indicating that the local loading of the wall must be greater than in the case of an axial ignited cylindrical charge. Numerous reflected wave and interaction processes with Mach wave formations can be identified. These pictures demonstrate that the flow field at this type of tests is very complex and that a quantitative analysis is not easy.

Examples of the flow field in *top view* of *axially* and *face ignited confined* charges are given in Figures 142 and 143. It seems that a noticeable part of the water in the detonation cloud is retained by the embankment and the Jersey barriers at least in the visualized time instant. Especially in the case of the face ignited confined charge (Figure 143)

This effect appears not so marked in *side view* observation. Examples are shown in the following sequences of shadowgraphs. Shown in Figure 144 is the wave propagation at a detonation of an *axially ignited confined* cylindrical charge. Small particles of the containment can be seen in front of the cloud. Their speed is so high that bow waves are created. It is evident that some of this particles hit the front wall of the building before the arrival of the blast wave. If a pressure gage is impacted by such particles then it is not surprising that the pressure signals are disturbed. It is also evident that the bursting of the confinement is a random process and not exactly reproducible. Therefore one has

to taken into account that the results of tests under the same conditions can be more or less different. This is one of the reasons why tests with non ideal blasting compositions should be repeated several times to get an information about the possible variations.

In the case of a *face ignited confined* cylindrical charge the significant effect is the jet formation in forward direction. Shadowgraphs of the detonation of such a charge in *side view* are represented in Figure 145. Unfortunately due to the water concentration inside the cloud details of the flow field in that region cannot be visualized at tests with confined charges. Nevertheless even the contours of the detonation cloud mediate an impression of the complex effects if a building is attacked by the detonation of such a charge.

Cylindrical Charges, Pressure Measurements. To obtain more detailed information on the pressure distribution the number of gages installed into the front wall of the model was raised to 16 gages. Their locations are specified in Figure 146. To demonstrate the position in relation to the original edifice the Figure overlays the schematic to a photograph of the destroyed facade.

The measured pressure-time histories at the distinct locations differ remarkably. As expected from the visualized flow fields as represented in former shadowgraphs the scatter of the data from test to test is noticeable. Especially at tests with confined charges the peak pressures near the axis of the cylindrical charge show much greater values than in the farther vicinity. As an example pressure records of a face ignited confined charge are given in Figure 147. These four records represents the measured time histories of the gages No 4 , 8, 12, 16, respectively. They are located in the lowest row in the front wall (see Figure 146). Shadowgraphs of the same test are shown in Figure 145. The pressure peaks at gage position No 12 are significantly greater than at the other locations.

The records demonstrate also another difficulty. Some of the pressure-time curves are double peaked, one of them is single peaked. (This observation is valid also for the other gages). It is a question of definition how to compare the values of the peak pressure at the different measuring stations. To overcome this problem we prefer to compare the overpressure-impulses which seems to be a better characterization of the front wall loading. In the given example the maximum delivered impulse to the wall at location No 12 is by a factor of about two greater than at the other positions. If the maximum pressure peaks are compared than a factor of about four is found. At analyzing the measured peak pressures – just to mention another fact - it must be taken into account that the rise time of the used gages is about 2 μ s. This means that for steep and very short pressure pulses possibly the correct values can not be captured. But in real cases this is normally of insignificant influence of the loading or the reaction of a building.

The experiments reported here served more or less as feasibility tests. More precise information on the loading of the front wall of the Khobar Towers building can be found in [13]. There results of additional tests, using the four types of cylindrical charges, are combined with those obtained at investigations we described in this report.

Section 5

Tables and Figures

Table 1. Survey of the performed experiments for the Single Room Configuration, Model 1.

Visualization 24 – spark camera	Pressure Measurement	Mach number
Test No	Test No	M_∞
14780		1.11
14781		1.21
14782		1.31
14783		1.41
14784		1.32
14785		1.43
14786		1.54
14787		1.92
	14820	1.11
	14821	1.21
	14822	1.30
	14823	1.31
	14824	1.41
	14825	1.52
	14826	1.93
14831	14831	1.32
14832	14832	1.33
15167	5167 CS	1.52
15168	5168 CS	1.62
15169	5169 CS	1.72
15170	5170 CS	1.78
15170	5171 CS	1.53
15172	5172 CS	1.91
15172	5173 CS	2.02
15174	5174 CS	2.05
15175	5175 CS	2.18
Color – Schlieren Single Spark		
14891		1.41
14892		1.41
14893		1.41
14894		1.41
14895		1.41
14896		1.41
14897		1.41

Table 2. Survey of performed experiments for the Single Room Configuration, Model 2.

Visualization 24 – spark camera	Pressure Measurement	Mach number
Test No	Test No	M_∞
14772		1.11
14773		1.22
14774		1.32
14775		1.41
14776		1.32
14777		1.42
14778		1.54
14779		1.92
	14814	1.93
	14815	1.51
	14816	1.43
	14817	1.31
	14818	1.22
	14819	1.14
14858	14858	1.32
14859	14859	1.31
14860	14860	1.31
	15108	1.46
	15109	1.45
	15110	1.52
	15111	1.35
	15112	1.93
	15113	1.23
	15114	1.12
15176		1.55
15177		1.62
15178		1.71
15179		1.79
15180		1.91
15181		2.04
15182		2.15
	5183 CS	1.55
	5184 CS	1.62
	5185 CS	1.70
	5186 CS	1.79
	5187 CS	1.95
	5188 CS	2.05
	5189 CS	2.17
Color – Schlieren Single Spark		
14884		1.44
14885		1.44
14886		1.43
14887		1.44
14888		1.42
14889		1.43
14890		1.44

Table 3. Survey of performed experiments for the Single Room Configuration, Model 3.

Visualization 24 – spark camera	Pressure Measurement	Mach number
Test No	Test No	M_∞
14795		1.11
14796		1.21
14797		1.31
14798		1.40
14799		1.54
17800		1.93
	14805	1.30
	14806	1.21
	14807	1.11
	14808	1.11
	14809	1.30
	14810	1.20
	14811	1.43
	14812	1.53
	14813	1.94
	5190 CS	2.17
	5191 CS	2.03
	5192 CS	1.93
	5193 CS	1.78
	5194 CS	1.71
	5195 CS	1.62
	5196 CS	1.53
15197		1.54
15198		1.59
15199		1.70
15200		1.77
15201		1.94
15202		2.01
15203		2.13

Table 4. Survey of performed experiments for the Room Corridor Configuration, Model 4.

Visualization 24 – spark camera	Pressure Measurement	Mach number
Test No	Test No	M_∞
14760		1.11
14761		1.22
14762		1.33
14763		1.40
14764		1.52
14765		1.93
	14843	1.43
	14844	1.93
	14845	1.53
	14846	1.31
	14847	1.21
	14848	1.11
	14849	1.20
	14850	1.21
	5204 CS	1.54
15205	5205 CS	1.52
15206	5206 CS	1.59
15207	5207 CS	1.70
15208	5208 CS	1.79
15209	5209 CS	1.93
15210	5210 CS	2.03
15211	5211 CS	2.16
Color – Schlieren Single Spark		
14864		1.31
14865		1.31
14866		1.31
14867		1.31
14868		1.31
14869		1.31
14870		1.40
14871		1.42
14872		1.43
14873		1.43
14874		1.40
14875		1.41
14876		1.42
14877		1.43
14878		1.44
14879		1.43
14880		1.42
14881		1.42
14882		1.43
14883		1.42

Table 5. Survey of the performed experiments for the Room Corridor Configuration, Model 5.

Visualization 24 – spark camera	Pressure Measurement	Mach number
Test No	Test No	M_s
14788		1.11
14789		1.21
14790		1.31
14791		1.40
14792		1.53
14793		1.92
14794		1.33
	14833	1.31
	14834	1.31
	14835	1.22
	14836	1.11
	14837	1.44
	14838	1.52
	14839	1.92
	14840	1.43
	14841	1.94
	14842	1.43
15212	5212 CS	2.14
15213	5213 CS	2.02
15214	5214 CS	1.93
15215	5215 CS	1.78
15216	5216 CS	1.69
15217	5217 CS	1.60
15218	5218 CS	1.52

Table 6. Survey of the performed experiments for the Room Corridor Configuration, Model 6.

Visualization 24 – spark camera	Pressure Measurement	Mach number
Test No	Test No	M_∞
14766		1.11
14767		1.21
14768		1.32
14769		1.41
14770		1.53
14771		1.89
	14851	1.11
	14852	1.20
	14853	1.31
	14854	1.38
	14855	1.53
	14856	1.95
	14857	1.46
	15093	1.46
	15094	1.49
	15095	1.54
	15096	1.66
	15097	1.77
	15098	2.08
	15099	1.89
	15100	2.02
	15101	1.40
15102		1.40
15103		1.53
15104		1.46
15105		1.67
15106		1.74
15107		1.90

Table 7. Survey of the performed experiments for the Single - Story System, Version A.

Visualization 24 – spark camera	Pressure Measurement	Mach number
Test No	Test No	M_∞
	001 SS	1.22
	002 SS	1.32
15149	003 SS	1.30
15150	004 SS	1.22
15151	005 SS	1.43
15152	006 SS	1.51
	007 SS	1.58
15153	009 SS	1.63
15154	008 SS	1.71
15155	010 SS	1.79
15156	011 SS	1.79
15157	012 SS	1.93
15158	013 SS	2.03
15159	014 SS	2.23
15160	015 SS	2.16
15161	016 SS	1.11
15162	017 SS	1.32
15163		1.31
15164		1.42
15165		1.53
15166		1.61

Table 8. Survey of the performed experiments for the Single - Story System, Version B.

Visualization 24 – spark camera	Pressure Measurement	Mach number
Test No	Test No	M_∞
15219	5219 CS	1.21
15220	5220 CS	1.31
15221	5221 CS	1.41
15222	5222 CS	1.54
15223	5223 CS	1.61
15224	5224 CS	1.73
15225	5225 CS	1.78
15226	5226 CS	1.93
15227	5227 CS	2.04
15228		2.03
15229	5229 CS	2.19
15230	5230 CS	1.11

Table 9. Survey of the performed experiments for the Stairwells, 2 - D Version.

Visualization 24 – spark camera	Pressure Measurement	Mach number
Test No	Test No	M_s
14691		1.11
14692		1.22
14693		1.33
14694		1.41
14695		1.52
14712		2.17
14713		2.16
14745		1.59
14746		1.69
Color – Schlieren Single Spark		
14715		1.52
14716		1.52
14717		1.52
14718		1.54
14719		1.54
14720		1.55
14721		1.55
14722		1.55
14723		1.55
14724		1.55
14725		1.55
14726		1.32
14727		1.34
14728		1.32
14729		1.33
14730		1.32
14747		1.61
14748		1.61
14749		1.61
14750		1.60
14751		1.61

Table 10. Survey of the performed experiments for the Stairwells, 3 - D Version.

Visualization 24 – spark camera	Pressure Measurement	Mach number
Test No	Test No	M_s
14696		1.22
14697		1.33
14698		1.11
14699		1.51
14700		1.44
14701		1.44
14710		2.10
14711		2.10
Color – Schlieren Single Spark		
14732		1.32
14733		1.32
14734		1.32
14735		1.32
14736		1.32
14737		1.32
14738		1.32
14739		1.32
14740		1.32
14741		1.33
14742		1.33
14743		1.33
14744		1.31

Table 11. Survey of the performed experiments for the Straight Duct.

Visualization 24 – spark camera	Pressure Measurement	Mach number
Test No	Test No	M_s
15367	5367 CM	1.33
	5368 CM	1.22
15369	5369 CM	1.22
15370	5370 CM	1.31
15371	5371 CM	1.12
15372	5372 CM	1.41
15373	5373 CM	1.53
15374	5374 CM	1.62
15375	5375 CM	1.70
15376	5376 CM	1.82
15377	5377 CM	1.89
15378	5378 CM	2.04
15379	5379 CM	2.20

Table 12. Survey of the performed experiments for the T-shaped Duct.

Visualization 24 – spark camera	Pressure Measurement	Mach number
Test No	Test No	M_s
	5321 CM	1.32
	5322 CM	1.32
15323	5323 CM	1.31
	5324 CM	1.22
15325	5325 CM	1.21
15326	5326 CM	1.12
15327	5327 CM	1.41
15328	5328 CM	1.49
15329	5329 CM	1.60
15330	5330 CM	1.71
15331	5331 CM	1.79
15332	5332 CM	1.94
15333	5333 CM	2.04
15334	5334 CM	2.18

Table 13. Survey of the performed experiments for the L-shaped Duct.

Visualization 24 – spark camera	Pressure Measurement	Mach number
Test No	Test No	M_s
15380	5380 CM	1.35
15381	5381 CM	1.42
15382	5382 CM	1.22
15383	5383 CM	1.11
15384	5384 CM	1.52
15385	5385 CM	1.60
15386	5386 CM	1.71
15387	5387 CM	1.78
15388	5388 CM	1.94
15389	5389 CM	1.99
15390	5390 CM	2.16

Table 14. Survey of the performed experiments for the Double L-shaped Duct.

Visualization 24 – spark camera	Pressure Measurement	Mach number
Test No	Test No	M_s
16391	5391 CM	1.12
15392	5392 CM	1.22
15393	5393 CM	1.33
15394	5394 CM	1.42
15395	5395 CM	1.54
15396	5396 CM	1.62
15397	5397 CM	1.68
15398	5398 CM	1.80
15399	5399 CM	1.94
15400	5400 CM	2.04
15401	5401 CM	2.18
15402	5402 CM	1.11

Table 15. Survey of the available data from the small-scale experiments in the scaled multi-chamber system.

	Pressure Measurements	Visualization – Single-Shot Shadowgraphs	
	File No.	Shadowgraph No.	Time after ignition
Standard configuration: 0.5-g NP-charge centered in detonation chamber			
	013.MC	15133	300 μ s
	014.MC	15134	450 μ s
	009.MC	15127	600 μ s
	015.MC	15136	750 μ s
	010.MC	15128	900 μ s
	011.MC	15131	1200 μ s
	012.MC	15132	1500 μ s
	018.MC	15139	2000 μ s
Influence of charge location			
upper right	017.MC	15138	450 μ s
upper right	021.MC	15142	600 μ s
upper right	020.MC	15141	1200 μ s
upper right	019.MC	15140	2000 μ s
lower left	016.MC	15137	450 μ s
lower left	022.MC	15143	600 μ s
lower left	023.MC	15144	1200 μ s
lower left	024.MC	15145	2000 μ s
Influence of a venting hole (diameter d)			
standard	028.MC	15285	450 μ s
standard	029.MC	15286	1200 μ s
8 mm	030.MC	15287	450 μ s
8 mm	031.MC	15288	1100 μ s
8 mm	032.MC	15289	1200 μ s
15 mm	033.MC	15290	450 μ s
20 mm	034.MC	15291	450 μ s
20 mm	035.MC	15292	1200 μ s
25 mm	037.MC	15294	450 μ s
25 mm	038.MC	15295	450 μ s
25 mm	036.MC	15293	1200 μ s
Influence of the charge weight			
standard	-----	15417	900 μ s
standard	040.MC	15418	900 μ s
0.53 g NP	052.MC	15431	900 μ s
0.52 g NP	056.MC	15435	900 μ s
0.35 g NP	041.MC	15419	900 μ s
0.32 g NP	045.MC	-----	
0.30 g NP	046.MC	15425	900 μ s
0.25 g NP	042.MC	15420	900 μ s
0.22 g NP	047.MC	15426	900 μ s

Table 15. Survey of the available data from the small-scale experiments in the scaled multi-chamber system. (Continued)

	Pressure Measurements	Visualization – Single-Shot Shadowgraphs	
	File No.	Shadowgraph No.	Time after ignition
Influence of the charge weight			
0.21 g NP	048.MC	15427	900 μ s
0.20 g NP	043.MC	15421	900 μ s
0.10 g NP	049.MC	15428	900 μ s
0.06 g NP	044.MC	15422	900 μ s
0.06 g NP	051.MC	15430	900 μ s
HX2 ¹⁾	026.MC	15147	750 μ s
HX2	057.MC	15480	900 μ s
HX2	027.MC	15148	1080 μ s
HX2	025.MC	15146	2000 μ s
exploding wire	058.MC	15481	900 μ s
0.52 g NP + 0.06 g Al	053.MC	15432	900 μ s
0.48 g NP + 0.10g Al	054.MC	15433	900 μ s
0.46 g NP + 0.09 g Al	055.MC	15434	900 μ s

¹⁾ HX2 is a commercially available, non-spherical ignitor containing approximately 40 mg NP

Table 16. Survey of the available data from the small-scale experiments in the closed detonation chamber.

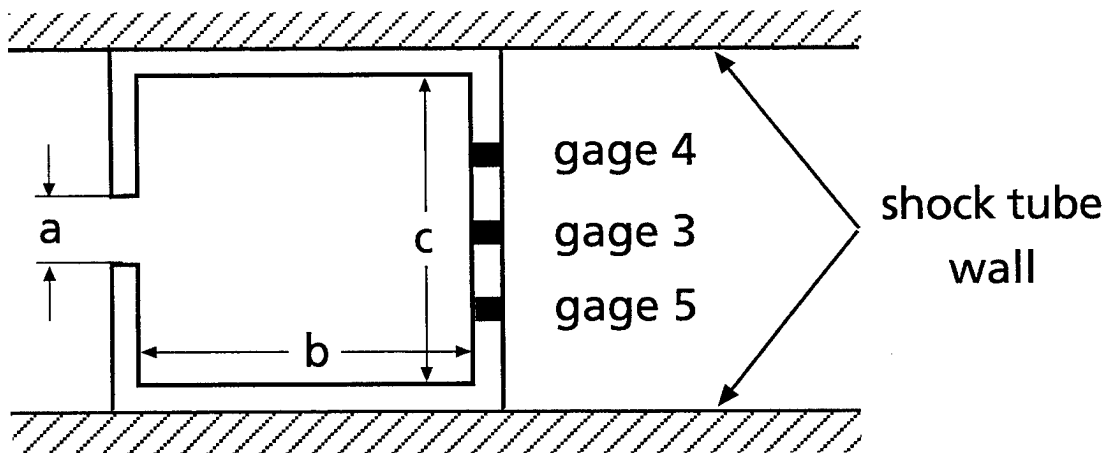
Charge	Pressure Measurements	Visualization – 24-frames shadowgraphs	
	File No.	Shadowgraph No.	Time between frames
HX2 ¹⁾	-----	15456	20 μ s
HX2	000.KM	15457	20 μ s
HX2	002.KM	15459	20 μ s
0.05 g NP	015.KM	15460	15 μ s
0.08 g NP	014.KM		
0.18 g NP	003.KM		
0.20 g NP	011.KM		
0.22 g NP	005.KM		
0.22 g NP	010.KM		
0.25 g NP	004.KM		
0.26 g NP	013.KM		
0.27 g NP	012.KM		
0.40 g NP	016.KM		
0.40 g NP	017.KM		
0.50 g NP	006.KM		
0.53 g NP	007.KM		
0.70 g NP	001.KM		
1.01 g NP	009.KM		
1.02 g NP	008.KM		

¹⁾ HX2 is a commercially available, non-spherical ignitor containing approximately 40 mg NP

Table 17. Gage positions and gage-charge distances for the small-scale model of the Khobar Towers building.

No	Gage Position	
	Height above Ground [cm]	Linear Distance from Charge [cm]
1	1.0	12.60
2	2.6	12.87
3	4.5	13.38
4	6.8	14.32
5	10.5	16.40

Single room configuration



① $a = 1.62 \text{ cm}$	② $a = 1.62 \text{ cm}$	③ $a = 3.24 \text{ cm}$
$b = 9.0 \text{ cm}$	$b = 18.0 \text{ cm}$	$b = 18.0 \text{ cm}$
$c = 9.0 \text{ cm}$	$c = 9.0 \text{ cm}$	$c = 9.0 \text{ cm}$
$\frac{A}{V} = 0.02 \text{ cm}^{-1}$	$\frac{A}{V} = 0.01 \text{ cm}^{-1}$	$\frac{A}{V} = 0.02 \text{ cm}^{-1}$

Figure 1. Single room configuration; A = Area of the opening, V = Volume of the room.

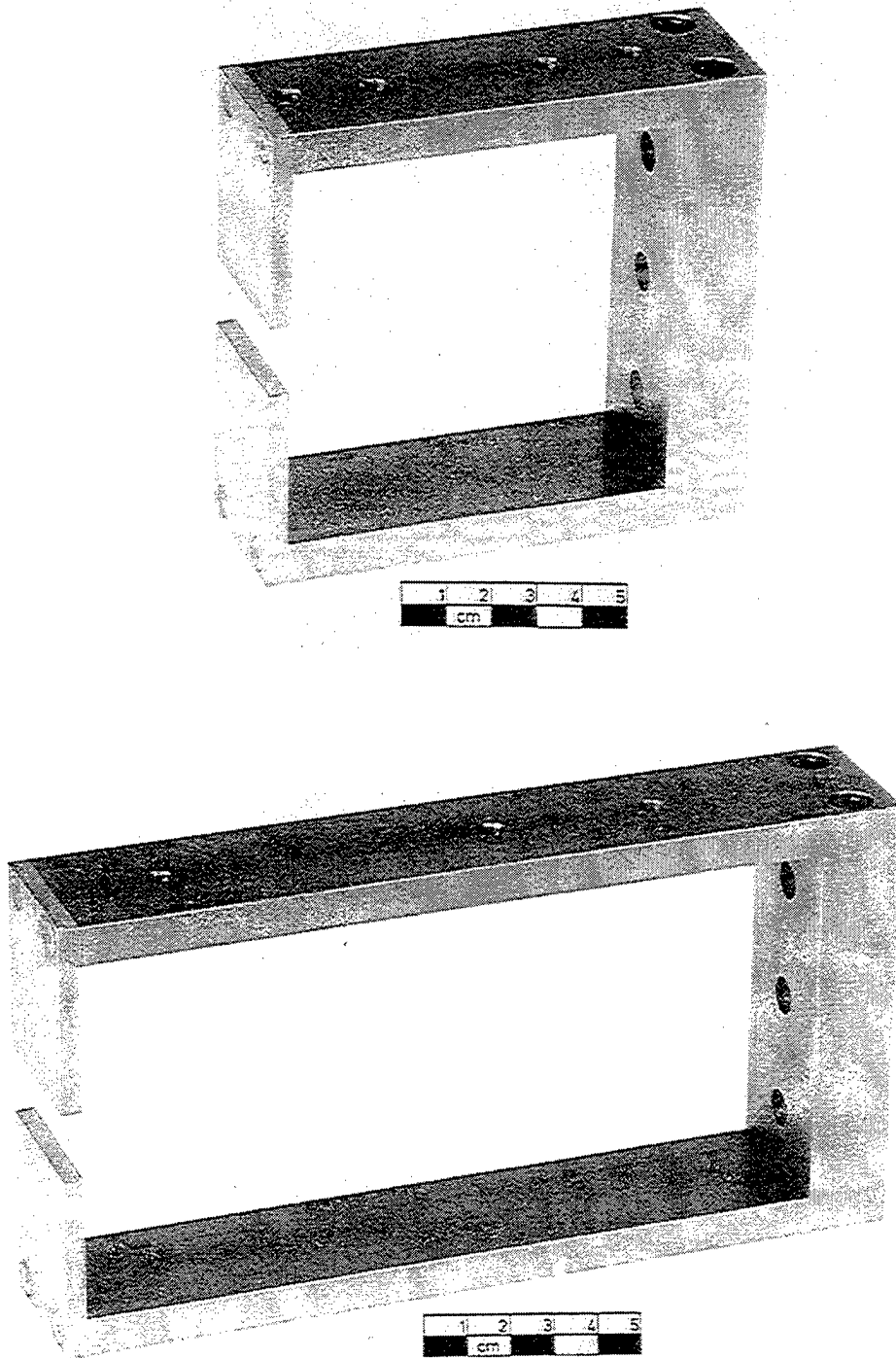
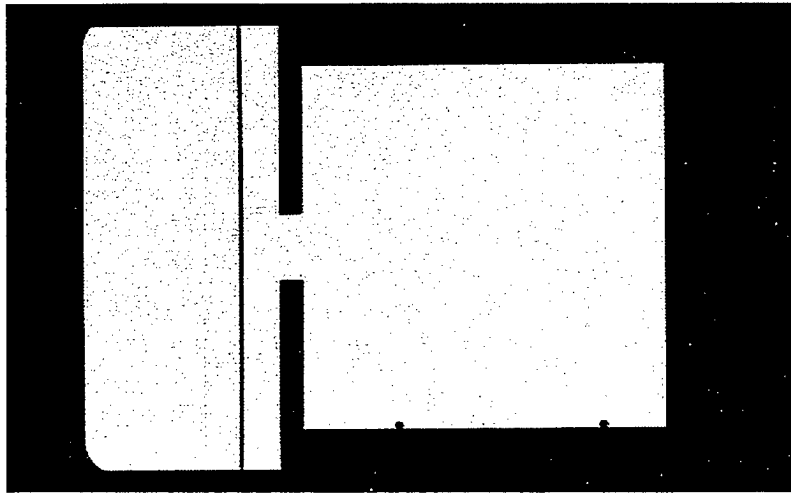
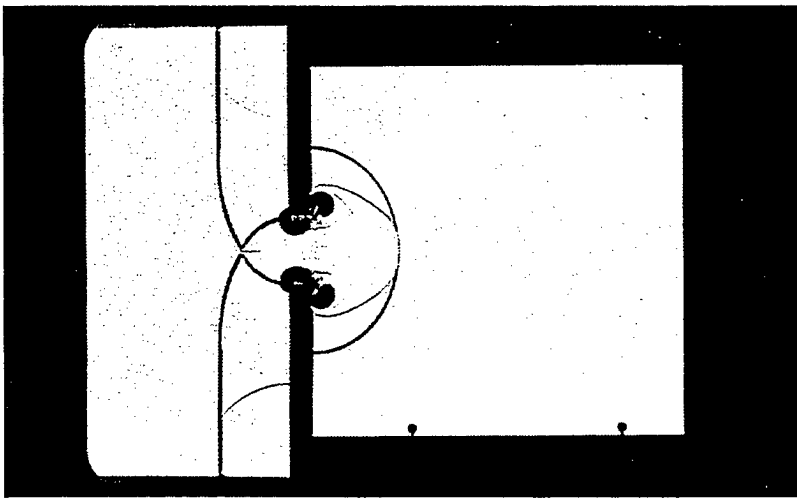


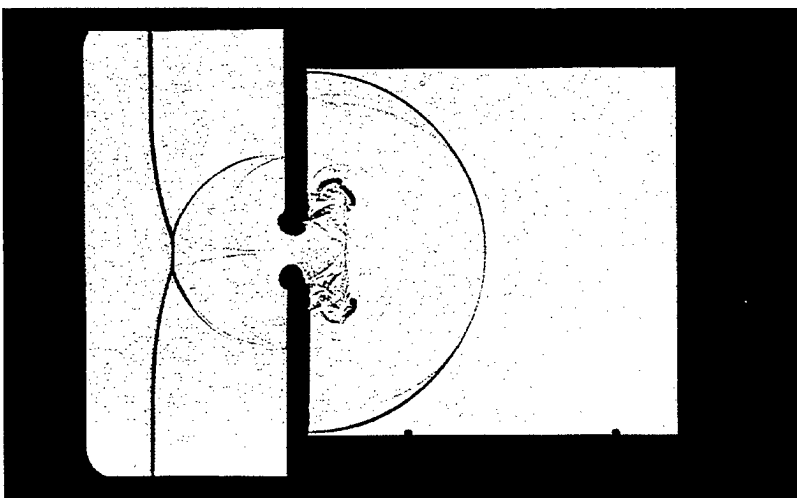
Figure 2. Single room models according to the dimensions, given in Figure 1. At tests, pressure gages will be placed in the bore holes of the back wall.



a) $t = -0,020$ ms

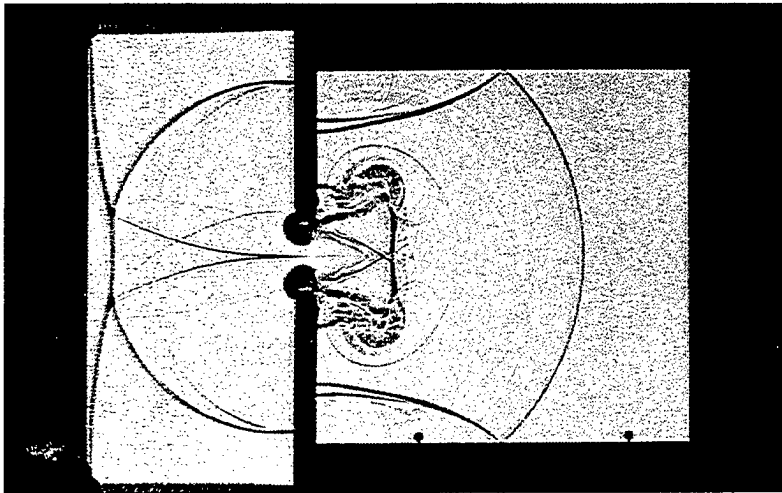


b) $t = 0,055$ ms

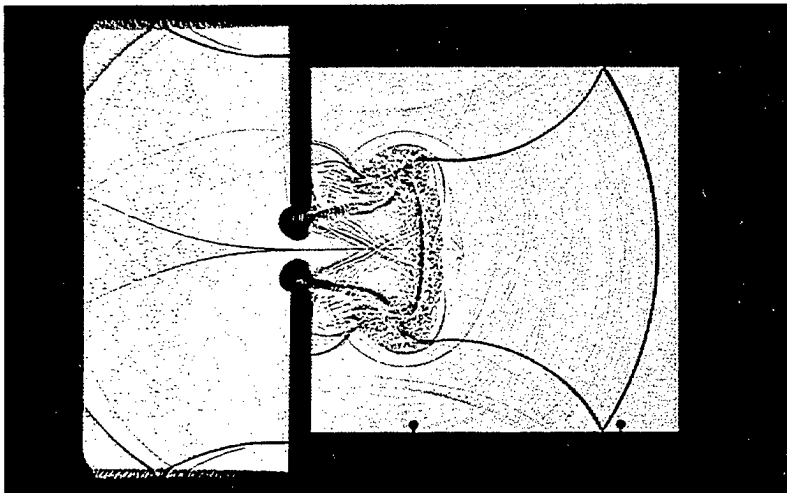


c) $t = 0,105$ ms

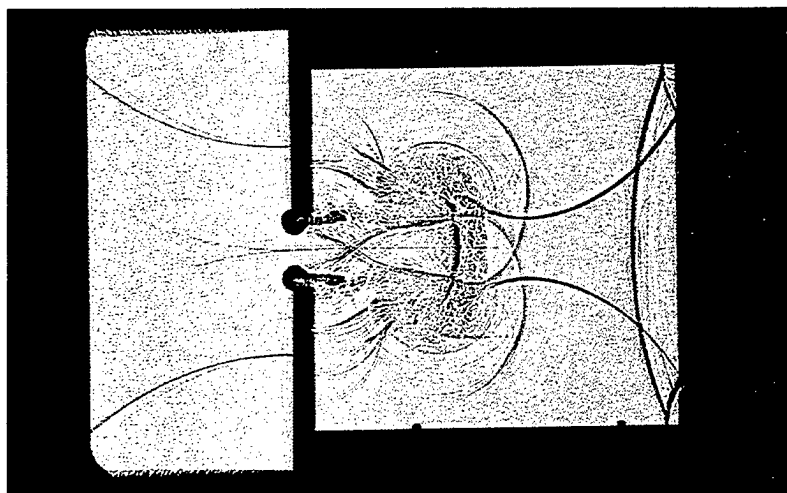
Figure 3. Single room configuration, model 1; (test 14 783) shadow pictures; $M_5 = 1,41$.



d) $t = 0,155 \text{ ms}$

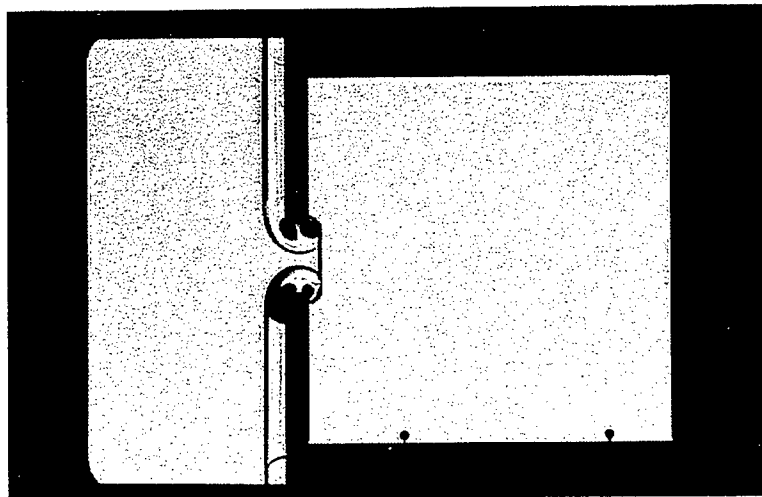


e) $t = 0,205 \text{ ms}$

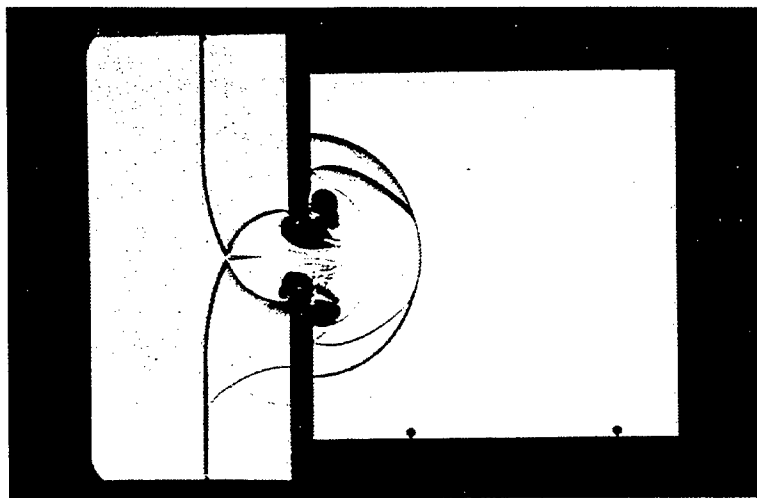


f) $t = 0,255 \text{ ms}$

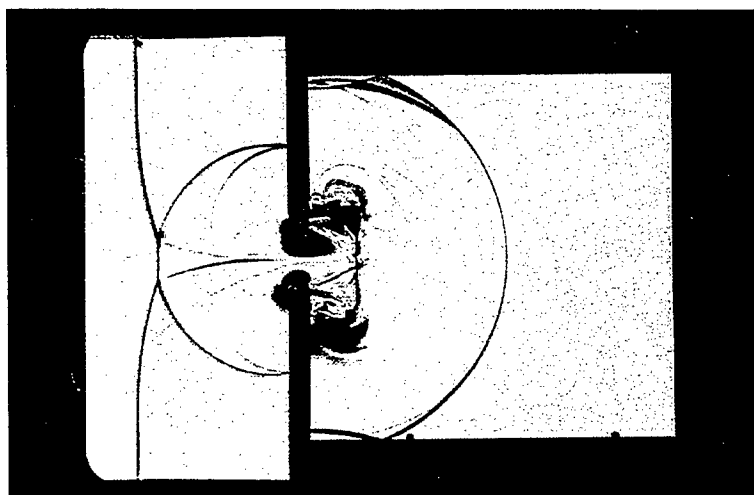
Figure 3. Single room configuration, model 1; (test 14783) shadow pictures; $M_5 = 1,41$. (Continued)



a) $t = 0,0175 \text{ ms}$

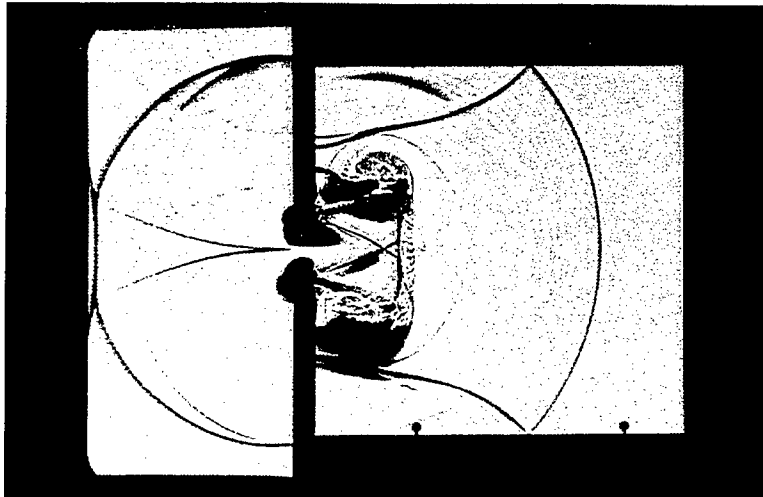


b) $t = 0,0675 \text{ ms}$

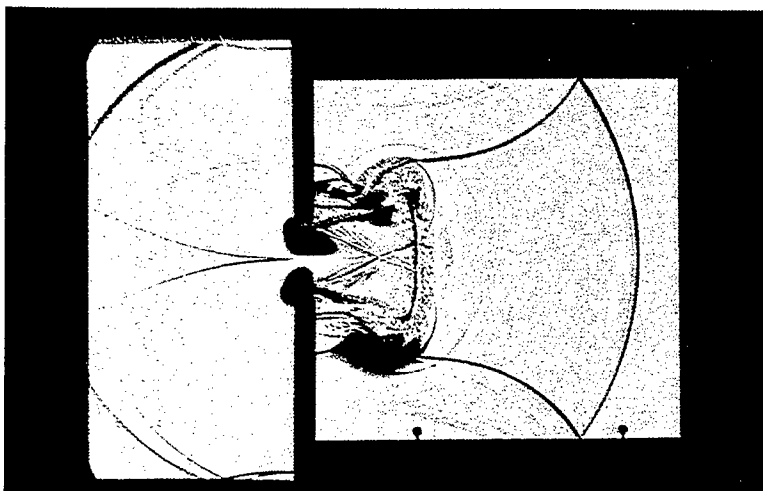


c) $t = 0,1175 \text{ ms}$

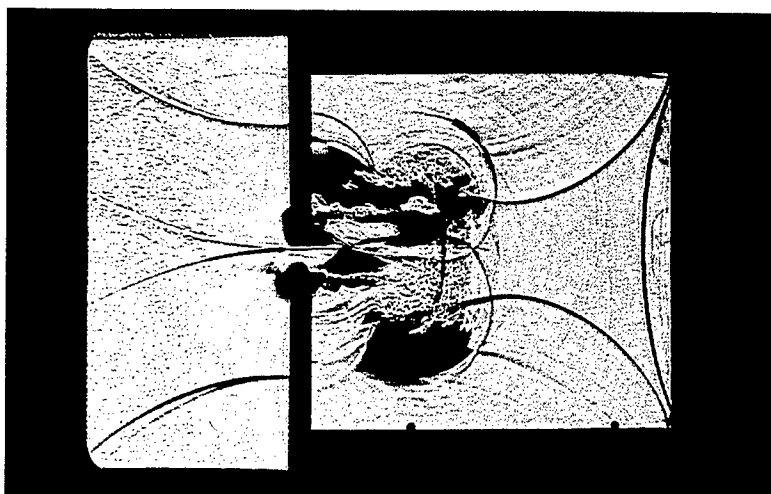
Figure 4. Single room configuration, model 1; (test 14 783) schlieren pictures; $M_5 = 1,41$.



d) $t = 0,1675 \text{ ms}$

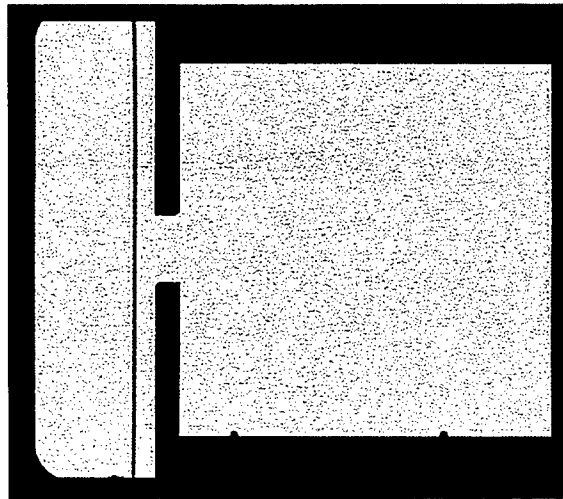


e) $t = 0,1925 \text{ ms}$

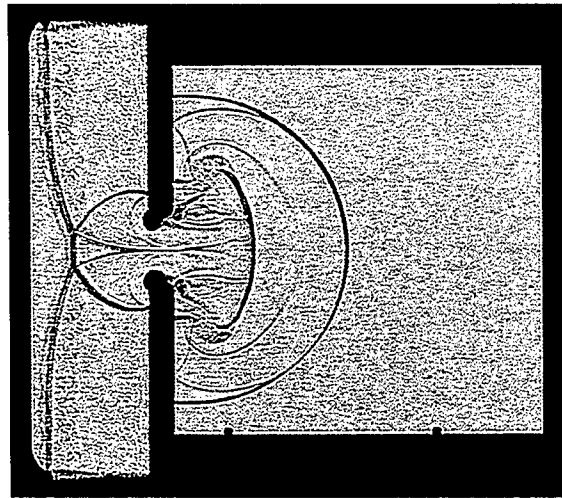


f) $t = 0,2425 \text{ ms}$

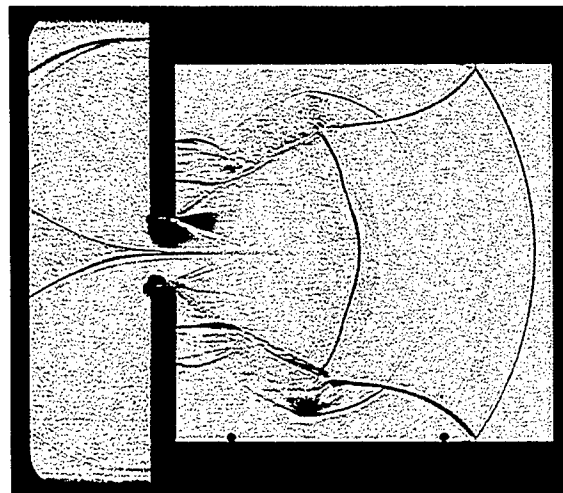
Figure 4. Single room configuration, model 1; (test 14 783) schlieren pictures; $M_S = 1,4$. (Continued)



a) $t = -0,170 \text{ ms}$



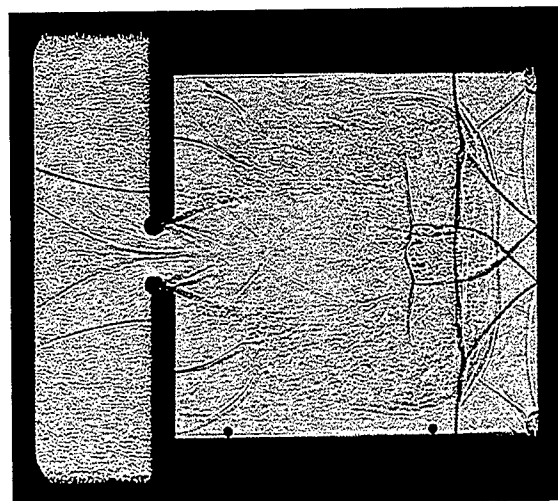
b) $t = -0,090 \text{ ms}$



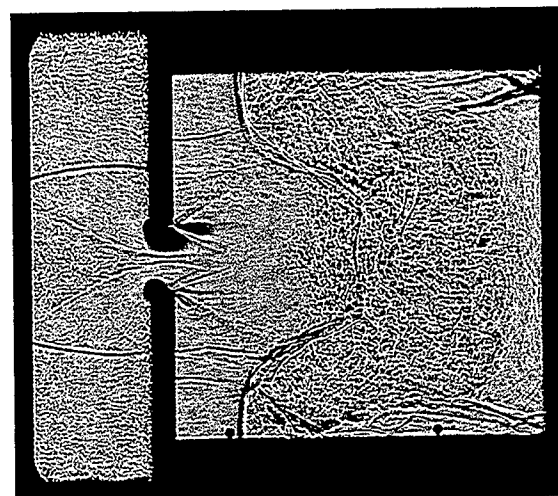
c) $t = -0,010 \text{ ms}$

Figure 5. Single room configuration, model 1; (test 15 174) shadow pictures; $M_5 = 2,05$.

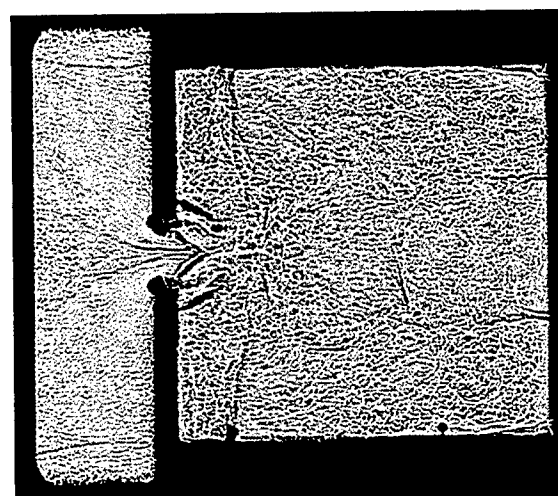
(The time scale in this series is based on the arrival of the first shock wave at the pressure gage in the center of the back wall)



d) $t = 0,070 \text{ ms}$

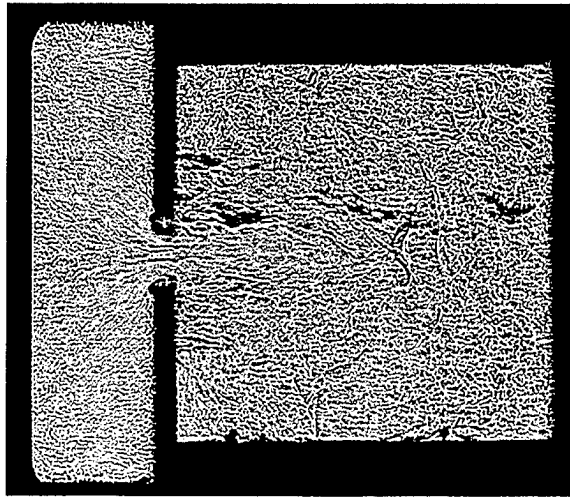


e) $t = 0,150 \text{ ms}$

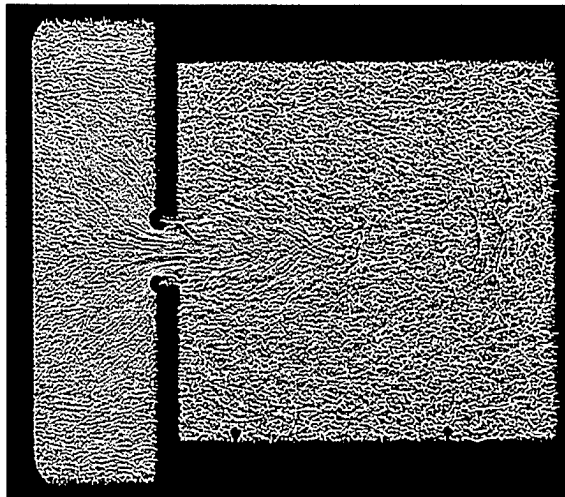


f) $t = 0,230 \text{ ms}$

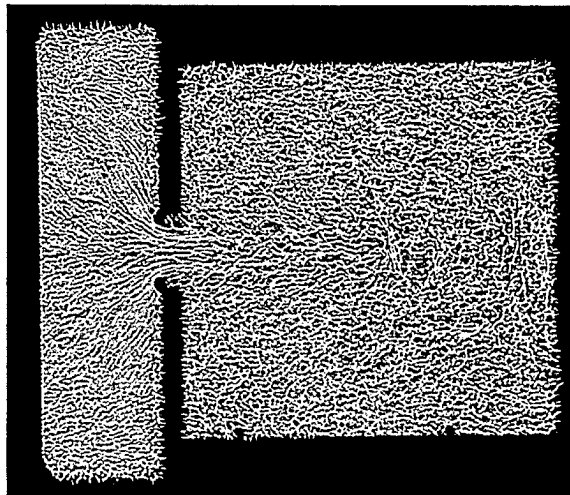
Figure 5. Single room configuration, model 1; (test 15 174) shadow pictures; $M_5 = 2,05$. (Continued)



g) $t = 0,310 \text{ ms}$

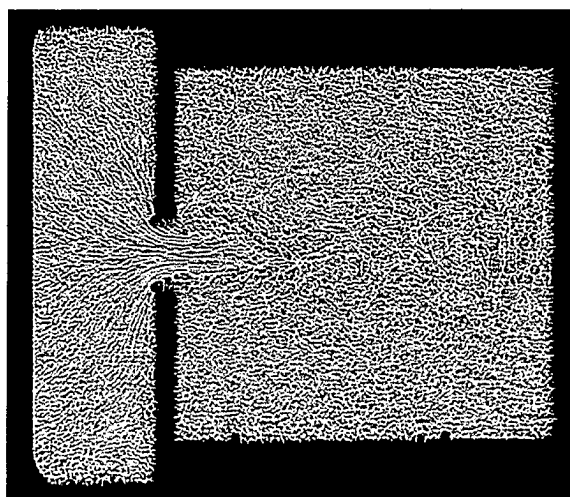


h) $t = 0,390 \text{ ms}$

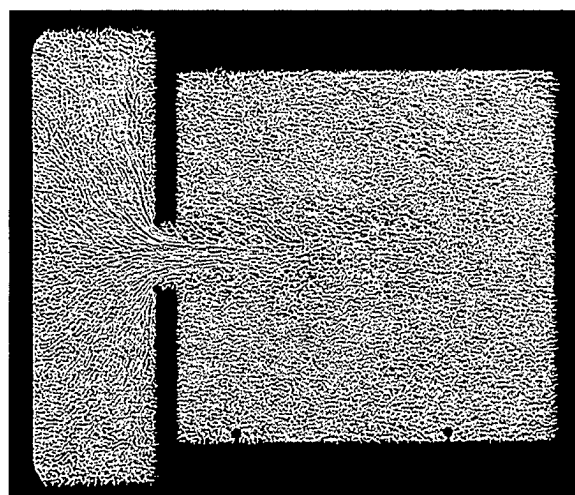


i) $t = 0,550 \text{ ms}$

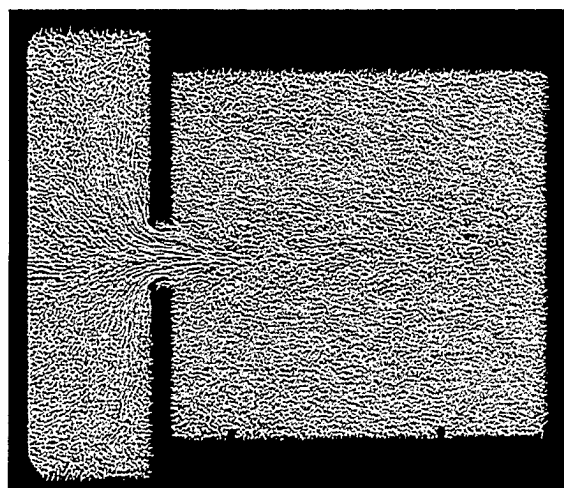
Figure 5. Single room configuration, model 1; (test 15 174)
shadow pictures; $M_S = 2,05$. (Continued)



k) $t = 0,870 \text{ ms}$

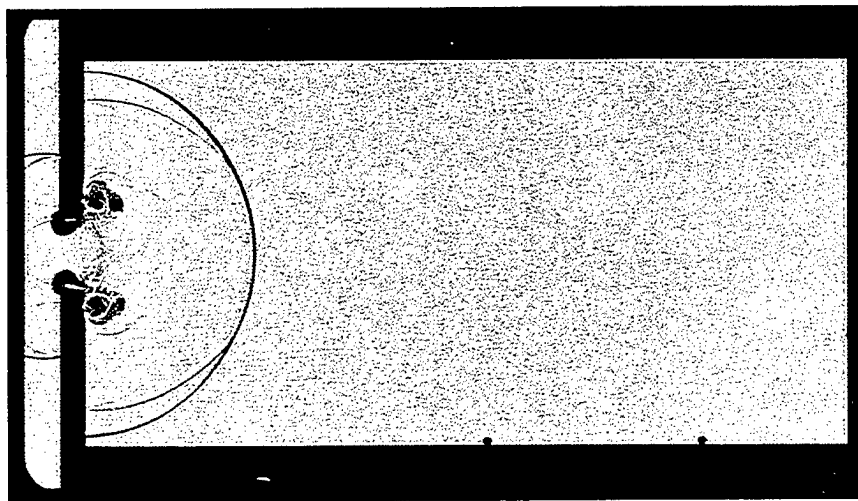


l) $t = 1,190 \text{ ms}$

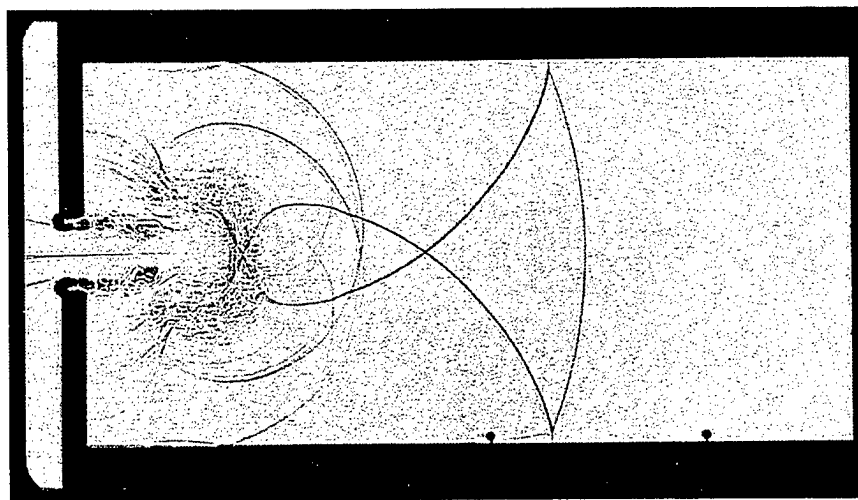


m) $t = 1,510 \text{ ms}$

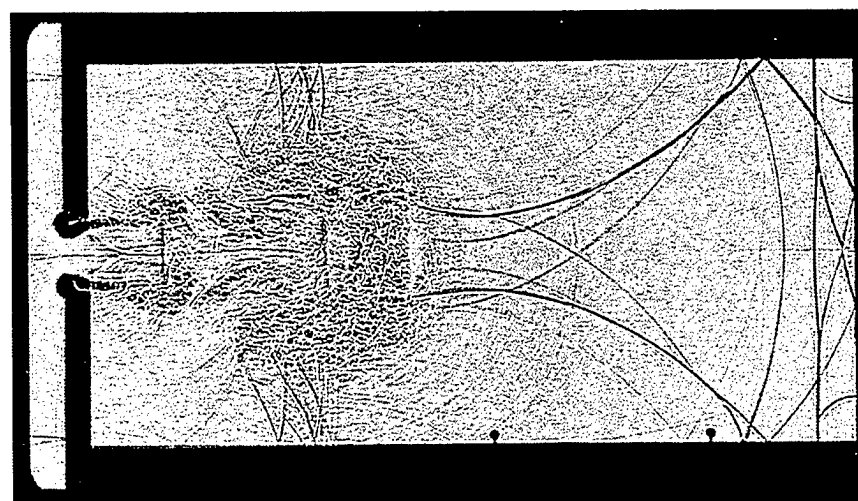
Figure 5. Single room configuration, model 1; (test 15 174) shadow pictures; $M_5 = 2,05$. (Continued)



a) $t = 0,105 \text{ ms}$

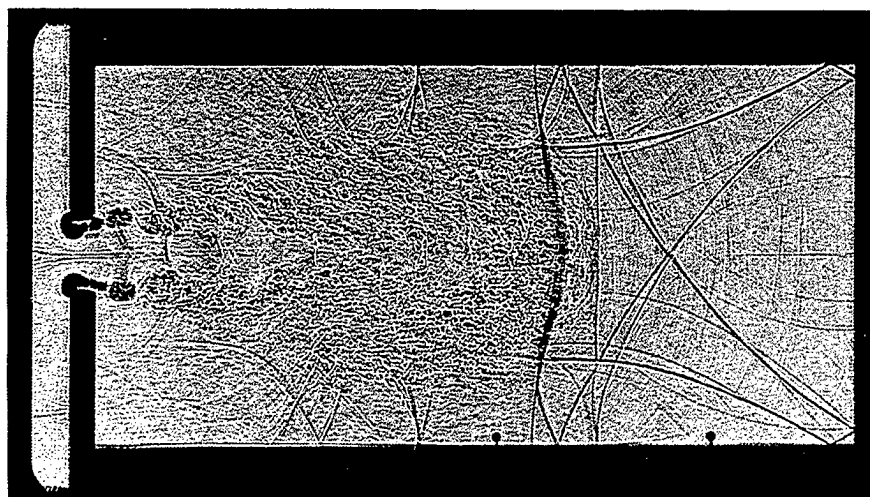


b) $t = 0,305 \text{ ms}$

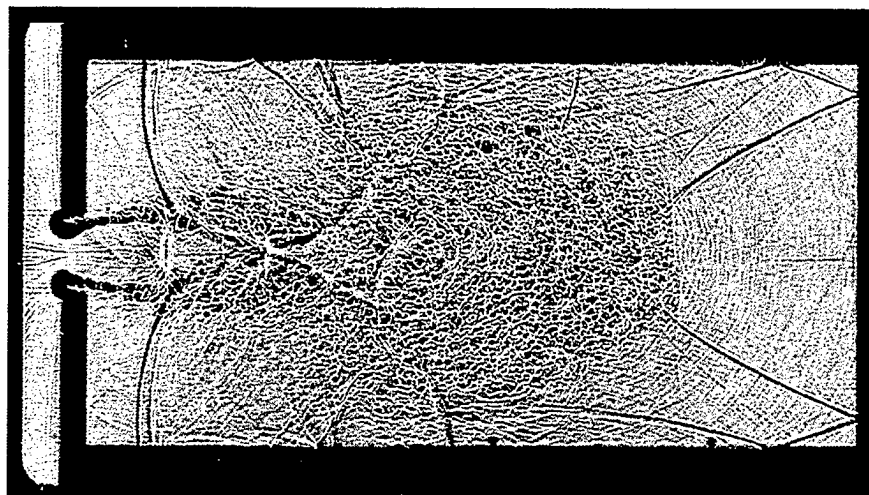


c) $t = 0,505 \text{ ms}$

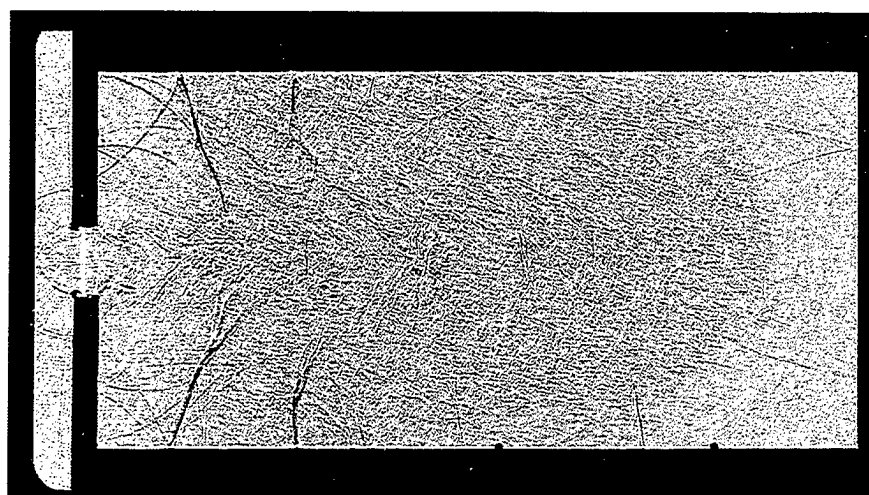
Figure 6. Single room configuration, model 2, (test 14 860) shadow pictures; $M_5 = 1,31$.



d) $t = 0,705 \text{ ms}$

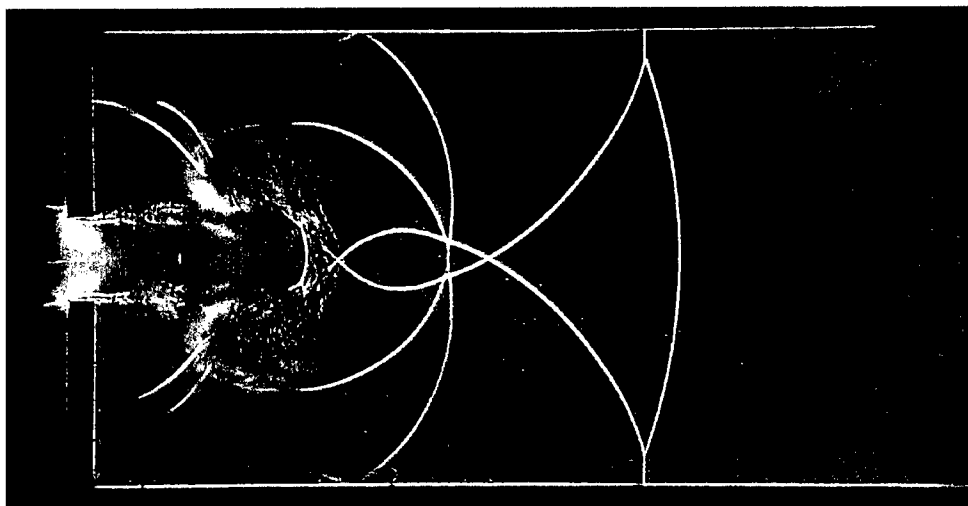


e) $t = 0.905 \text{ ms}$

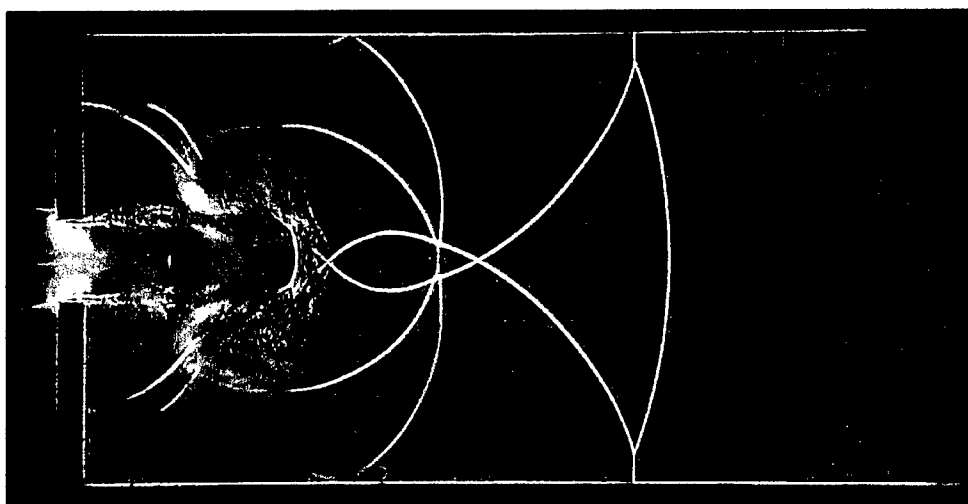


f) $t = 1,105 \text{ ms}$

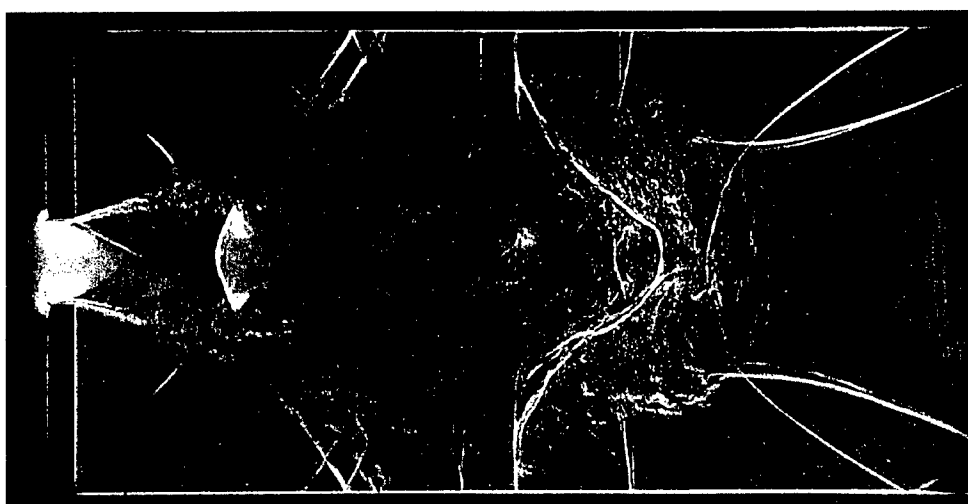
Figure 6. Single room configuration, model 2, (test 14 860) shadow pictures; $M_5 = 1,31$. (Continued)



a) $t = 0.285\text{ms}$
(test: 14 886)

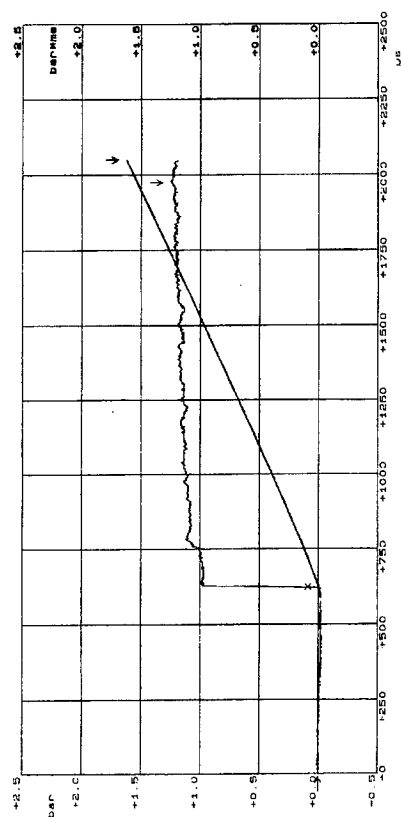


b) $t = 0.585\text{ ms}$
(test: 14 889)

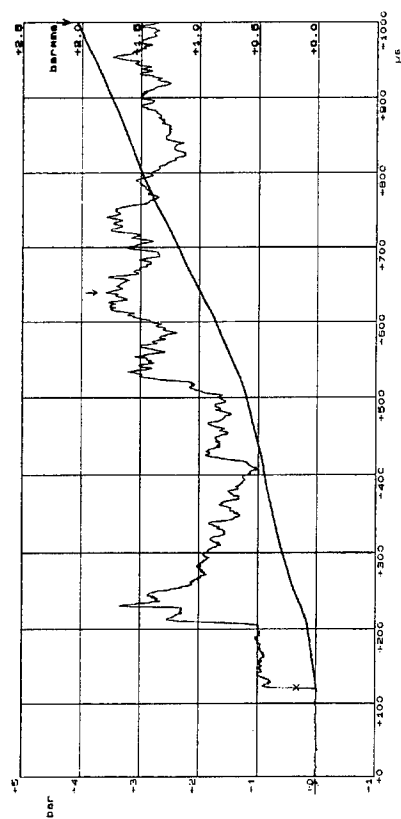


c) $t = 0.685\text{ ms}$
(test: 14 890)

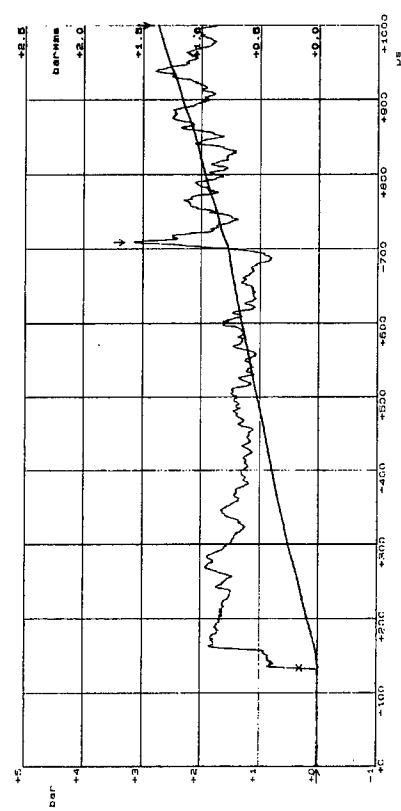
Figure 7. Single room configuration, model 2 color-schlieren pictures; $M_S = 1,31$.



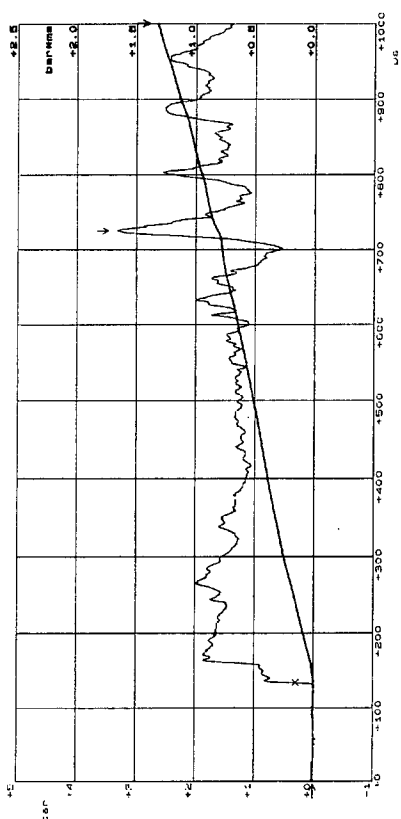
a) 520 mm in front of model entrance



b) Middle gage of back wall (gage 3)

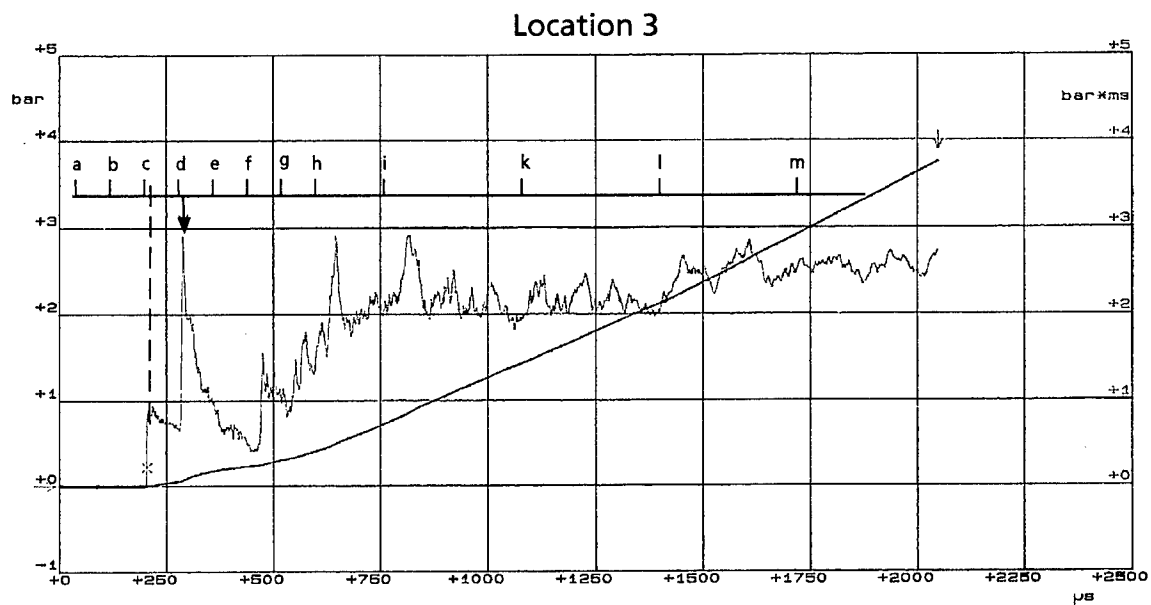


c) Upper gage position (gage 4)

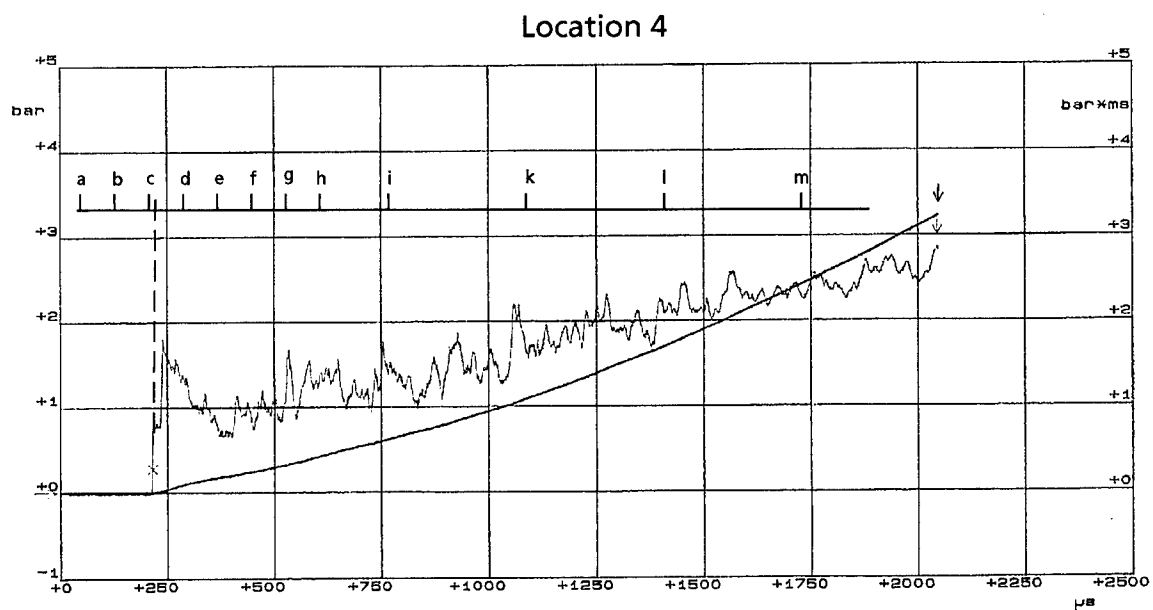


d) Lower gage position (gage 5)

Figure 8. Pressure-time and overpressure impulse histories of single room configuration, model 1, $M_5 = 1.41$ (test: 14 73).



a) Gage location 3



b) Gage location 4

Figure 9. Pressure-time histories in a single room configuration, model 1
 $M_S = 2.05$; (test: 15 175).

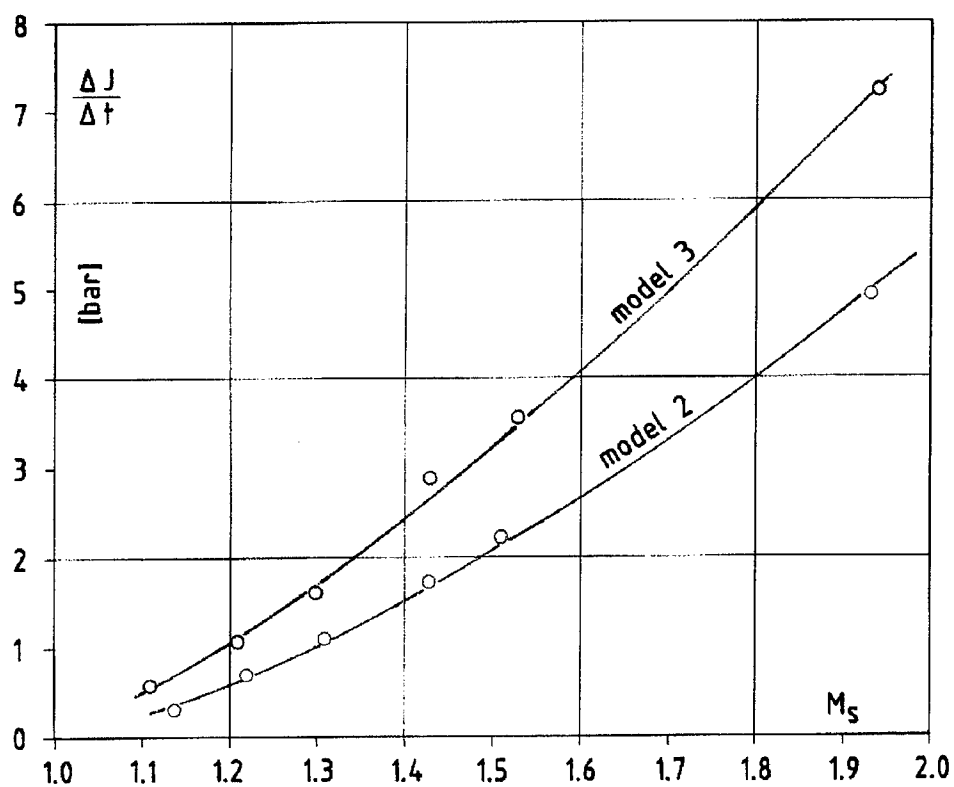


Figure 10. Impulse-rise at $t = 1$ ms vs shock Mach number. Single room configuration; model 2 and 3.

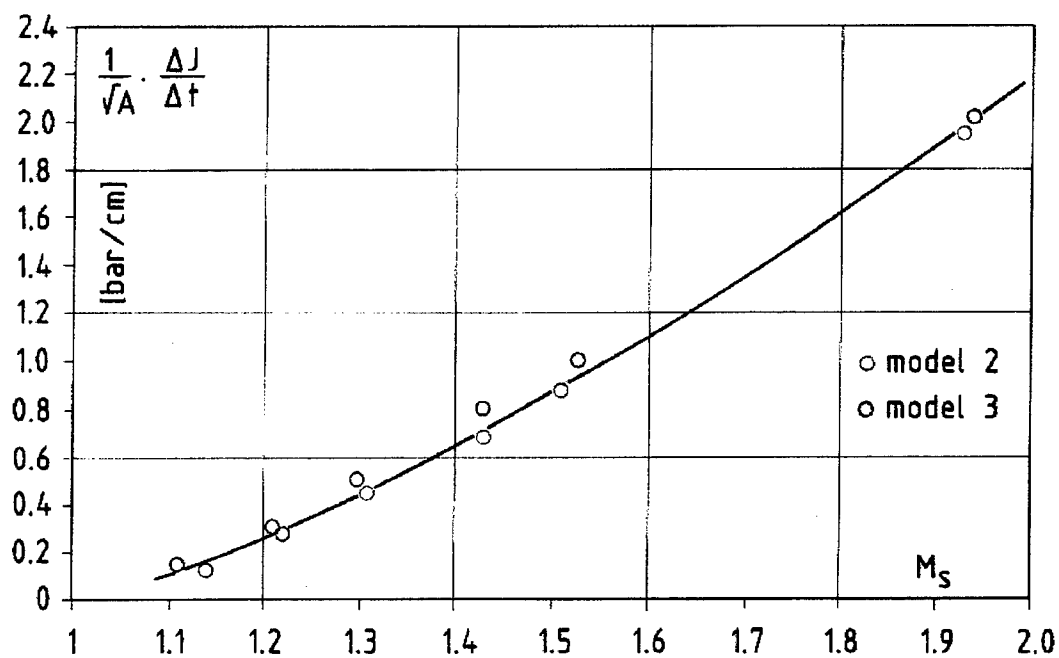


Figure 11. Scaled impulse-rise at $t = 1$ ms vs shock Mach number. Single room configuration; model 2 and 3.

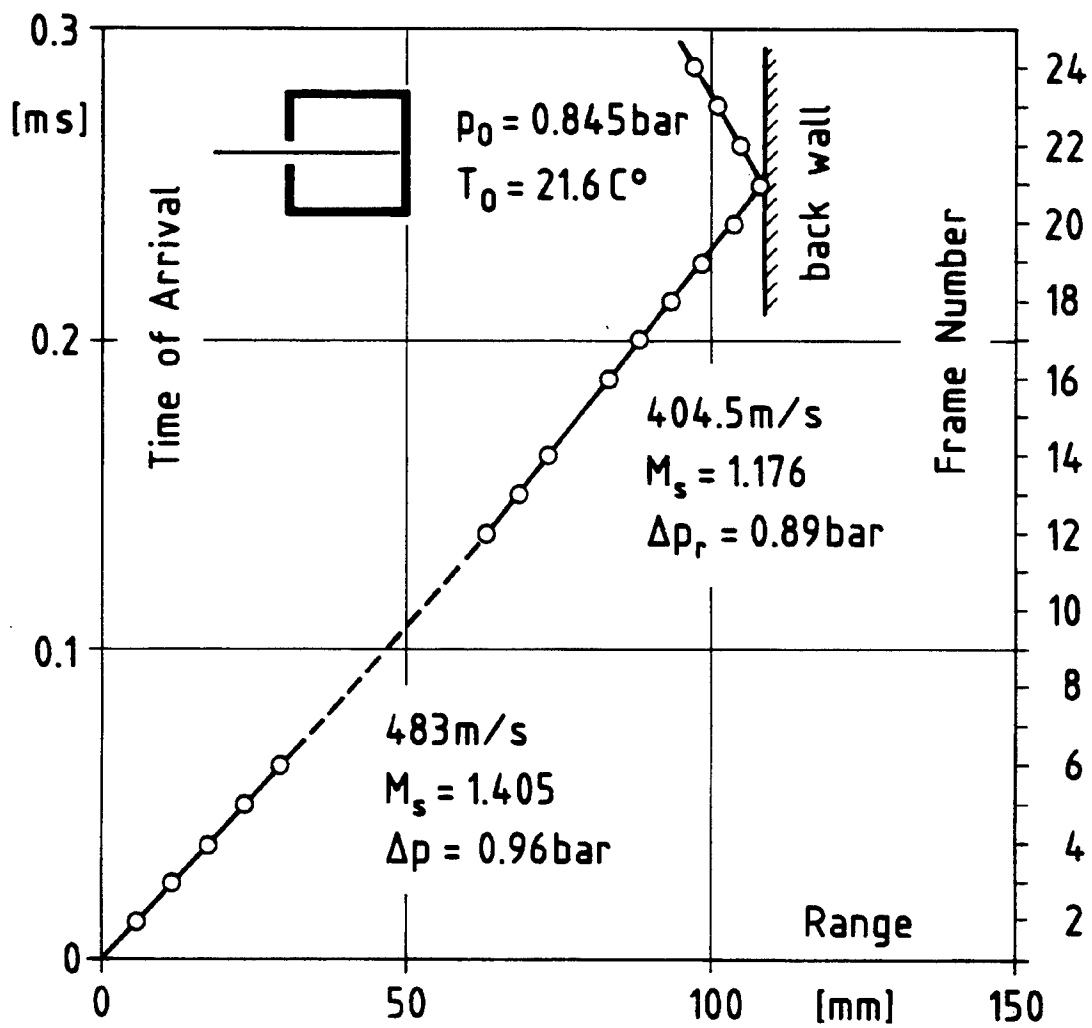
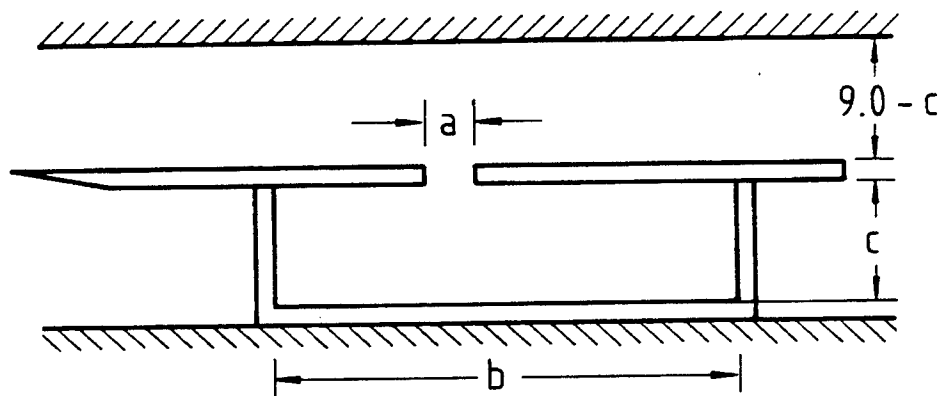


Figure 12. Time of arrival vs range of test 14 783. Single room configuration, model 1. (see Figures 3 and 4).

Room corridor configuration



④ $a = 1.62 \text{ cm}$
 $b = 18.0 \text{ cm}$
 $c = 4.5 \text{ cm}$
 $\frac{A}{V} = 0.02 \text{ cm}^{-1}$

⑤ $a = 0.81 \text{ cm}$
 $b = 18.0 \text{ cm}$
 $c = 4.5 \text{ cm}$
 $\frac{A}{V} = 0.01 \text{ cm}^{-1}$

⑥ $a = 2.59 \text{ cm}$
 $b = 18.0 \text{ cm}$
 $c = 7.2 \text{ cm}$
 $\frac{A}{V} = 0.02 \text{ cm}^{-1}$

Figure 13. Room corridor configurations. A = area of the opening, V = volume of the room.

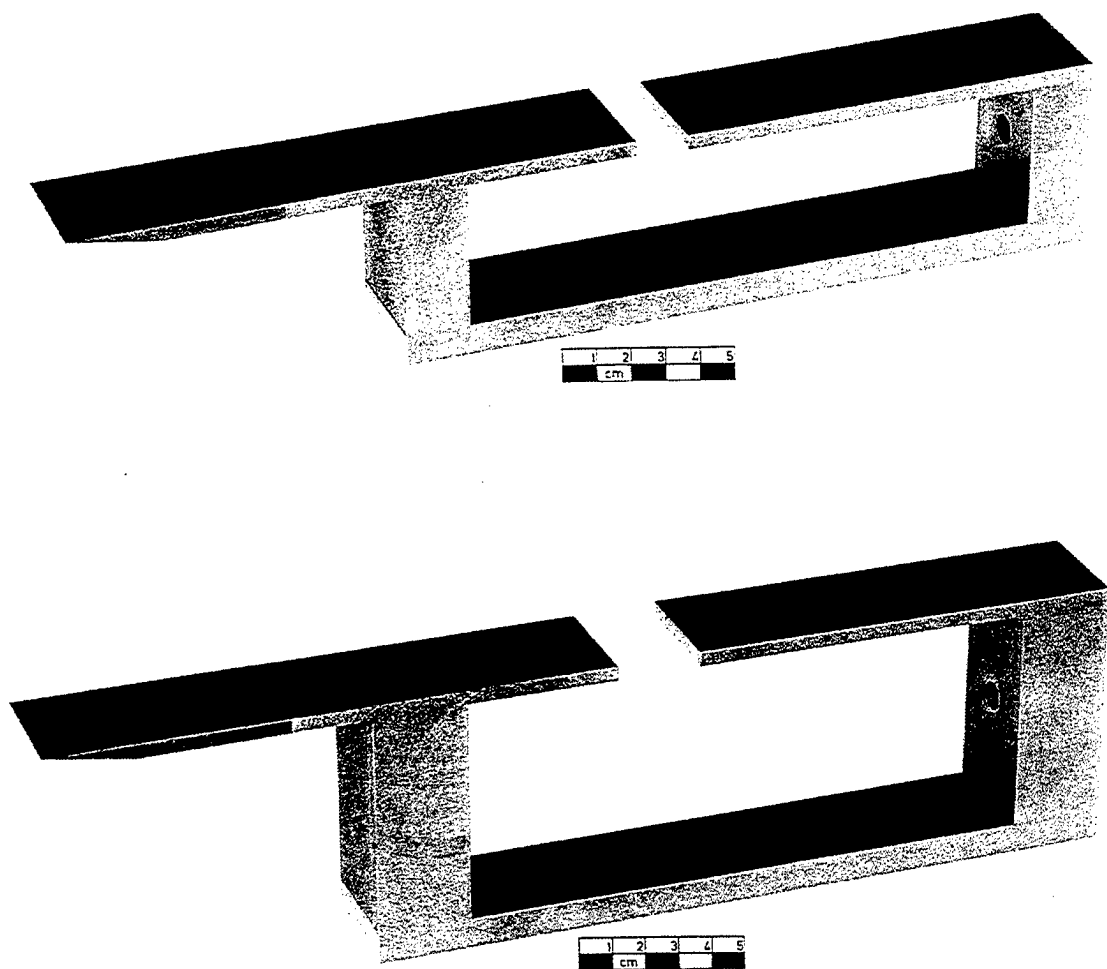
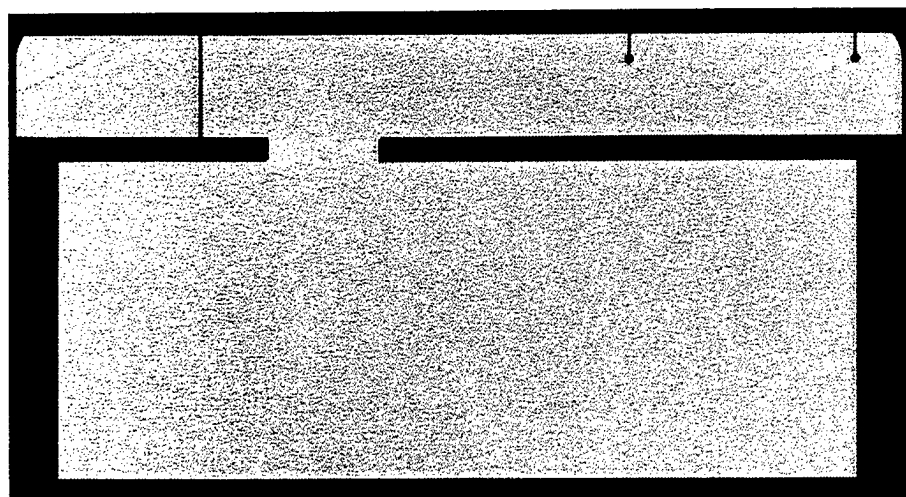
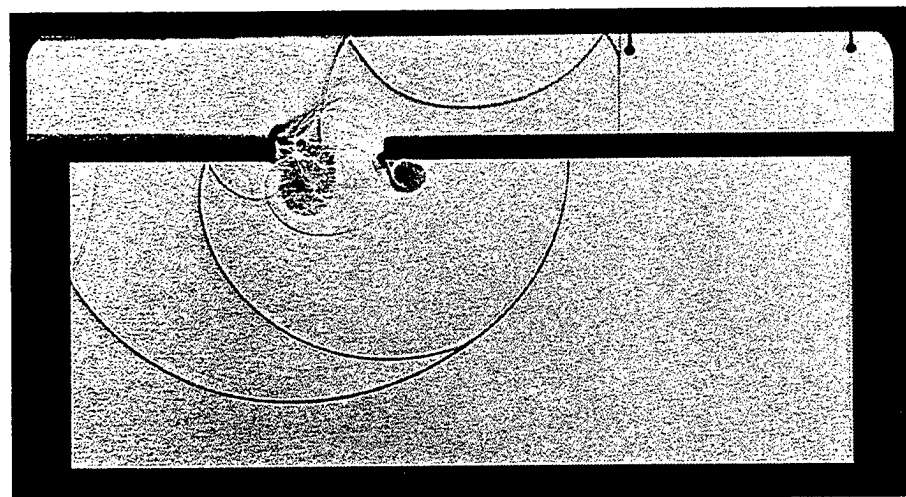


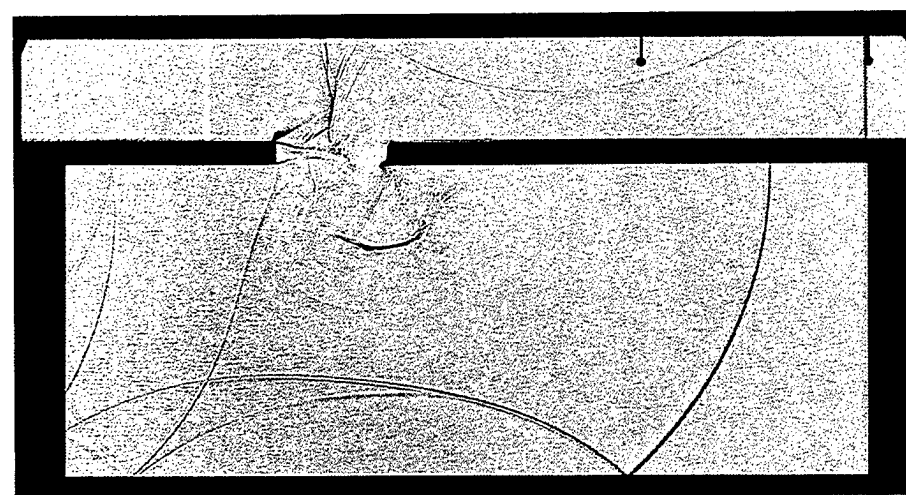
Figure 14. Room corridor models according to the dimensions given in Figure 13.



a) $t = 0.0305 \text{ ms}$

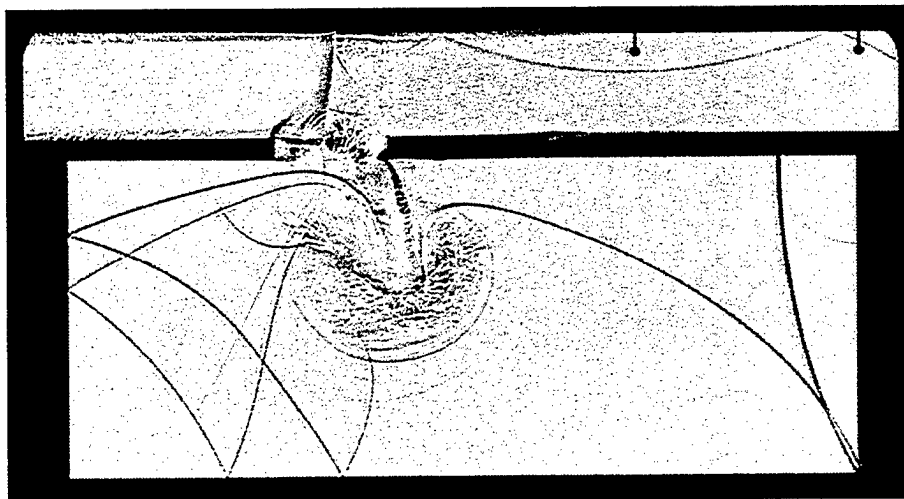


b) $t = 0.1690 \text{ ms}$

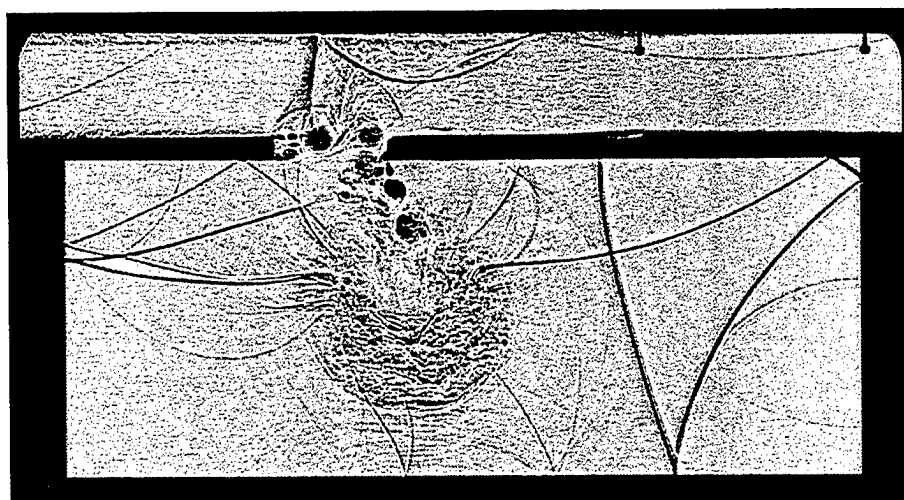


c) $t = 0.2830 \text{ ms}$

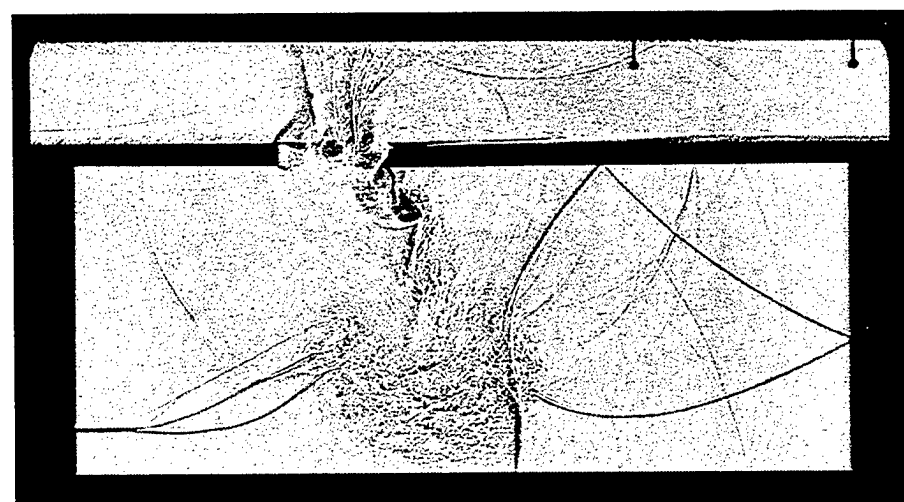
Figure 15. Room corridor configuration, model 6; shadow pictures, shock Mach number: $M_s = 1.41$; (test: 14 769).



d) $t = 0.3970 \text{ ms}$

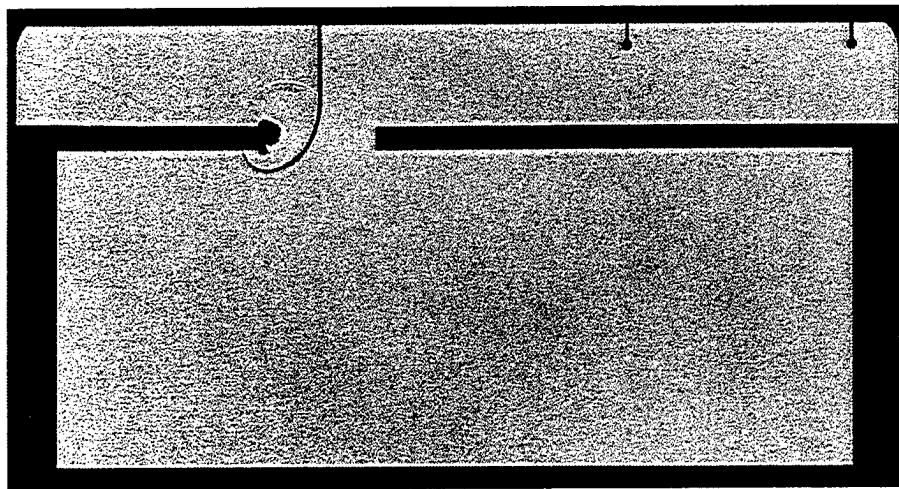


e) $t = 0.5110 \text{ ms}$

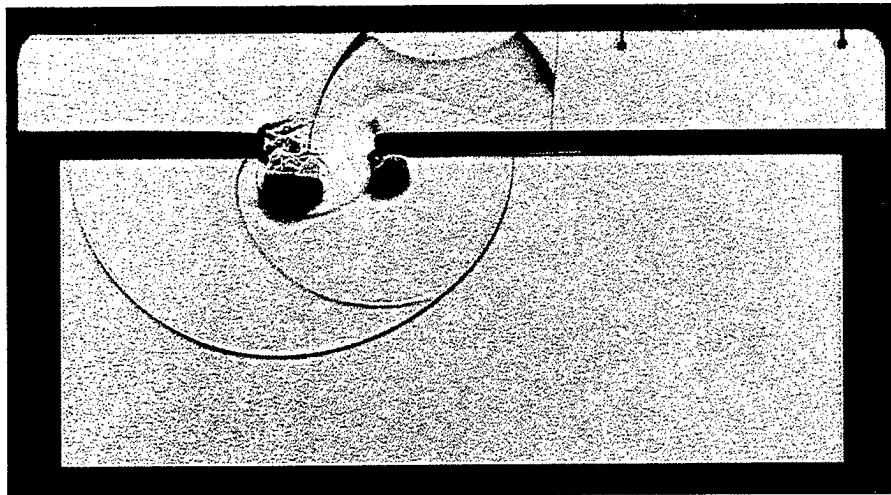


f) $t = 0.6250 \text{ ms}$

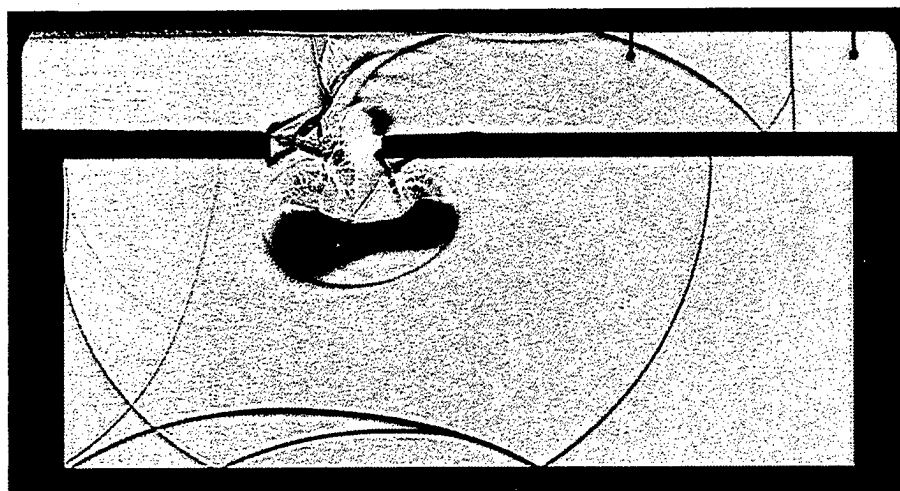
Figure 15. Room corridor configuration, model 6; shadow pictures, shock Mach number: $M_5 = 1.41$; (test: 14 769). (Continued)



a) $t = 0.0265$ ms

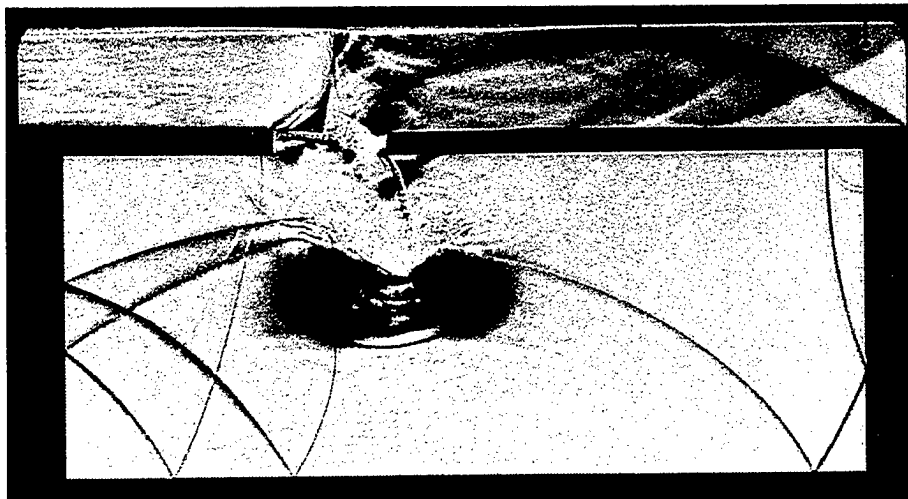


b) $t = 0.1405$ ms

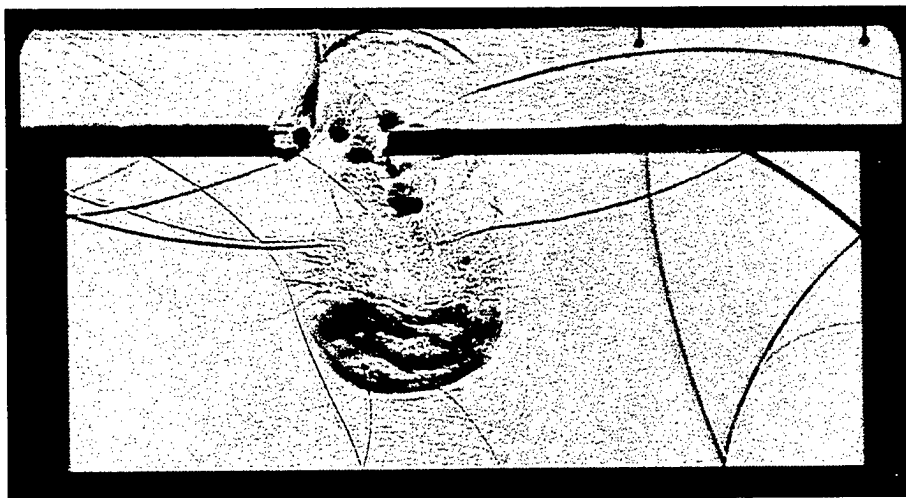


c) $t = 0.2545$ ms

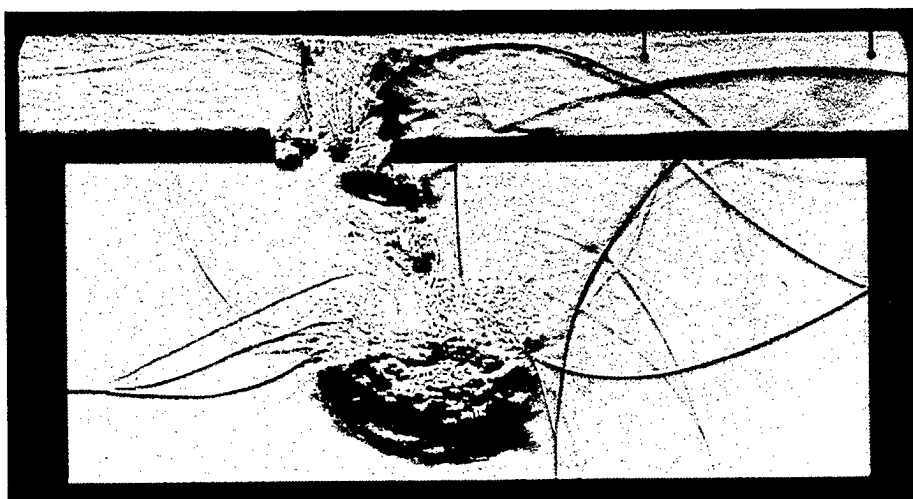
Figure 16. Room corridor configuration, model 6; schlieren pictures, shock Mach number: $M_s = 1.41$; (test: 14 769).



d) $t = 0.3685 \text{ ms}$

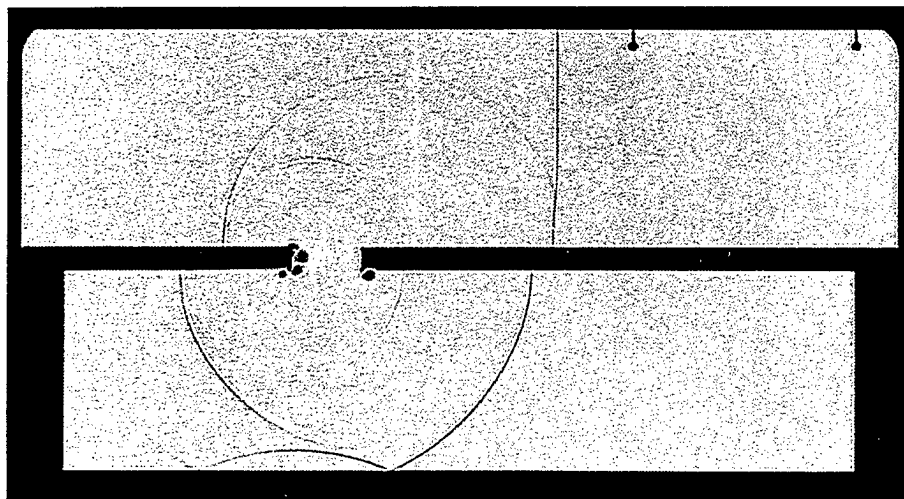


e) $t = 0.4825 \text{ ms}$

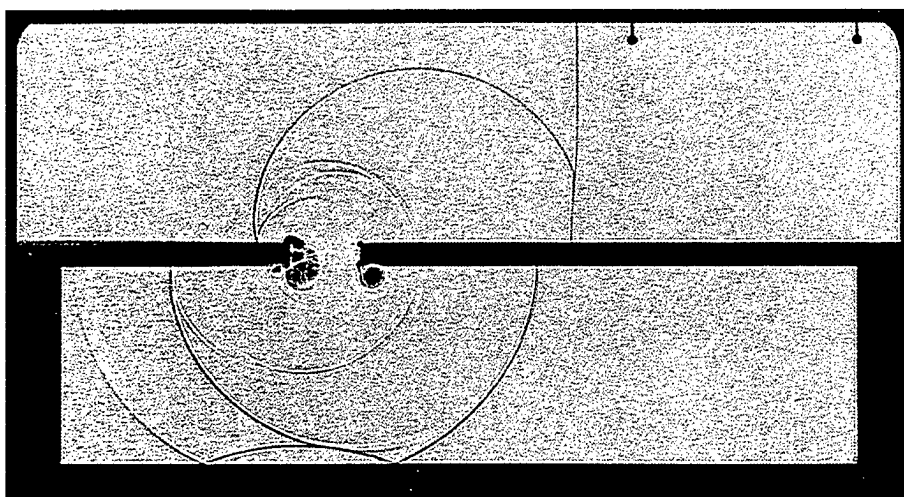


f) $t = 0.5965 \text{ ms}$

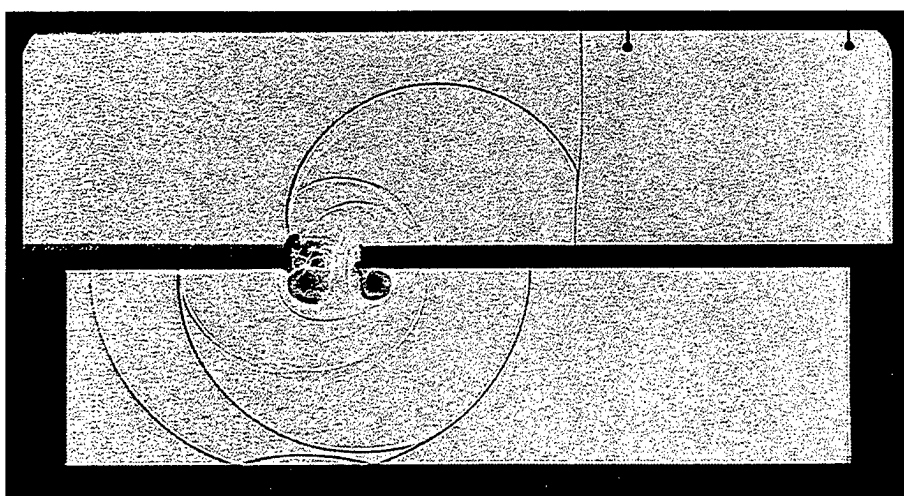
Figure 16. Room corridor configuration, model 6; schlieren pictures, shock Mach number: $M_s = 1.41$; (test: 14 769). (Continued)



a) $M_5 = 1.11$
(test 14 760/8)

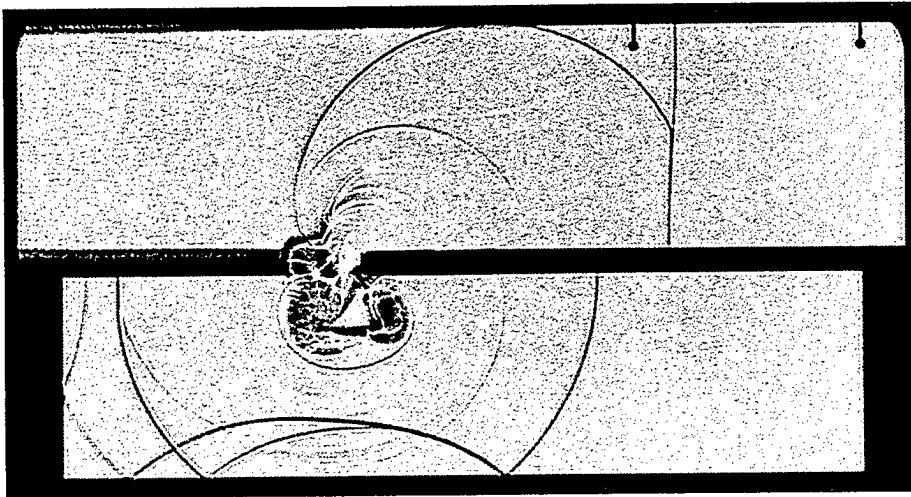


b) $M_5 = 1.22$
(test 14 761/8)

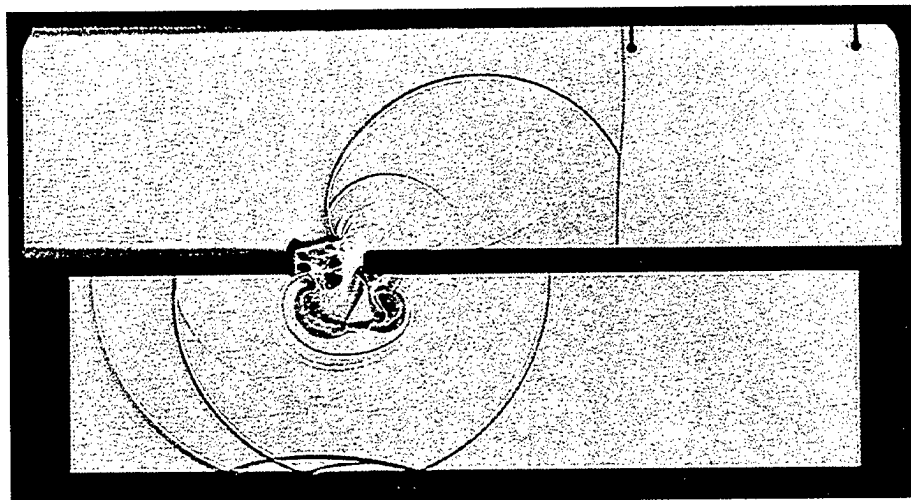


c) $M_5 = 1.33$
(test 14 762/8)

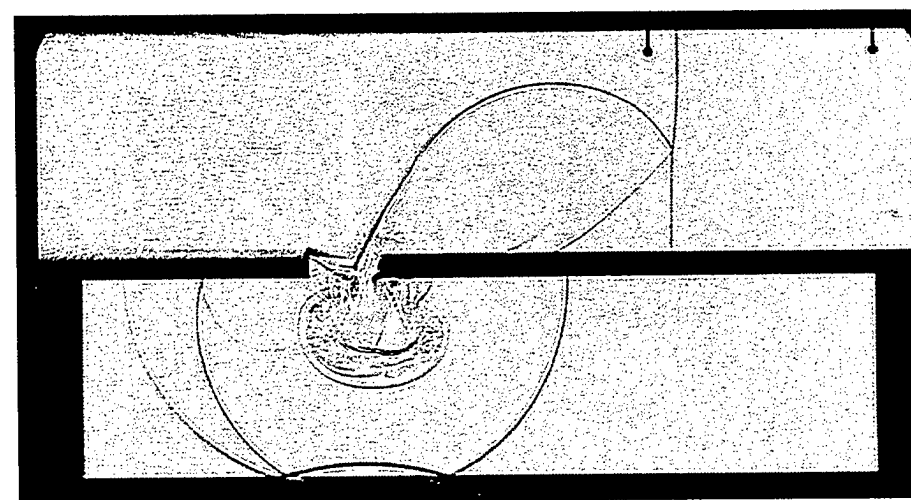
Figure 17. Room corridor configuration, model 5; shadow pictures, early times.



d) $M_S = 1.40$
(test 14 763/10)

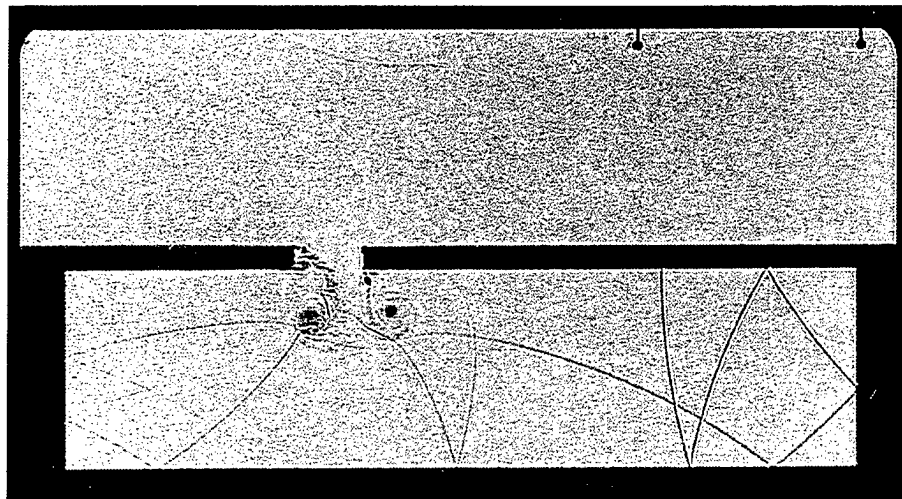


e) $M_S = 1.52$
(test 14 764/10)

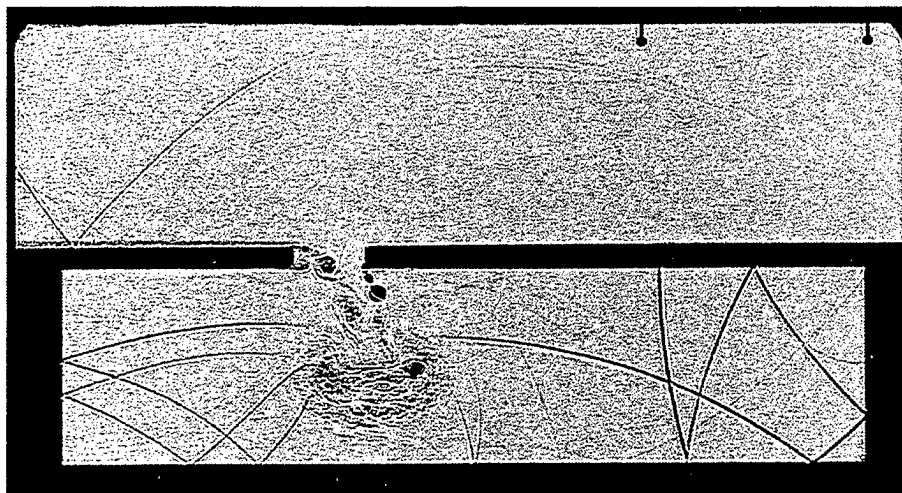


f) $M_S = 1.93$
(test 14 765/10)

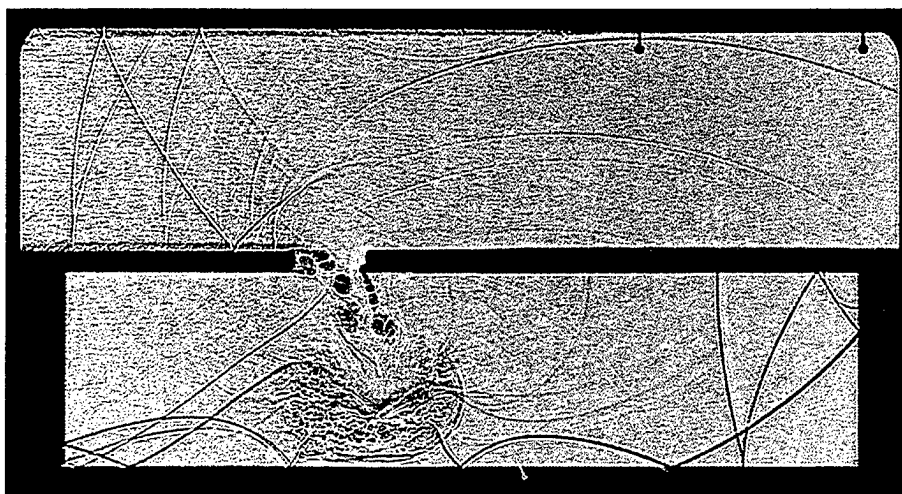
Figure 17. Room corridor configuration, model 5; shadow pictures, early times.(Continued)



a) $M_S = 1.11$
(test 14 760/20)

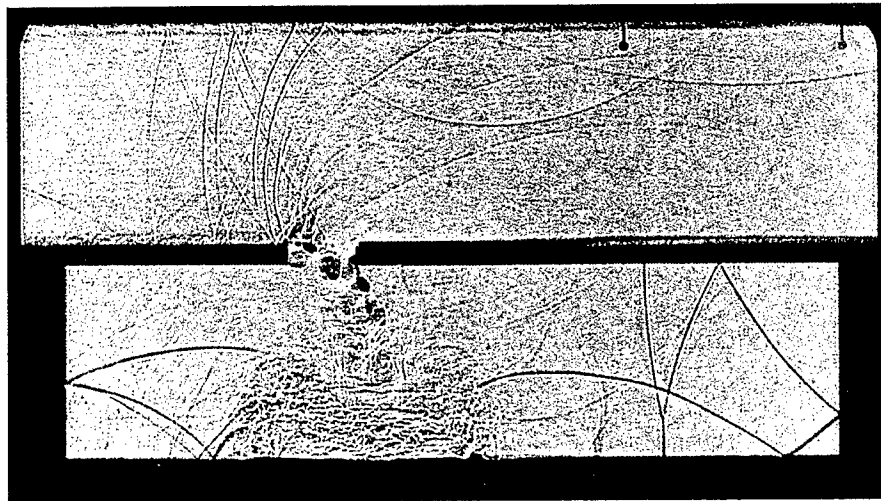


b) $M_S = 1.22$
(test 14 761/20)

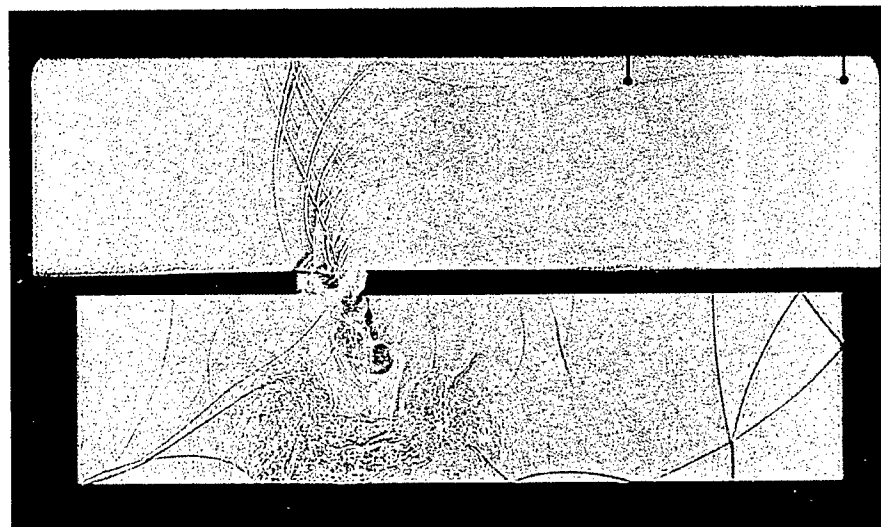


c) $M_S = 1.33$
(test 14 762/20)

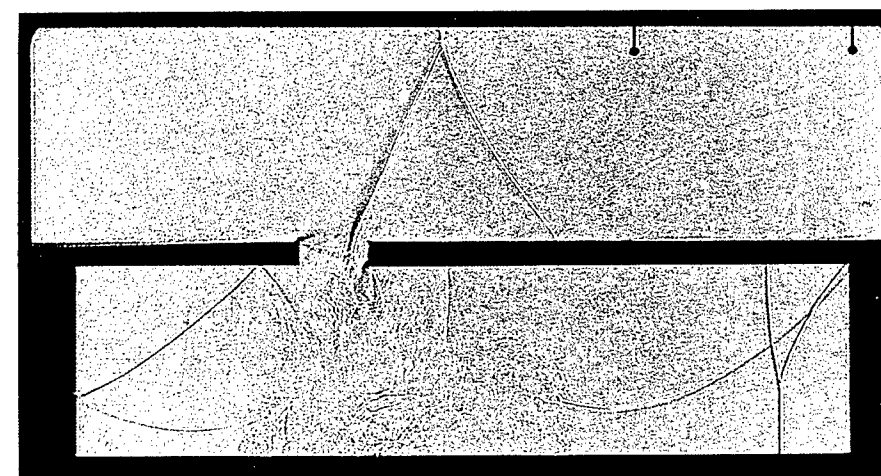
Figure 18. Room corridor configuration, model 4; shadow pictures, later times.



d) $M_s = 1.40$
(test 14 763/22)

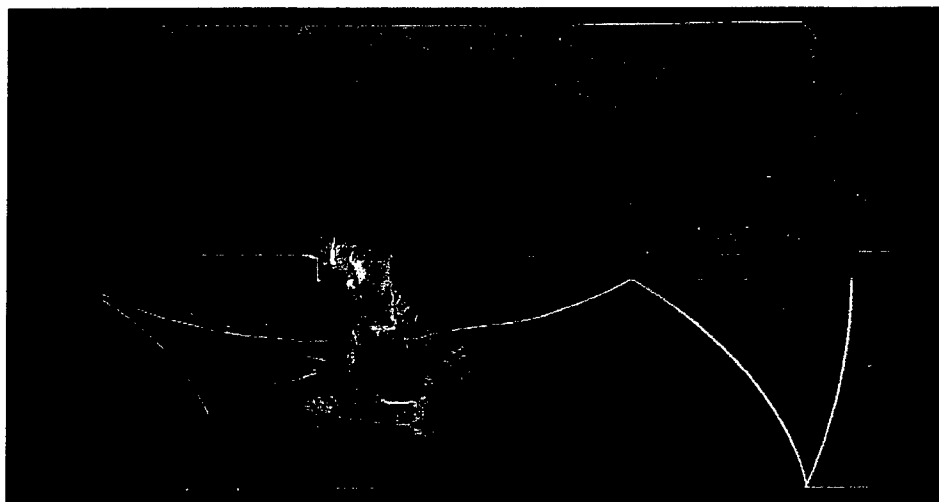


e) $M_s = 1.52$
(test 14 764/24)



f) $M_s = 1.93$
(test 14 765/24)

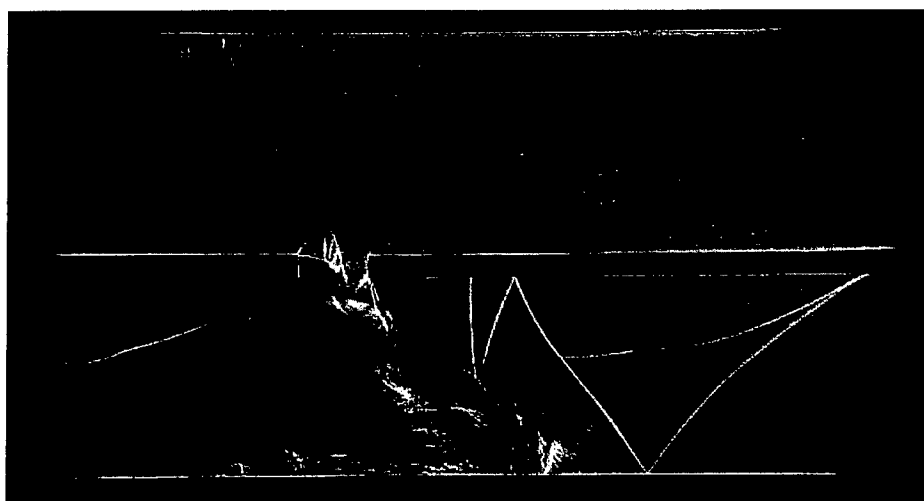
Figure 18. Room corridor configuration, model 4; shadow pictures, later times. (Continued)



a) $t = 0.299$ ms
(test 14 871)



b) $t = 0.399$ ms
(test 14 872)



c) $t = 0.522$ ms
(test 14 874)

Figure 19. Room corridor configuration, model 4; color schlieren pictures; shock Mach number: $M_s = 1.31$.

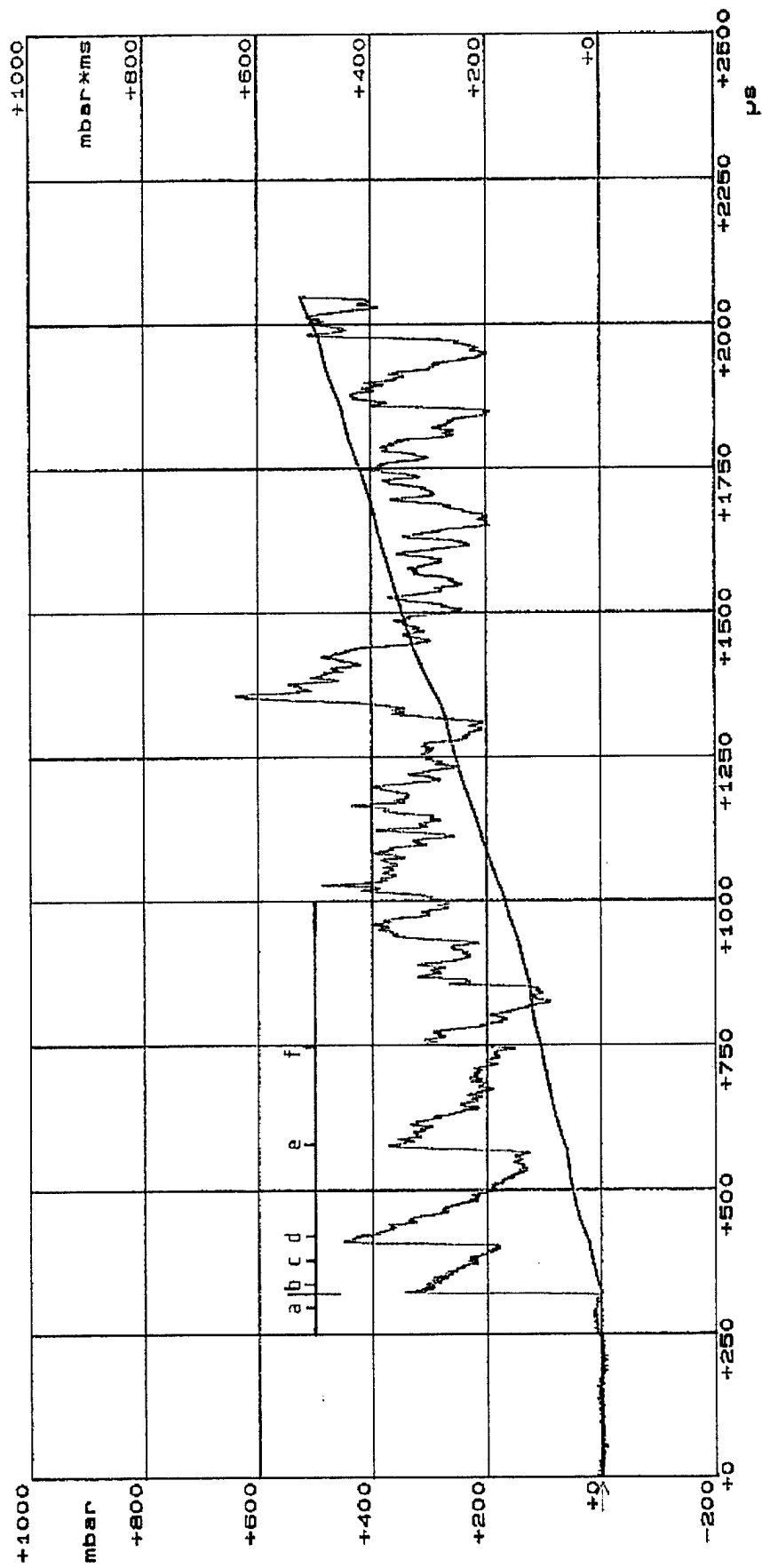
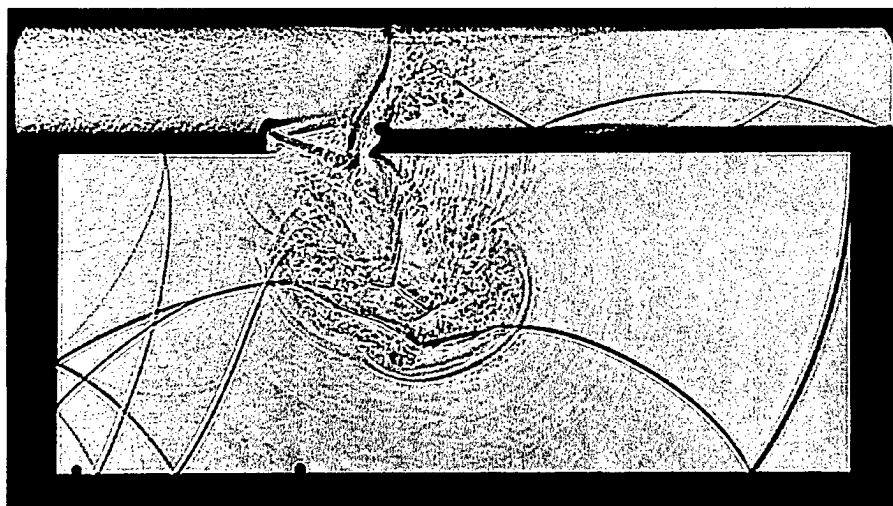
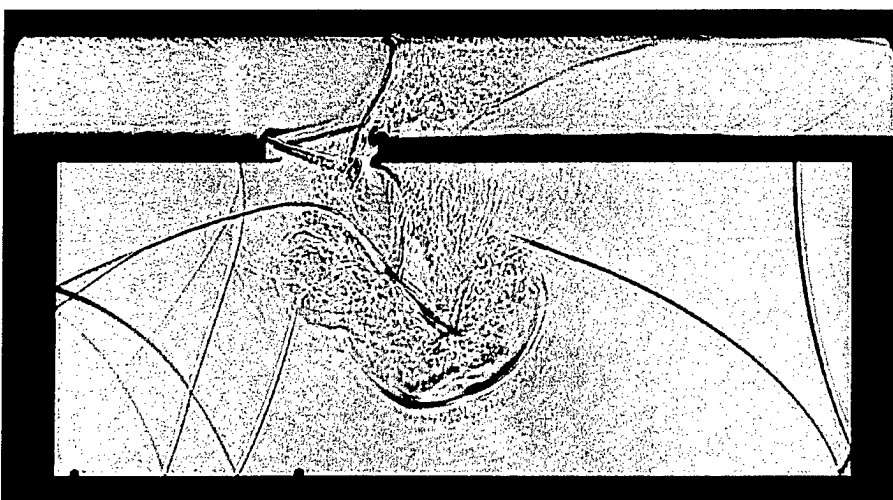


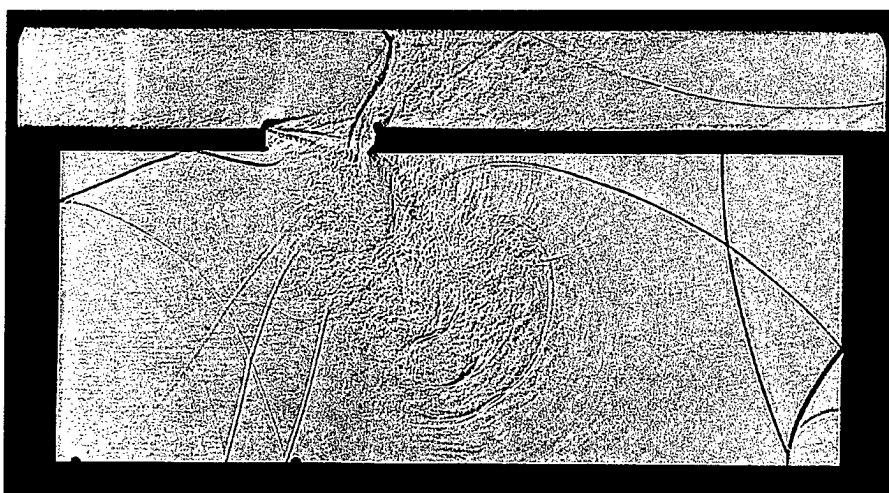
Figure 20. Pressure-time record at the end wall of a room corridor configuration, model 6. $M_s = 1.67$.
An additional scale is included for comparisons with the shadowgraph sequence of Figure 21.



a) $t = -0.020$ ms



b) $t = +0.020$ ms

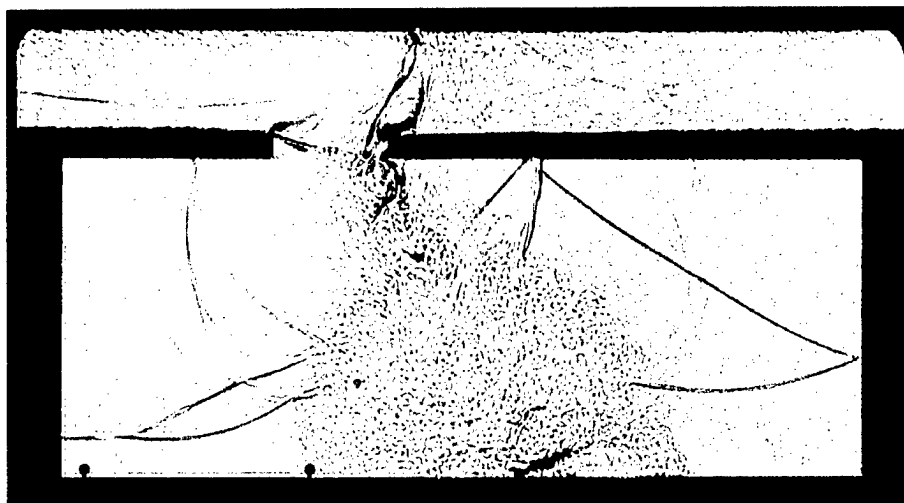


c) $t = 0.060$ ms

Figure 21. Shock- and flow visualization, room corridor model 6, $M_s = 1.67$ (test 15 105). Exposure time is related to the first peak of the pressure record (Figure 20).



d) $t = 0.100$ ms



e) $t = 0.260$ ms



f) $t = 0.420$ ms

Figure 21. Shock- and flow visualization, room corridor model 6, $M_s = 1.67$ (test 15 105). Exposure time is related to the first peak of the pressure record (Figure 20). (Continued)

Mean Overpressure

$$\bar{p} = \frac{1}{t_0} \int_0^{t_0} p(t) dt$$

$t_0 = 0.25\text{ms}$ for model ① $t_0 = 0.5\text{ms}$ for models ②-⑥

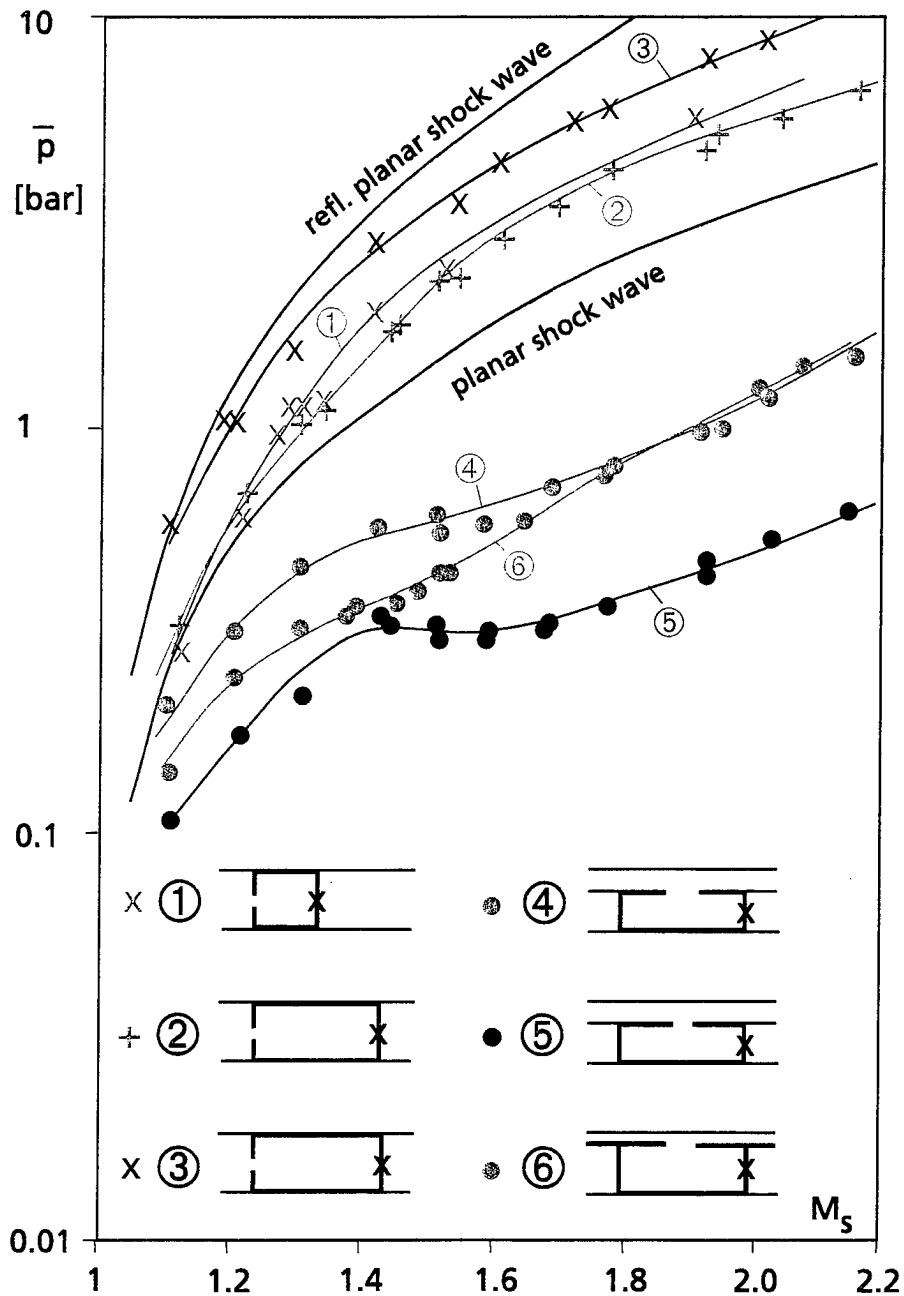


Figure 22. Shock Tube tests. Average pressure \bar{p} at the end-walls of single room (models 1 - 3) and room corridor configurations (models 4 - 6) for an averaging interval of $t_0 = 0.5$ ms (except model 1; $t_0 = 0.25$ ms).

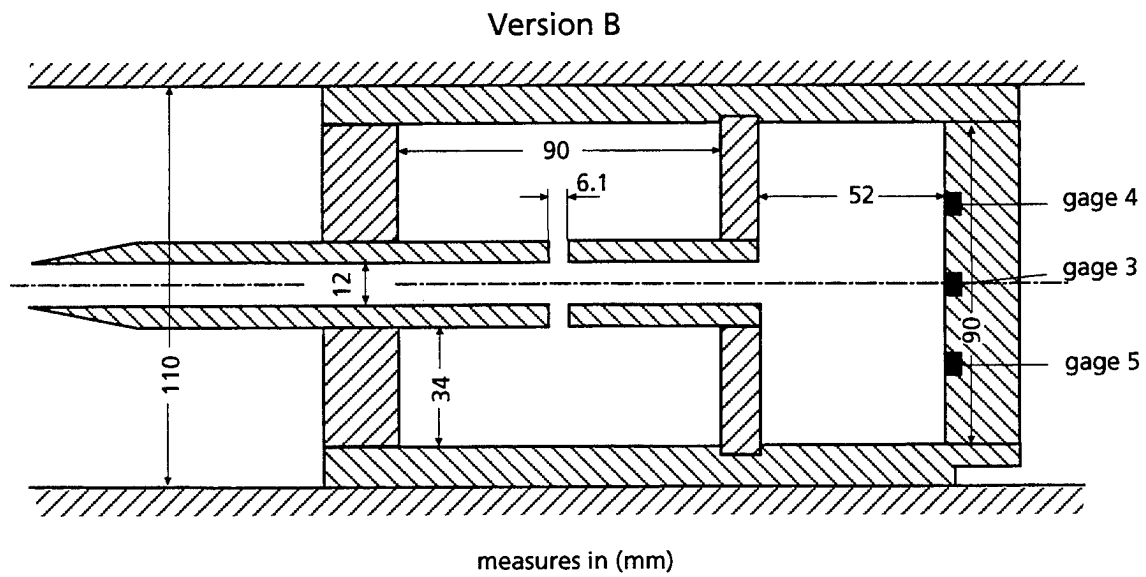
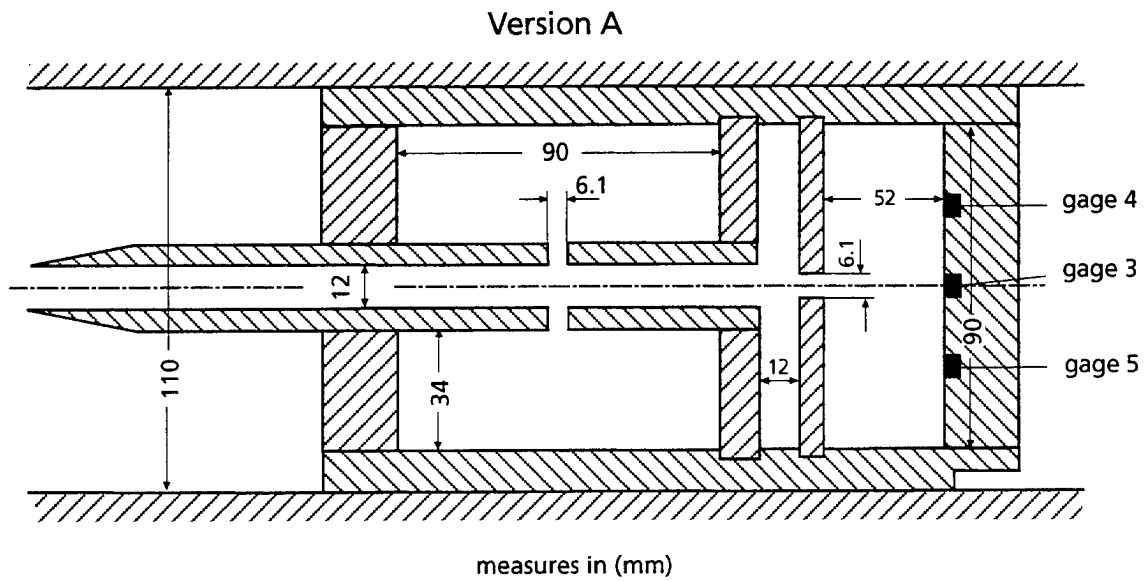
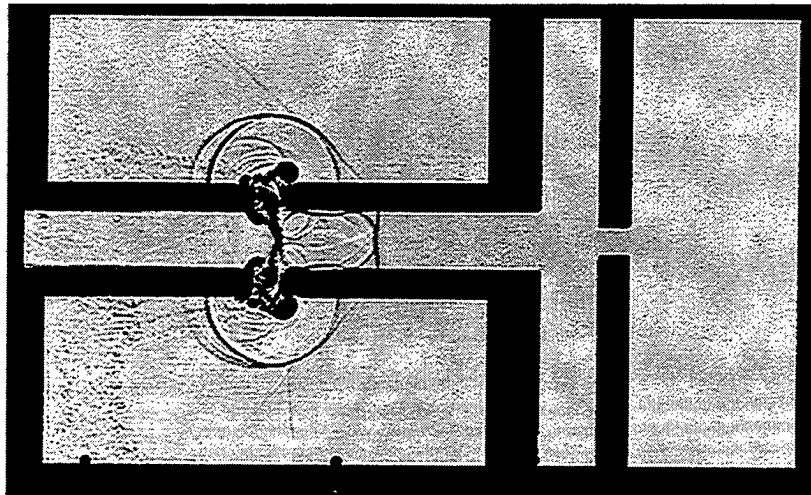
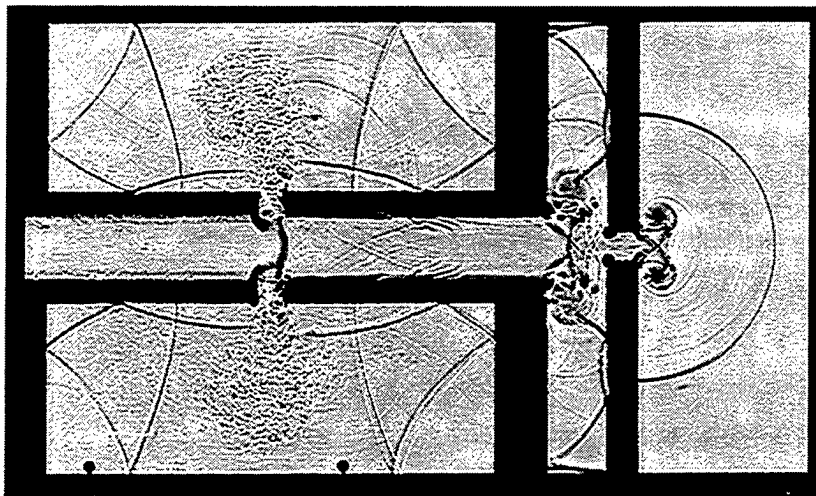


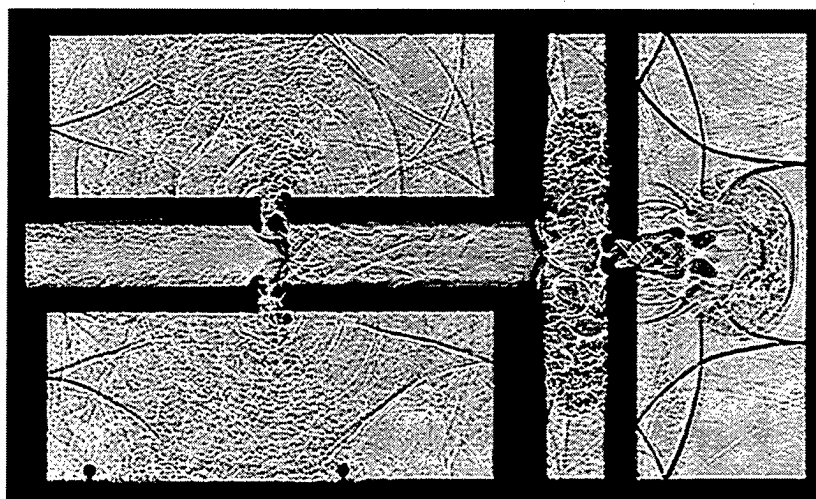
Figure 23. Sketch of the two versions of single story system for shock tube tests.



a) $t = 0.060$ ms

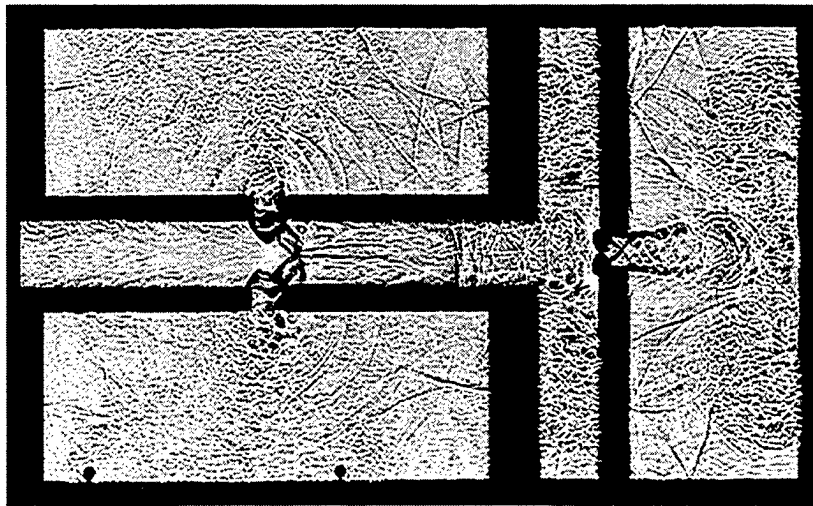


b) $t = 0.260$ ms

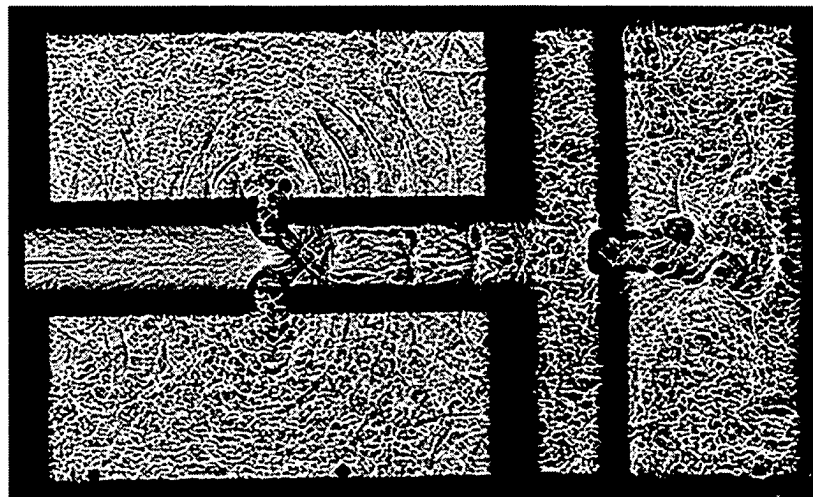


c) $t = 0.390$ ms

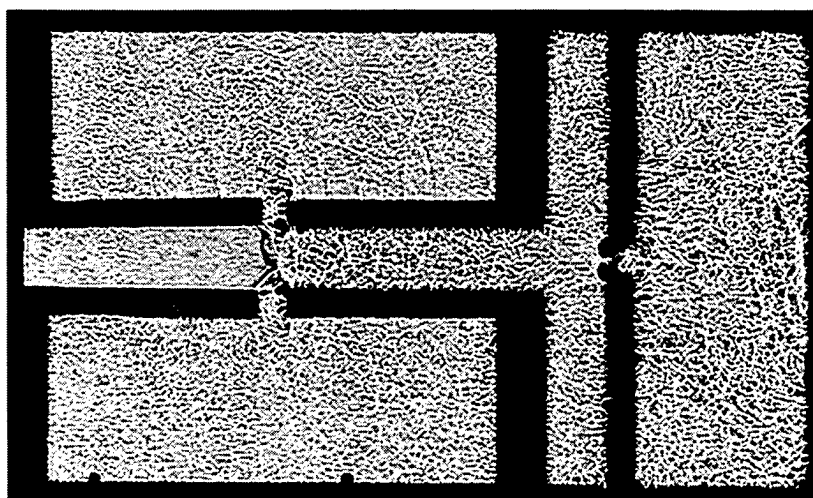
Figure 24. Flow in the single story system. Version A. $M_s = 1.63$; (test 15 153).



d) $t = 0.420$ ms

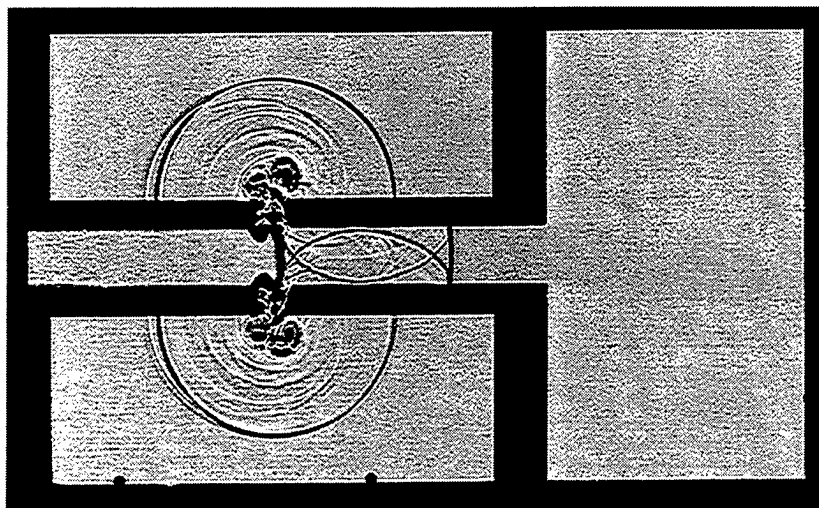


e) $t = 0.580$ ms

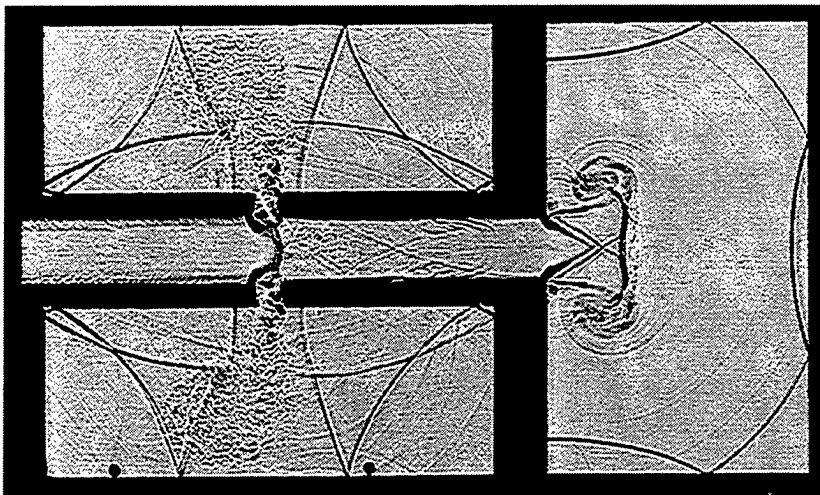


f) $t = 0.900$ ms

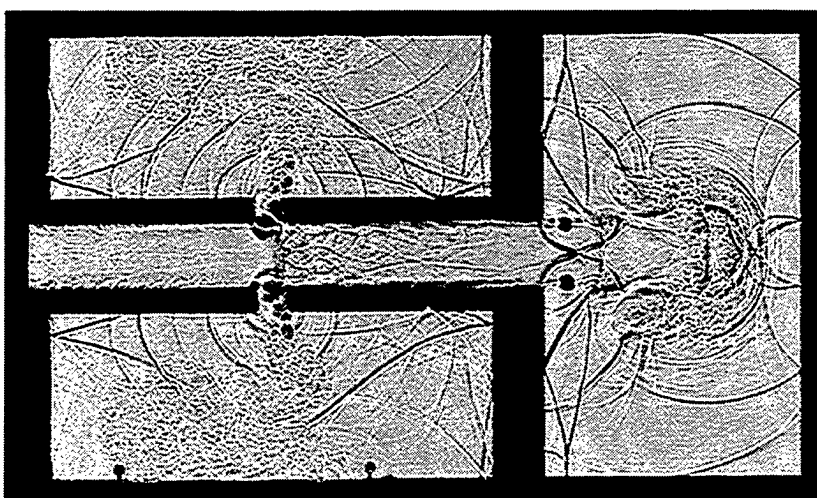
Figure 24. Flow in the single story system. Version A. $M_s = 1.63$; (test 15 153). (Continued)



a) $t = 0.045$ ms

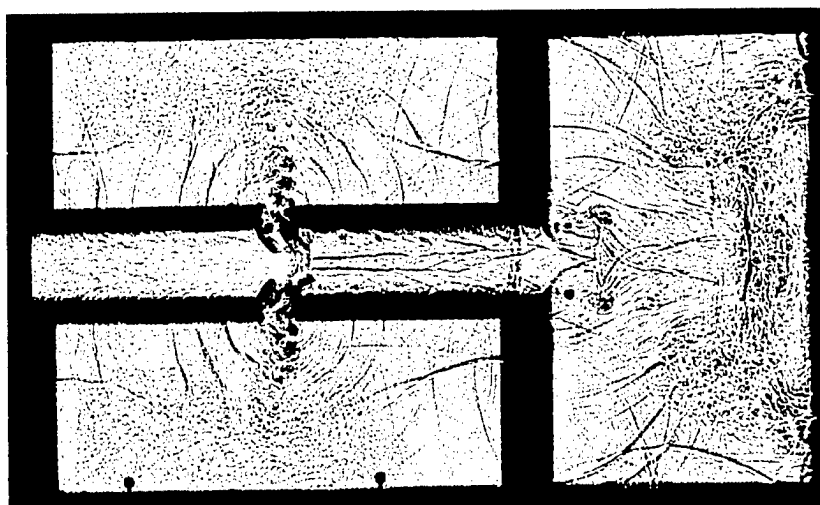


b) $t = 0.115$ ms

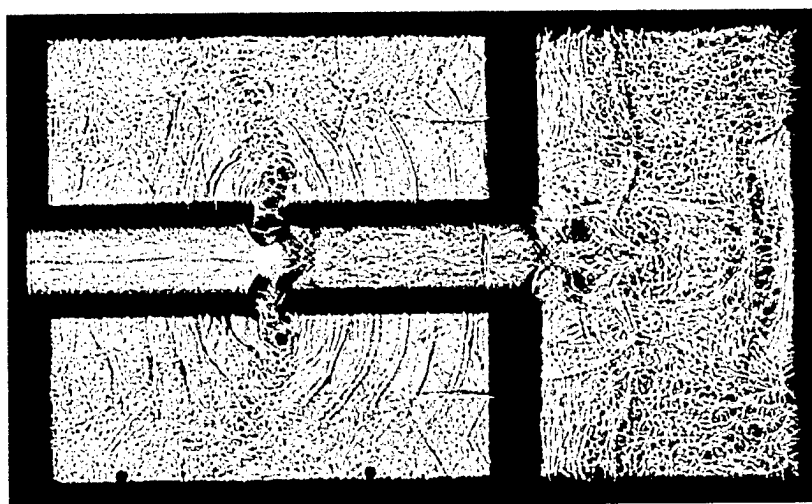


c) $t = 0.275$ ms

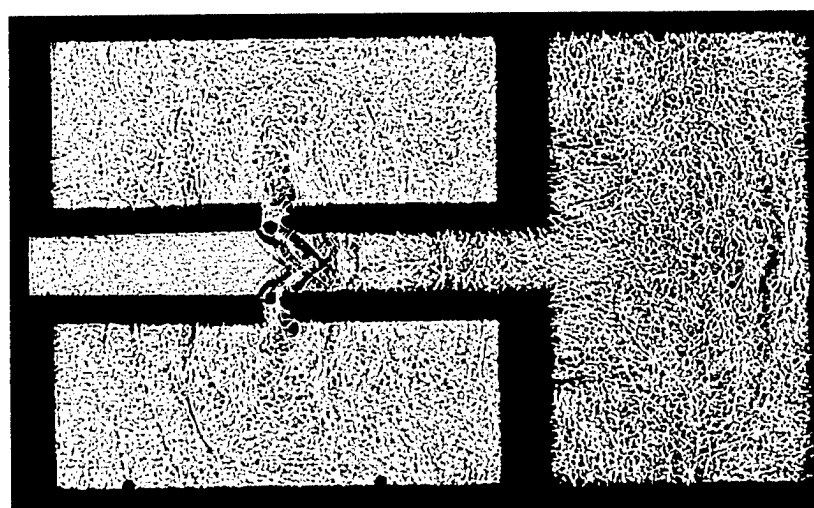
Figure 25. Flow in the single story system. Version B. $M_S = 1.61$; (test 15 223).



d) $t = 0.435$ ms

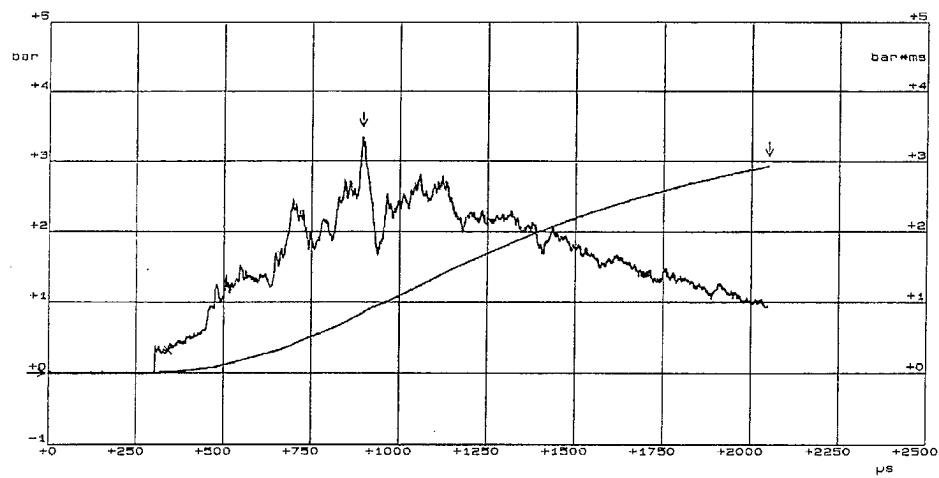


e) $t = 0.595$ ms

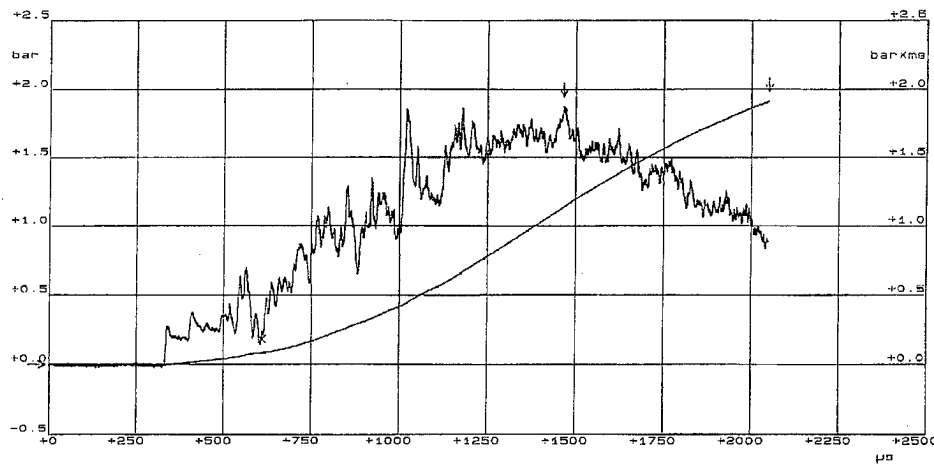


f) $t = 0.915$ ms

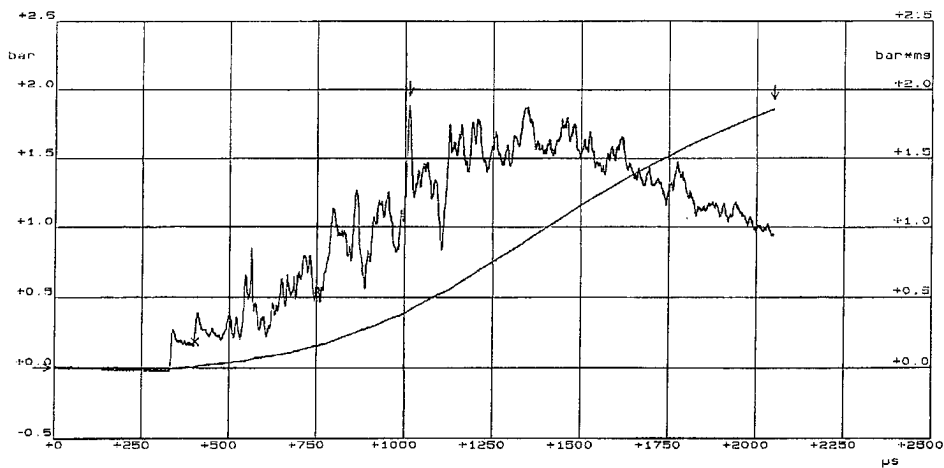
Figure 25. Flow in the single story system. Version B. $M_5 = 1.61$; (test 15 223). (Continued)



a) Location 3

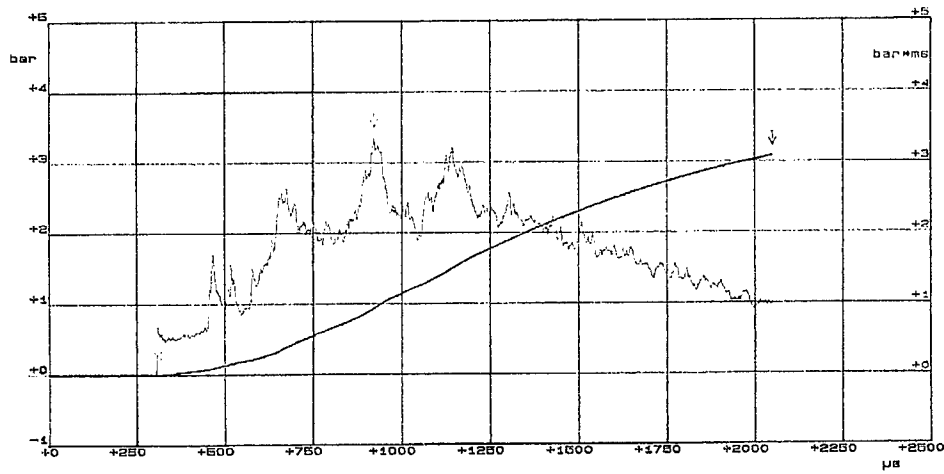


b) Location 4

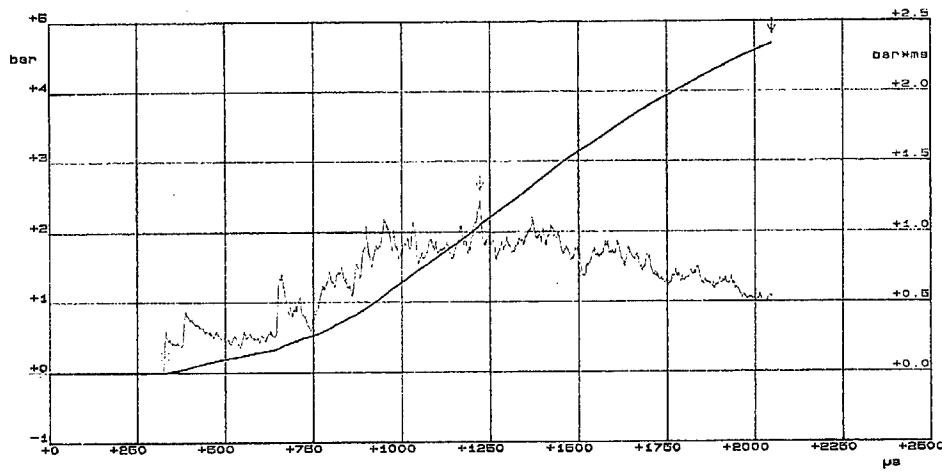


c) Location 5

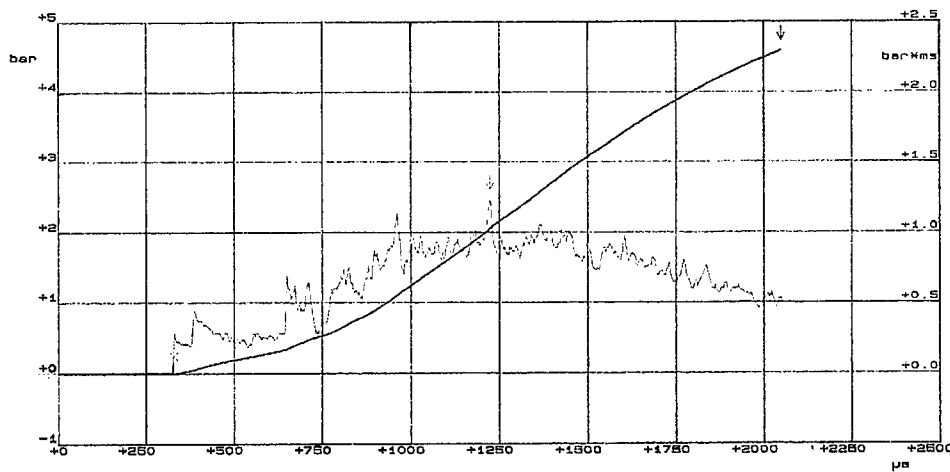
Figure 26. Pressure-time and impulse-time histories at different gage locations of the single story system, version A. $M_s = 1.63$; (test 15 153).



a) Location 3



b) Location 4



c) Location 5

Figure 27. Pressure-time and impulse-time histories at different gage locations of the single story system, version B, $M_s = 1.61$; (test 15 223).

Single - Story System

$$\text{Mean Overpressure : } \bar{p} = \frac{1}{t_0} \int_0^{t_0} p(t) dt$$

$$t_0 = 0.5 \text{ ms}$$

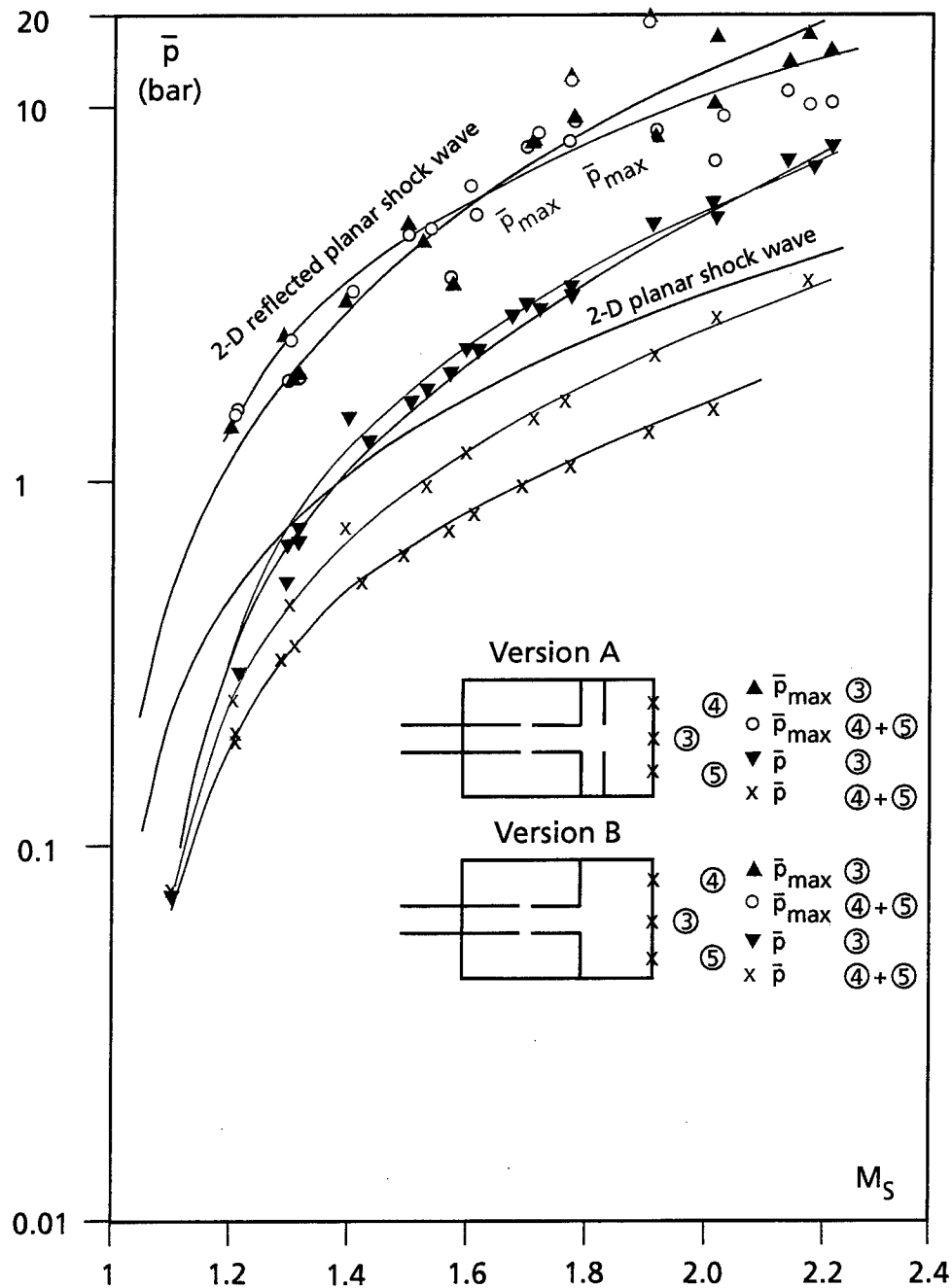
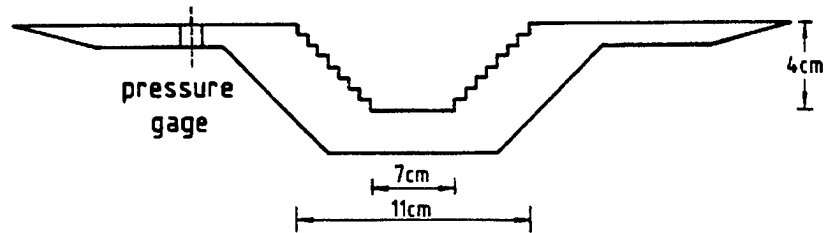


Figure 28. Mean overpressure vs shock Mach number M_s for single story systems version A and B.

stairwells configuration 2 - D version



stairwells configuration 3 - D version

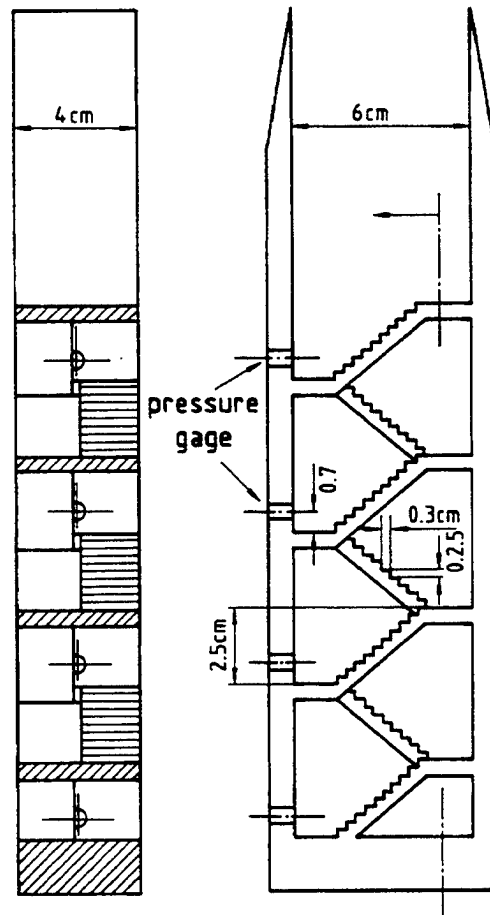


Figure 29. Stairwells configuration.

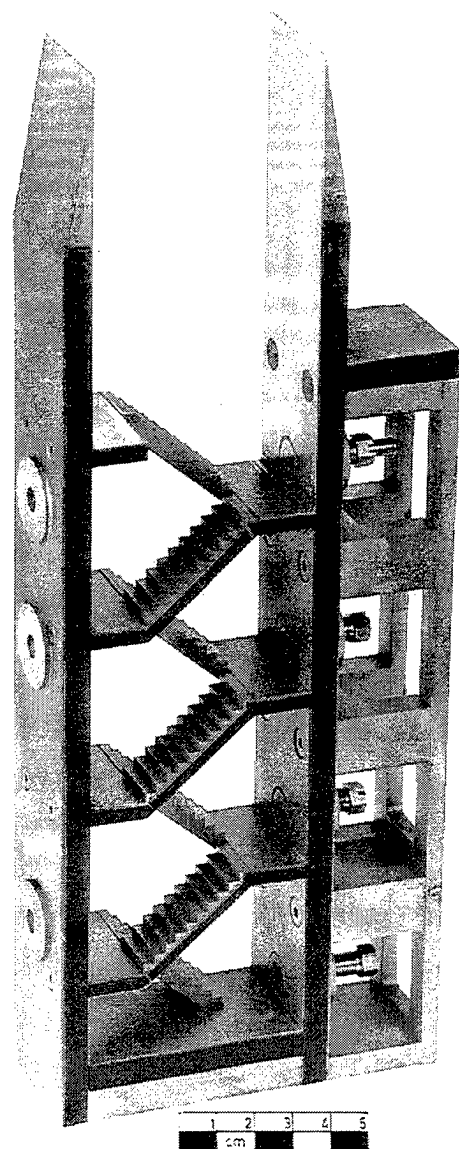
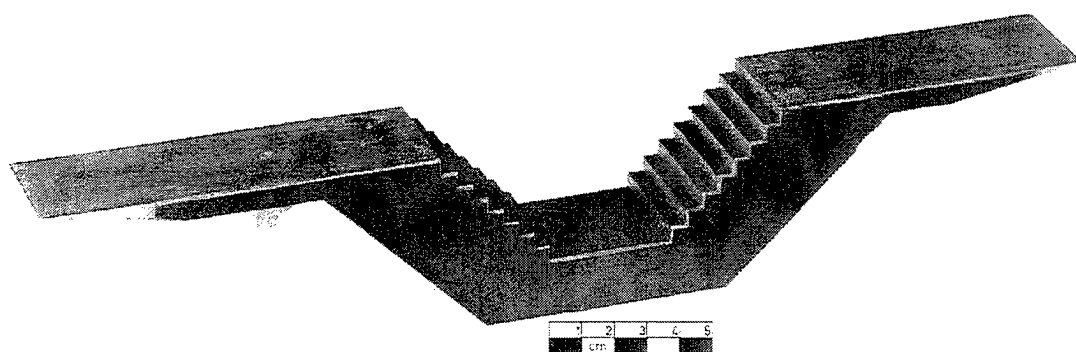


Figure 30. Stairwell models

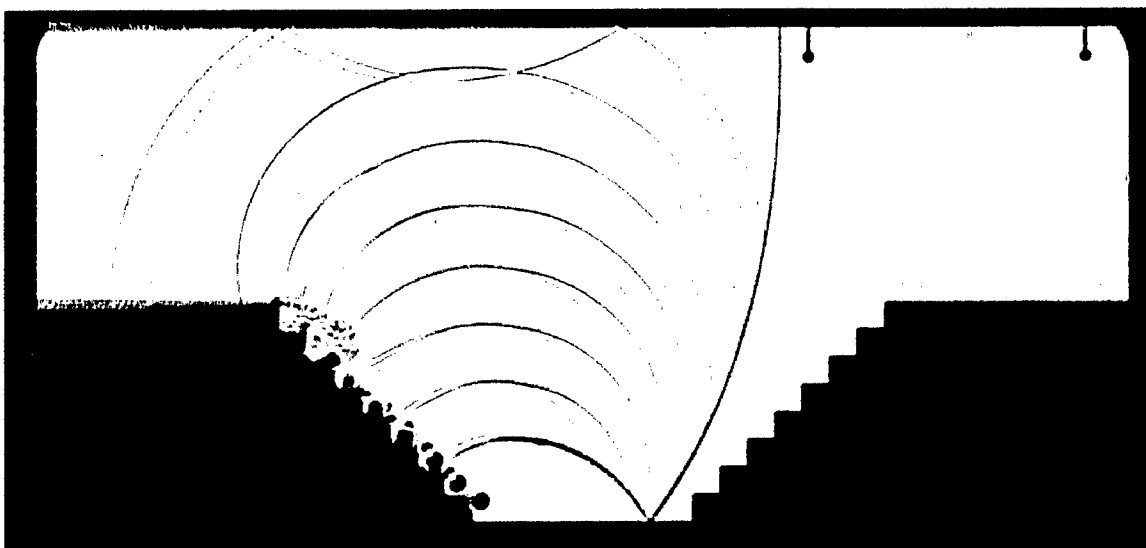
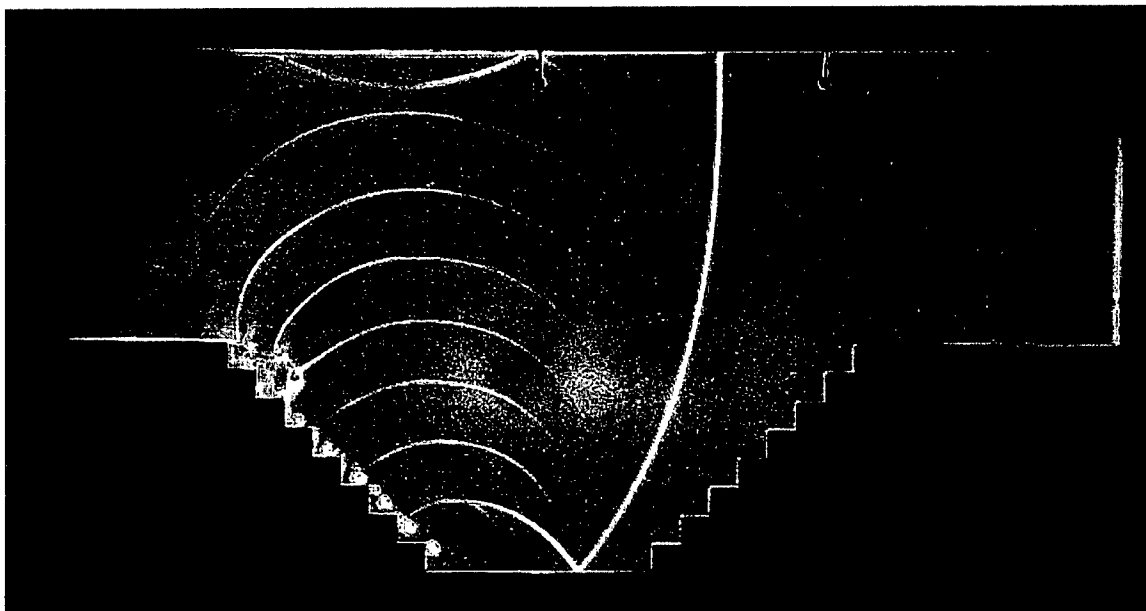
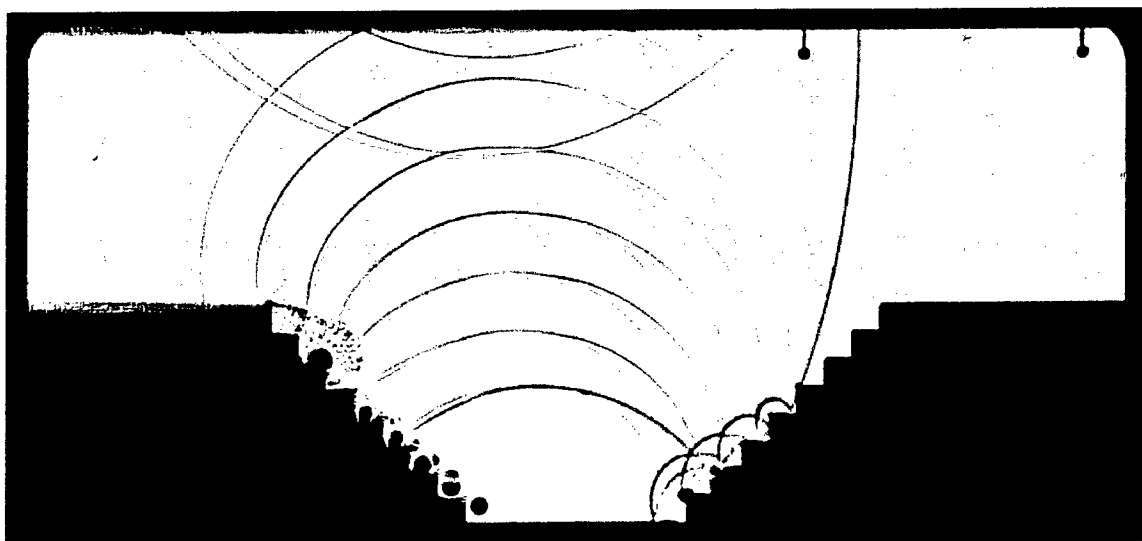
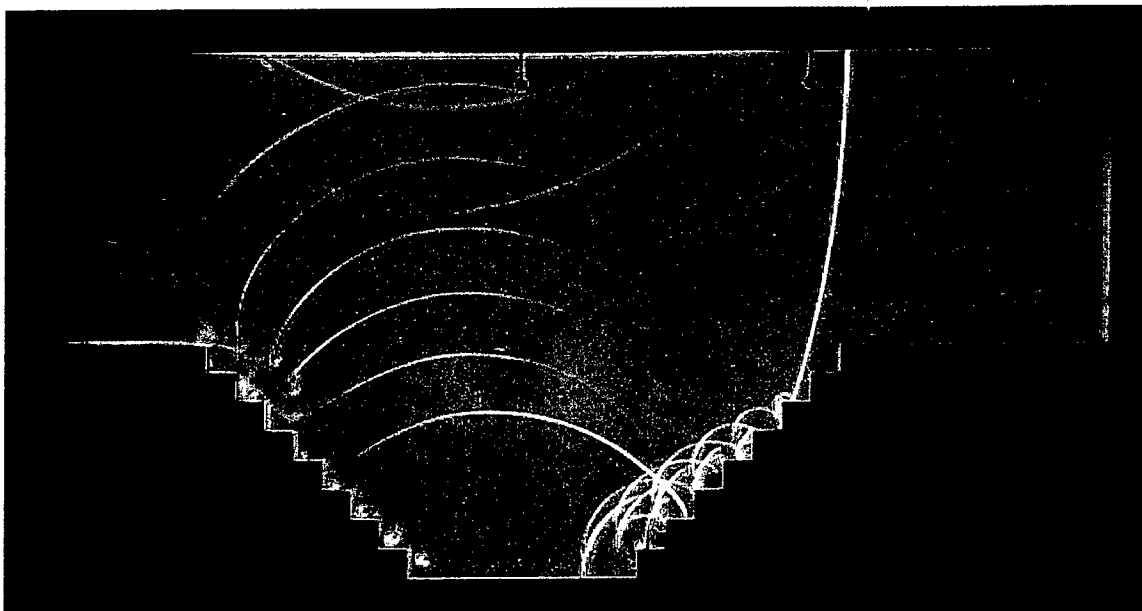
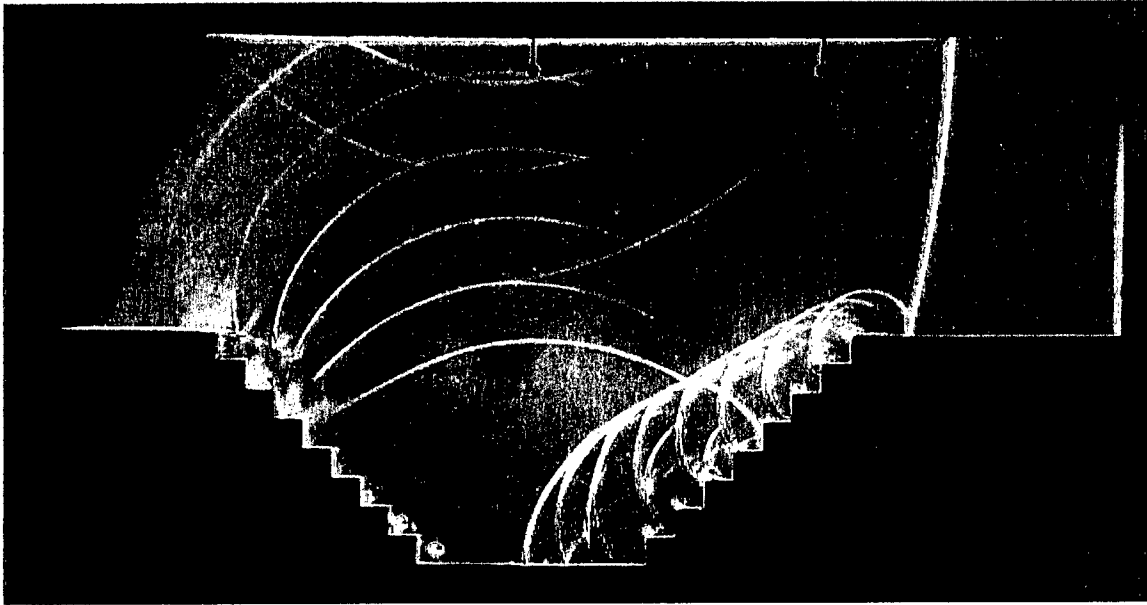


Figure 31. 2-D version of the stairwells configuration. Comparison of color schlieren (top) and shadow pictures (below), $M_s = 1.33$; $t = 0.185$ ms.

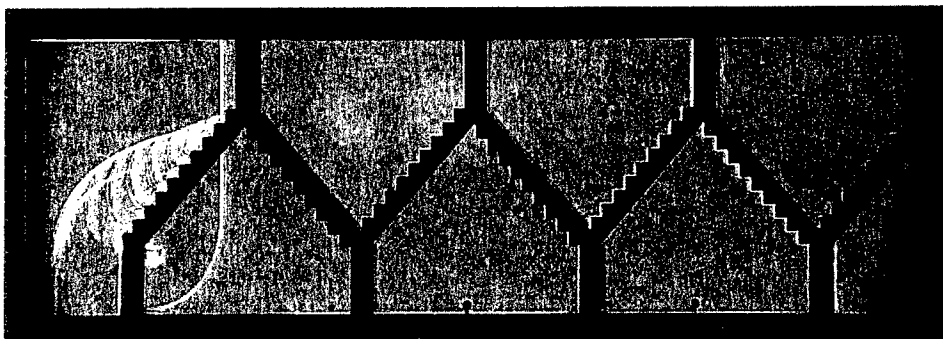


.Figure 31. 2-D version of the stairwells configuration. Comparison of color schlieren (top) and shadow pictures (below), $M_s = 1.33$, $t = 0.230$ ms. (Continued)



.Figure 31. 2-D version of the stairwells configuration. Comparison of color schlieren (top) and shadow pictures (below), $M_s = 1.33$, $t = 0.295$ ms. (Continued)

a) $t = 0.063$ ms
test 14 732;
14 697/4



b) $t = 0.103$ ms
test 14 733;
14 687/6

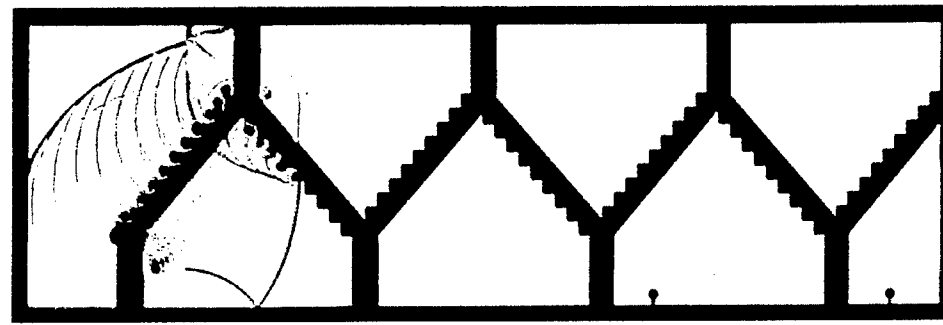
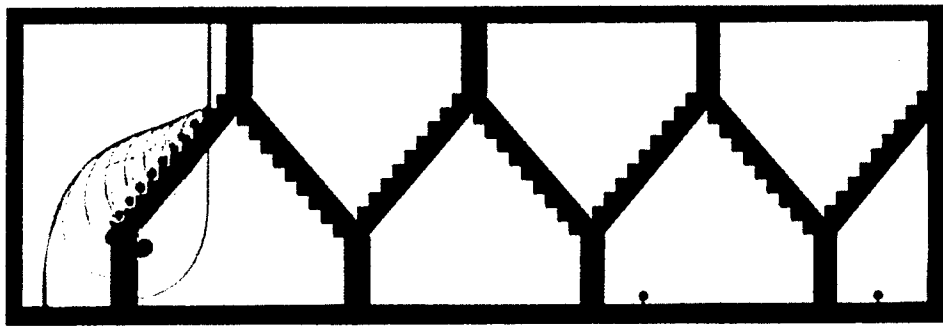
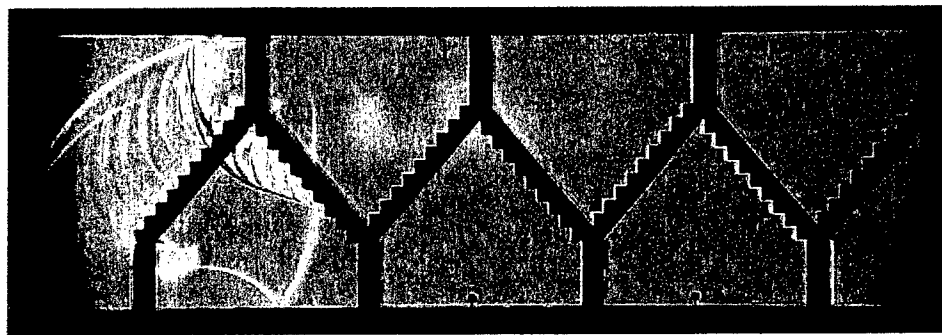
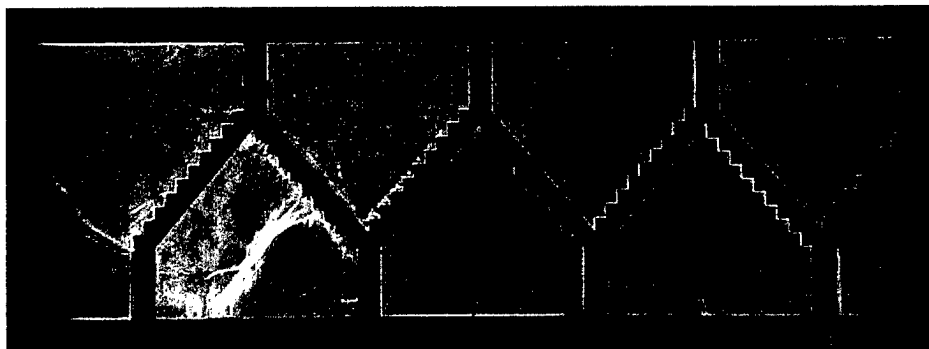


Figure 32. 3-D version of the stairwells configuration. Comparison of color schlieren and shadow pictures. $M_S = 1.33$.

c) $t = 0.223$ ms
test 14 736:
14 697/12



d) $t = 0.303$ ms
test 14 739:
14 697/16

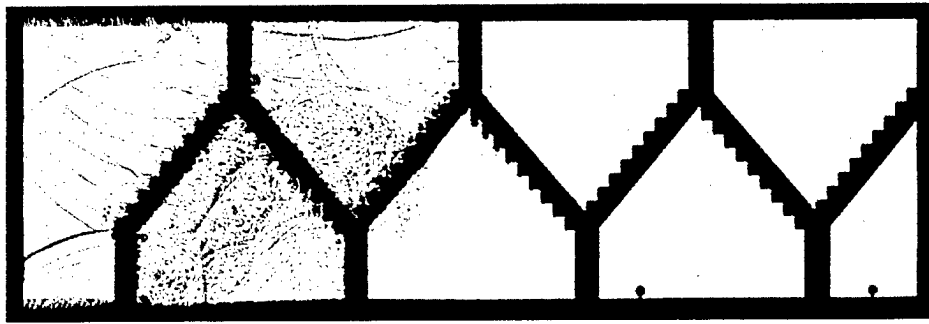
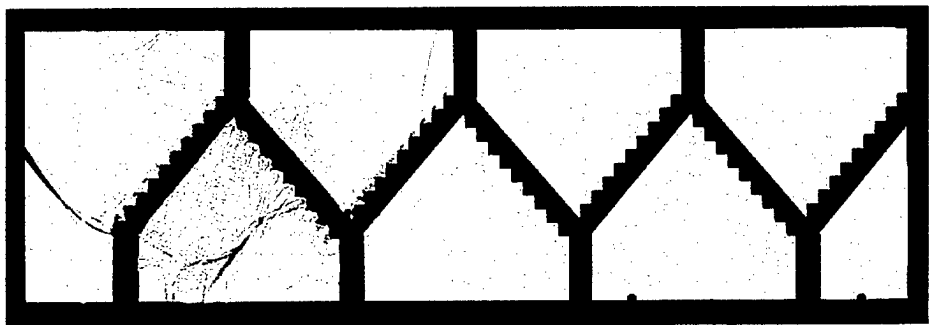
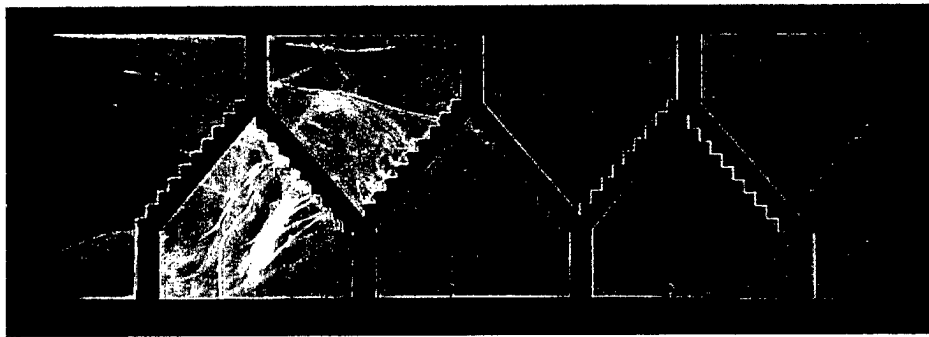
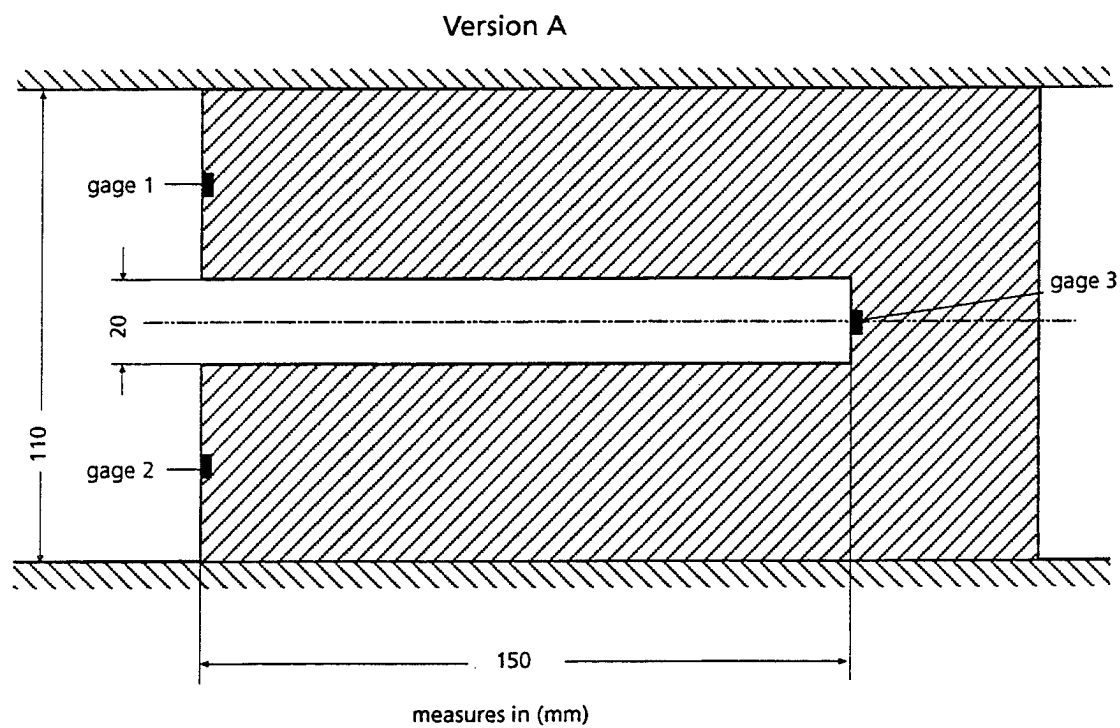


Figure 32. 3-D version of the stairwells configuration. Comparison of color schlieren and shadow pictures. $M_5 = 1.33$. (Continued)



Rb. 23.02.96

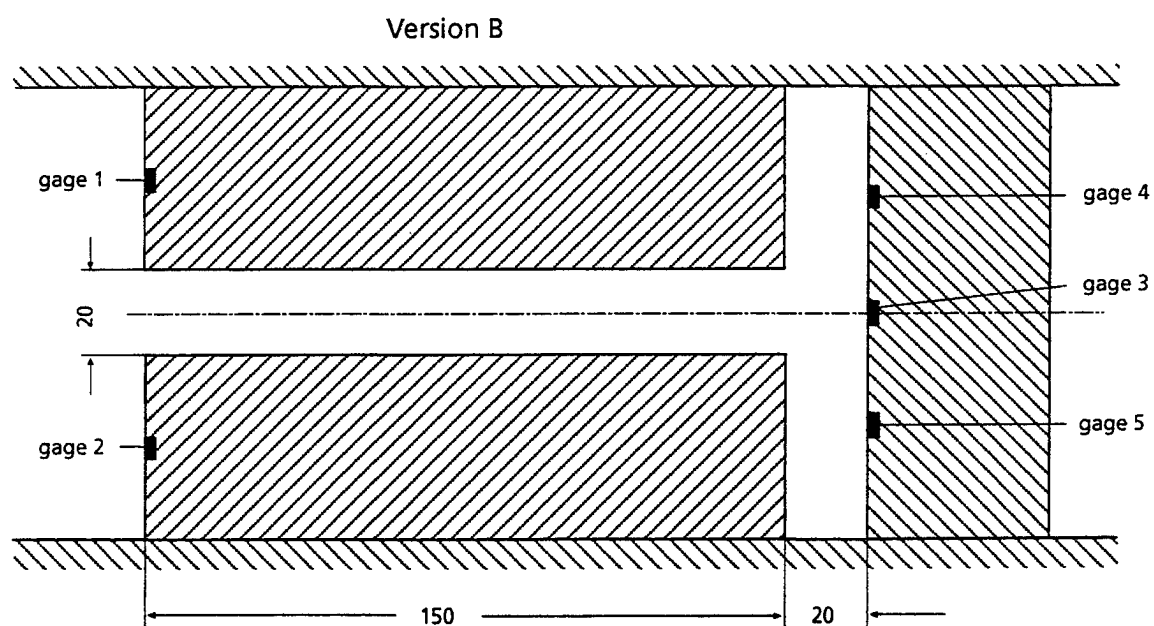


Figure 33. Duct systems for shock tube tests.

Duct Systems

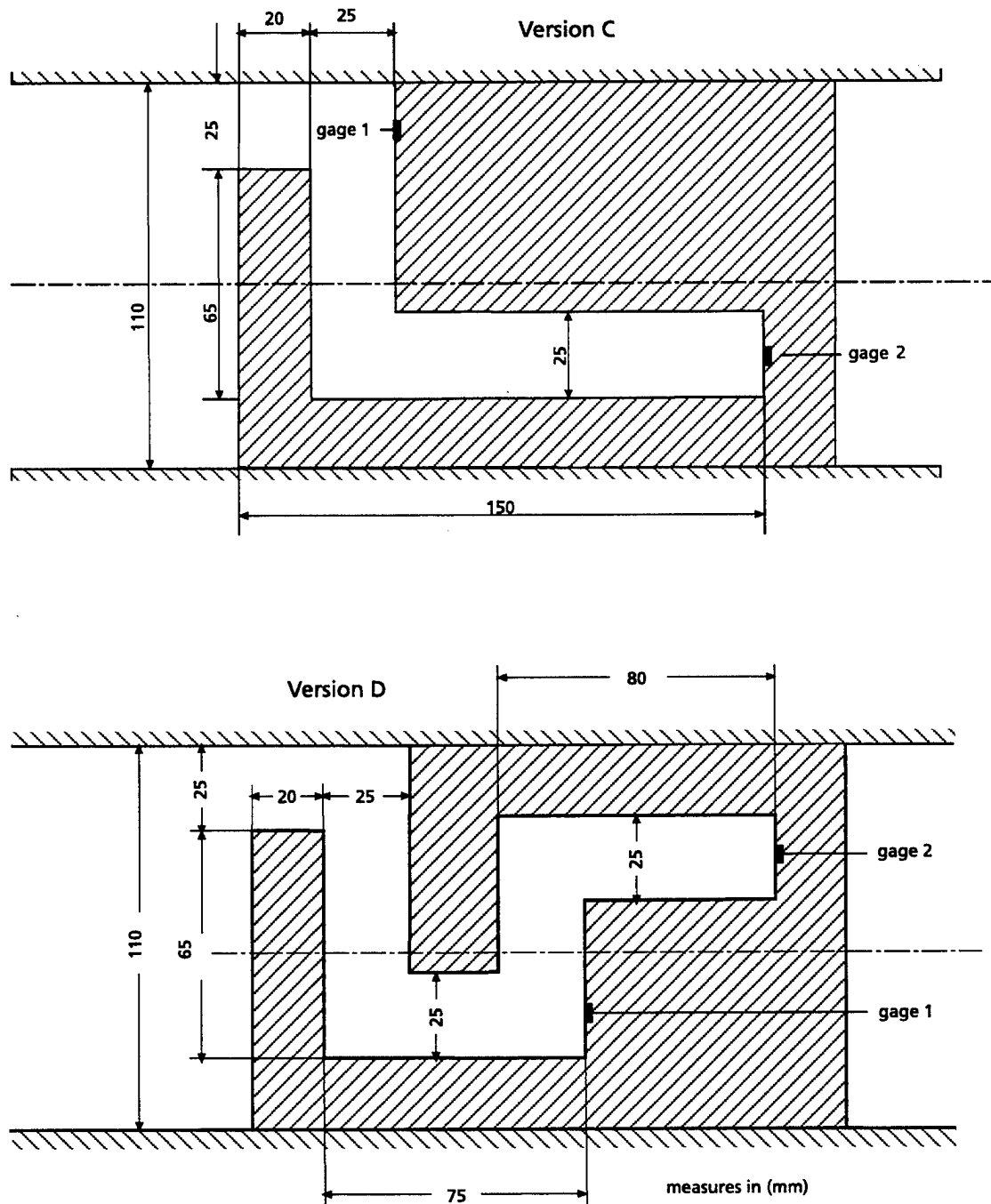


Figure 33. Duct systems for shock tube tests. (Continued)

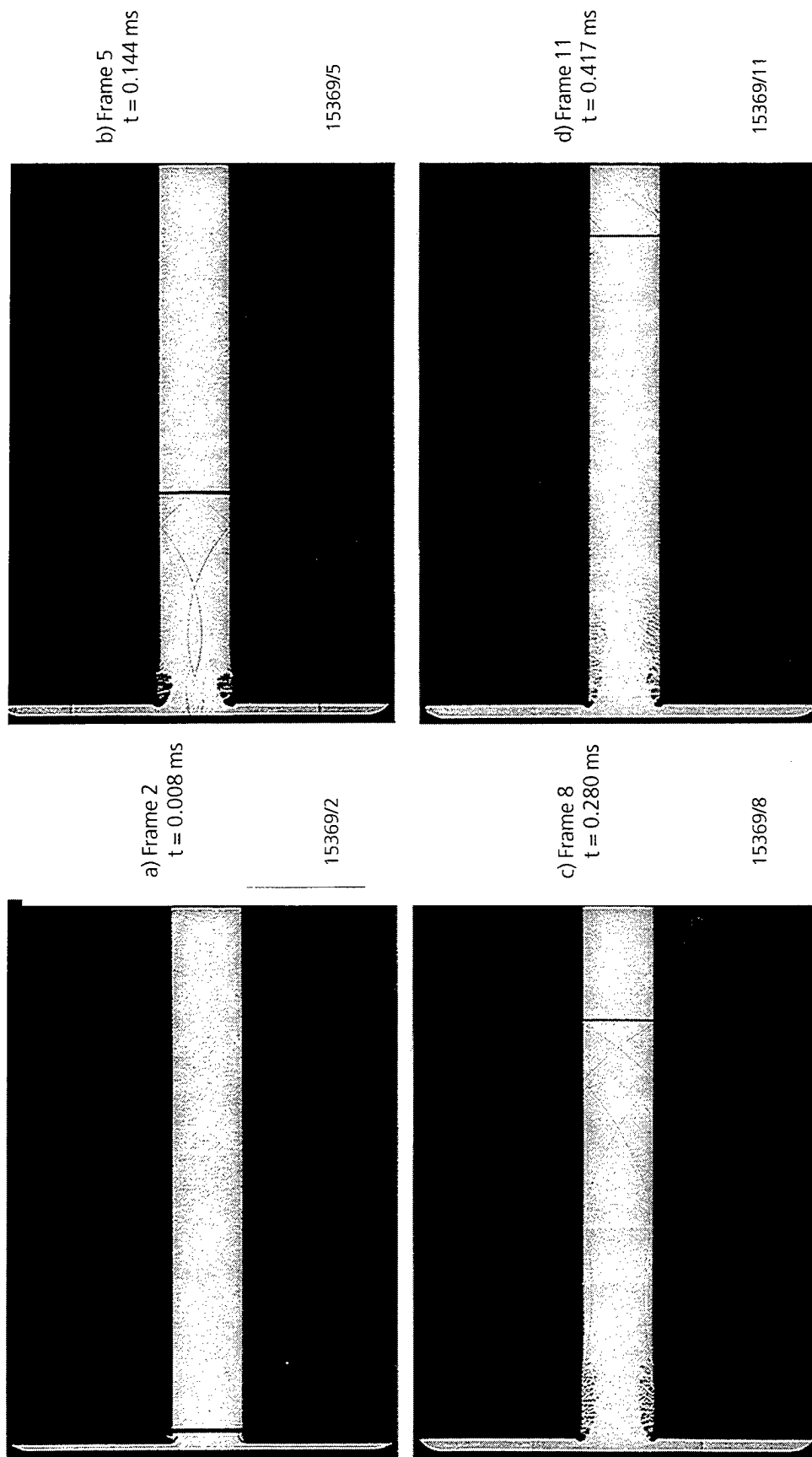
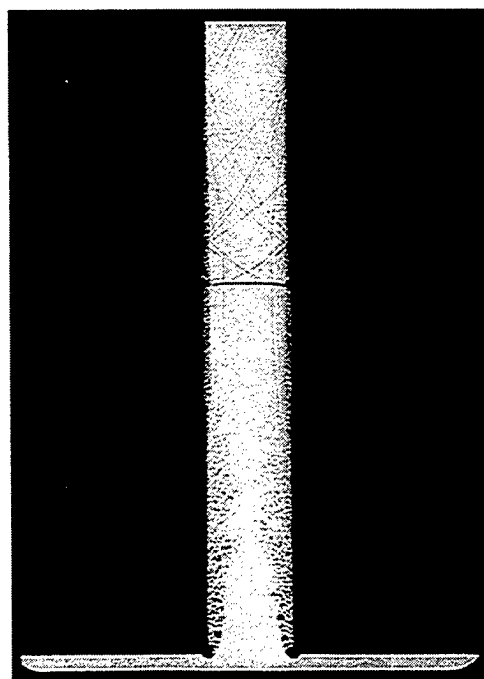
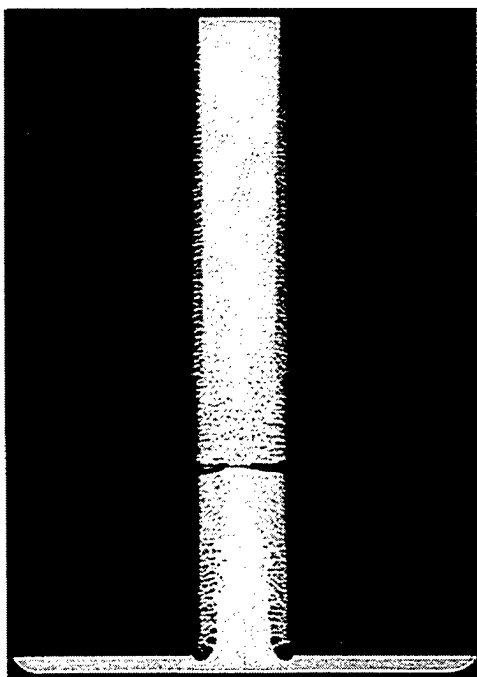


Figure 34. Shock wave propagation in a straight duct; $M_S = 1.22$.



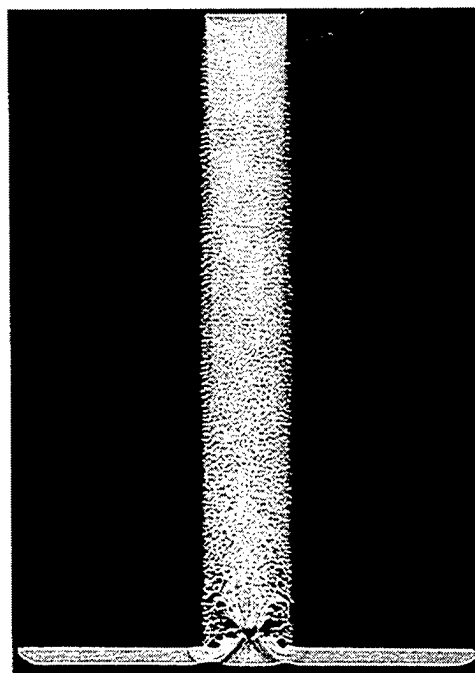
e) Frame 14
 $t = 0.553 \text{ ms}$

15369/14



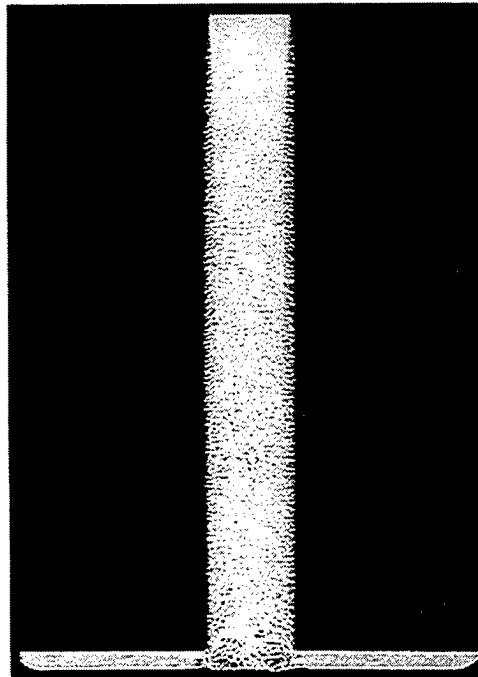
f) Frame 17
 $t = 0.690 \text{ ms}$

15369/17



g) Frame 20
 $t = 0.826 \text{ ms}$

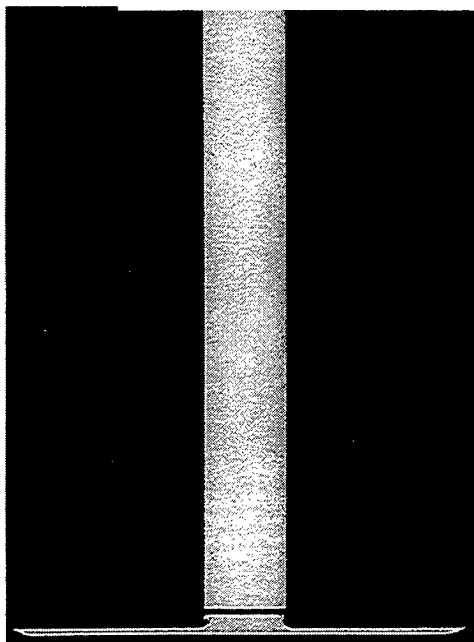
15369/20



h) Frame 23
 $t = 0.962 \text{ ms}$

15369/23

Figure 34. Shock wave propagation in a straight duct; $M_S = 1.22M_S = 1.22$. (Continued)



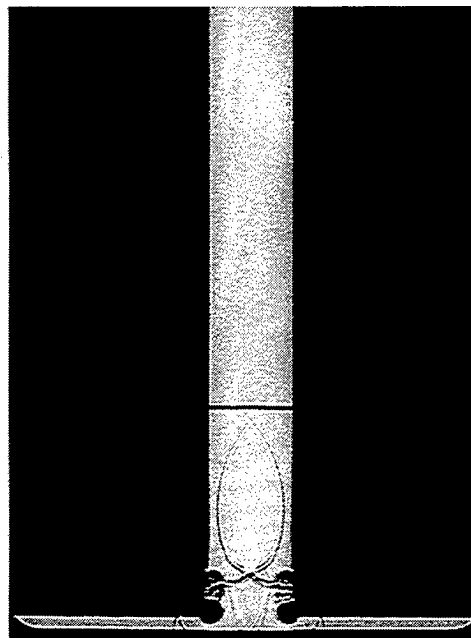
a) Frame 2
 $t = 0.006$ ms

15373/2



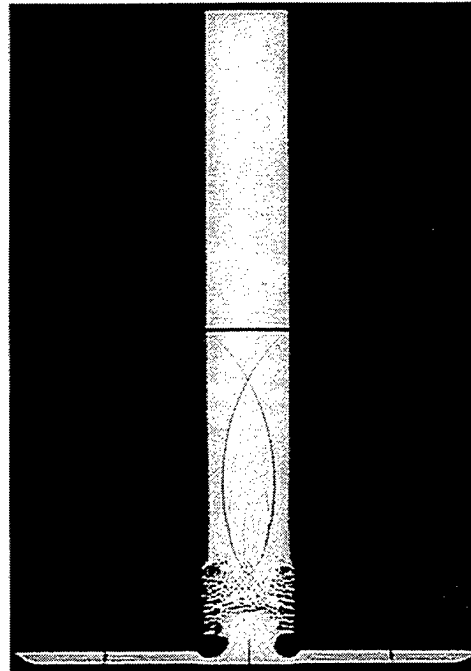
b) Frame 3
 $t = 0.052$ ms

15373/3



c) Frame 4
 $t = 0.097$ ms

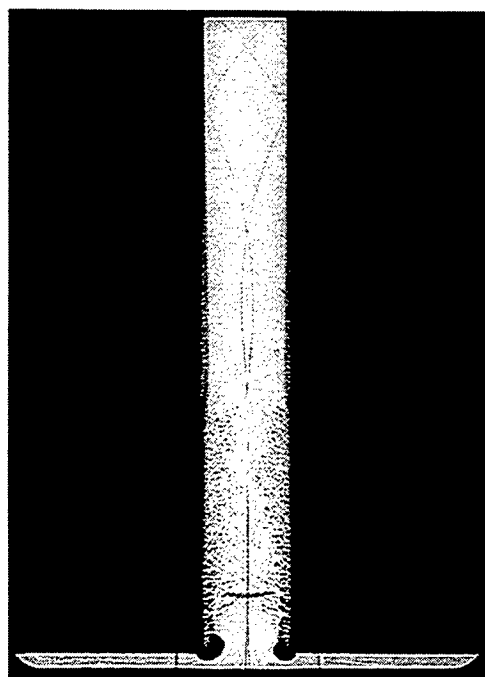
15373/4



d) Frame 5
 $t = 0.142$ ms

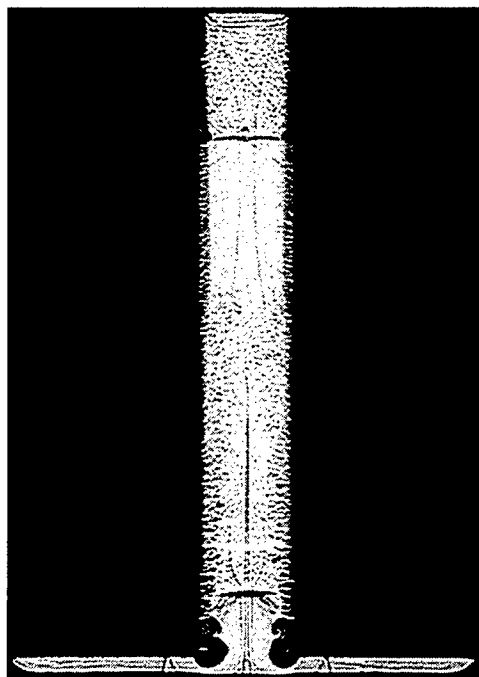
15373/5

Figure 35. Shock wave propagation in a straight duct, $M_s = 1.53$; (test 15 373).



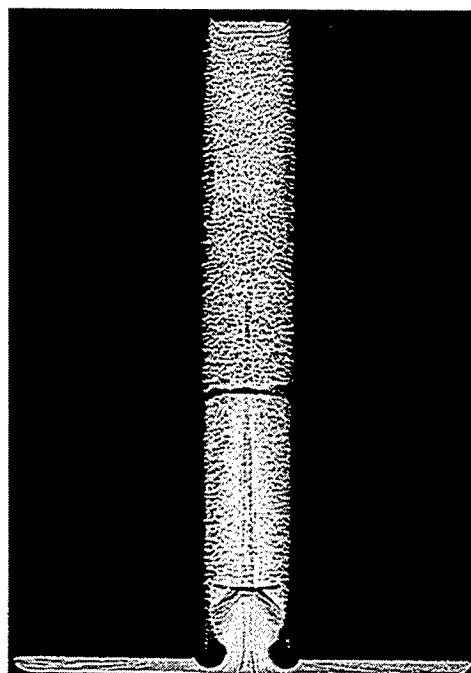
e) Frame 8
 $t = 0.279$ ms

15373/8



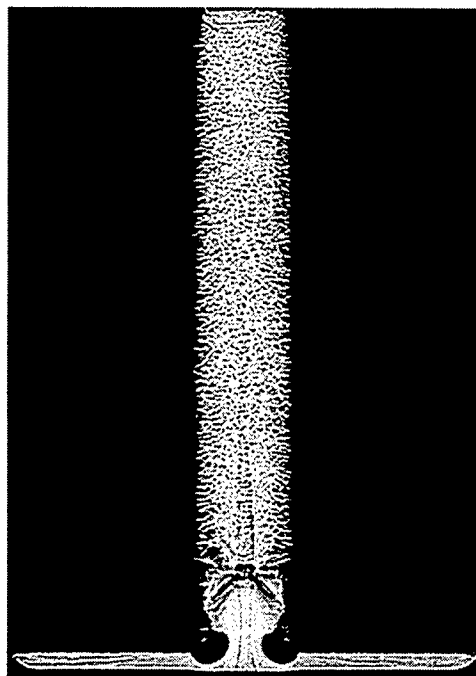
f) Frame 10
 $t = 0.370$ ms

15373/10



g) Frame 14
 $t = 0.551$ ms

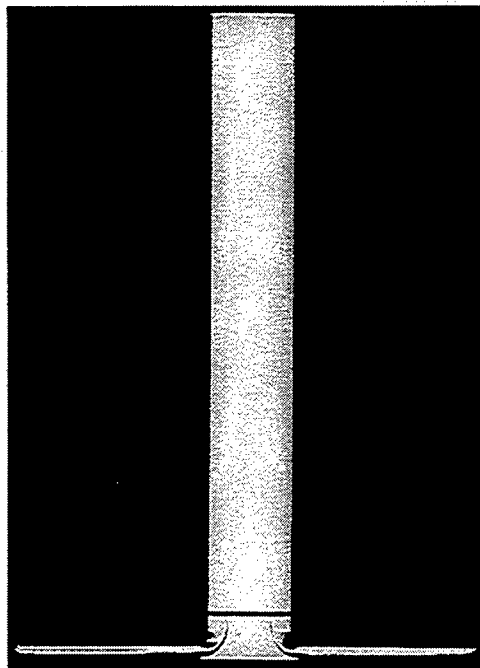
15373/14



h) Frame 17
 $t = 0.688$ ms

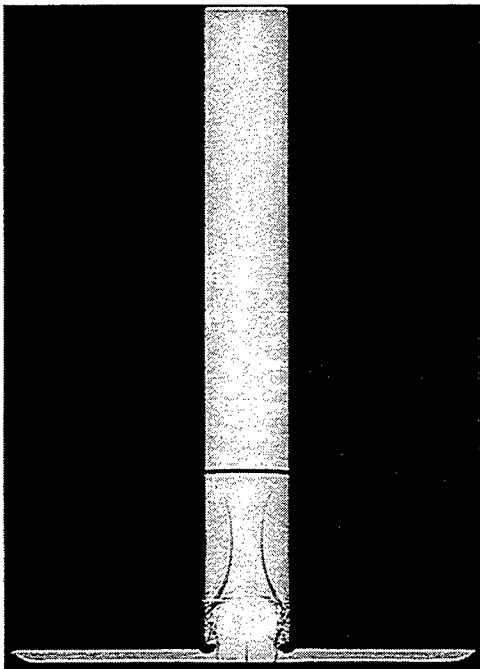
15373/17

Figure 35. Shock wave propagation in a straight duct, $M_s = 1.53$; (test 15 373). (Continued)



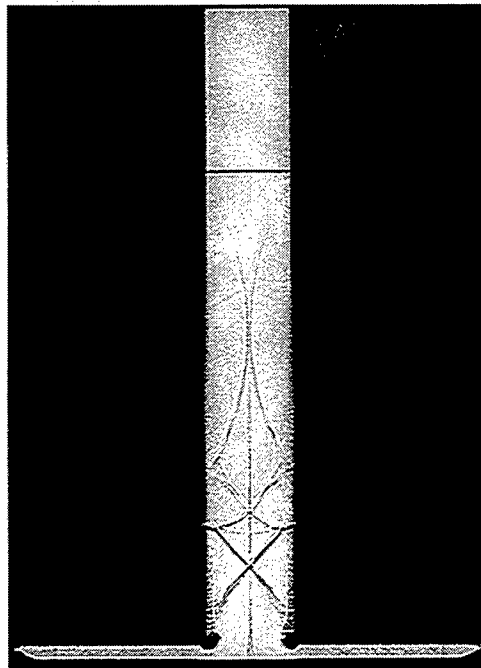
a) Frame 2
 $t = 0.008 \text{ ms}$

15369/2



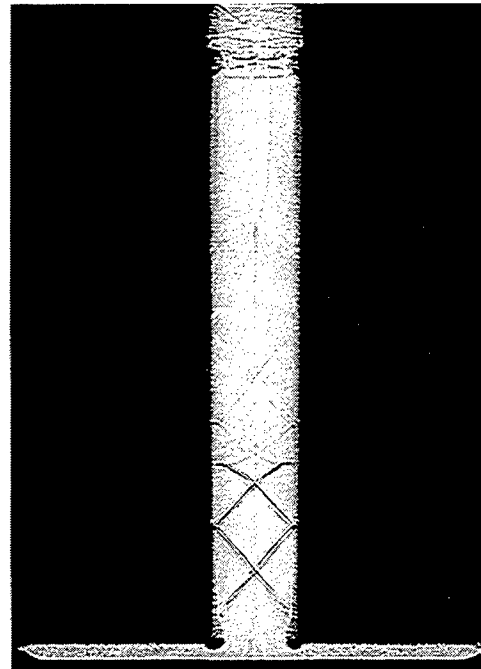
b) Frame 3
 $t = 0.551 \text{ ms}$

15379/3



c) Frame 8
 $t = 0.280 \text{ ms}$

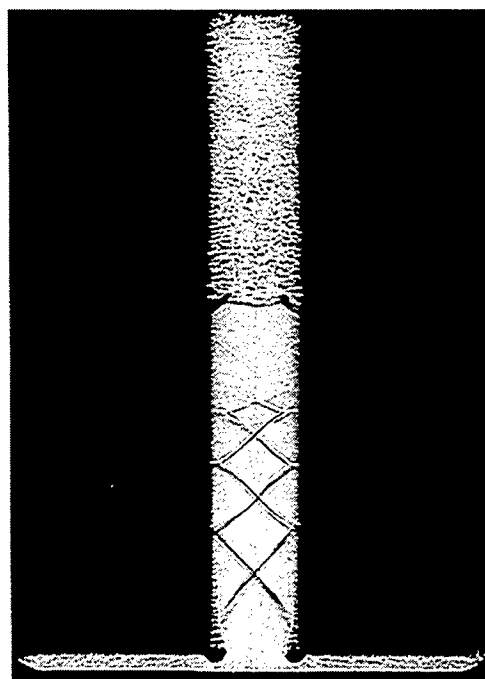
15369/8



d) Frame 14
 $t = 0.273 \text{ ms}$

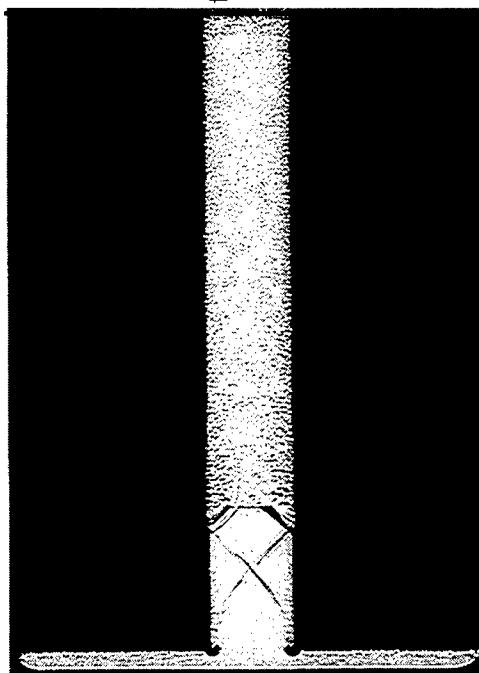
15379/7

Figure 36. Shock wave propagation in a straight duct; $M_s = 2.20$; (test 15379).



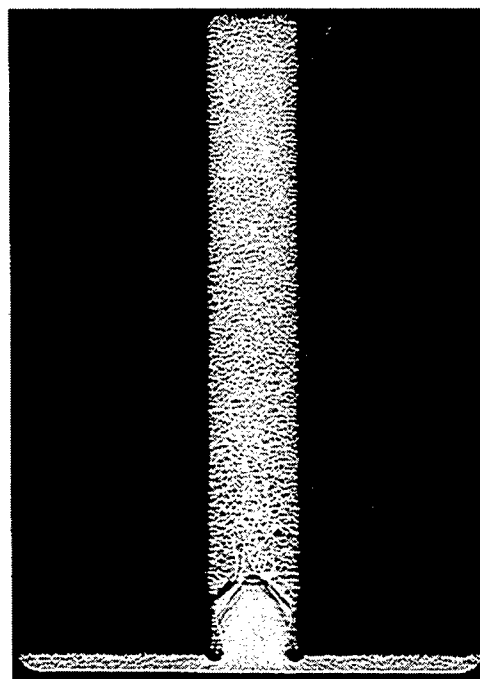
e) Frame 10
 $t = 0.373 \text{ ms}$

15379/10



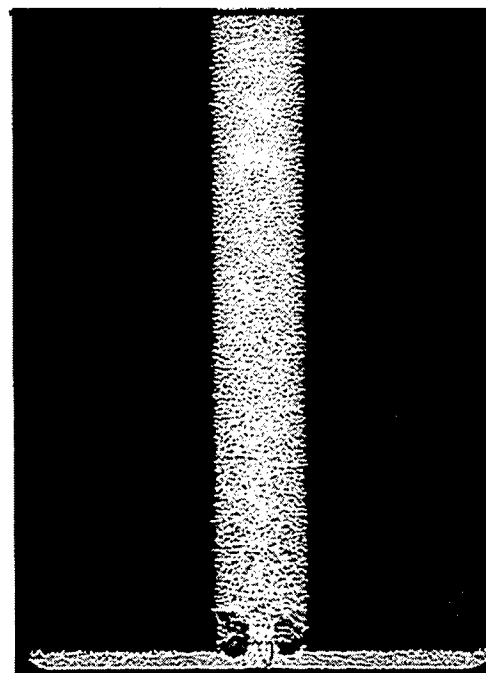
f) Frame 13
 $t = 0.510 \text{ ms}$

15379/13



g) Frame 14
 $t = 0.545 \text{ ms}$

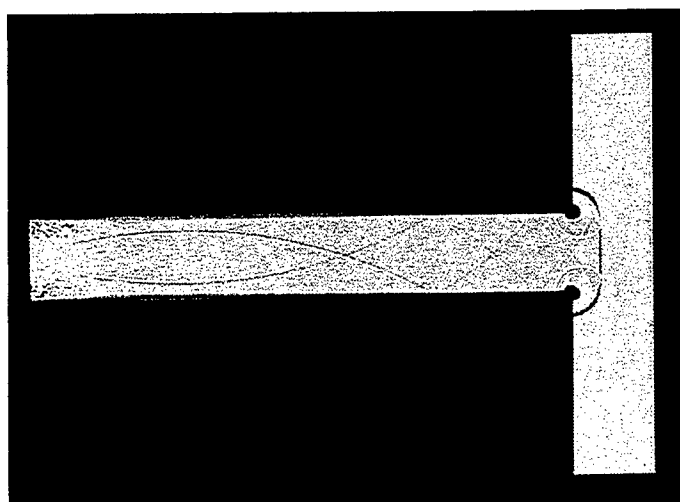
15379/14



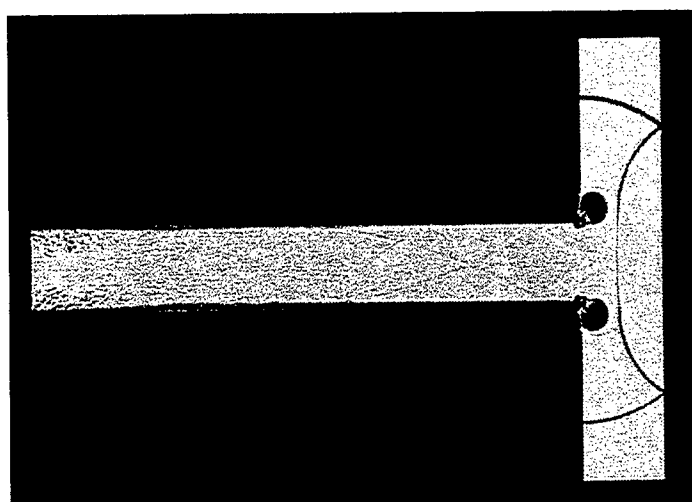
h) Frame 15
 $t = 0.600 \text{ ms}$

15379/15

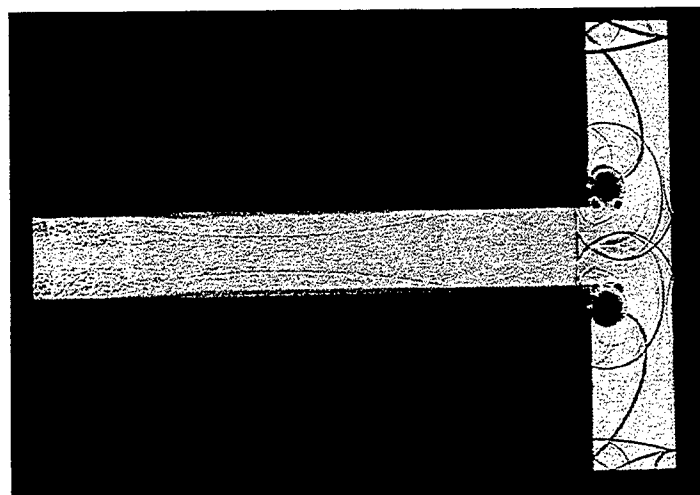
Figure 36. Shock wave propagation in a straight duct; $M_s = 2.20$; (test 15379). (Continued)



a) Frame 6,
 $t = 0.364$ ms

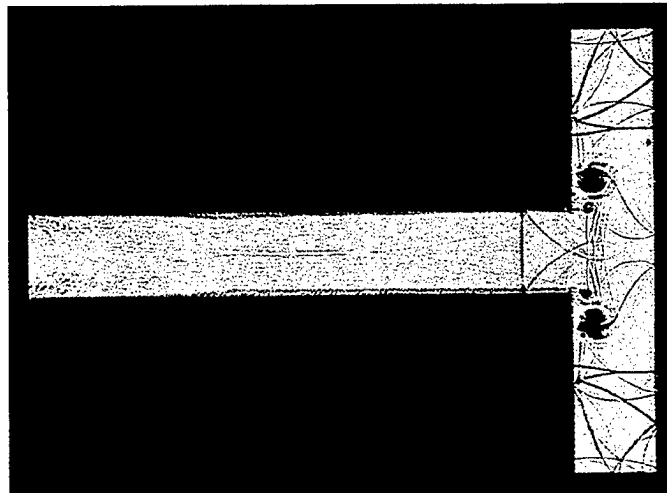


b) Frame 7,
 $t = 0.431$ ms

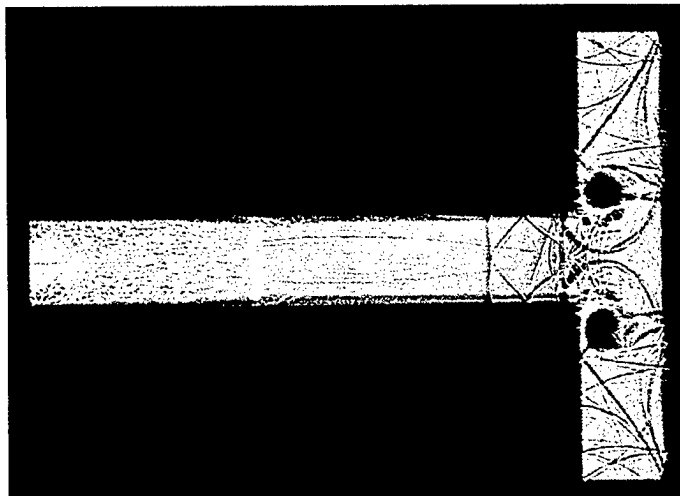


c) Frame 8,
 $t = 0.498$ ms

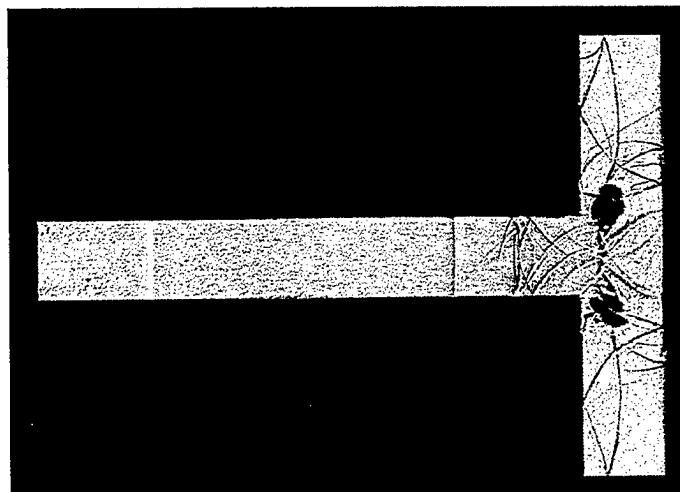
Figure 37. Shock wave propagation in a T-shaped duct, $M_5 = 1.21$; (test 15 325).



d) Frame 9,
 $t = 0.564 \text{ ms}$

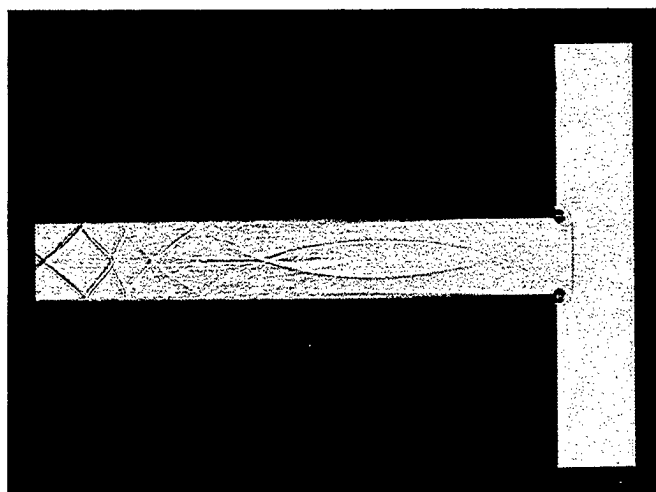


e) Frame 10,
 $t = 0.631 \text{ ms}$

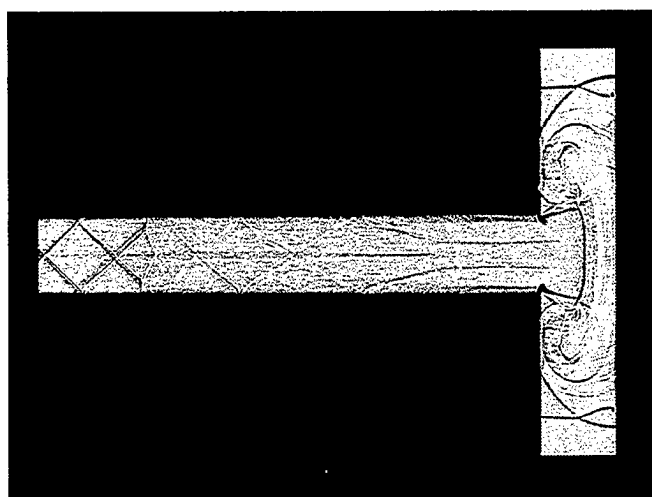


f) Frame 11,
 $t = 698 \text{ ms}$

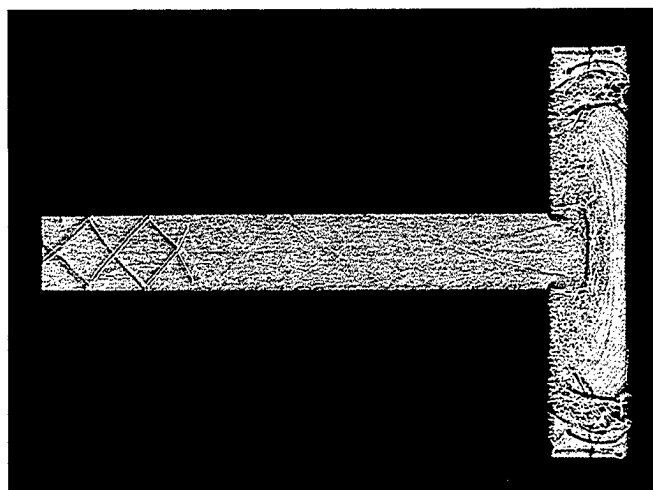
Figure 37. Shock wave propagation in a T-shaped duct, $M_5 = 1.21$; (test 15 325). (Continued)



a) Frame 4,
 $t = 0.197 \text{ ms}$

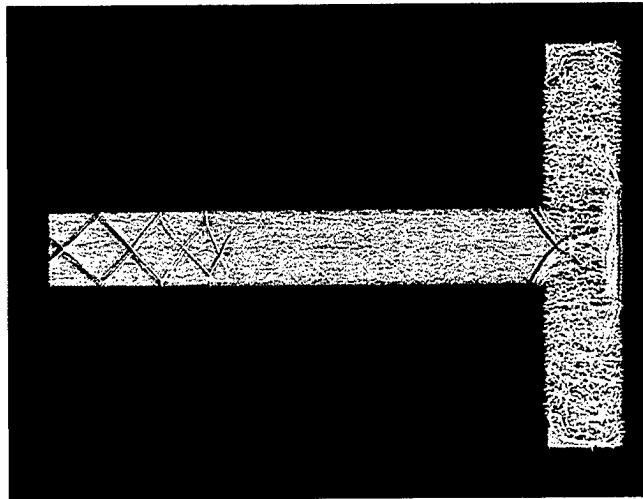


b) Frame 5,
 $t = 0.264 \text{ ms}$

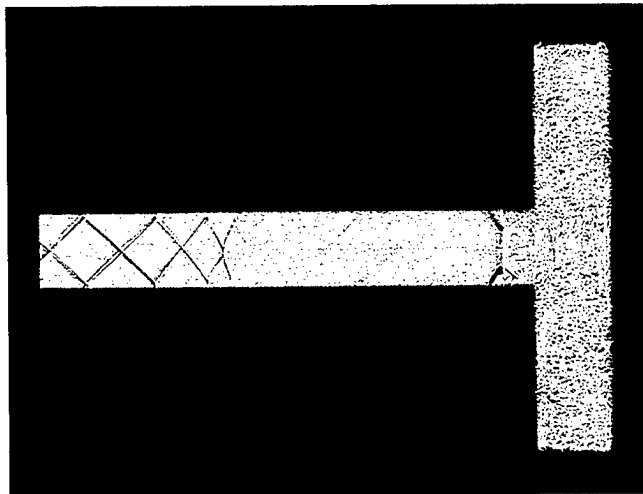


c) Frame 6,
 $t = 0.330 \text{ ms}$

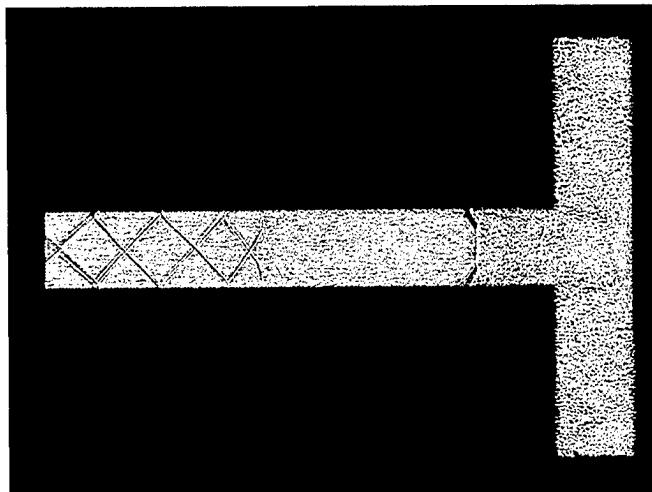
Figure 38. Shock wave propagation in a T-shaped duct, $M_s = 2.18$.



d) Frame 7,
 $t = 0.397$ ms

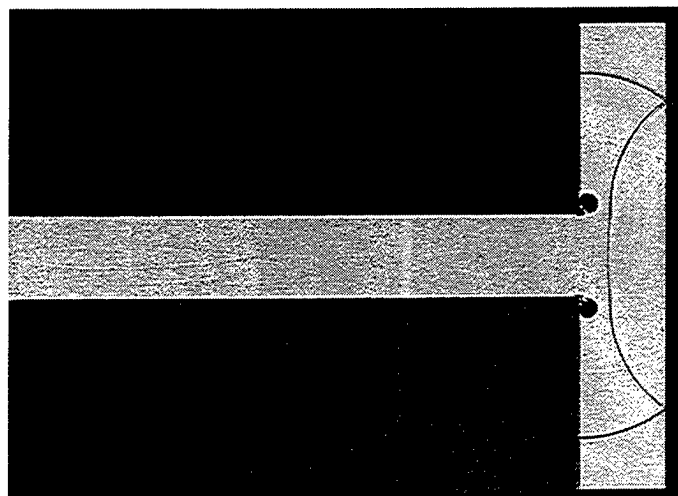


e) Frame 8
 $t = 0.364$ ms

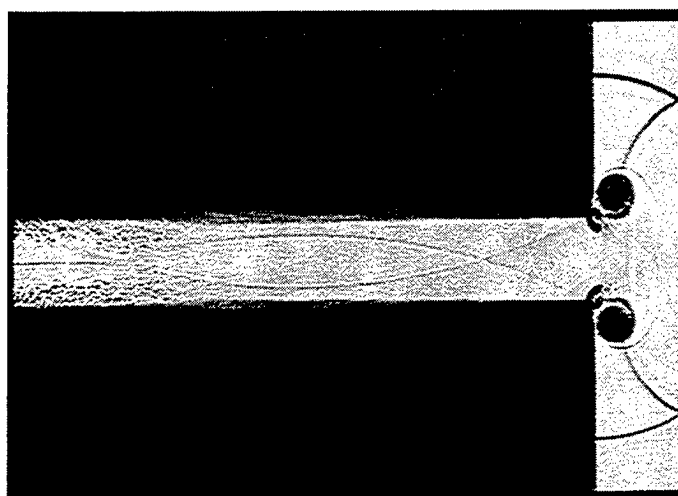


f) Frame 9
 $t = 0.530$ ms

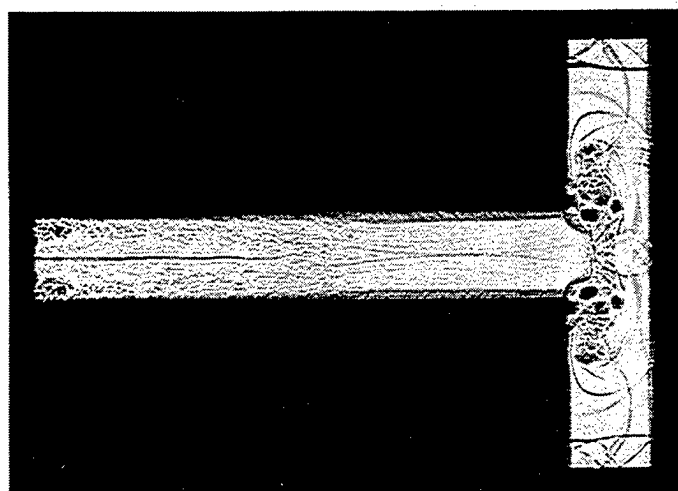
.Figure 38. Shock wave propagation in a T-shaped duct, $M_5 = 2.18$.(Continued)



a) $M_S = 1.11$
(test 15 326/8)

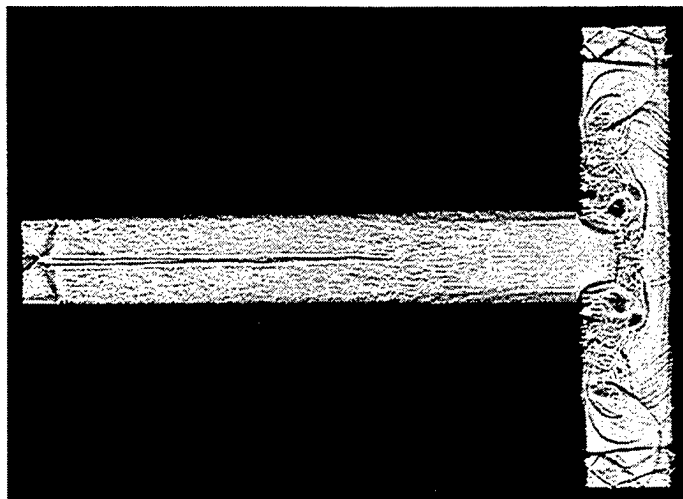


b) $M_S = 1.31$
(test 15 323/7)

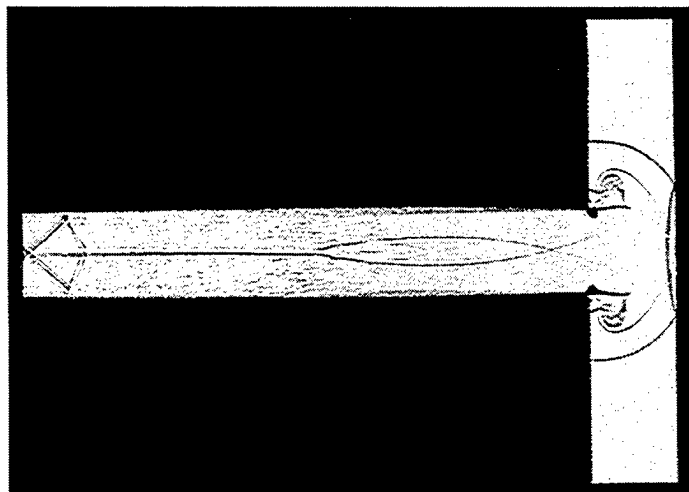


c) $M_S = 1.49$
(test 15 328/7)

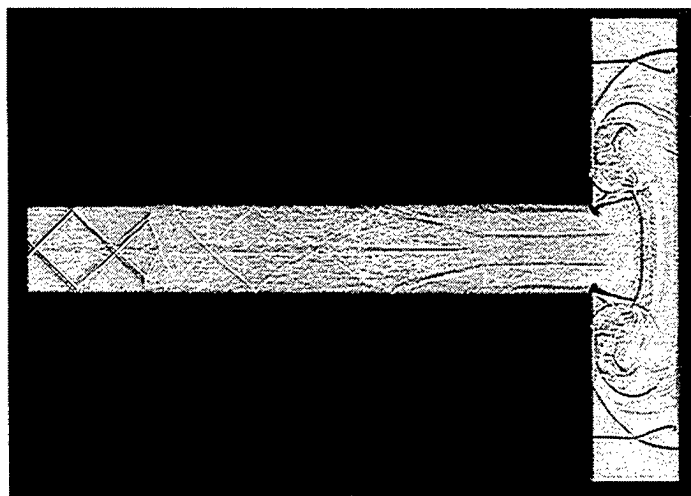
Figure 39. Inflow into a T-shaped duct at different Mach numbers.



d) $M_S = 1.71$
(test 15 330/7)

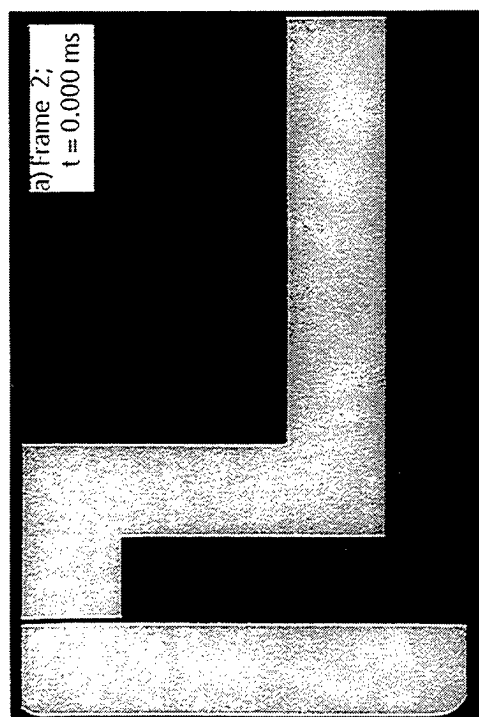


e) $M_S = 1.94$
(test 15 332/5)

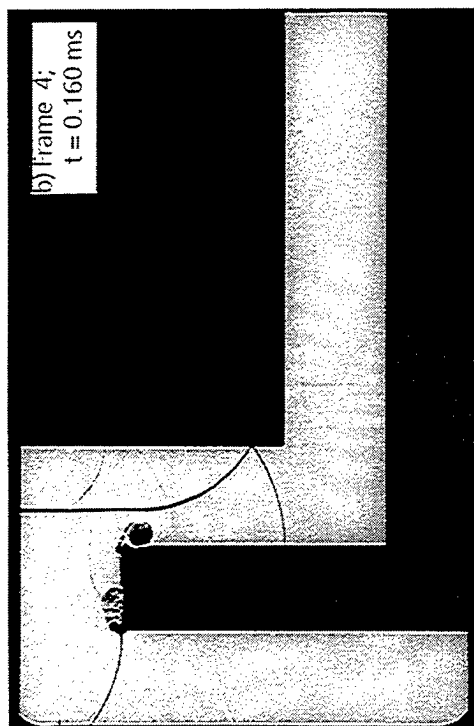


f) $M_S = 2.18$
(test 15 334/5)

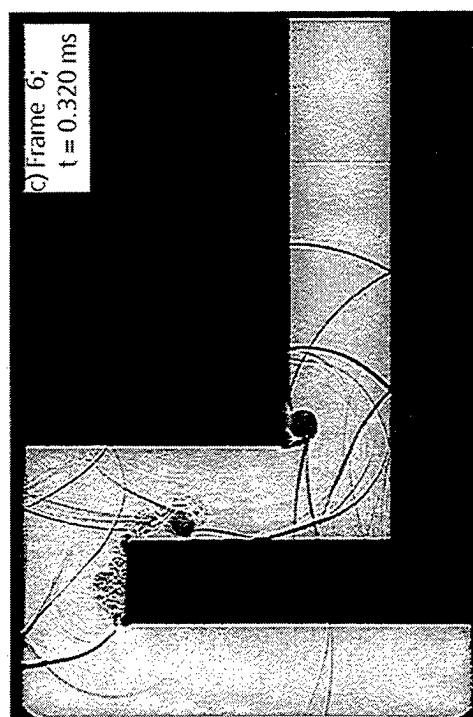
Figure 39. Inflow into a T-shaped duct at different Mach numbers. (Continued)



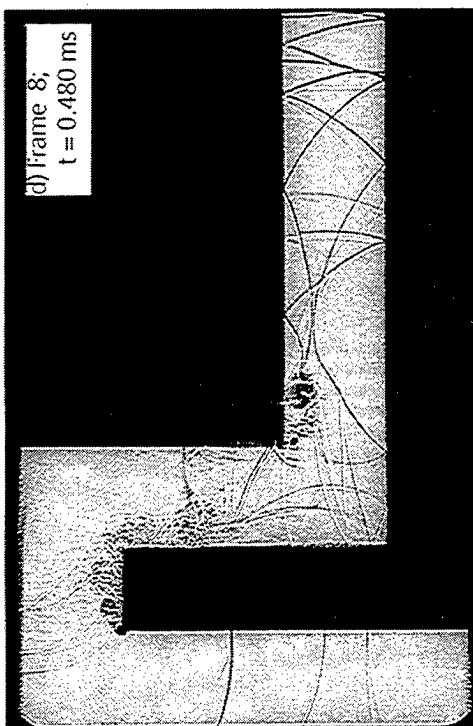
15382/2



15382/4

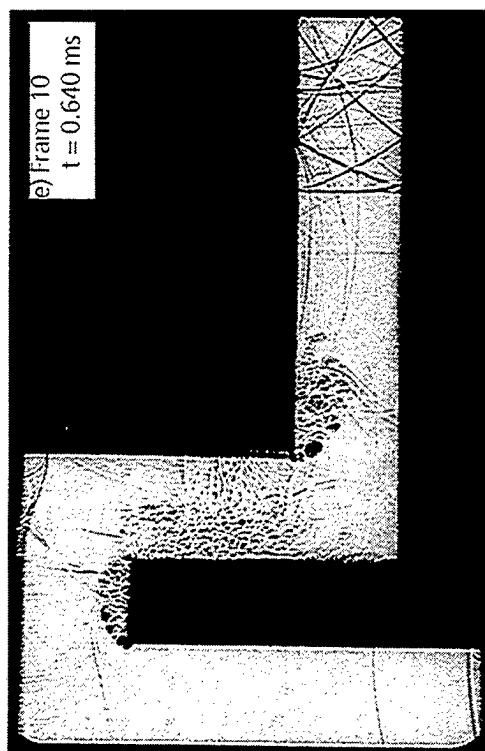


15382/6

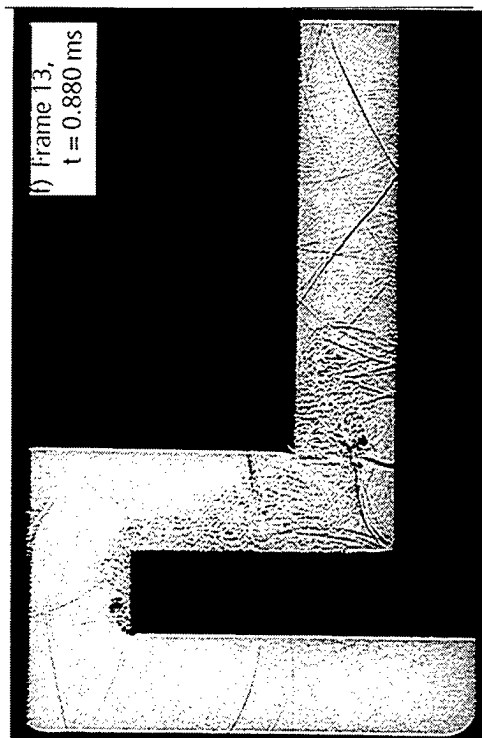


15382/8

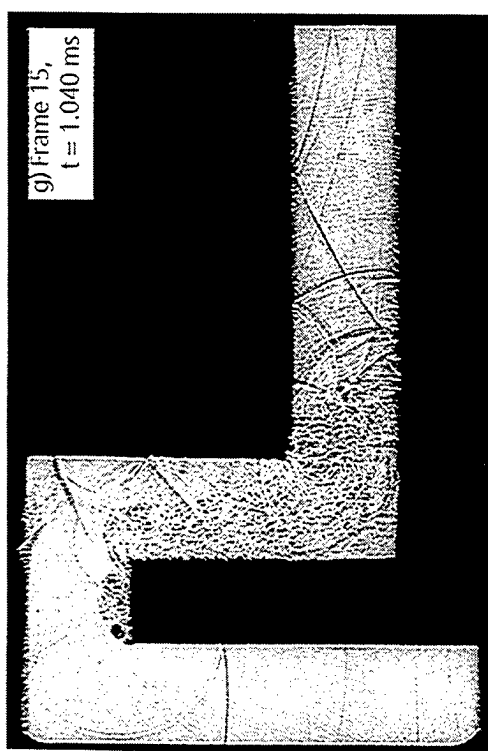
Figure 40. Shock wave propagation in a L-shaped duct; $M_s = 1.22$; test 15 382).



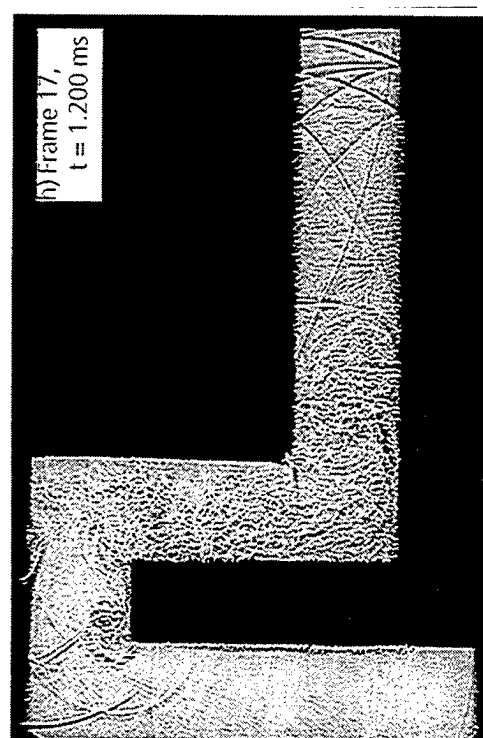
15382/10



15382/13



15382/15



15382/17

Figure 40. Shock wave propagation in a L-shaped duct; $M_s = 1.22$; test 15 382). (Continued)

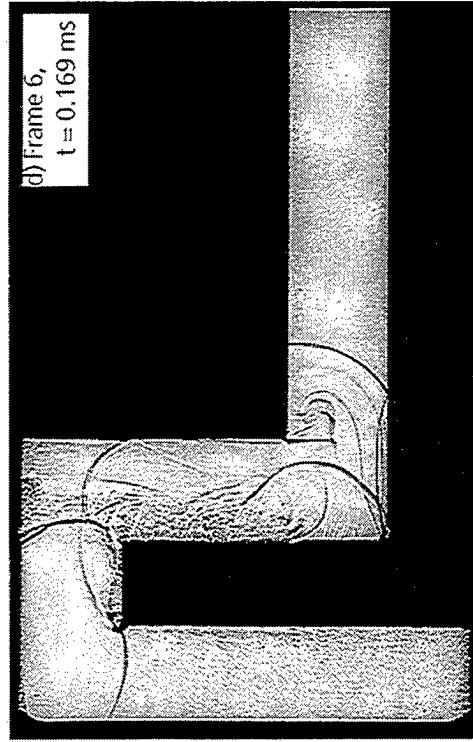
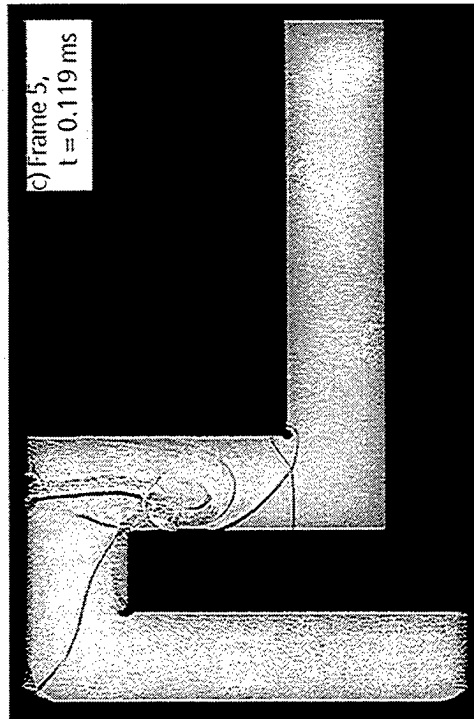
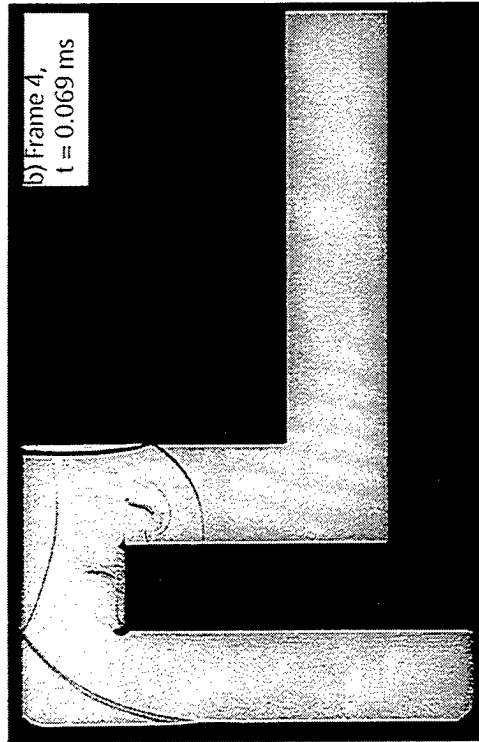
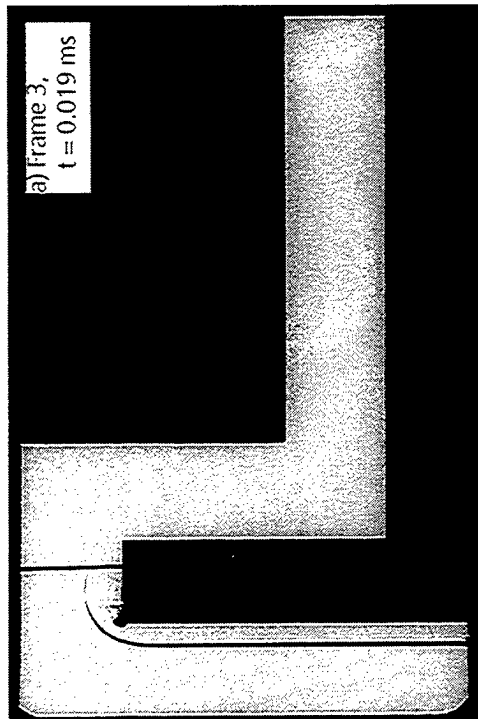


Figure 41. Shock wave propagation in a L-shaped duct, $M_s = 2.16$; (test 15 390).

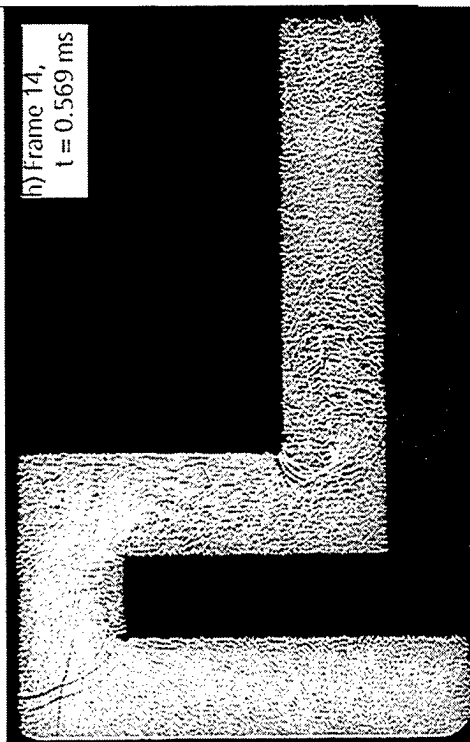
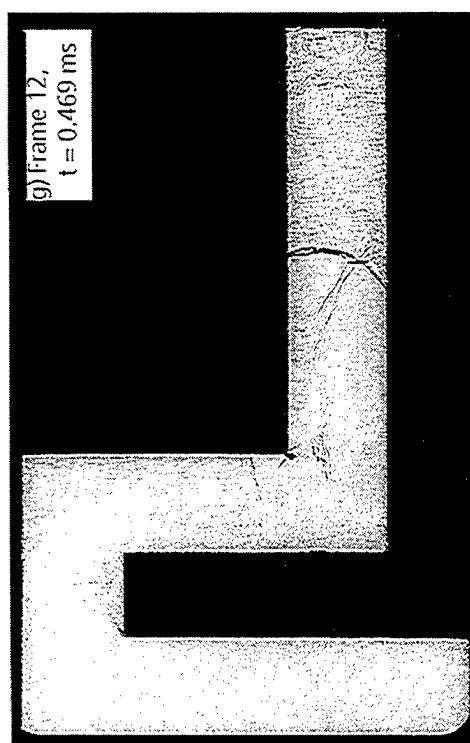
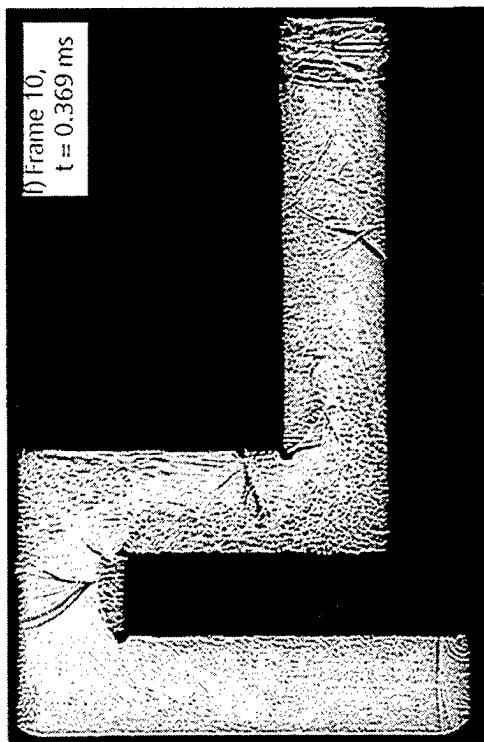
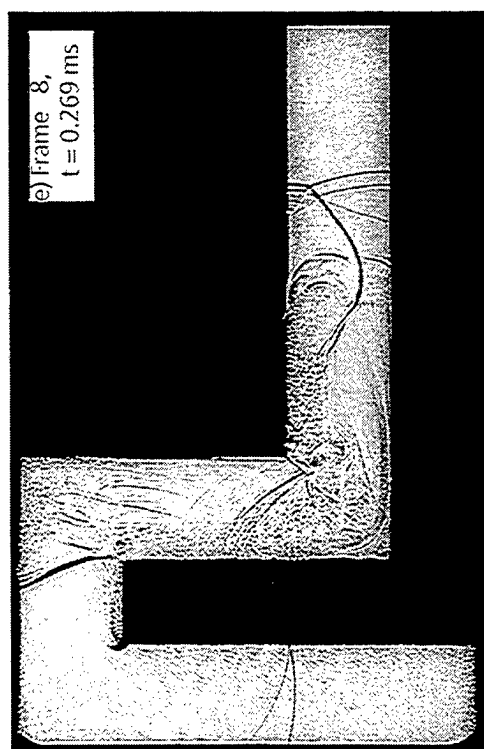


Figure 41. Shock wave propagation in a L-shaped duct, $M_S = 2.16$; (test 15 390). (Continued)

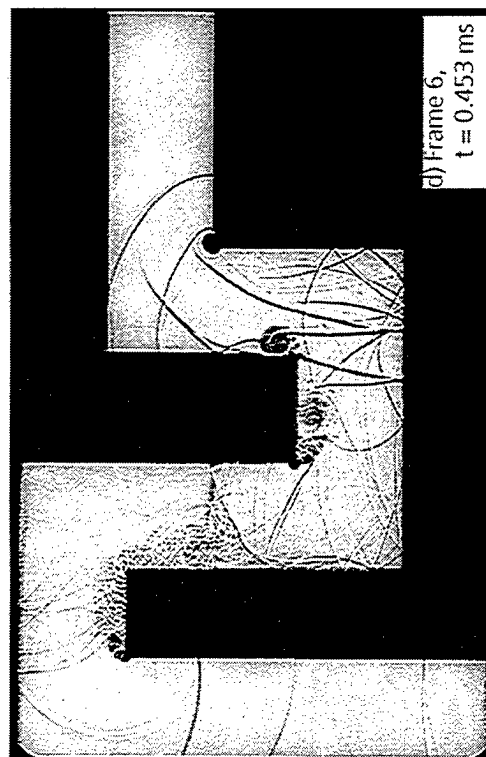
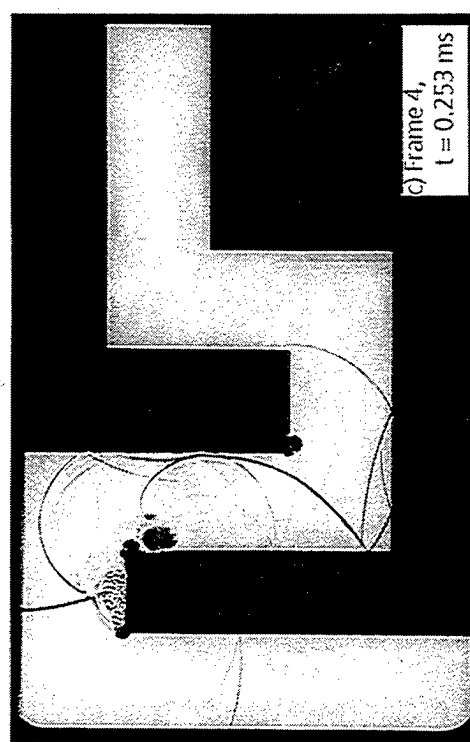
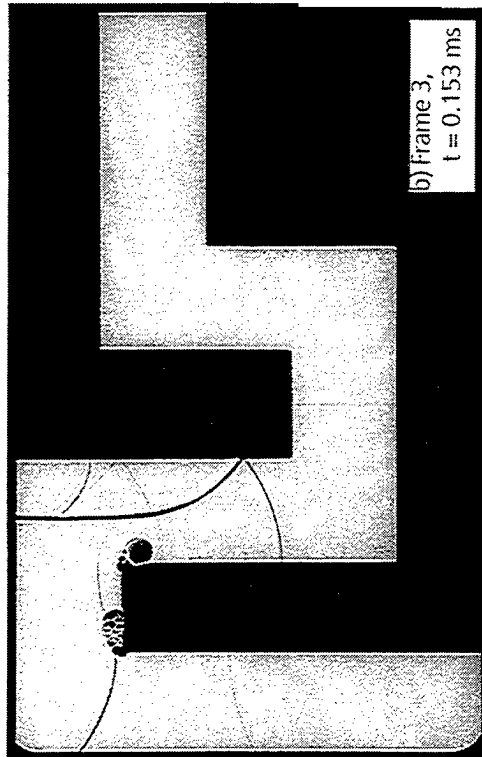
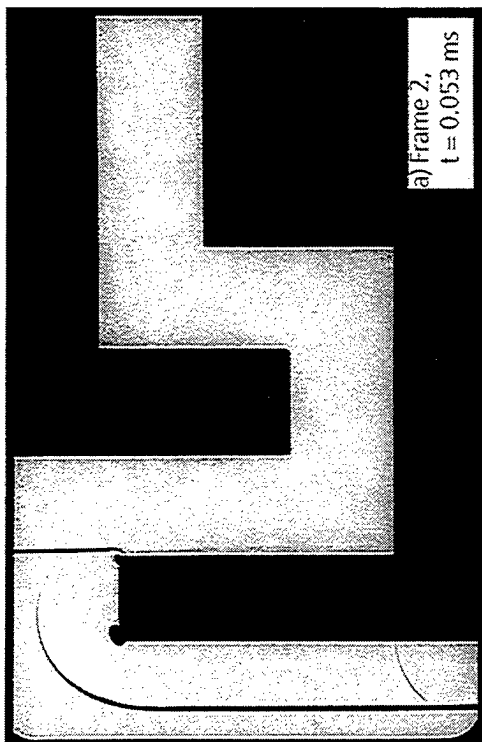
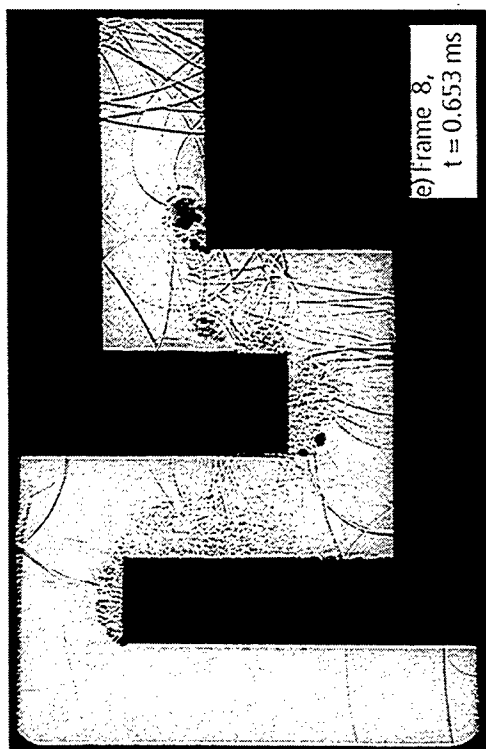
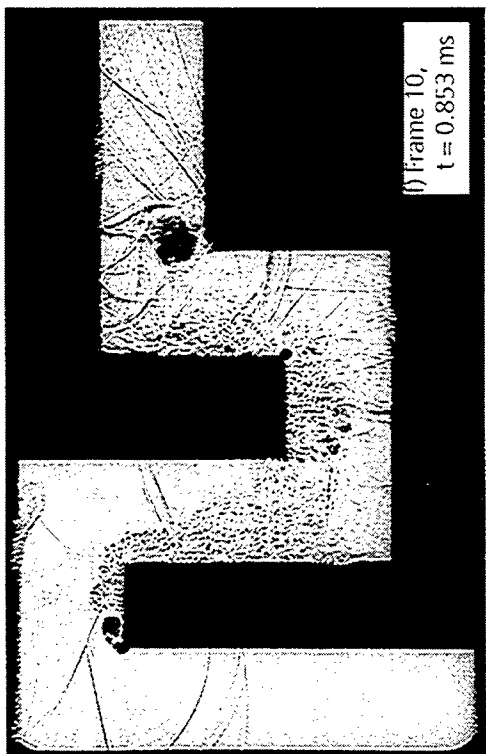


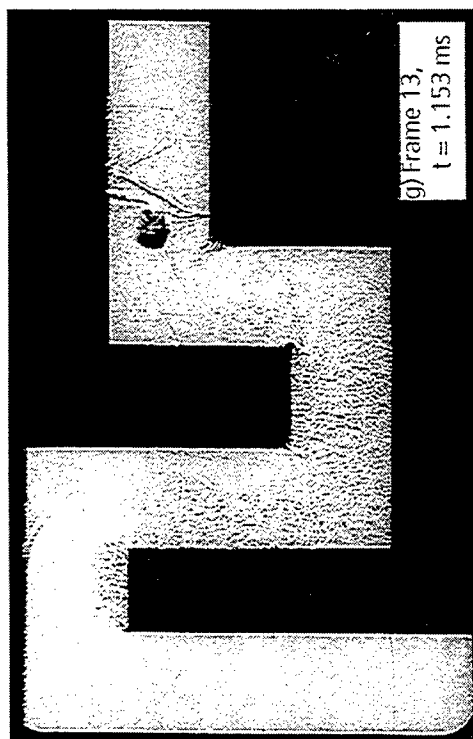
Figure 42. Shock wave propagation in a double L-shaped duct, $M_S = 1.22$; (test 15 392).



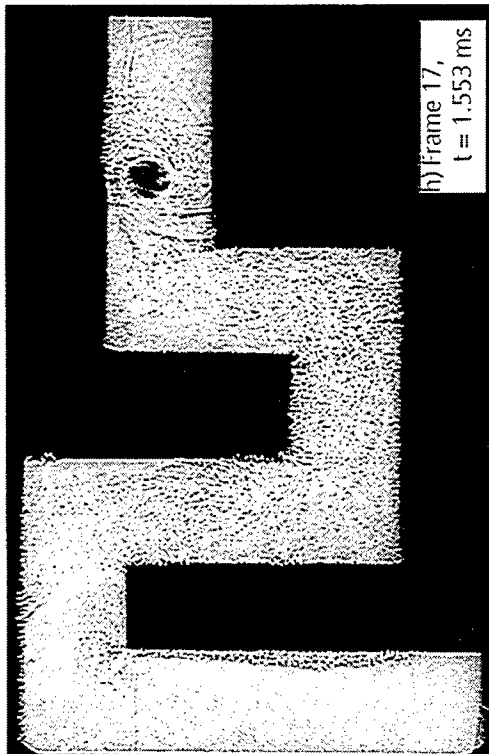
15392/8



15392/10



15392/13



15392/17

Figure 42. Shock wave propagation in a double L-shaped duct, $M_s = 1.22$; (test 15 392). (Continued)

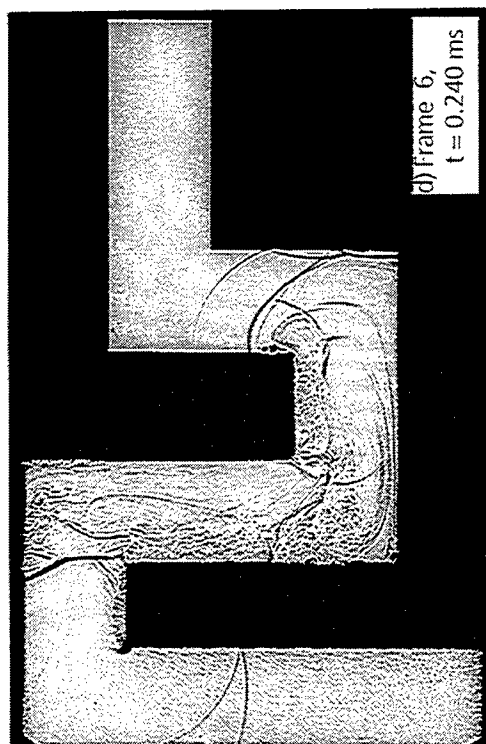
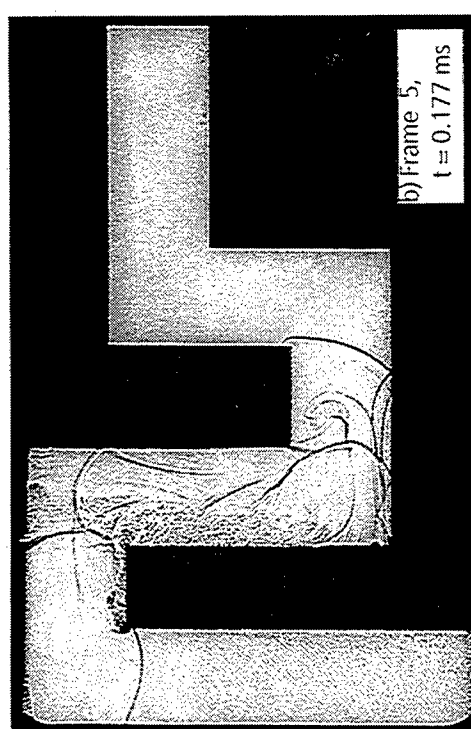
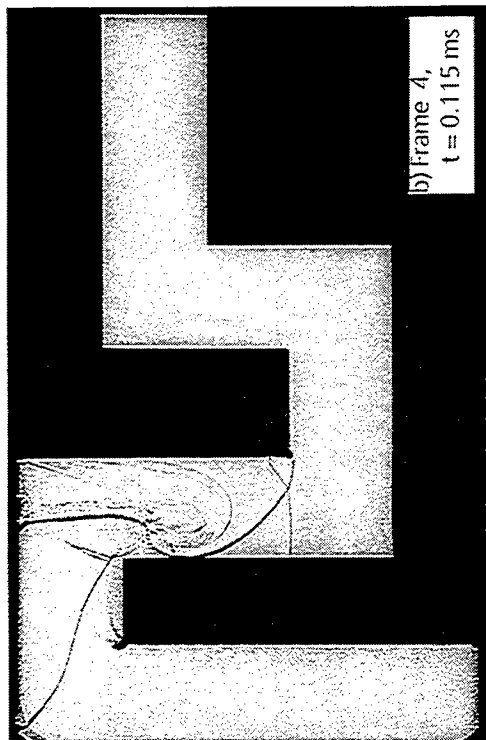
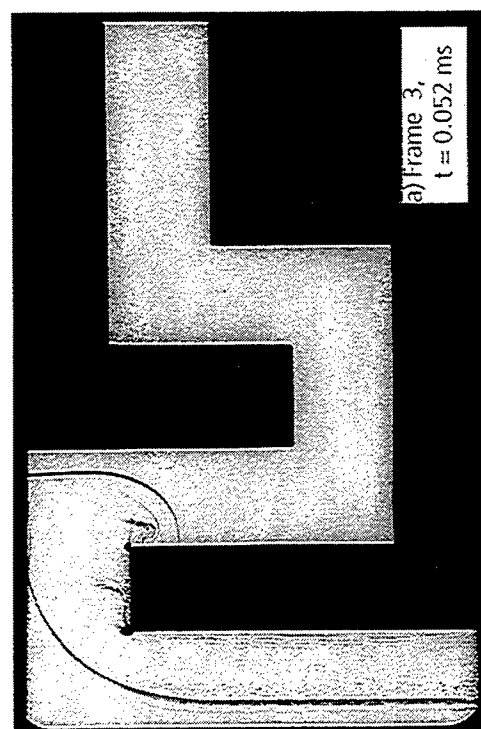


Figure 43. Shock wave propagation in a double L-shaped duct, $M_5 = 2.18$; (test 15 401).

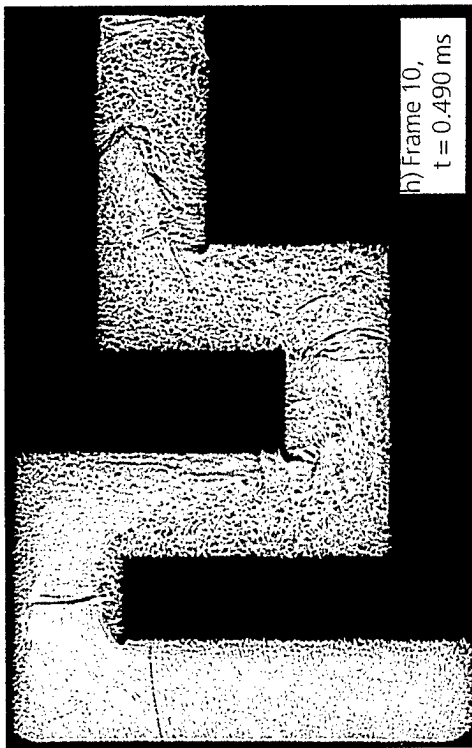
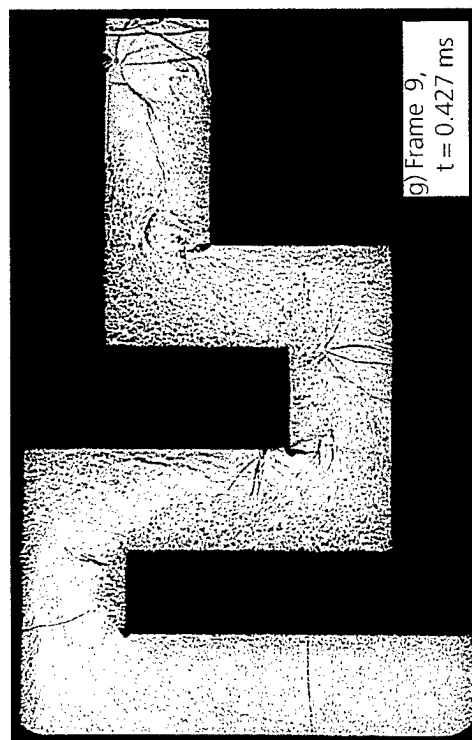
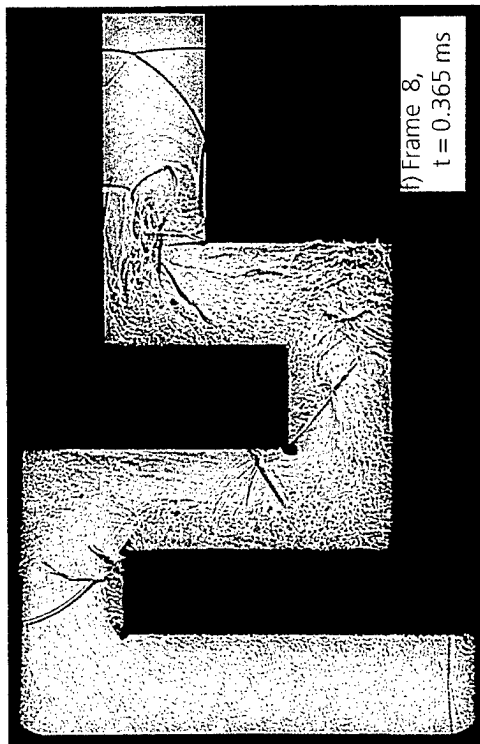
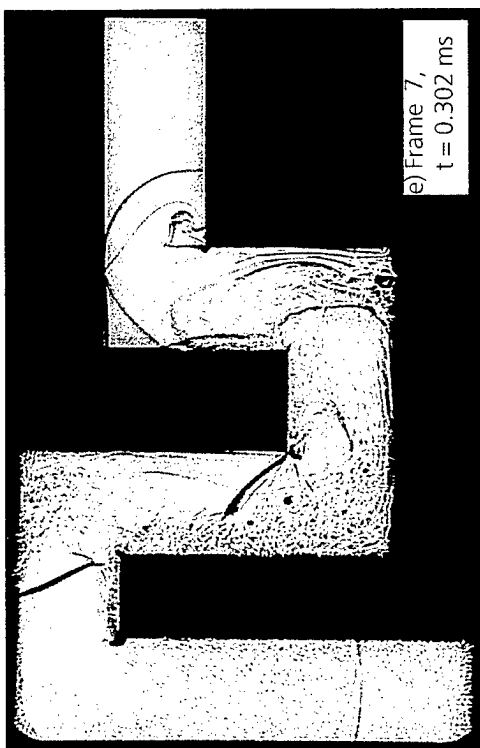
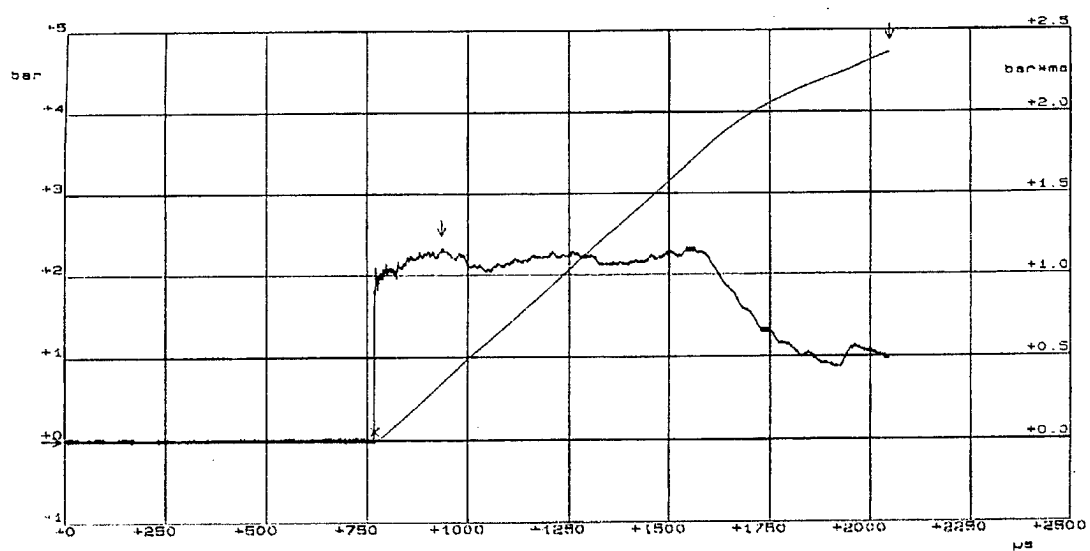
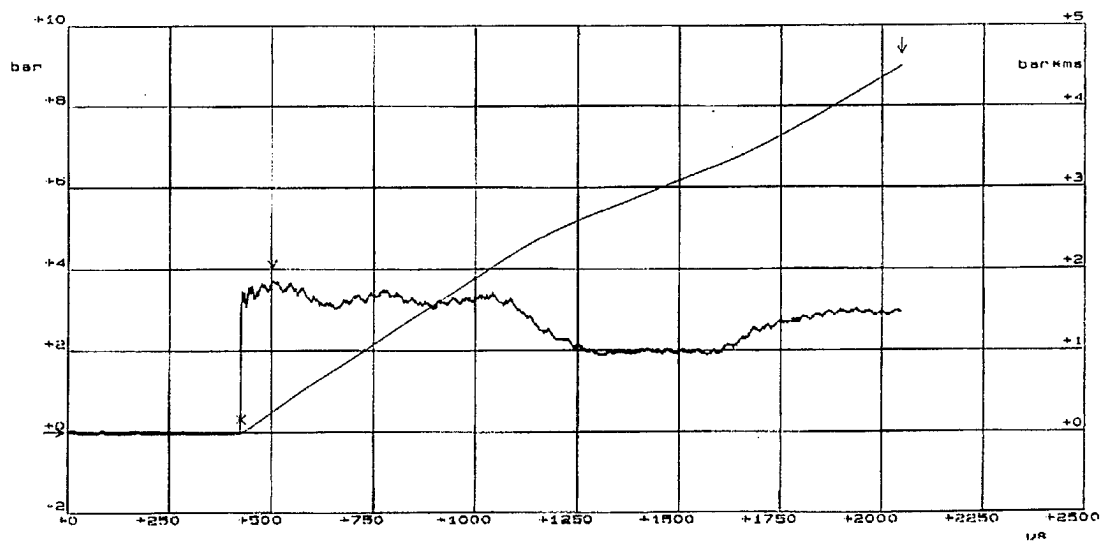


Figure 43. Shock wave propagation in a double L-shaped duct, $M_5 = 2.18$; (test 15 401). (Continued)



a). $M_s = 1.22$ (test 15 369)



b) $M_s = 2.20$ (test 15379)

Figure 44. Pressure records at the end wall of the straight duct; gage position 3 in version A of Figure 33.

Duct Model Version A

1. Peak

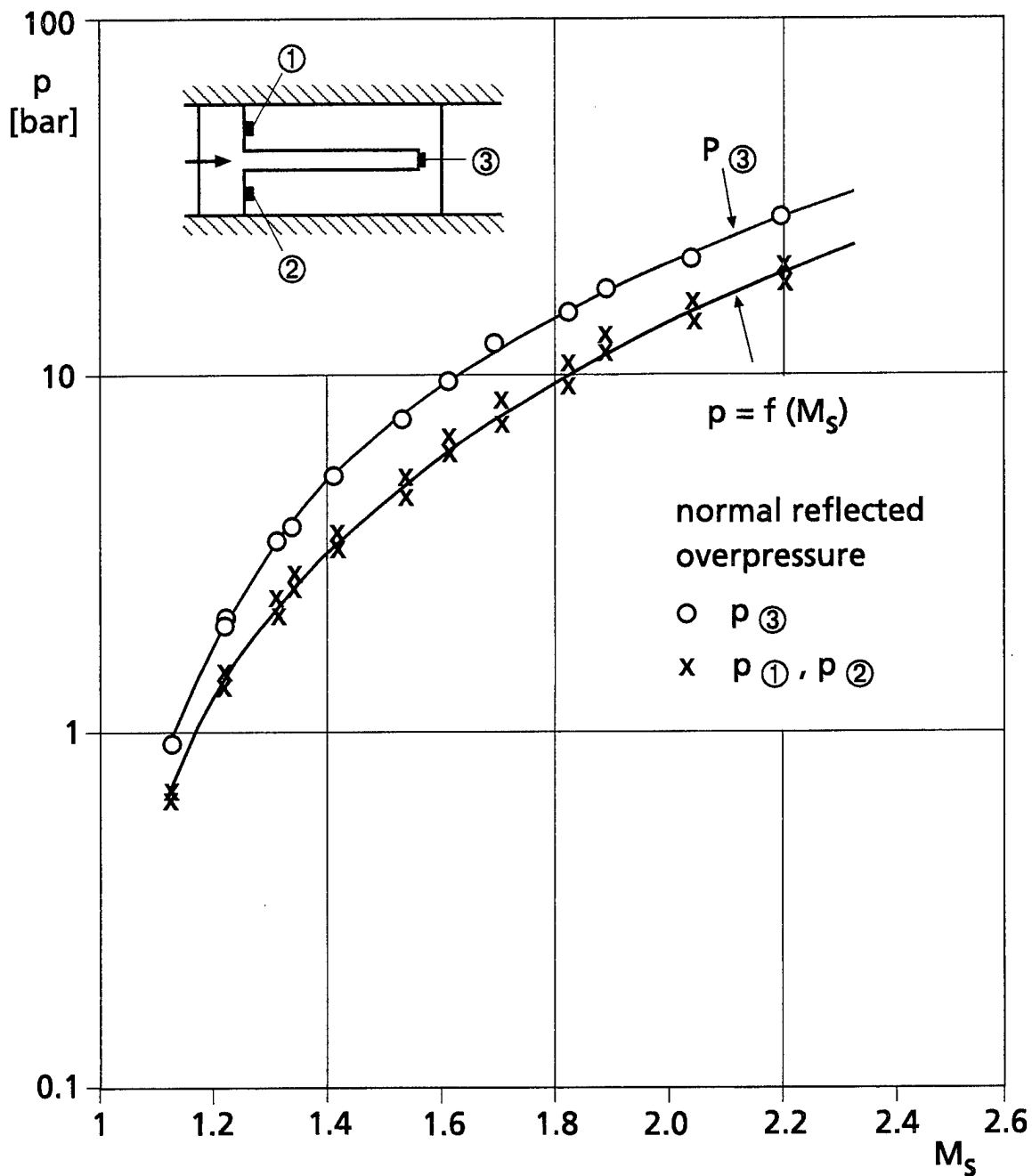


Figure 45. Overpressure of the first peak vs shock Mach number at the three gage positions in the straight duct. Given is also the normal reflected pressure of a planar shock wave (black line).

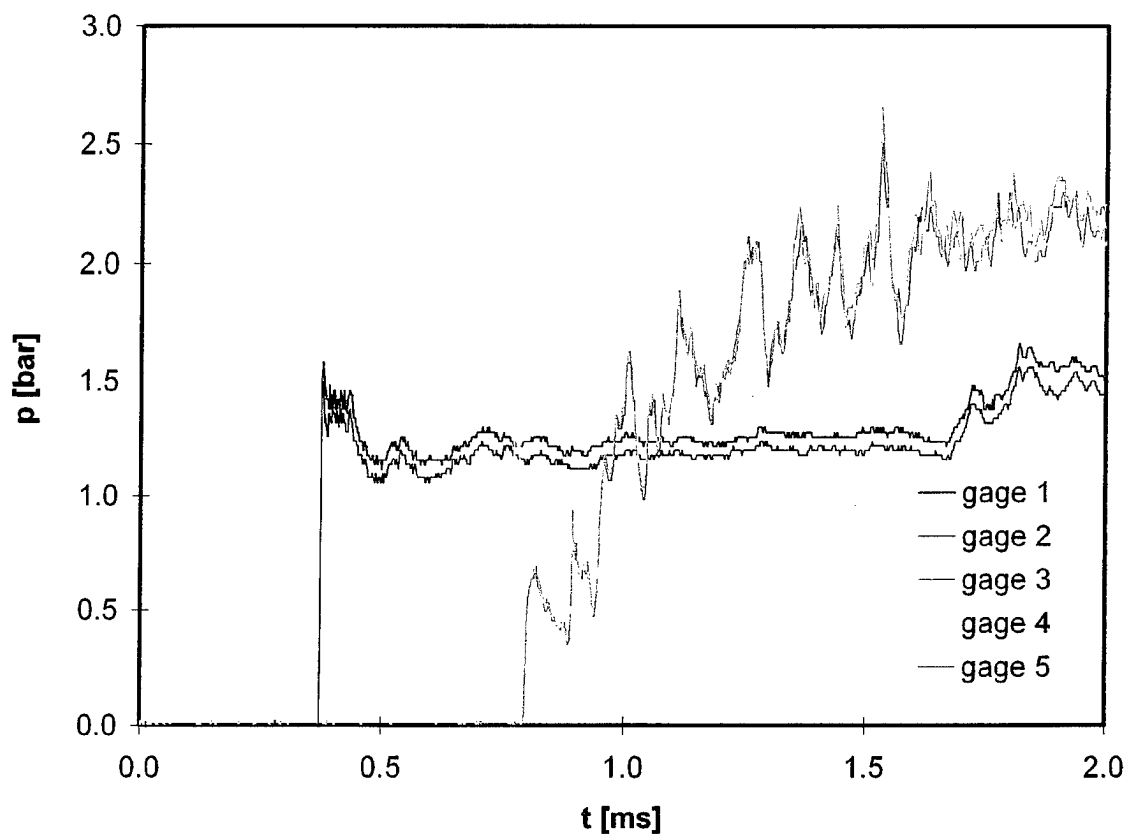


Figure 46. Pressure-time histories at gages 1 to 5 of the T-shaped duct.
 $M_S = 1.21$; (test 15 325).

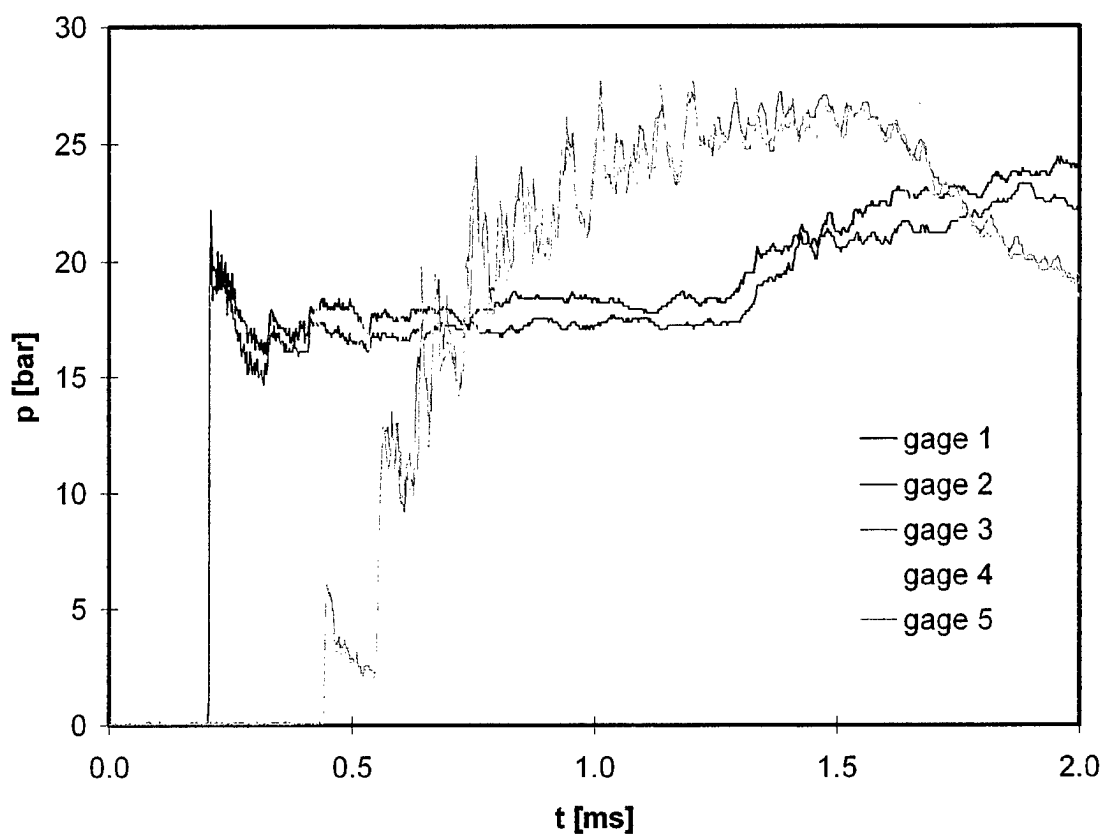
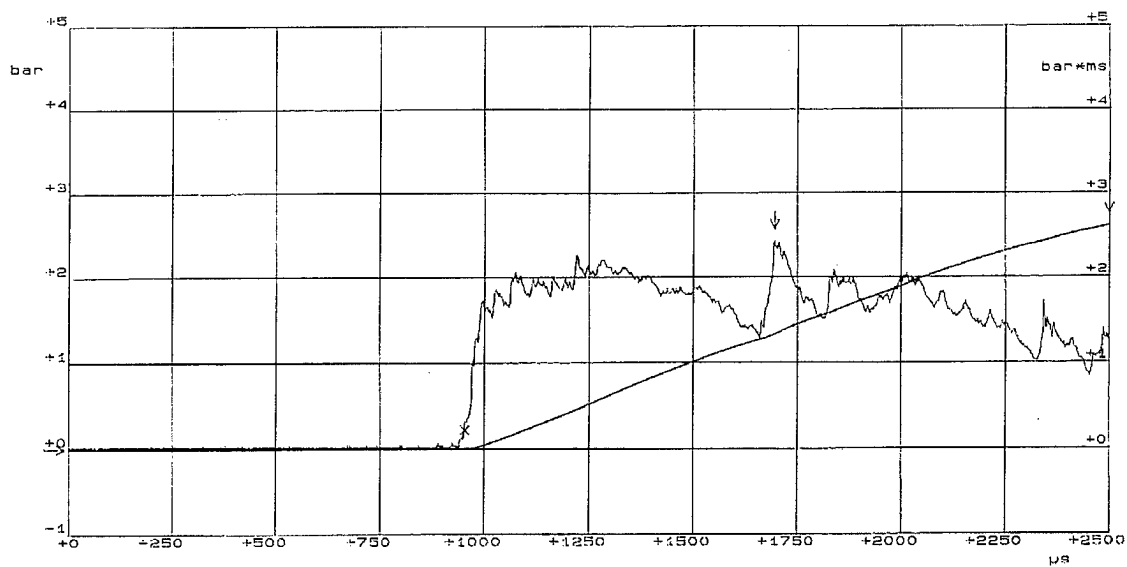
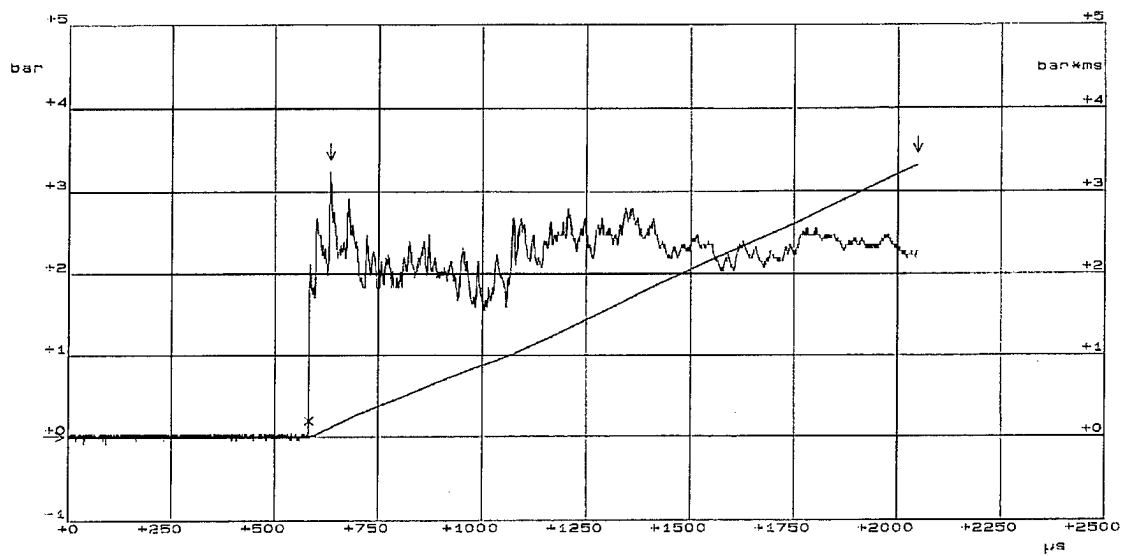


Figure 47. Pressure-time histories at gages 1 to 5 of the T-shaped duct.
 $M_S = 2.18$; (test 15 334).

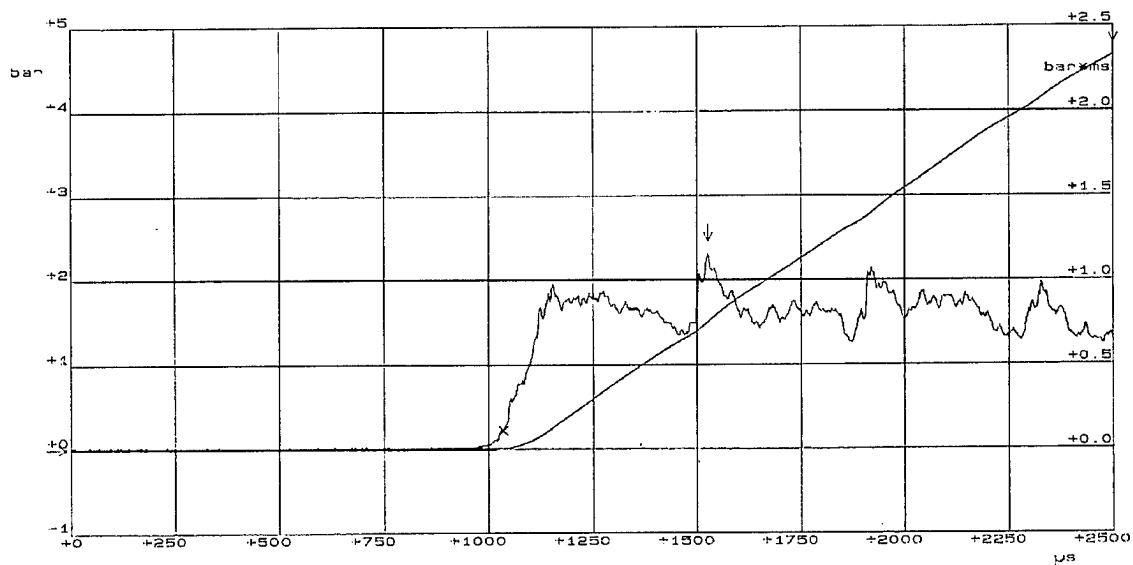


a) $M_5 = 1.22$, (test 15 382)

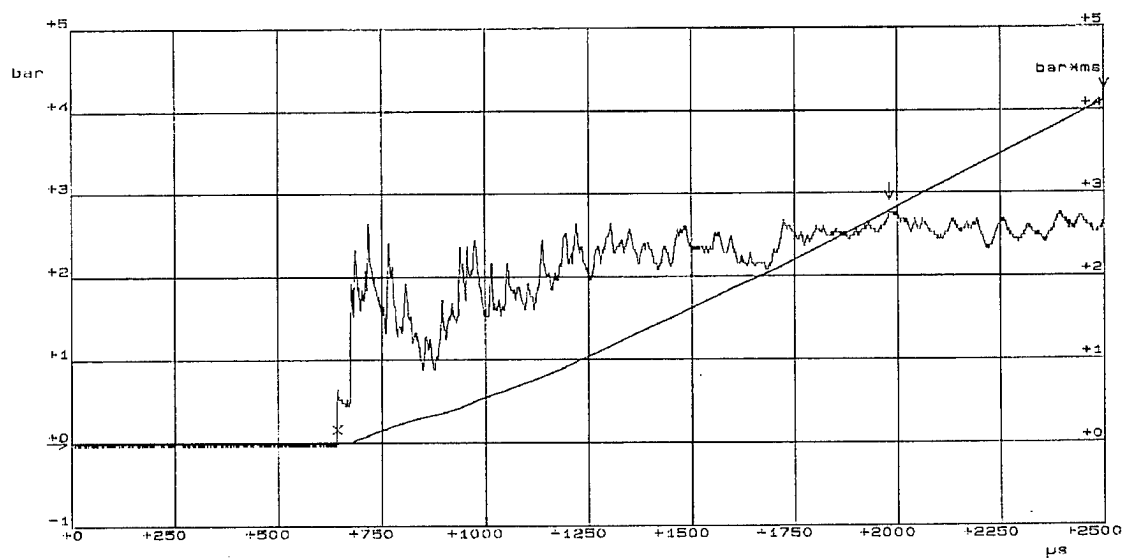


b) $M_5 = 2.16$, (test 15 390)

Figure 48. Pressure records at the end wall of the L-shaped duct.



a) $M_5 = 1.22$, (test 15 392)



b) $M_5 = 2.18$, (test 15 401)

Figure 49. Pressure records at the end wall of the double L-shaped duct.

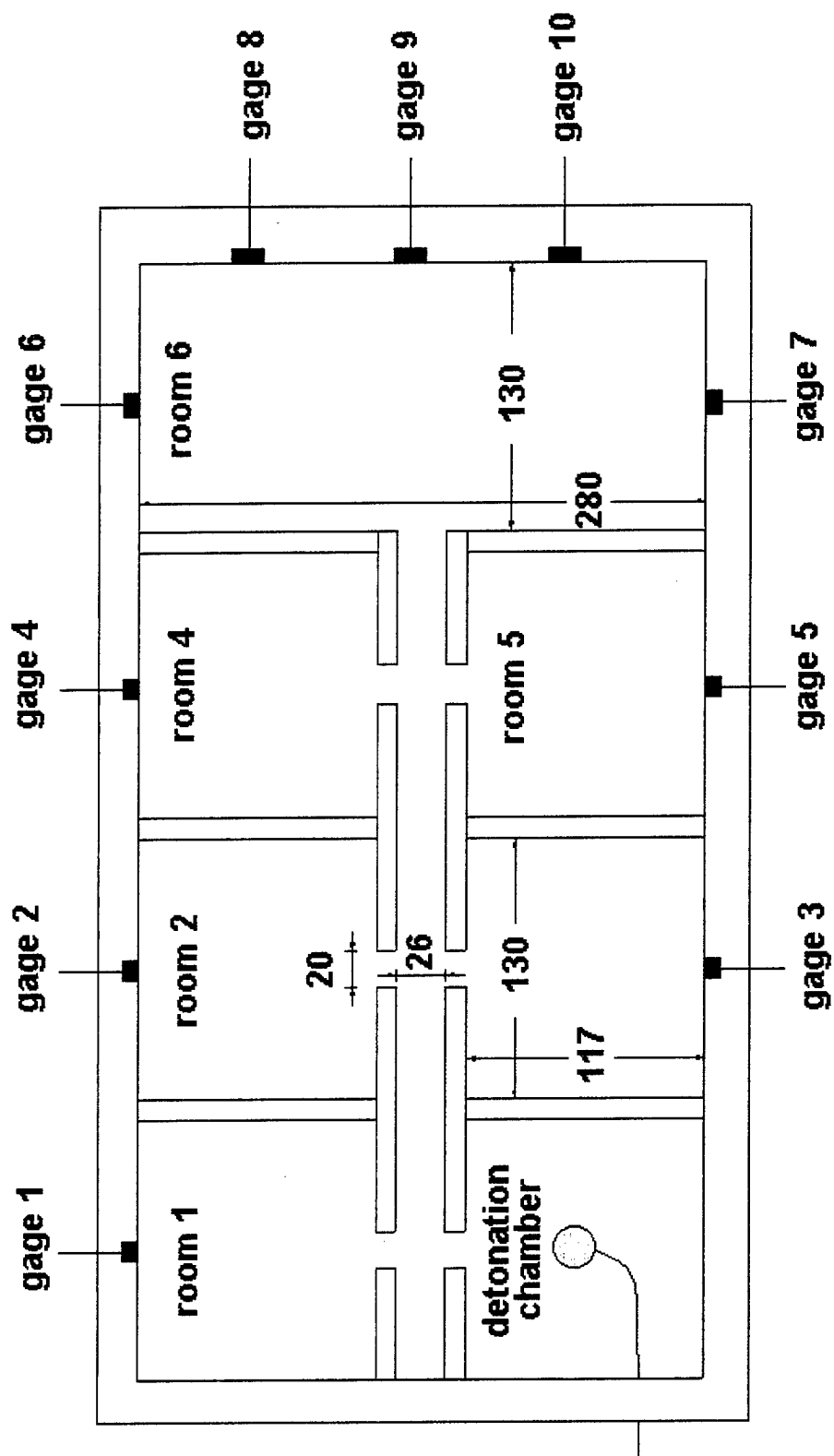


Figure 50. Schematic sketch of the multi-chamber configuration used for small-scale detonation experiments (dimensions in mm).

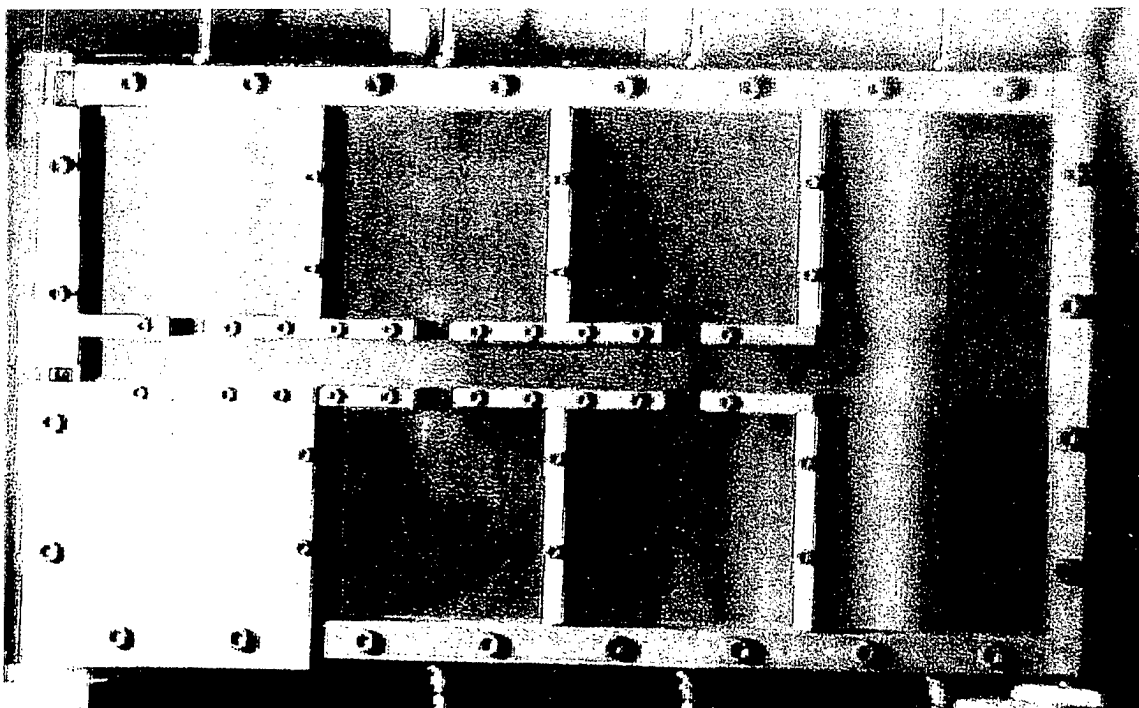


Figure 51. Photograph of the scaled chamber system.

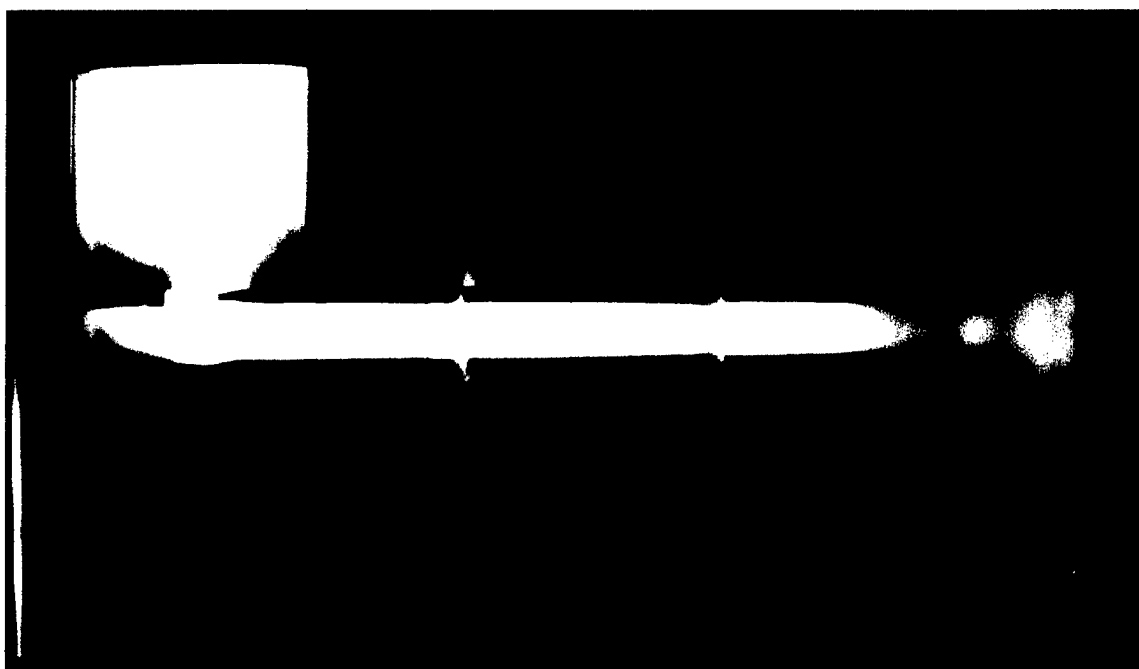


Figure 52. Self luminous plasma cloud after the detonation in the chamber system.

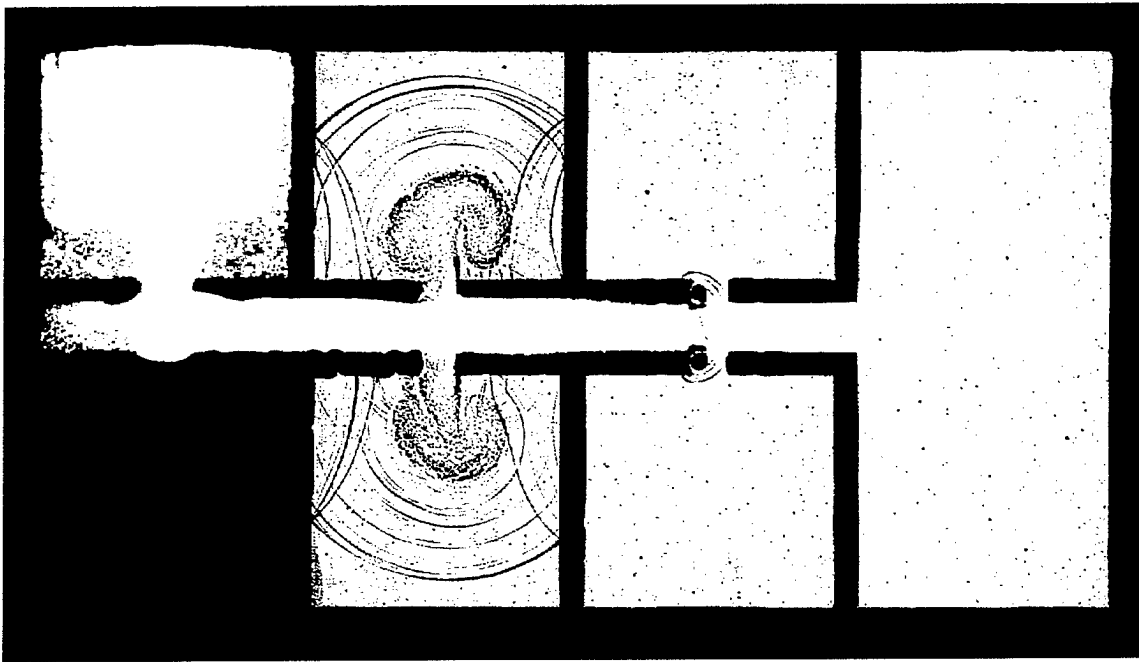


Figure 53. Blast propagation in the scaled chamber system. Time difference between ignition and exposure: $\Delta t = 450 \mu s$ (test 15134).

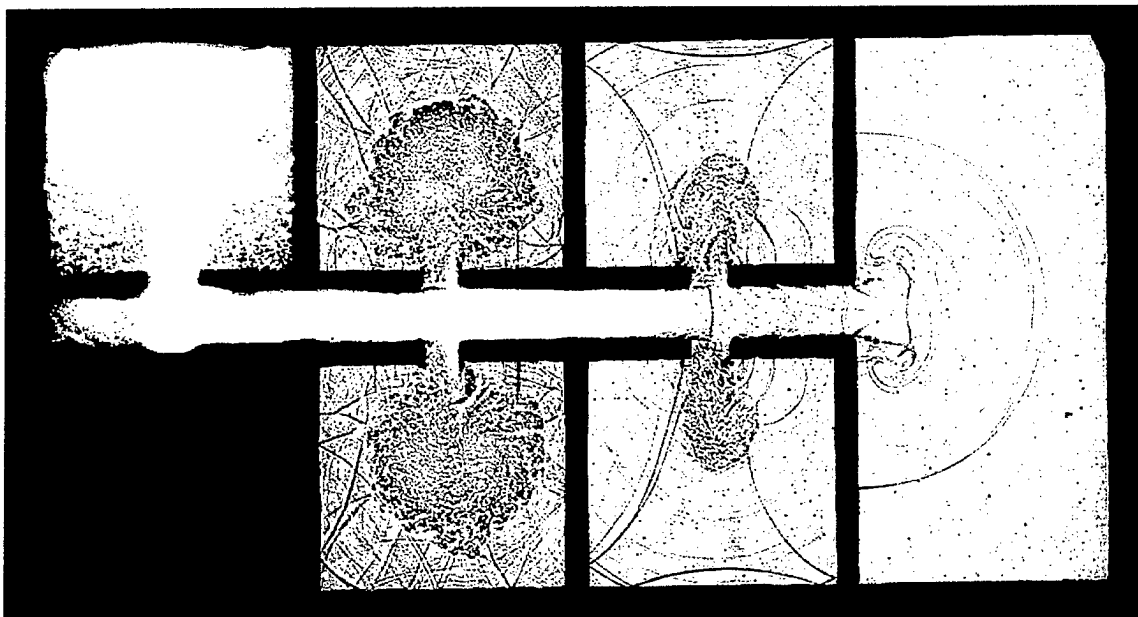


Figure 54. Blast propagation in the scaled chamber system; $\Delta t = 750 \mu s$ (test 15136).

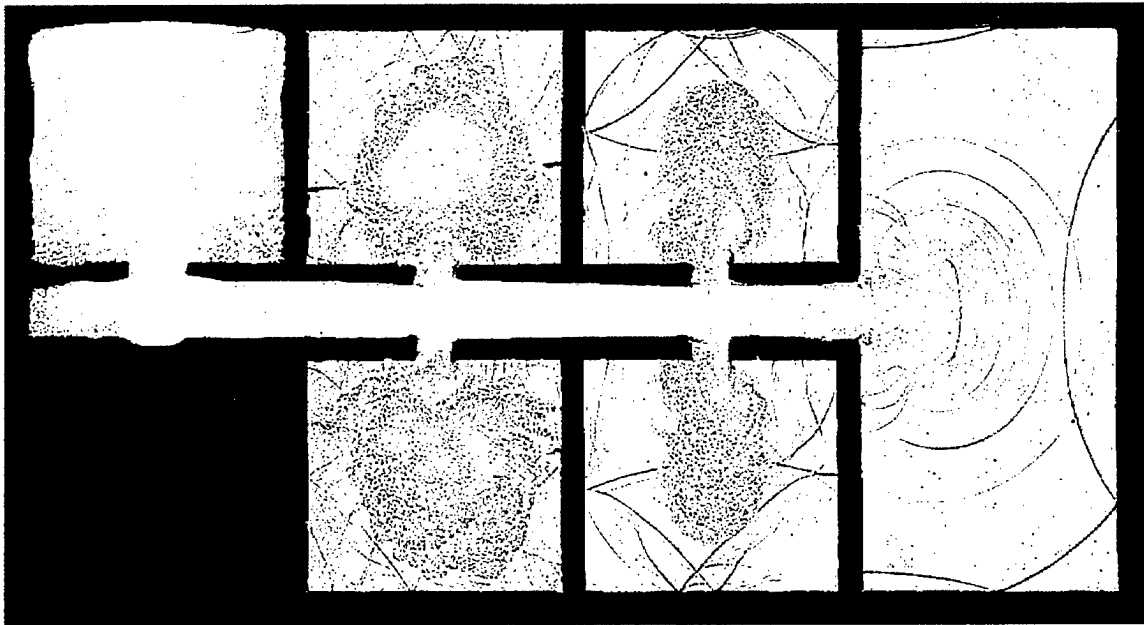


Figure 55. Blast propagation in the scaled chamber system; $\Delta t = 900 \mu s$ (test 15128).

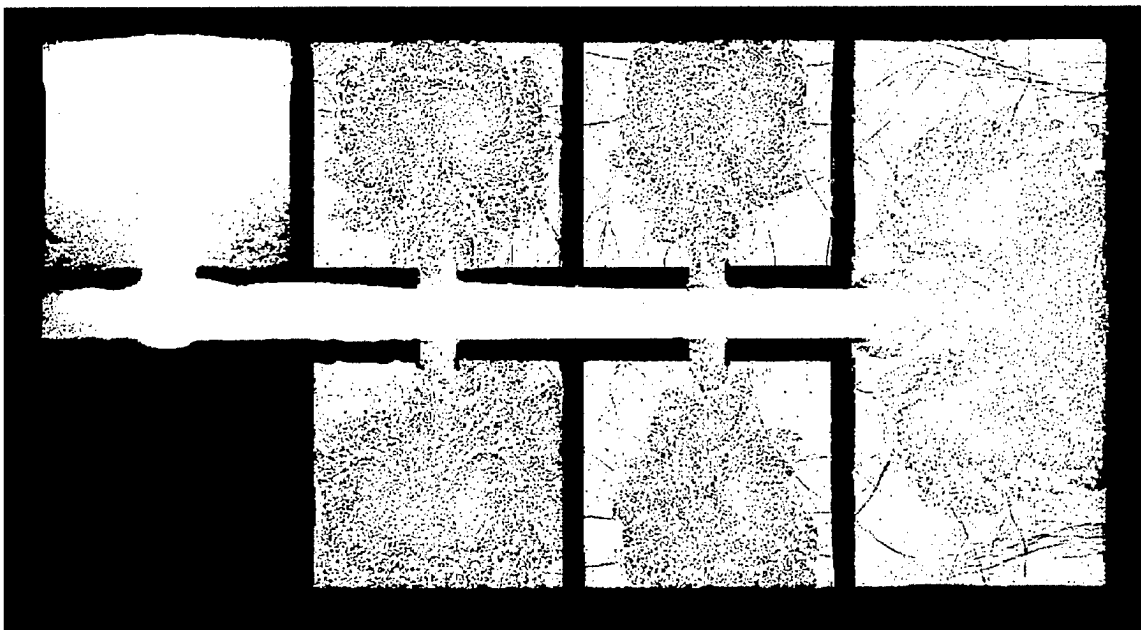


Figure 56. Blast propagation in the scaled chamber system; $\Delta t = 1500 \mu s$ (test 15132).

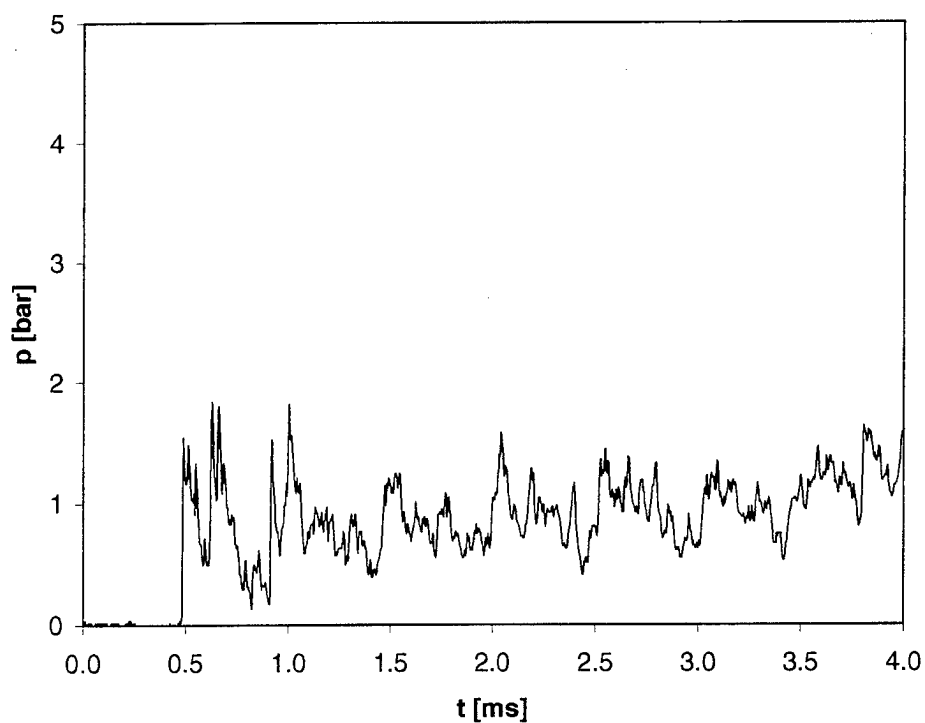
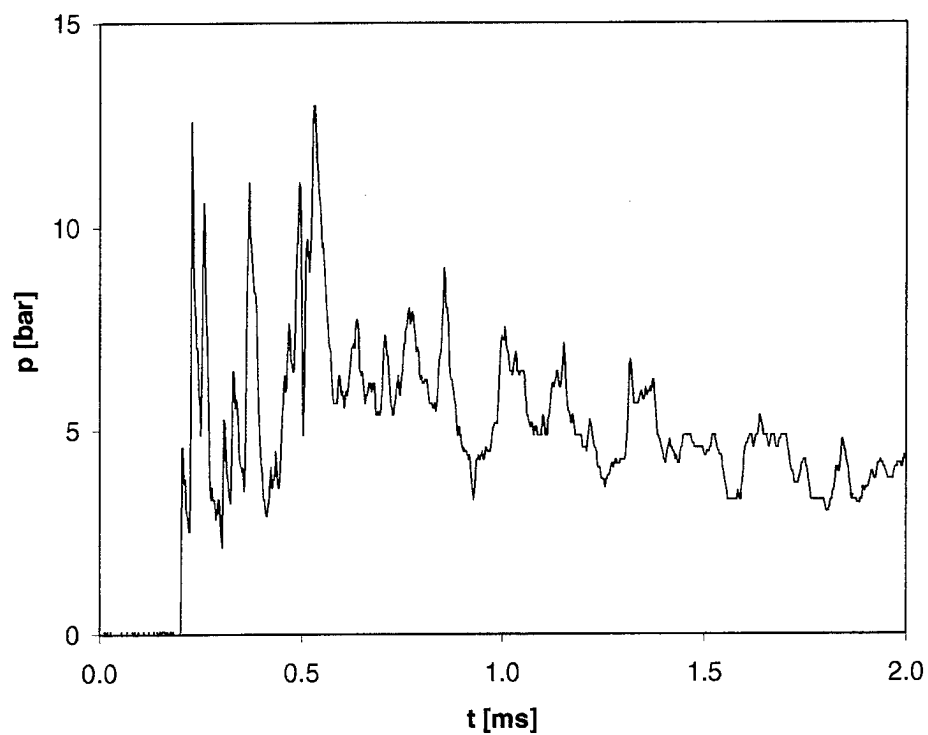


Figure 57. Pressure time history for a test in standard configuration, (spherical 0.5-g NP-charge centered in detonation chamber). Origin: test 0015.MC / 15136.

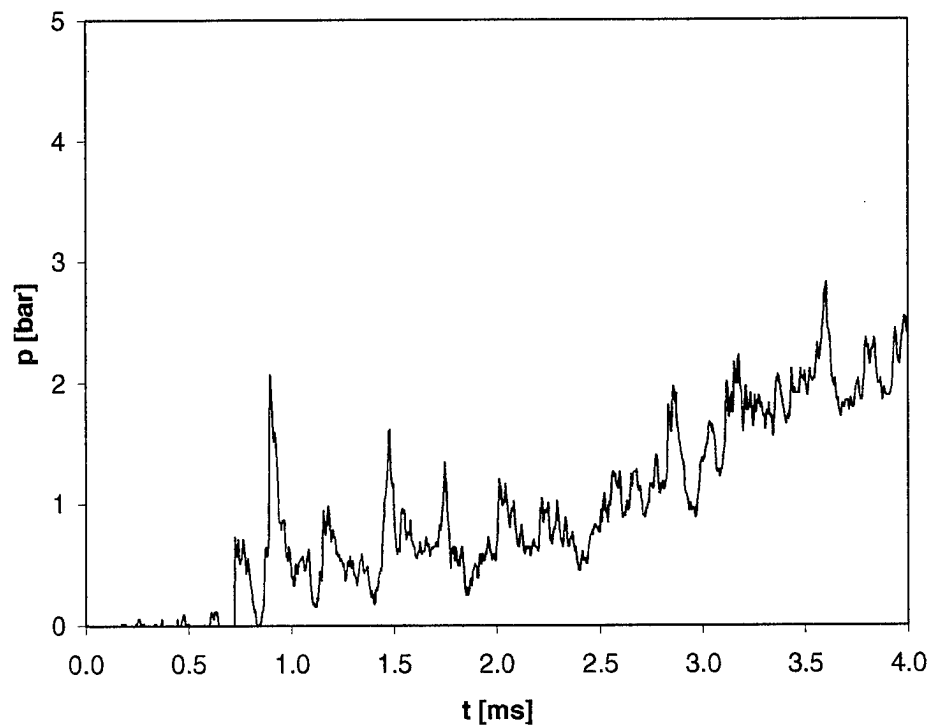
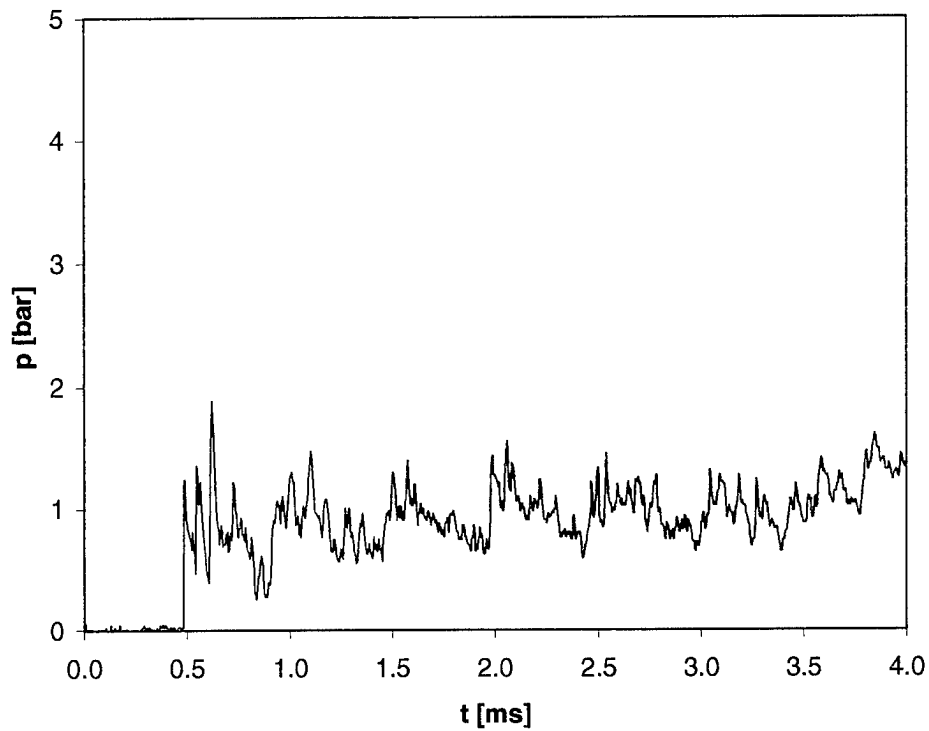
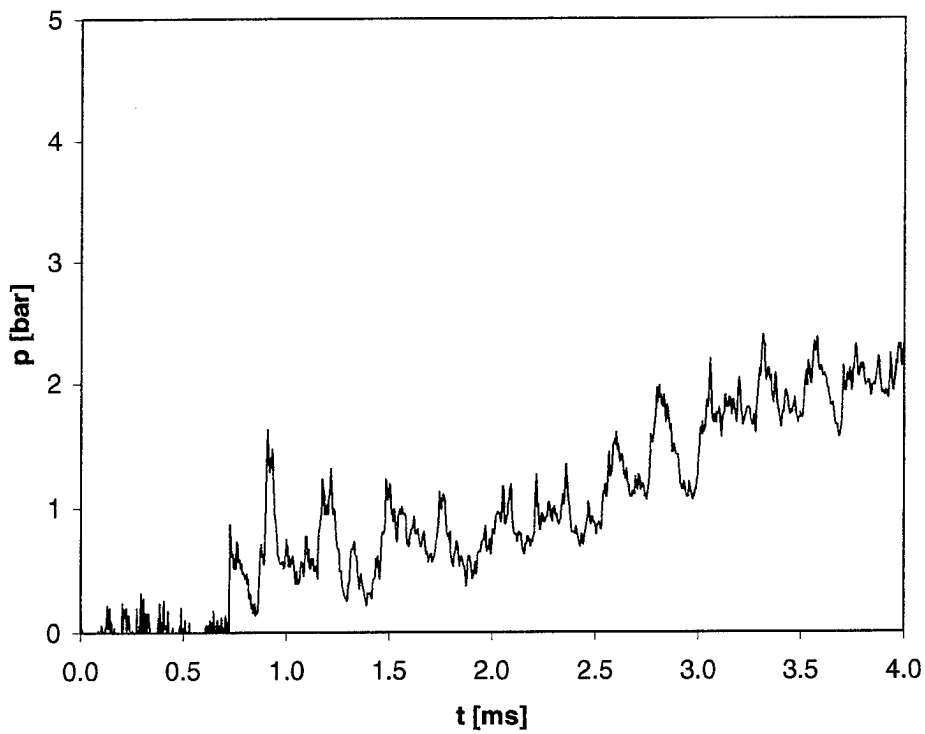
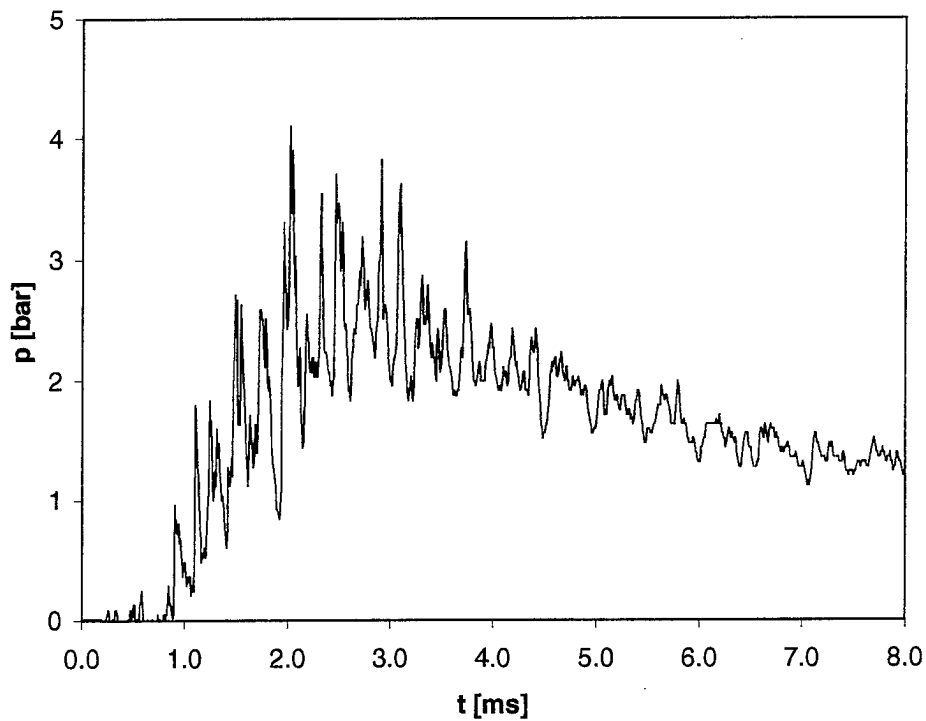


Figure 57. Pressure time history for a test in standard configuration, (spherical 0.5-g NP-charge centered in detonation chamber). Origin: test 0015.MC / 15136. (Continued)



e) Gage 5



f) Gage 6

Figure 57. Pressure time history for a test in standard configuration, (spherical 0.5-g NP-charge centered in detonation chamber). Origin: test 0015.MC / 15136. (Continued)

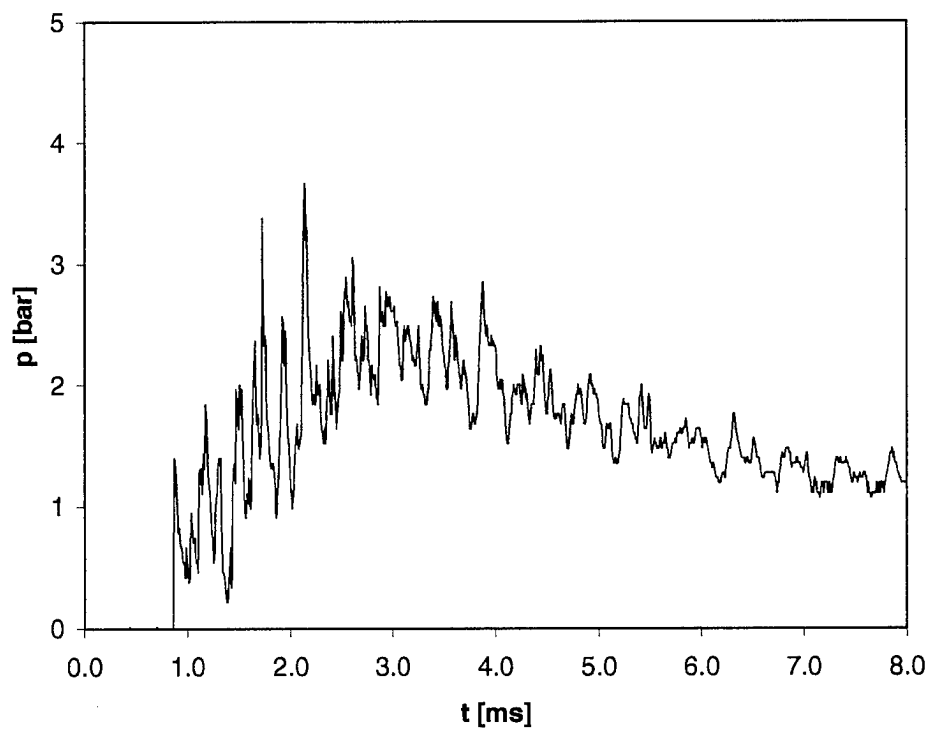
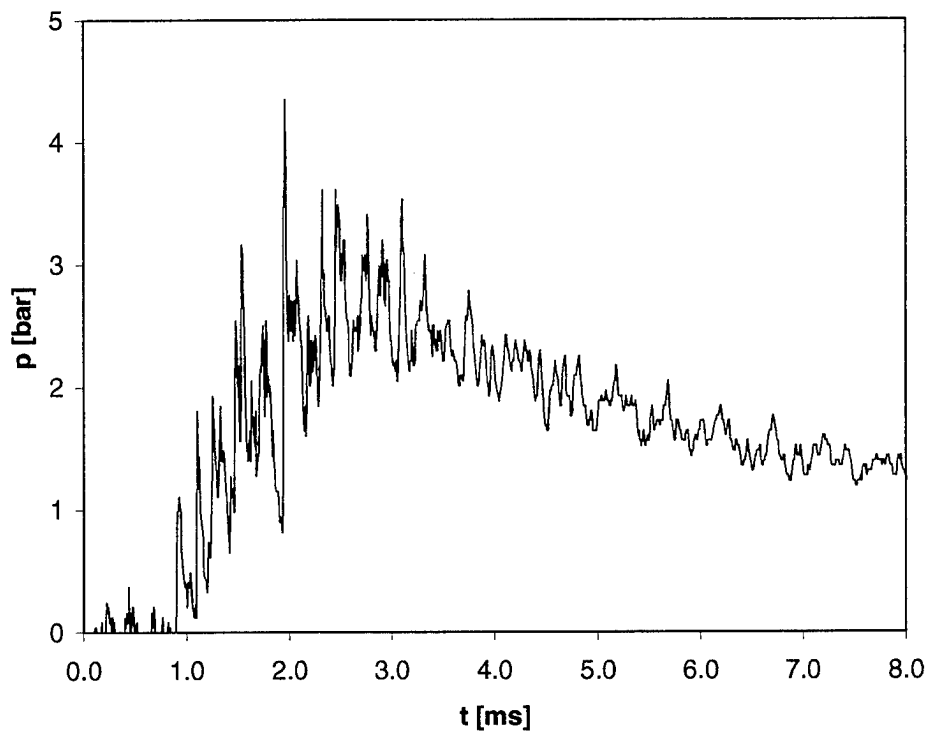
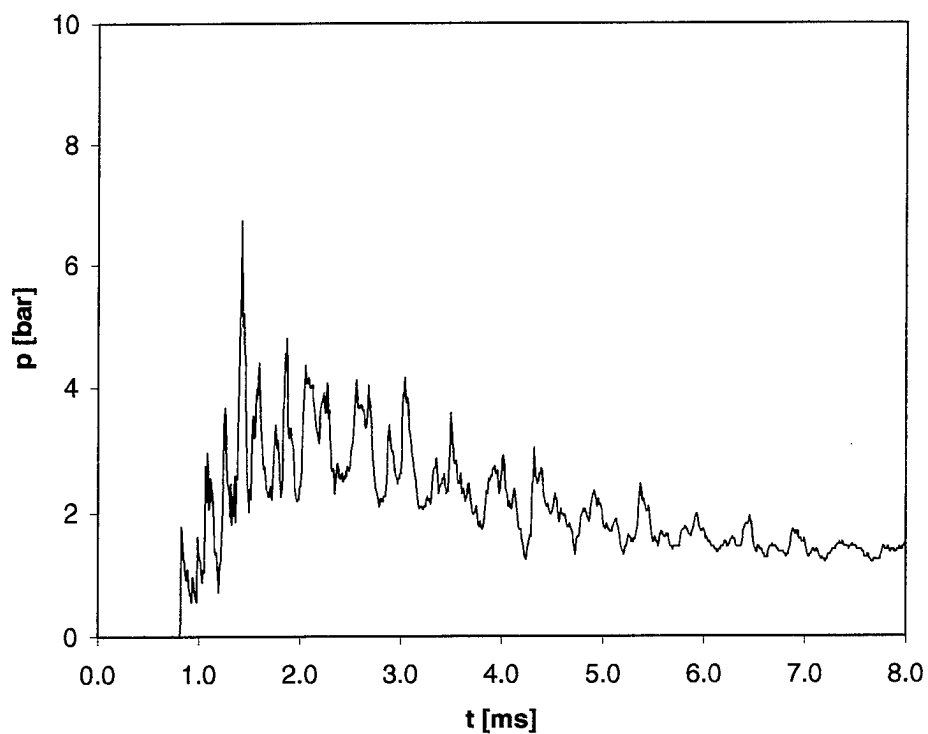
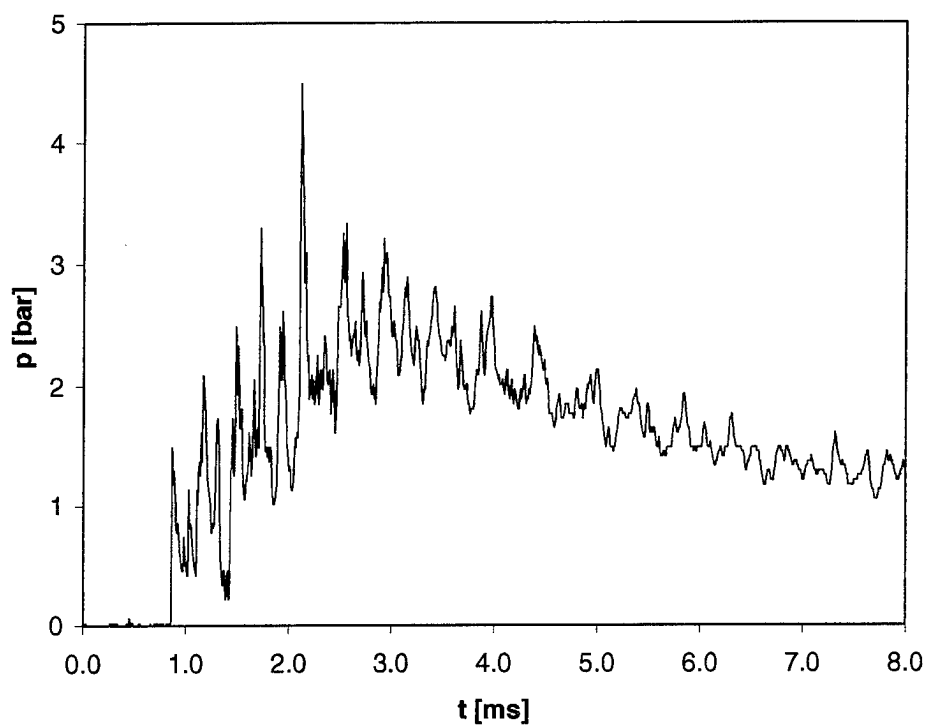


Figure 57. Pressure time history for a test in standard configuration,
(spherical 0.5-g NP-charge centered in detonation chamber).
Origin: test 0015.MC / 15136. (Continued)



i) Gage 9



j) Gage 10

Figure 57. Pressure time history for a test in standard configuration, (spherical 0.5-g NP-charge centered in detonation chamber). Origin: test 0015.MC / 15136. (Continued)

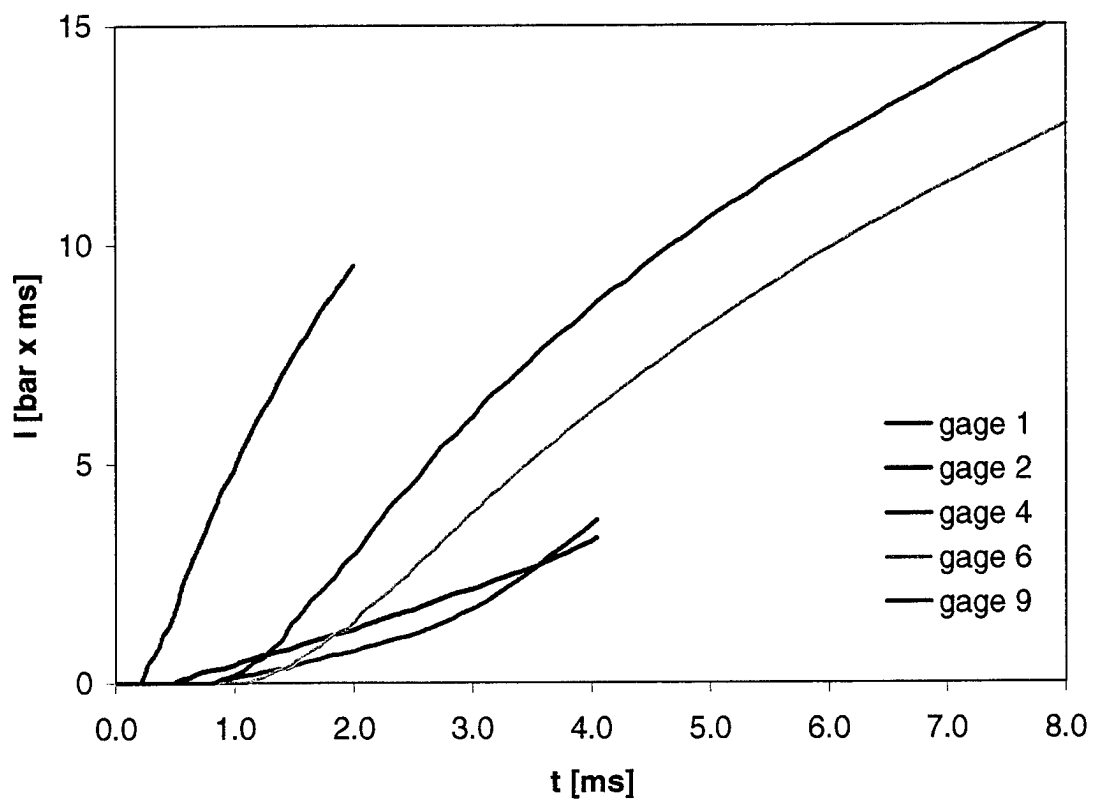


Figure 58. Overpressure impulses versus time for a test in standard configuration. $t = 0$ denotes detonation. Origin: test 0015.MC / 15236.

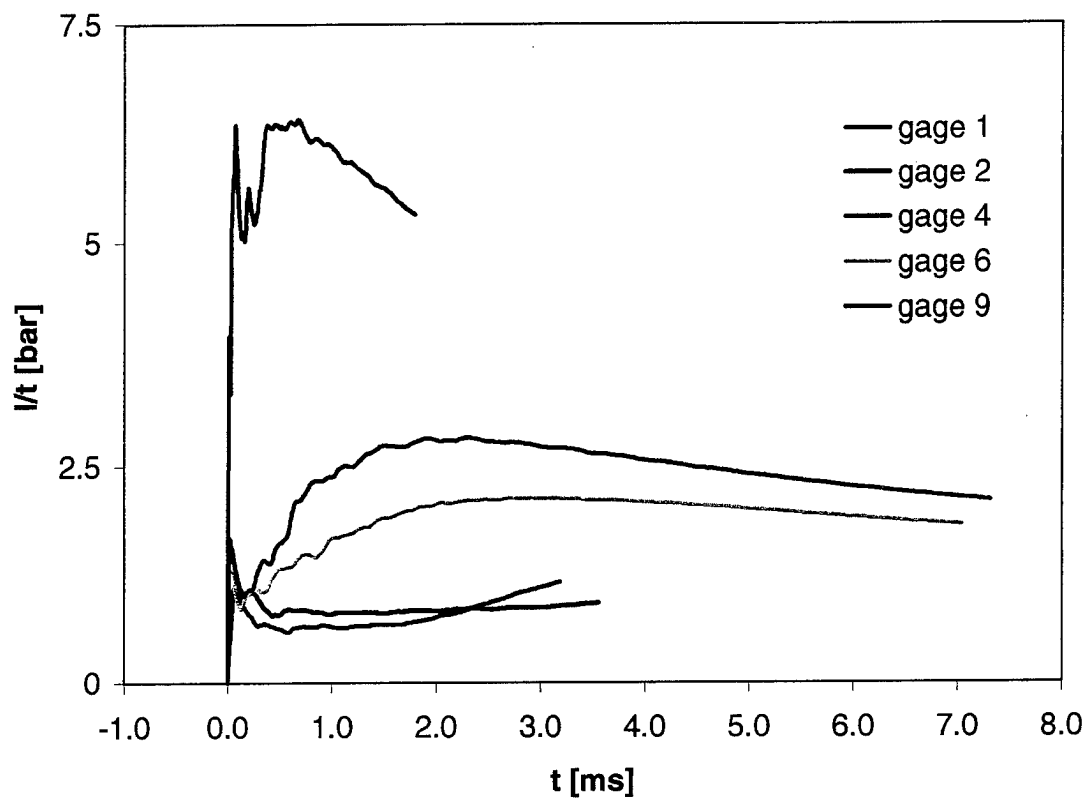


Figure 59. Average overpressure in terms of $I(t)/t$ for the records from Figure 58. Here $t = 0$ denotes the time of arrival.

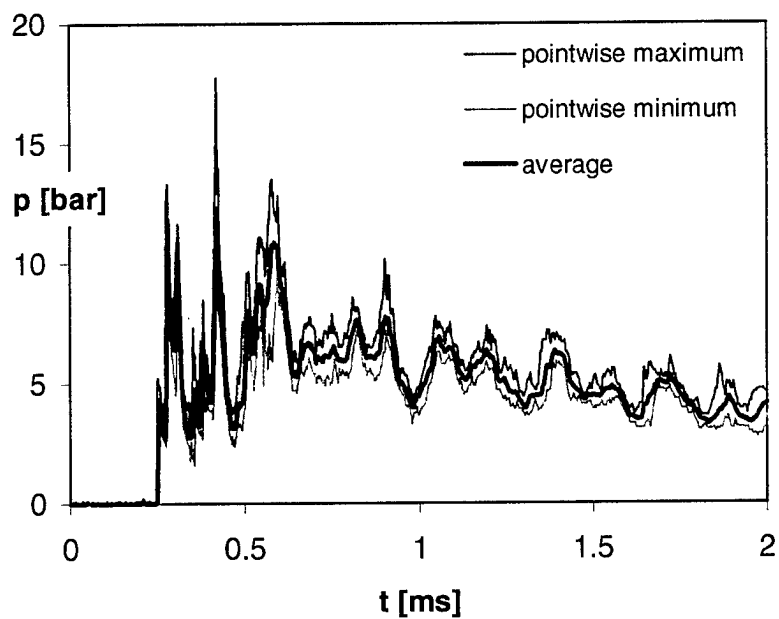


Figure 60. Ensemble-averaged overpressure and corresponding confidence bandwidth at gage1 for the standard configuration. Ensemble of eight tests.

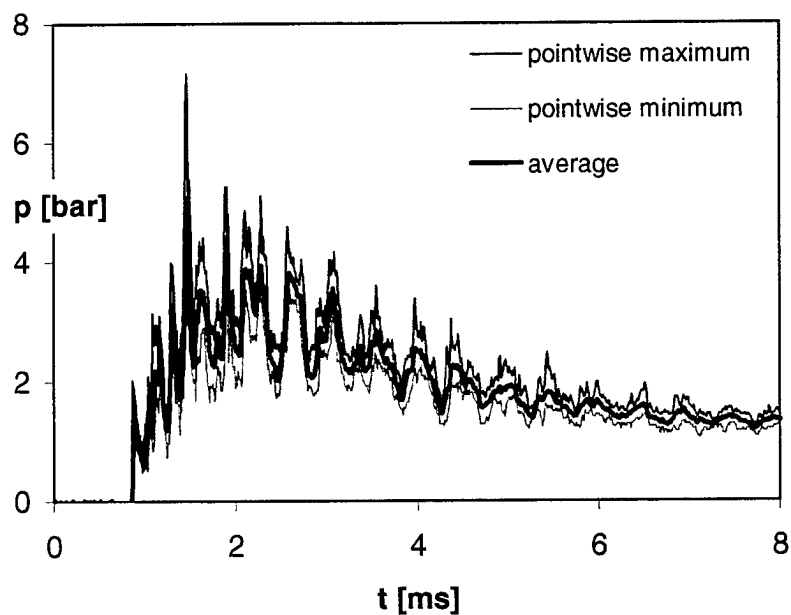


Figure 61. Ensemble-averaged overpressure and corresponding confidence bandwidth at gage 9 for the standard configuration. Ensemble of eight tests.

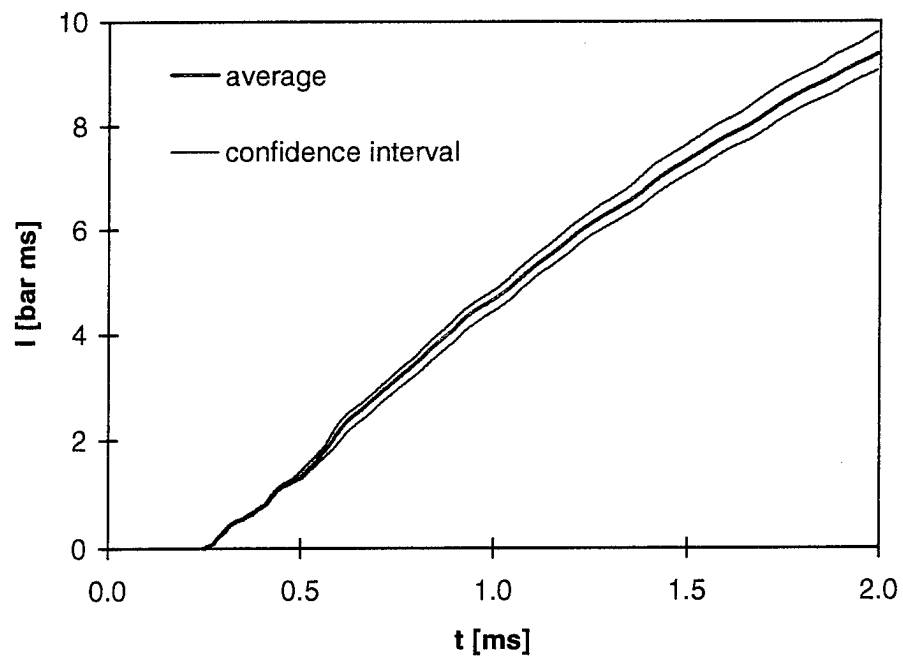


Figure 62. Ensemble-averaged overpressure impulse and corresponding confidence bandwidth at gage 1 for the standard configuration. Ensemble of eight tests.

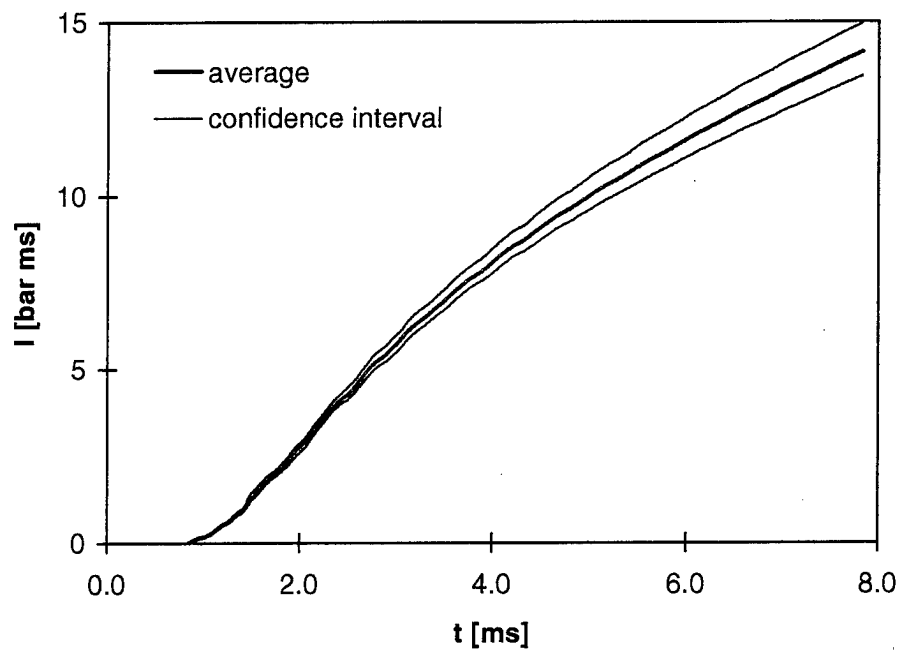


Figure 63. Ensemble-averaged overpressure impulse and corresponding confidence bandwidth at gage 9 for the standard configuration. Ensemble of eight tests.

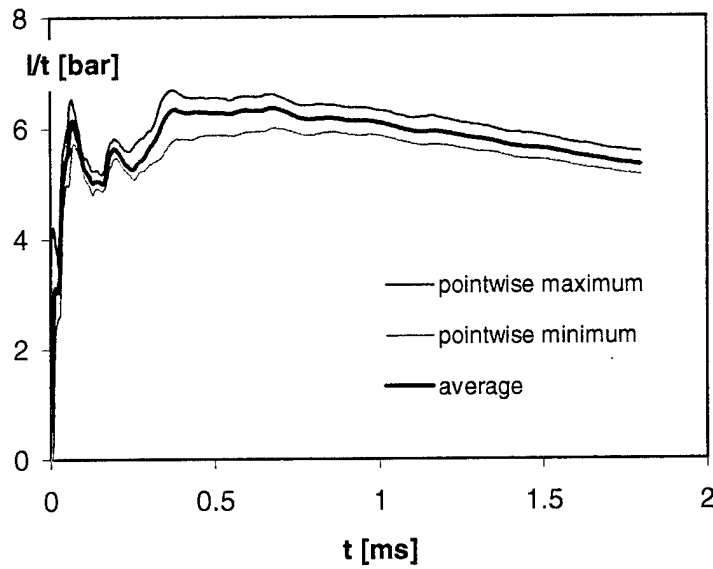


Figure 64. Ensemble-averaged mean overpressure in terms of $I(t)/t$ and corresponding confidence bandwidth at gage 1 for the standard configuration. Ensemble of eight tests.

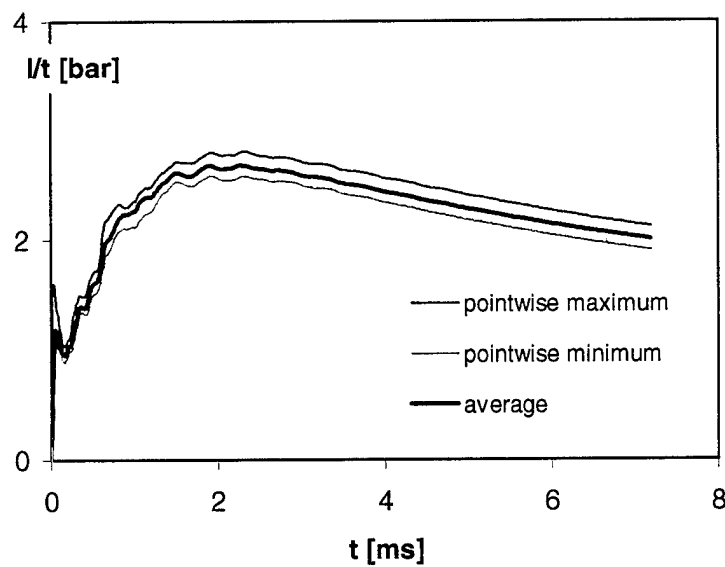


Figure 65. Ensemble-averaged mean overpressure in terms of $I(t)/t$ and corresponding confidence bandwidth at gage 9 for the standard configuration. Ensemble of eight tests.

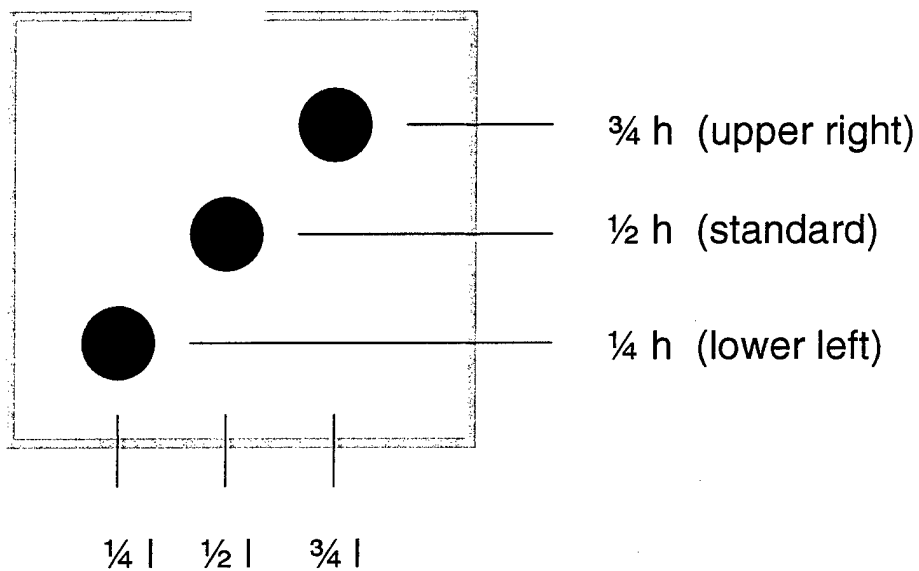
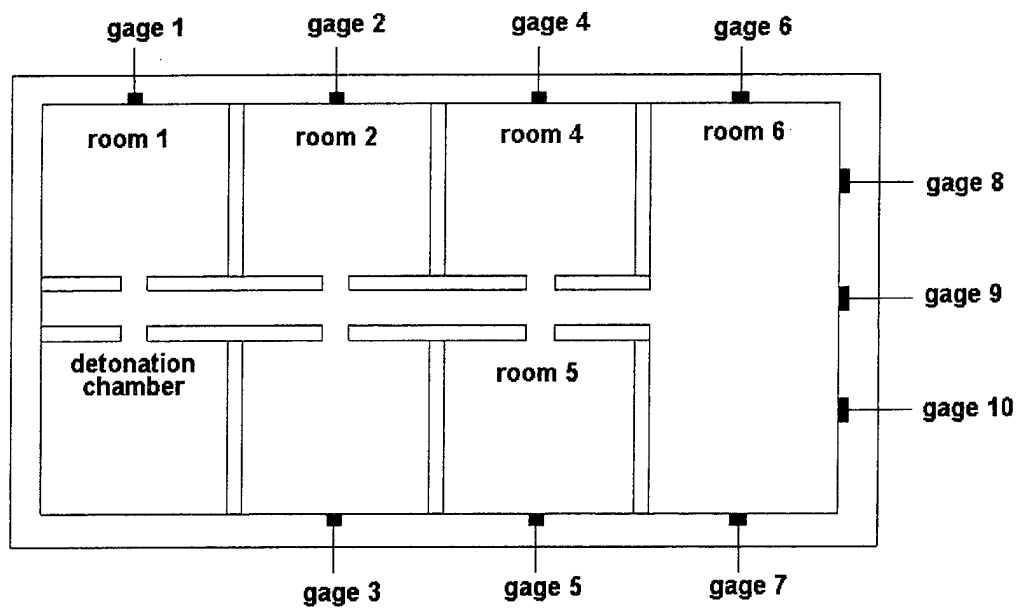


Figure 66. Schematic of the different charge locations in the detonation chamber.

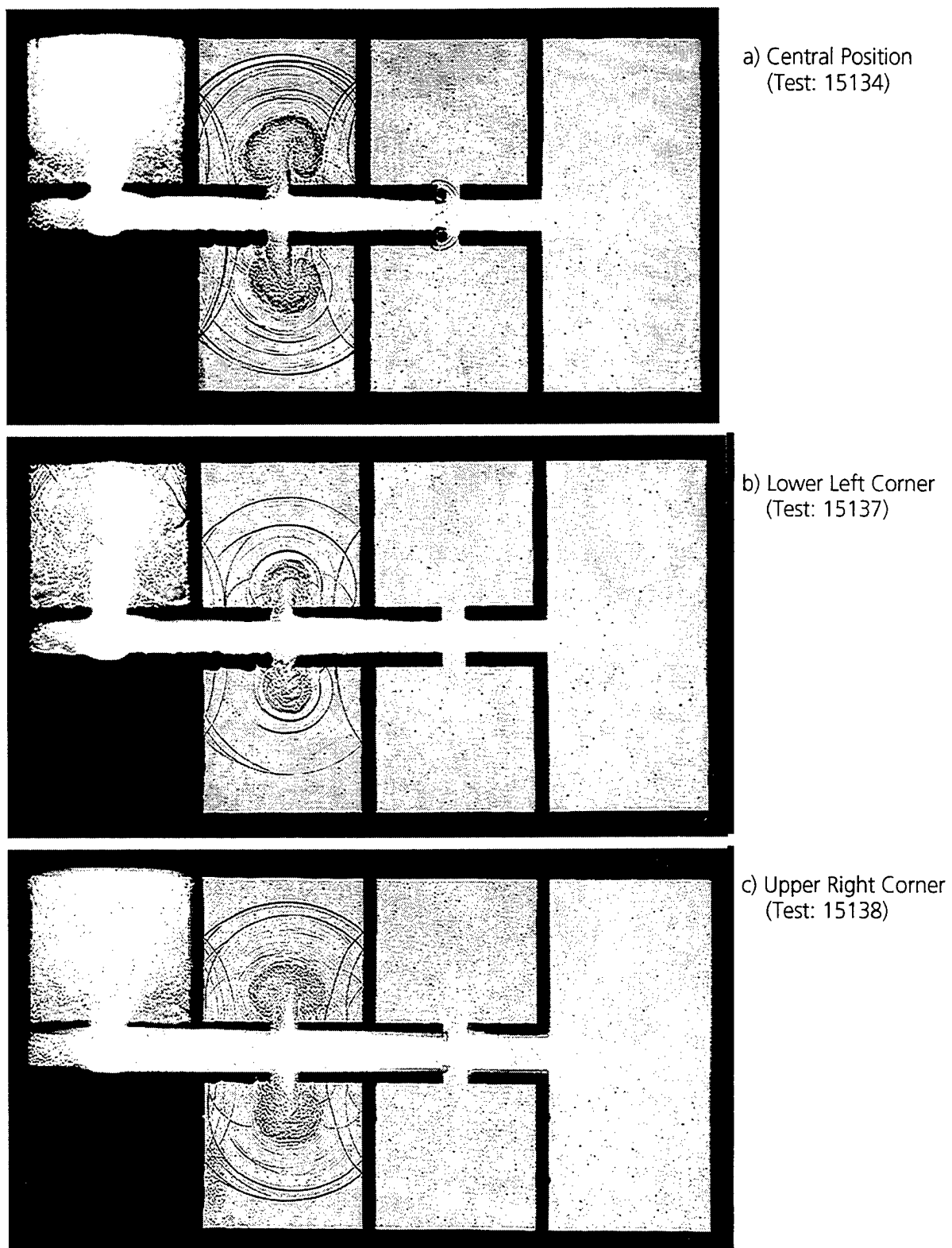
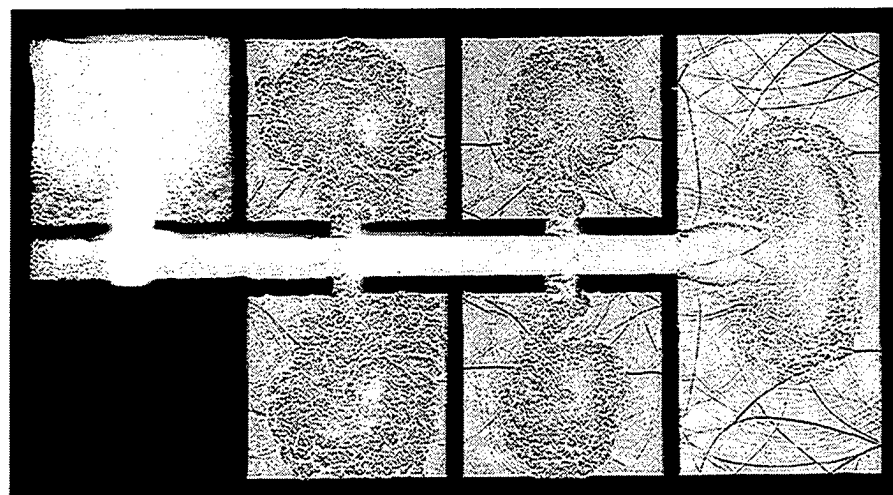
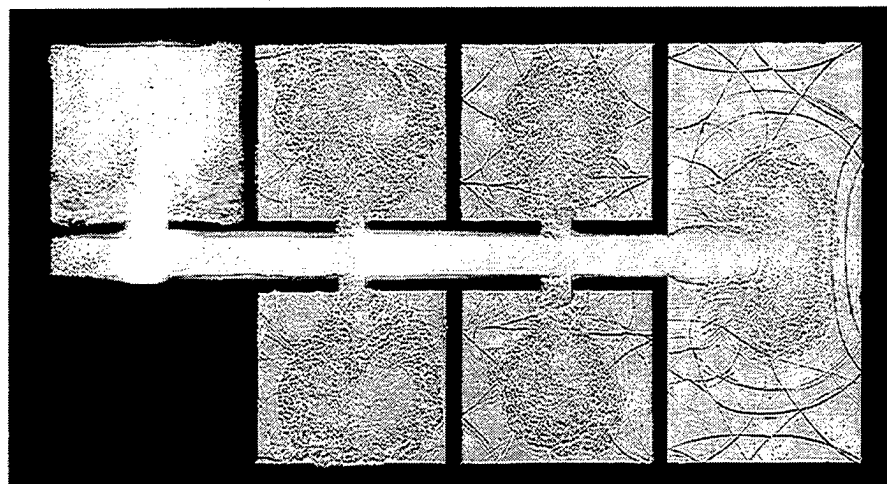


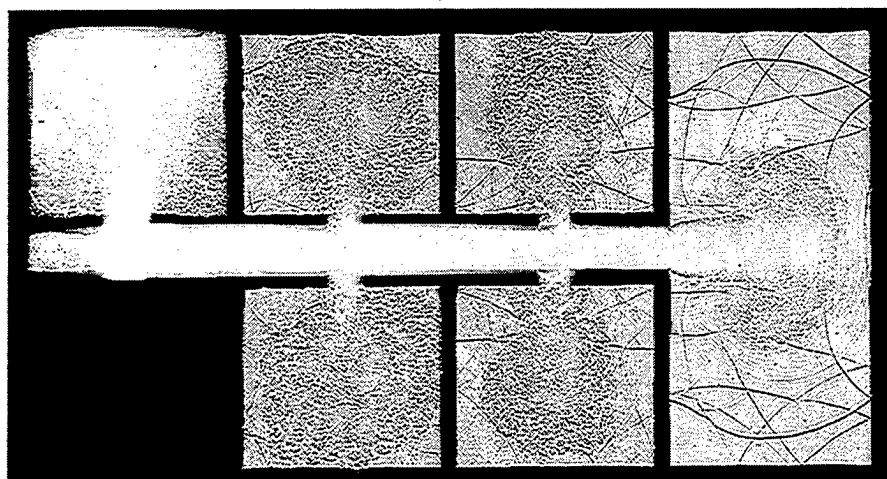
Figure 67. Blast propagation in the scaled chamber system for different charge locations;
 $\Delta t = 450 \mu s$.



a) Central Position
(Test: 15131)



b) Lower Left Corner
(Test: 15144)



c) Upper Right Corner
(Test: 15141)

Figure 68. Blast propagation in the scaled chamber-system for different charge locations;
 $\Delta t = 1200 \mu s$.

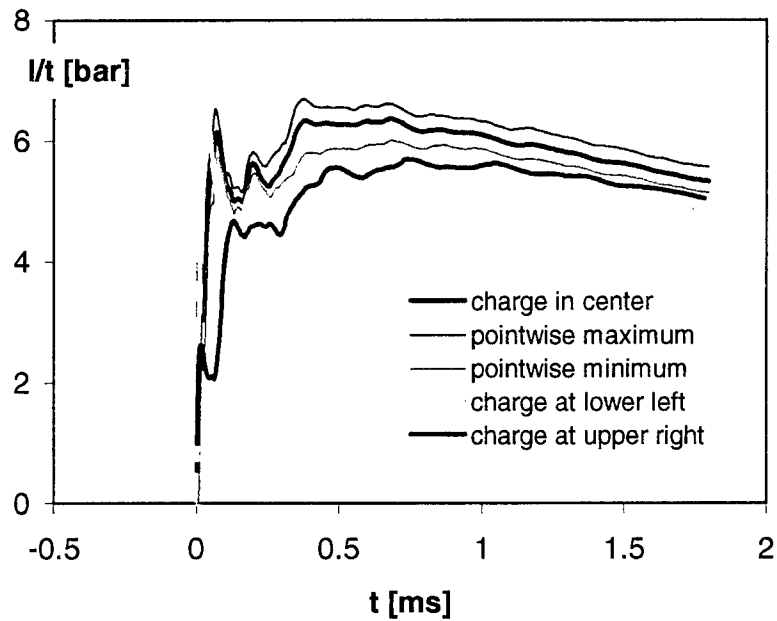


Figure 69. Comparison of the time-averaged pressure $I(t)/t$ at gage 1 for three different charge positions.

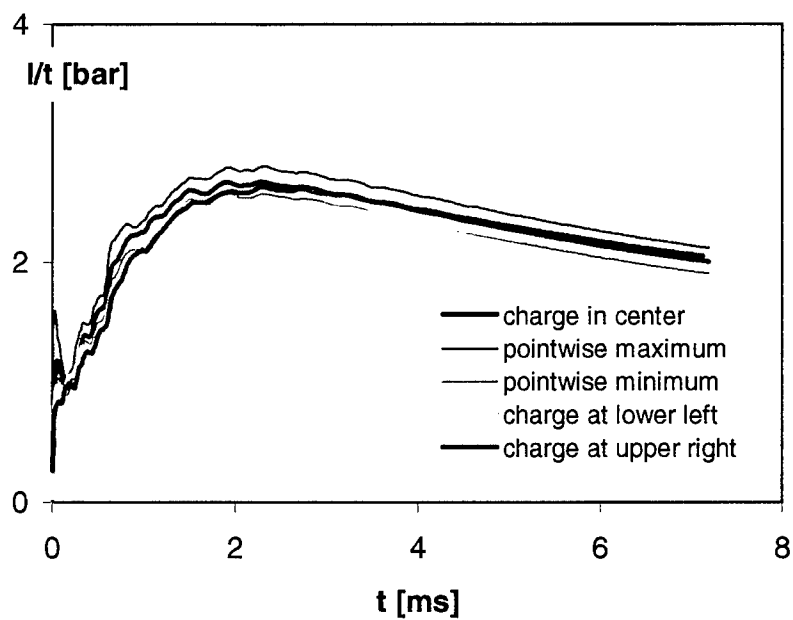


Figure 70. Comparison of the time-averaged pressure $I(t)/t$ at gage 9 for three different charge positions.

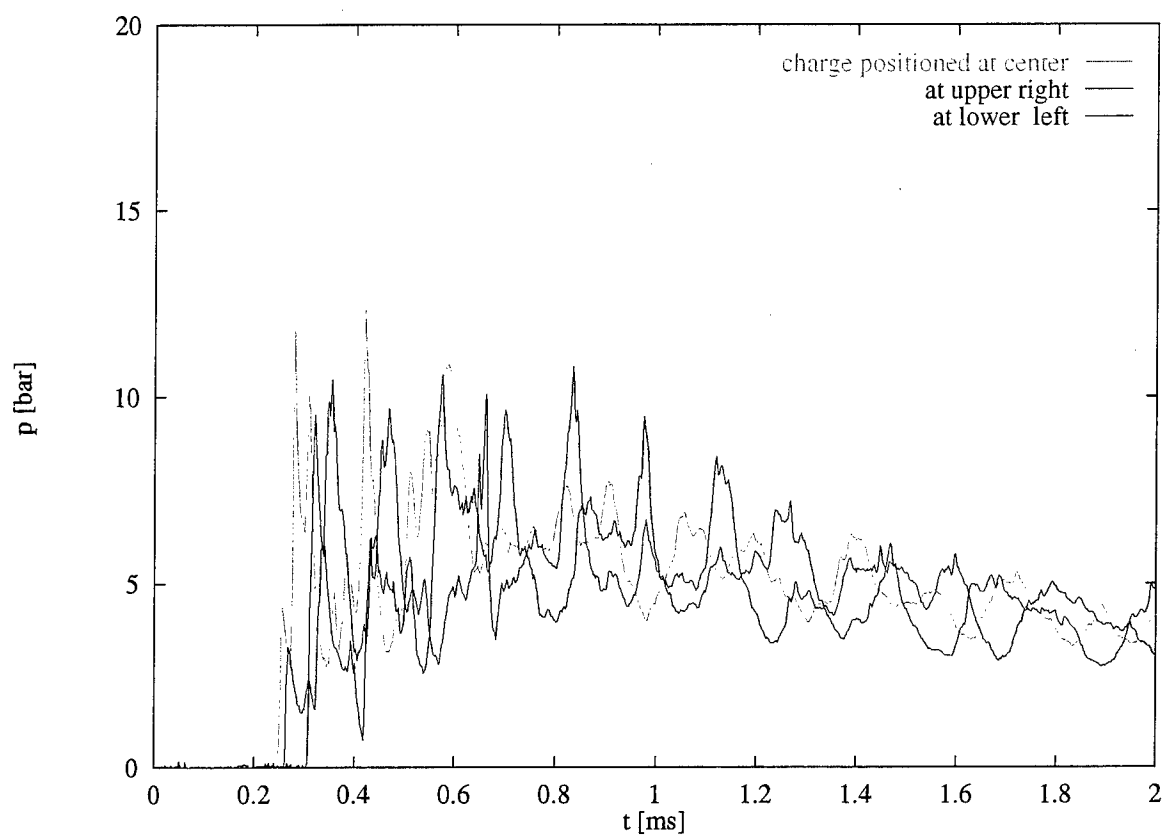


Figure 71. Ensembled-averaged pressure at gage 1 for three different charge locations.

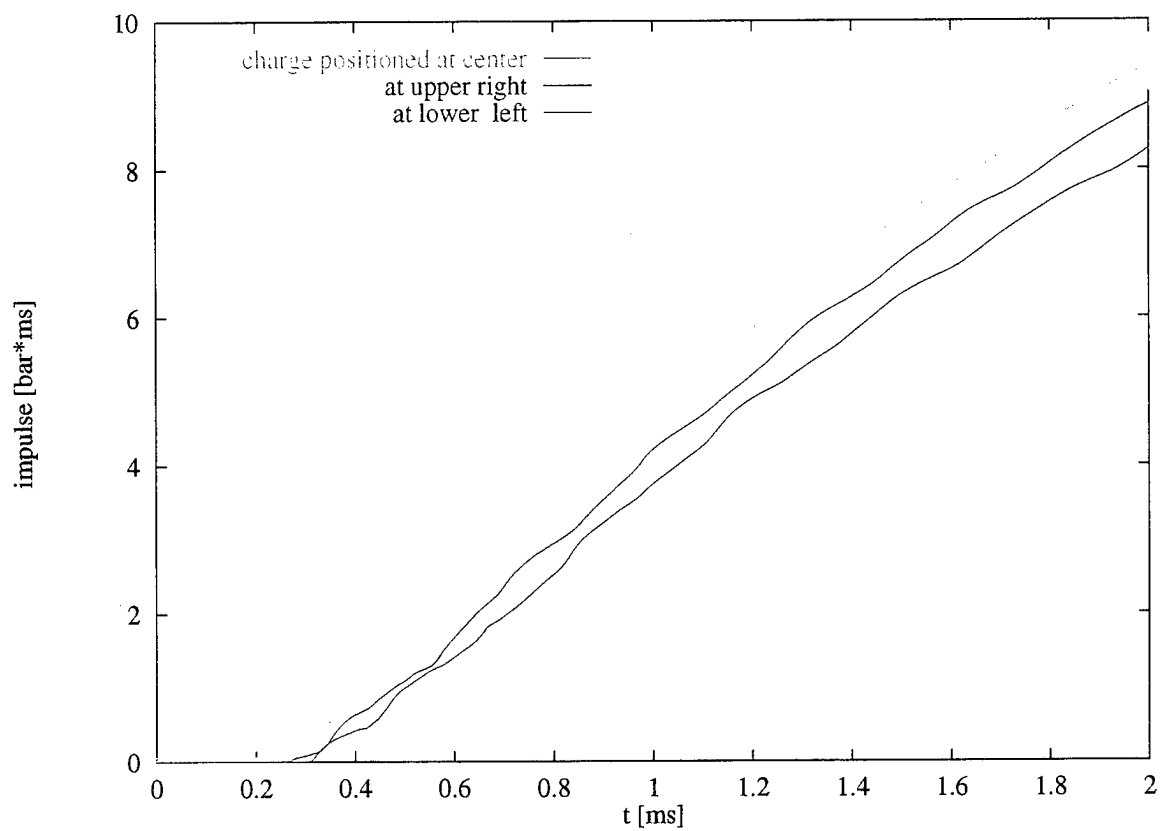


Figure 72. Ensemble-averaged overpressure impulse at gage 1 for three different charge positions (yellow: confidence band of standard experiments).

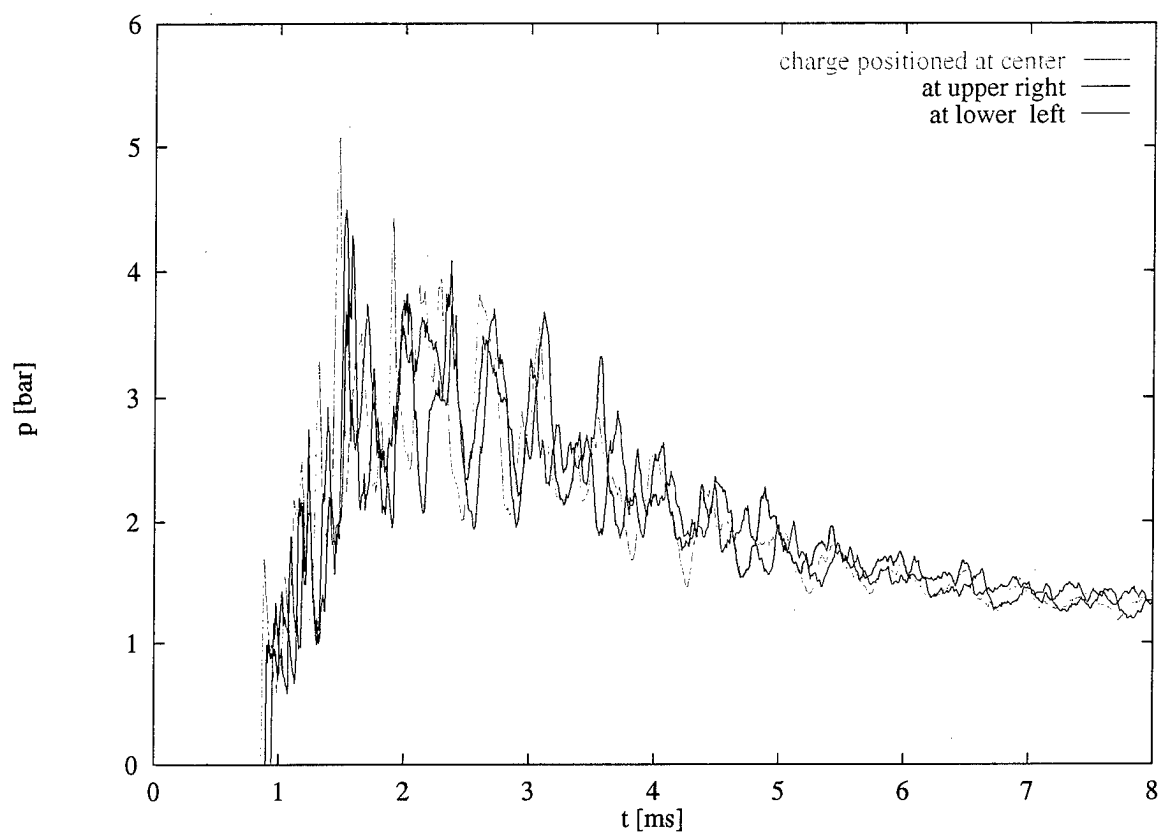


Figure 73. Ensemble-averaged pressure at gage 9 for three different charge positions.

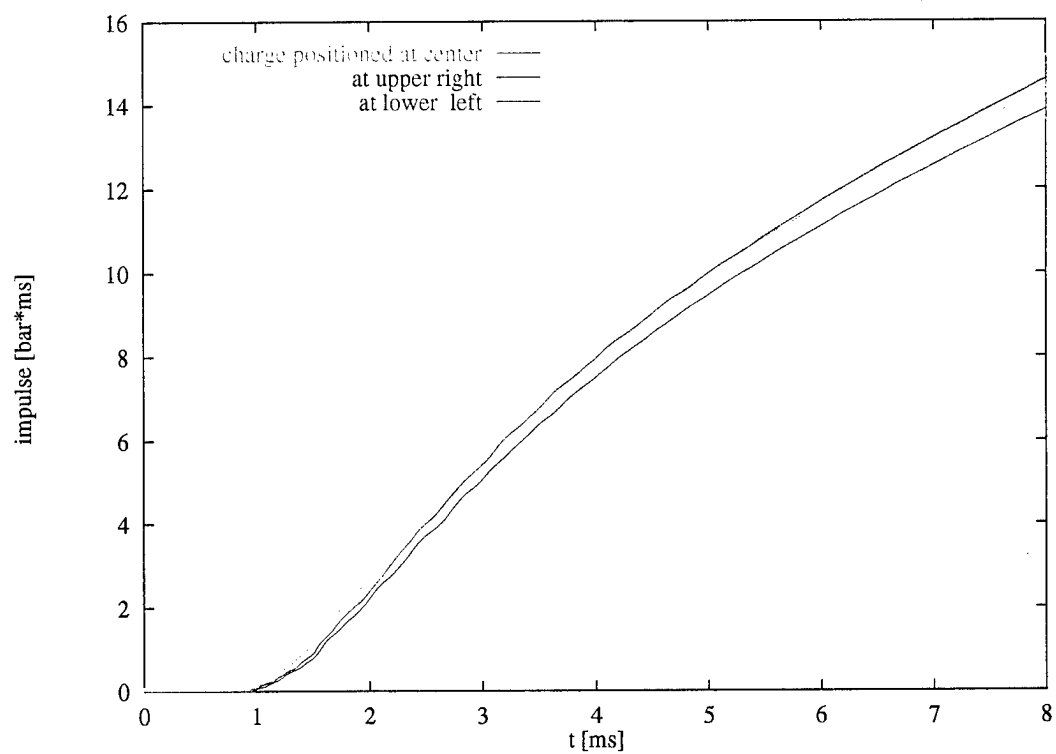
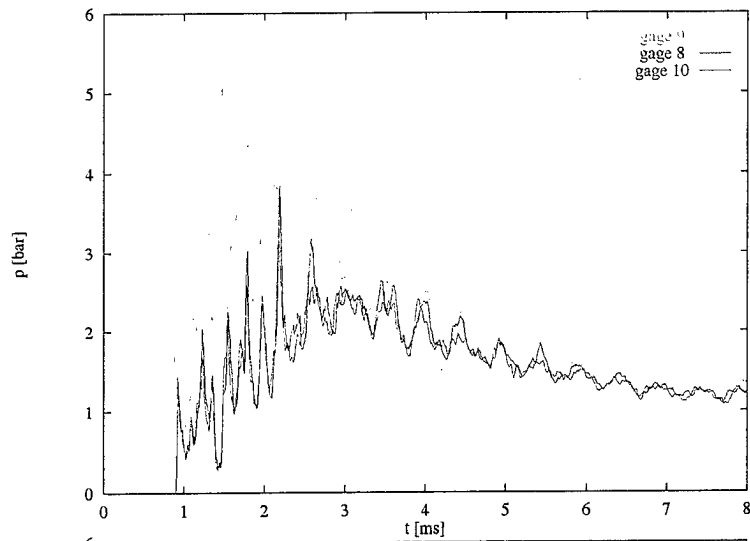
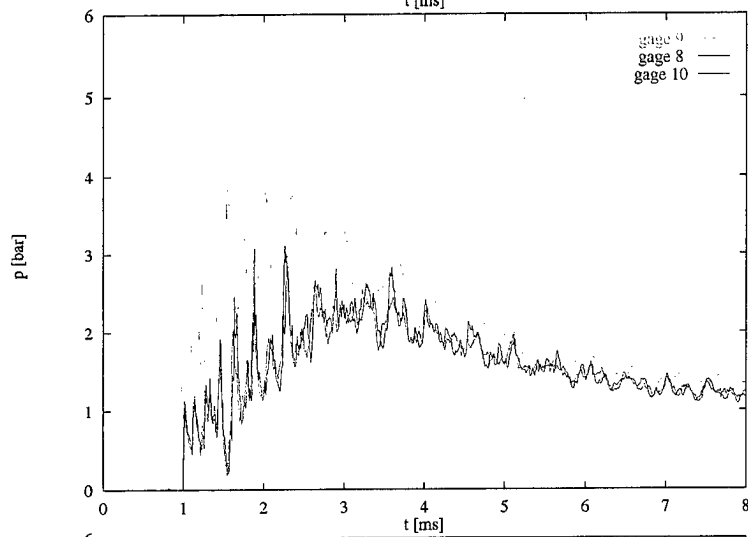


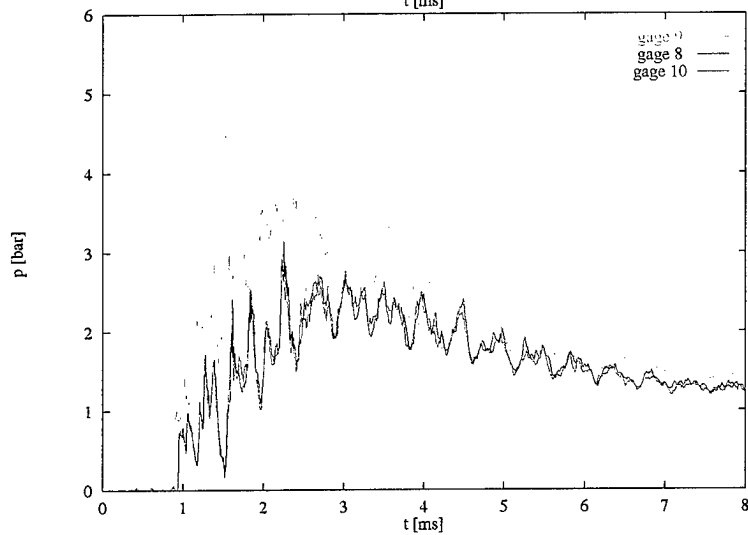
Figure 74. Ensemble-averaged overpressure impulse at gage 9 for three different charge positions. (yellow: confidence bandwidth of standard experiments).



a) Central Position

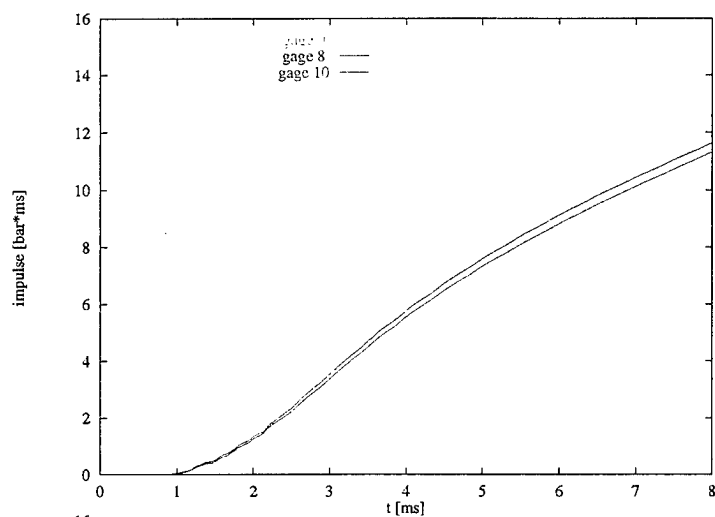


b) Lower Left Corner

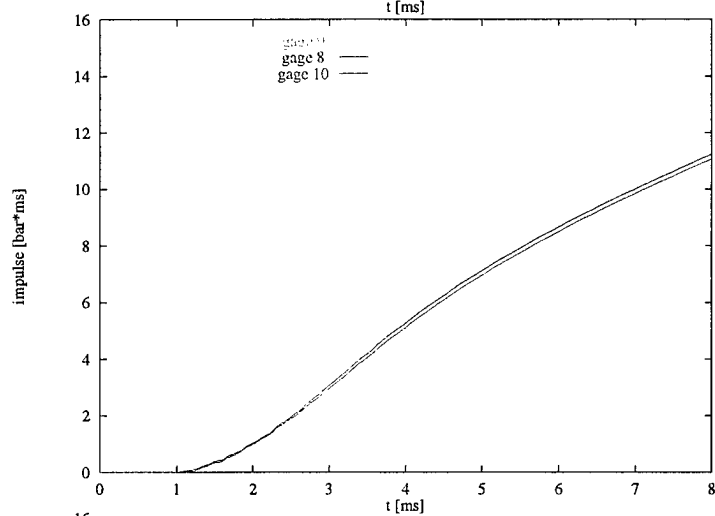


c) Upper Right Corner

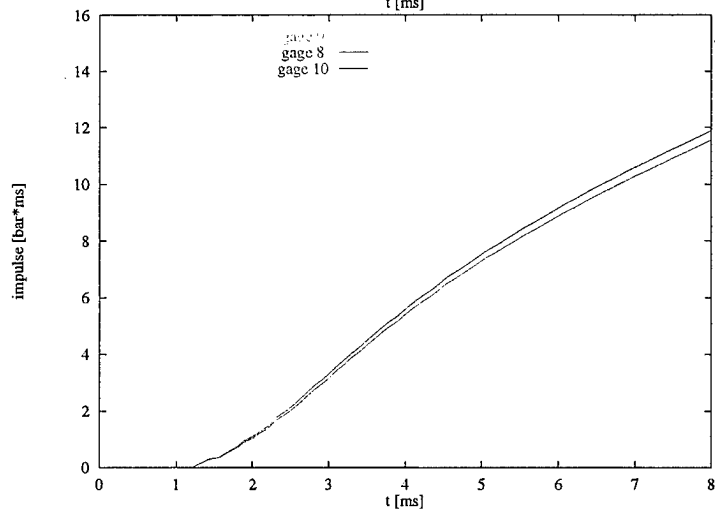
Figure 75. Ensemble-averaged pressure-time histories. Comparison of gage 8,9 and 10 for different charge locations.



a) Central Position

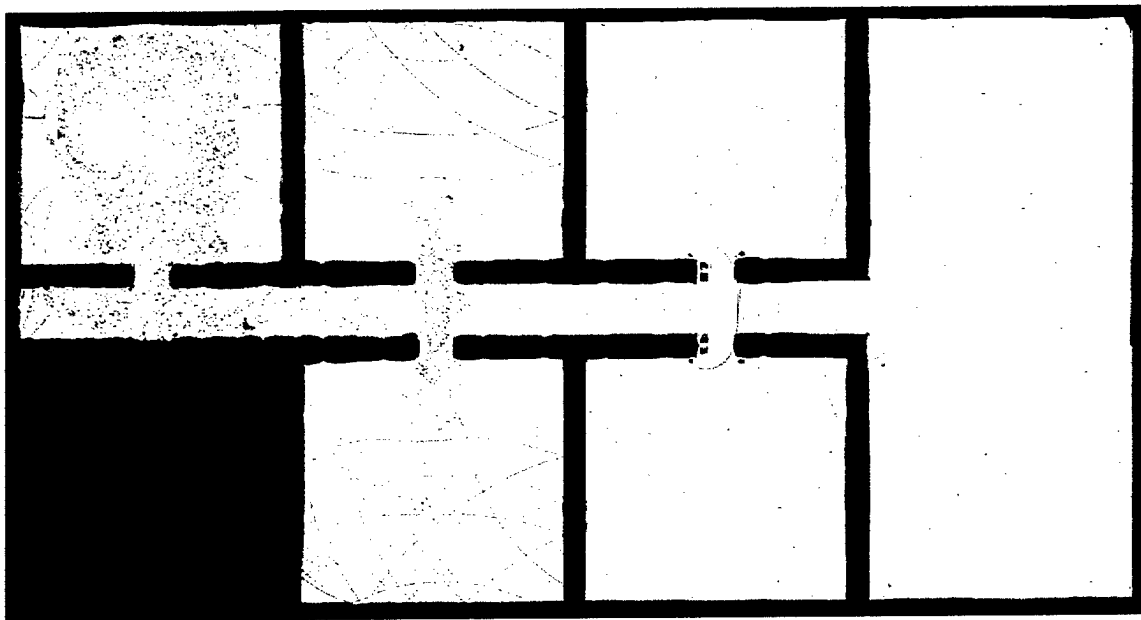


b) Lower Left Corner

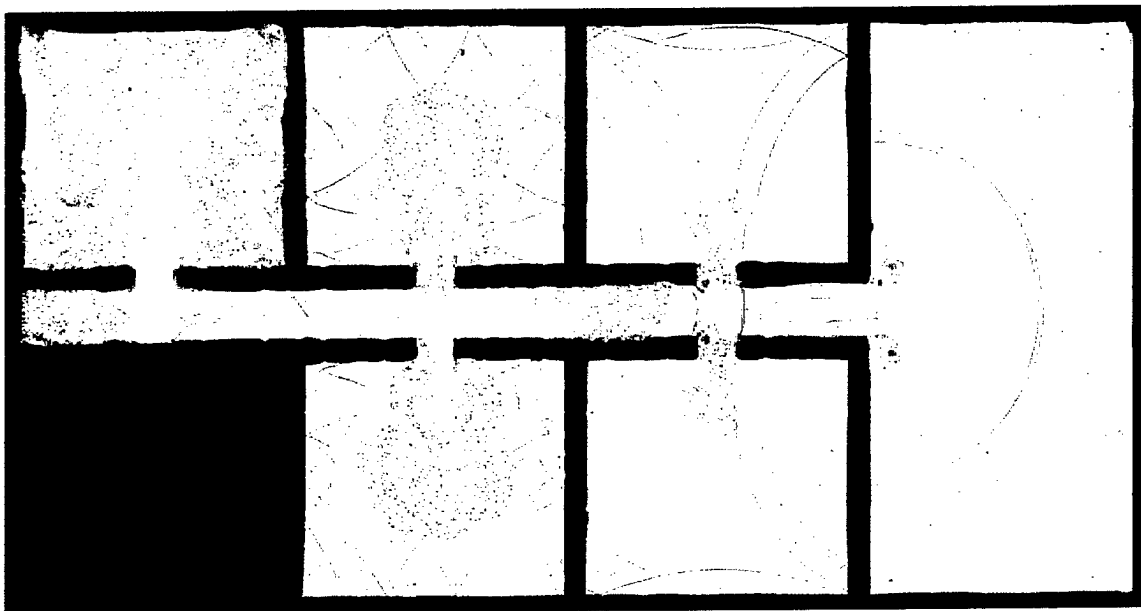


c) Upper Right Corner

Figure 76. Ensemble-averaged overpressure impulse histories. Comparison of gage 8,9 and 10 for different charge locations.

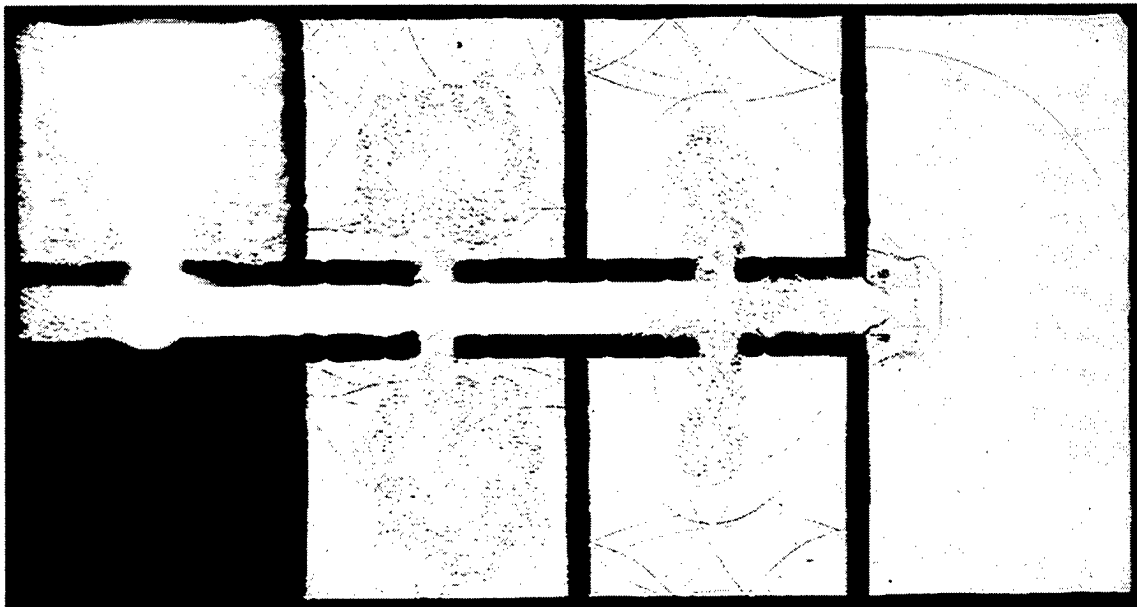


a) $W = 0.06$ g NP (test 15422)



b) $W = 0.20$ g NP (test 15421)

Figure 77. Influence of the charge weight on the wave propagation; $\Delta t = 900 \mu\text{s}$.

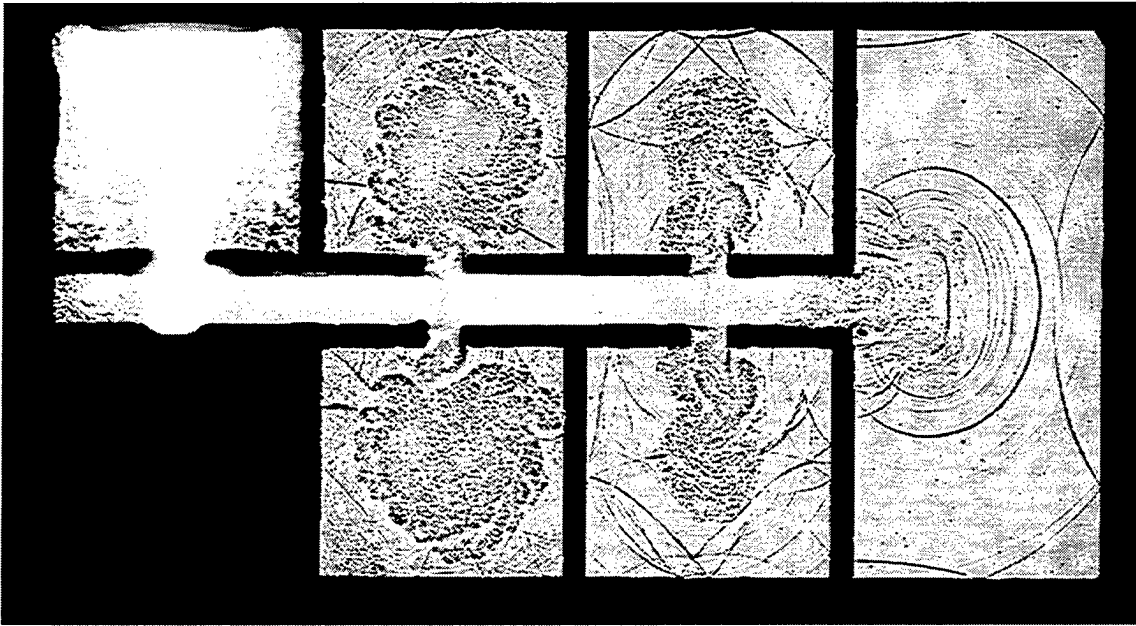


c) $W = 0.35$ g NP (test 15419)

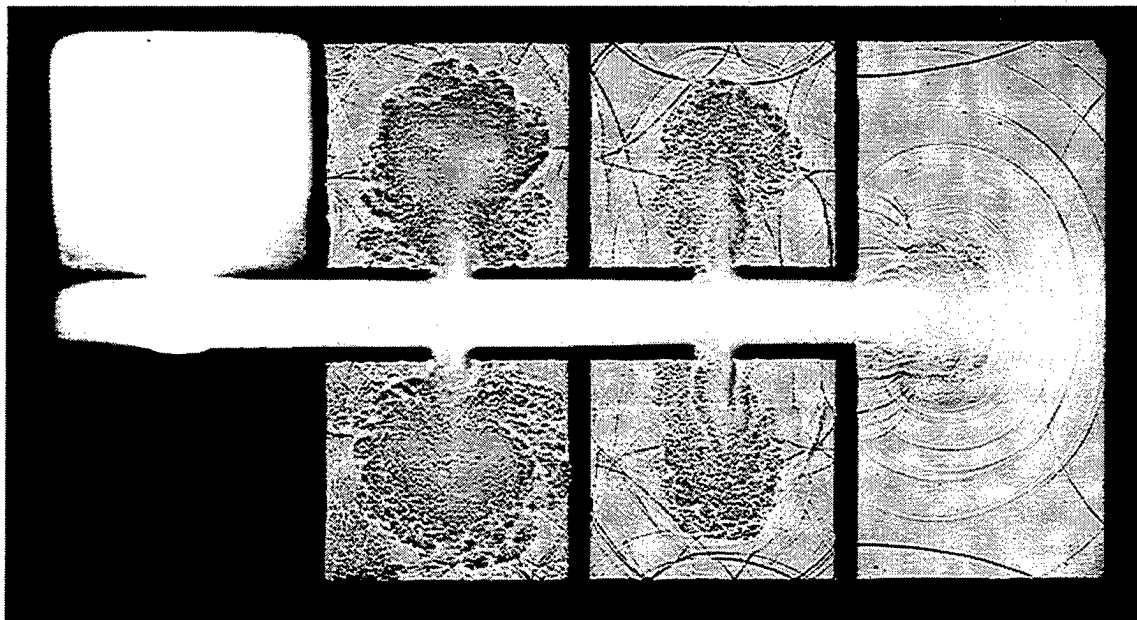


d) $W = 0.50$ g NP (test 15418)

Figure 77. Influence of the charge weight on the wave propagation; $\Delta t = 900 \mu s$.
(Continued)



a) $W = 0.50$ g NP (test 15431)



b) $W = 0.52$ g NP + 0.06 g Al (test 15432)

Figure 78. Influence of an Al-admixture to the NP-charge; $\Delta t = 900 \mu s$.



c) $W = 0.46 \text{ g NP} + 0.09 \text{ g Al}$ (test 15434)



d) $W = 0.48 \text{ g NP} + 0.10 \text{ g Al}$ (test 15433)

Figure 78. Influence of an Al-admixture to the NP-charge; $\Delta t = 900 \mu\text{s}$. (Continued)

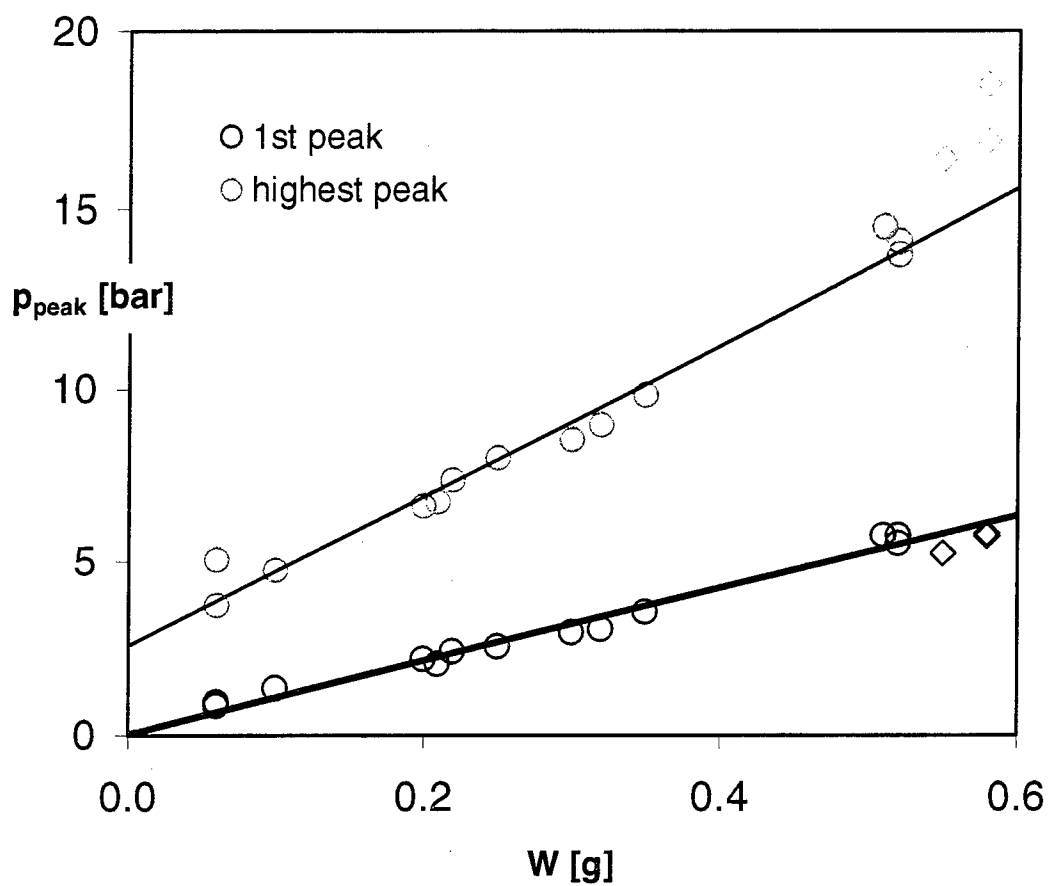
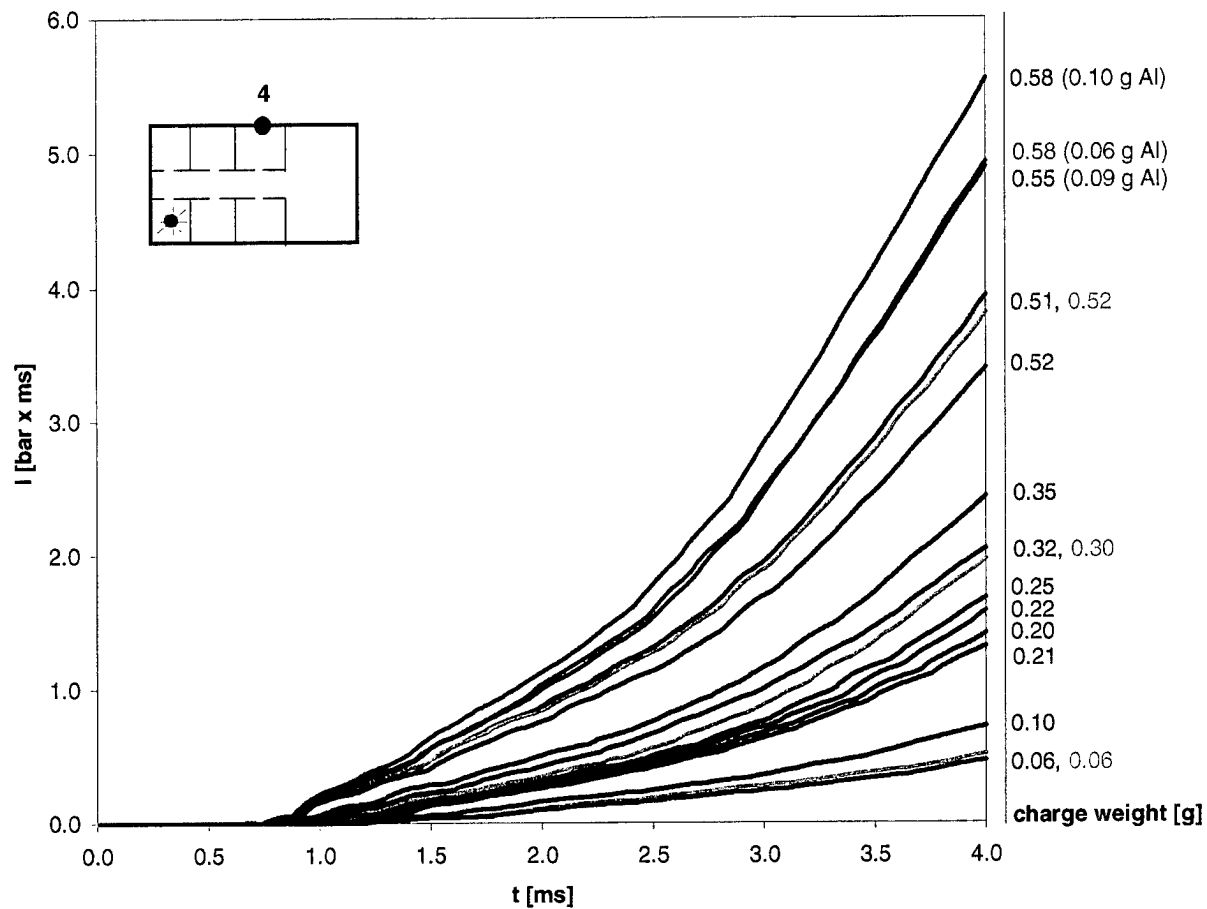
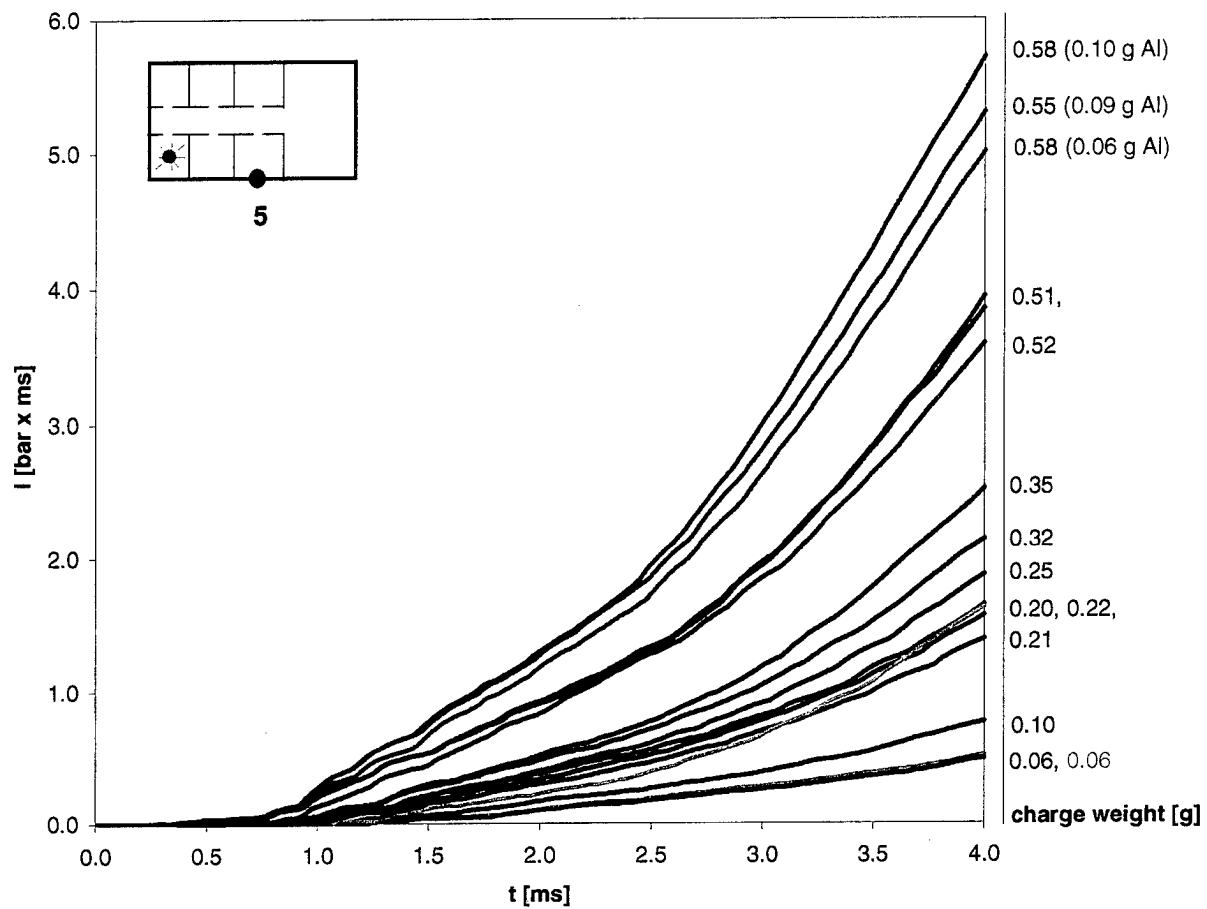


Figure 79. Peak values of the overpressure records at gage 1 as a function of charge weight (squares denote values from the three charges containing aluminum).



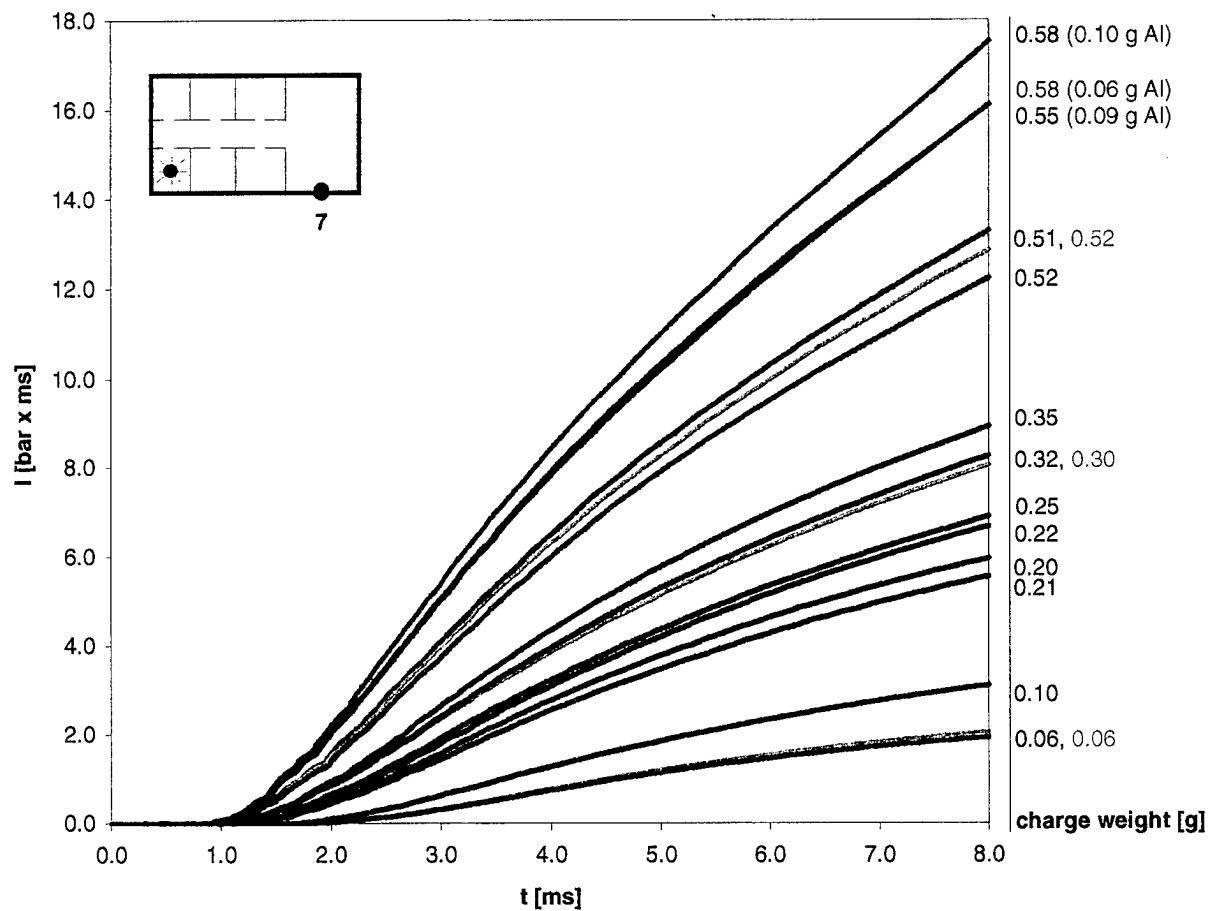
a) Gage Position 4

Figure 80. Impulse-time histories for different charge weights. Results for charges with an Al admixture are shown in red.



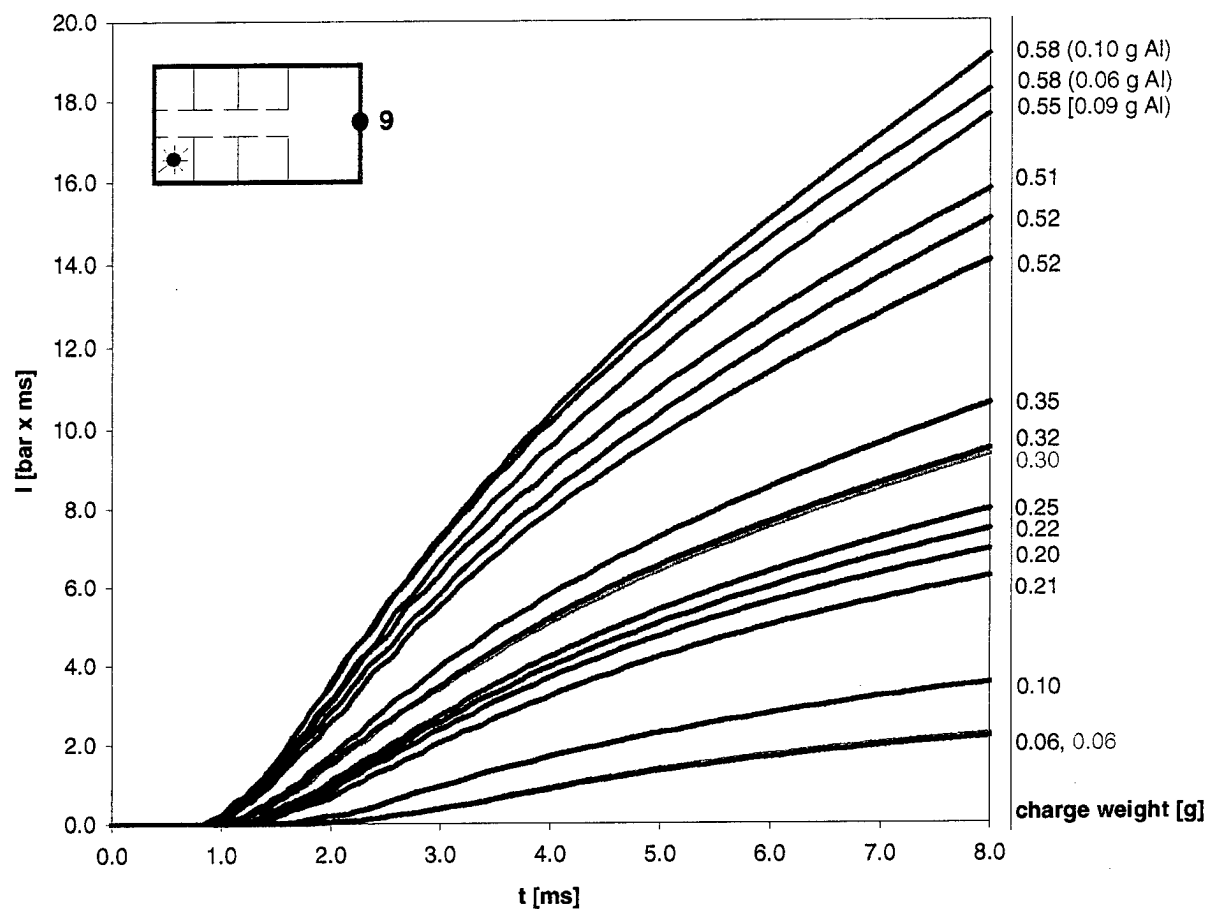
b) Gage Position 5

Figure 80. Impulse-time histories for different charge weights. Results for charges with an Al admixture are shown in red. (Continued)



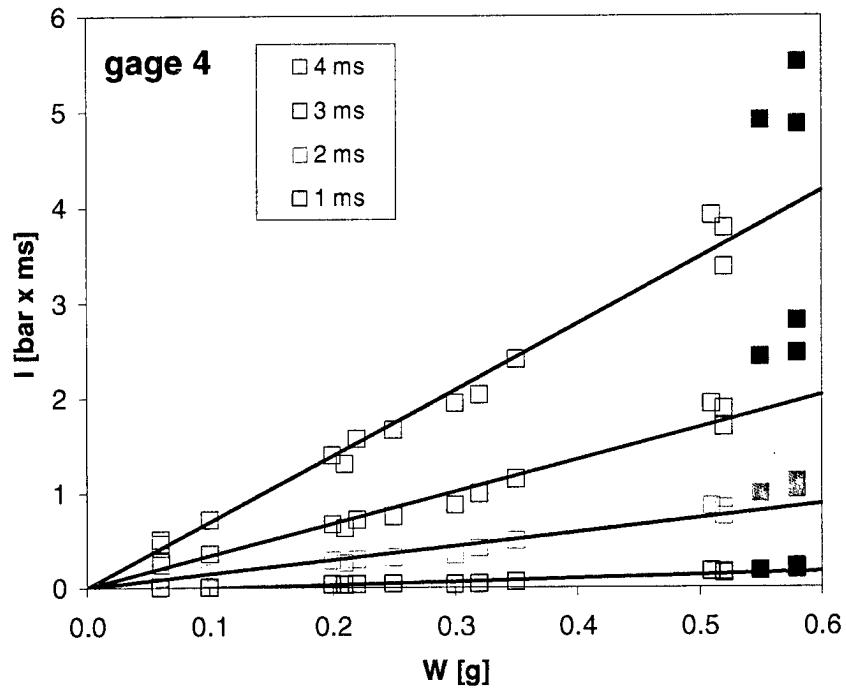
a) Gage Position 7

Figure 81. Impulse-time histories for different charge weights. Results for charges with an Al admixture are shown in red.

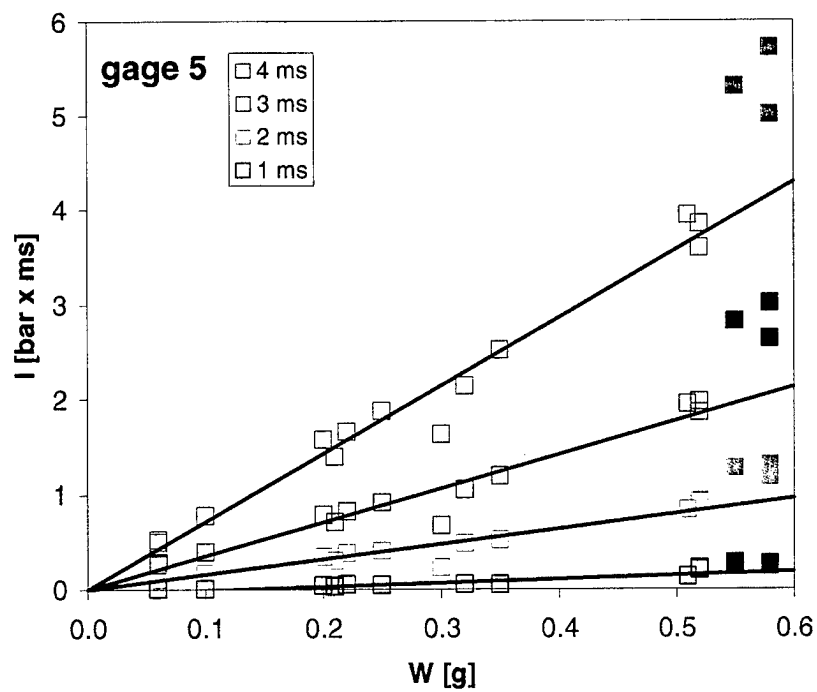


b) Gage Position 9

Figure 81. Impulse-time histories for different charge weights. Results for charges with an Al admixture are shown in red. (Continued)

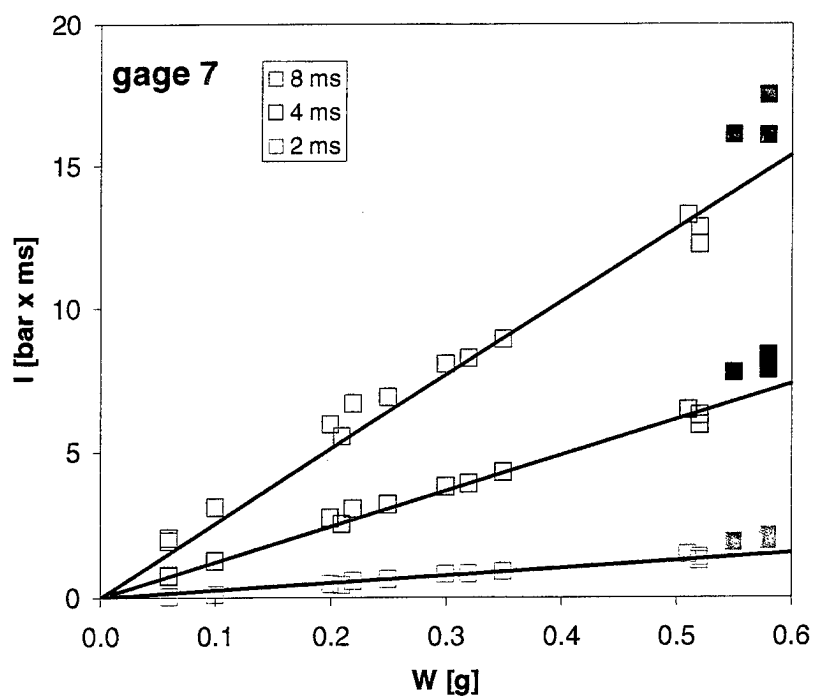


a) Gage Position 4

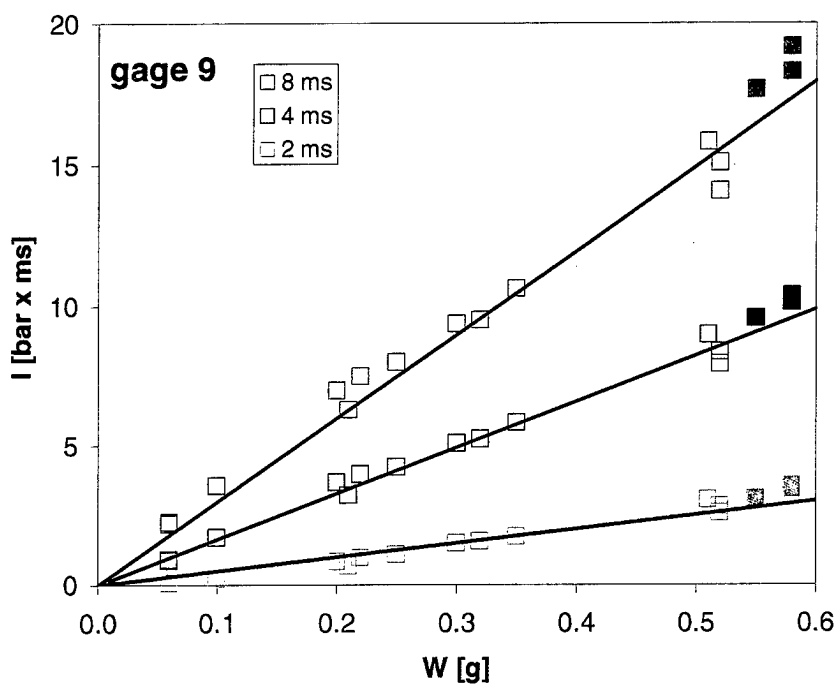


b) Gage position 5

Figure 82. Impulses as function of the charge weight after 1ms, 2ms, 3ms and 4ms resp.

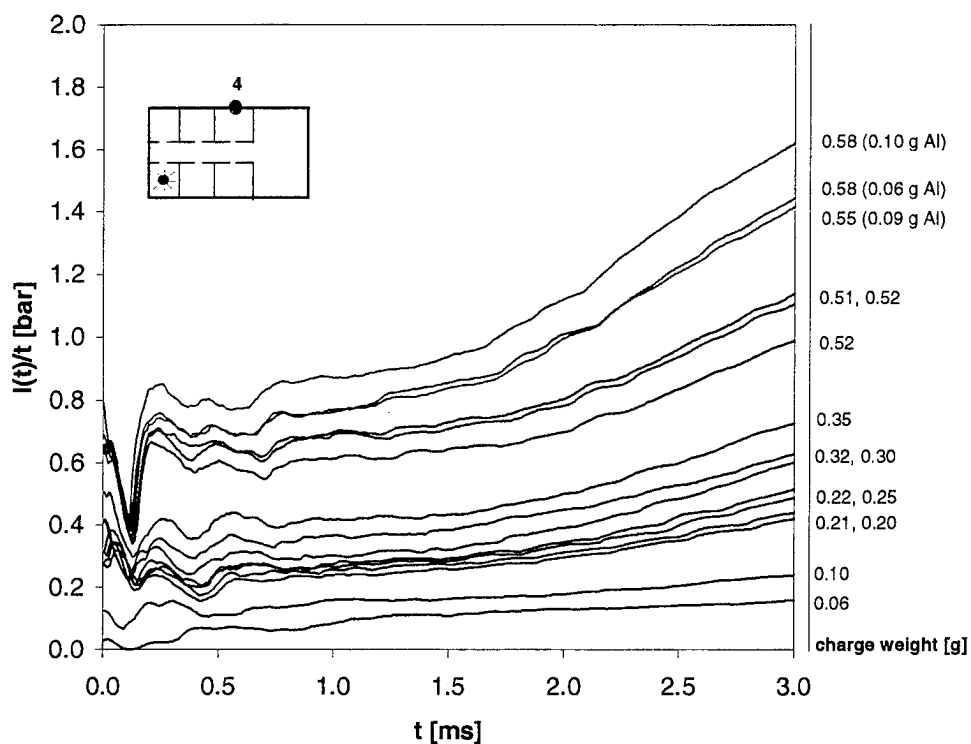


a) Gage Position 7

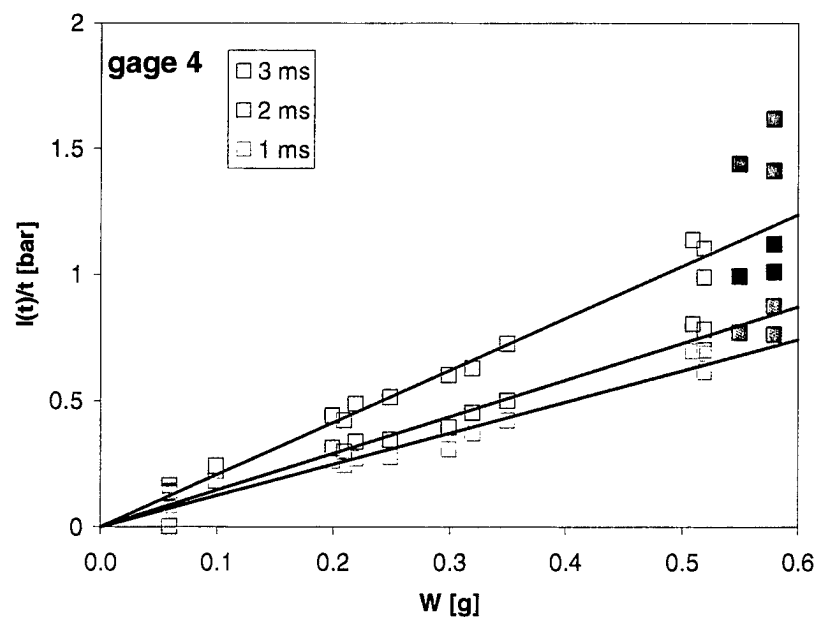


b) Gage Position 9

Figure 83. Impulses as function of the charge weight after 2ms, 4ms and 8ms resp.

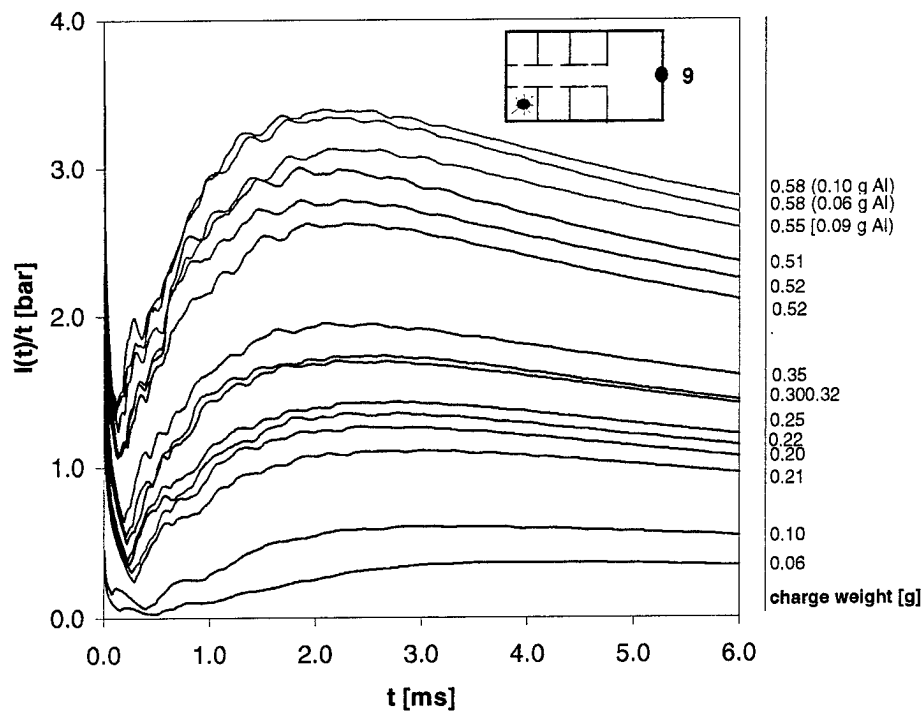


a) Time dependence for different charge weights.

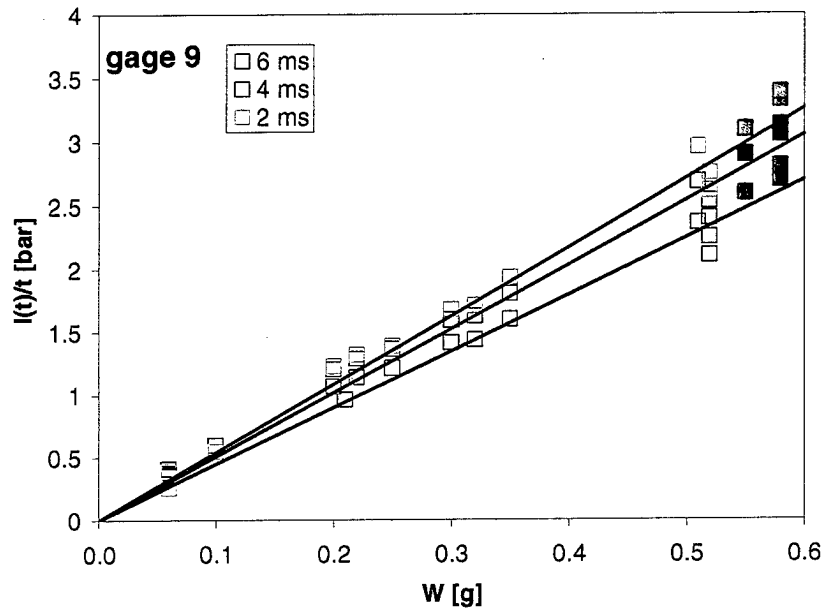


b) Dependence from charge weight at three different instants (filled symbols denote the values from Al-containing charges).

Figure 84. Time-averaged overpressure $I(t)/t$ at gage 4.



a) Time dependence for different charge weights.



b) Dependence from charge weight at three different instants (filled symbols denote the values from Al-containing charges).

Figure 85. Time-averaged overpressure $I(t)/t$ at gage 9.

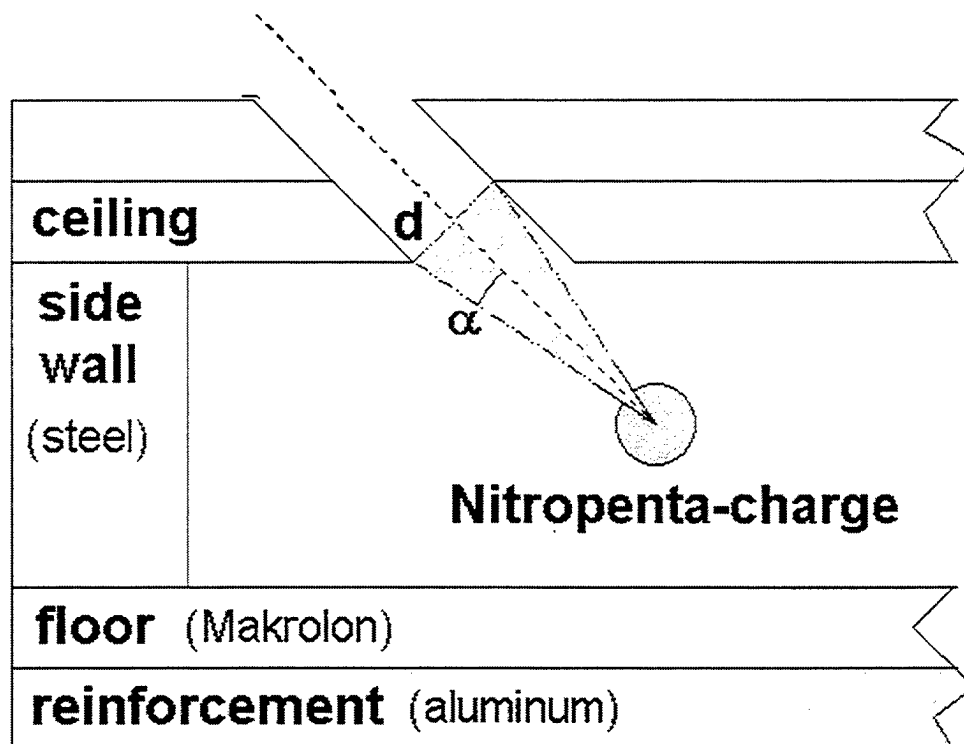
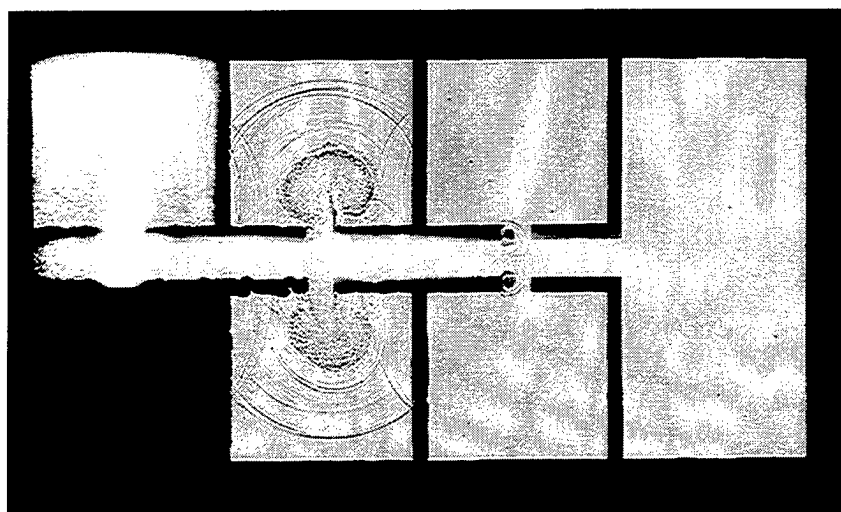


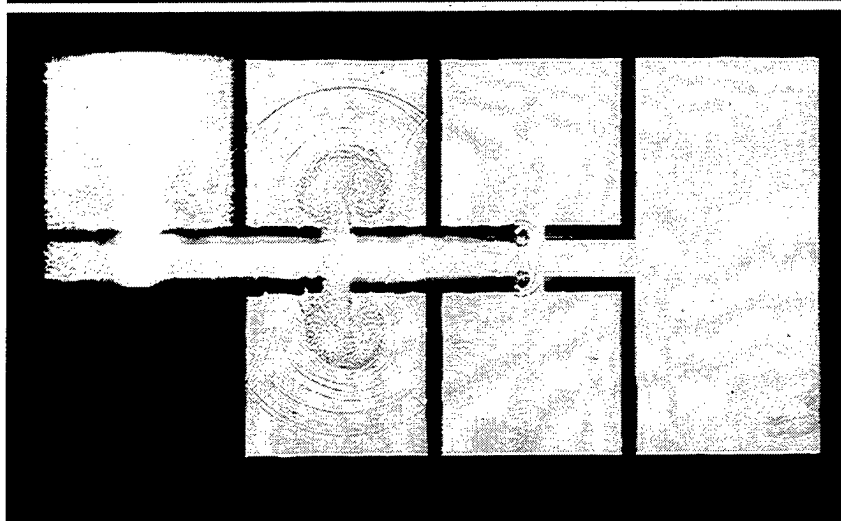
Figure 86. Schematic sketch of the bore hole arrangement used in the test series on the influence of venting holes. Variation of the diameter:

d [mm]	α
8	7°
15	12°
20	15°
25	17°

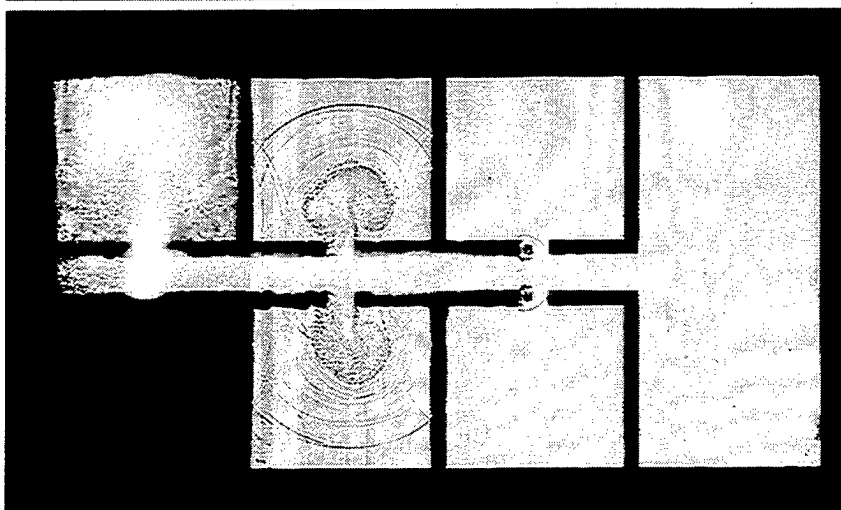
Configuration for all experiments: 0.5-g Nitropenta charge centered in detonation chamber.



a) Hole diameter 0 mm
(Test: 15825)



b) Hole diameter 8 mm
(Test: 15287)



c) Hole diameter 20 mm
(Test: 15291)

Figure 87. Influence of a venting hole on the blast propagation inside the scaled chamber system; $\Delta t = 450 \mu s$.

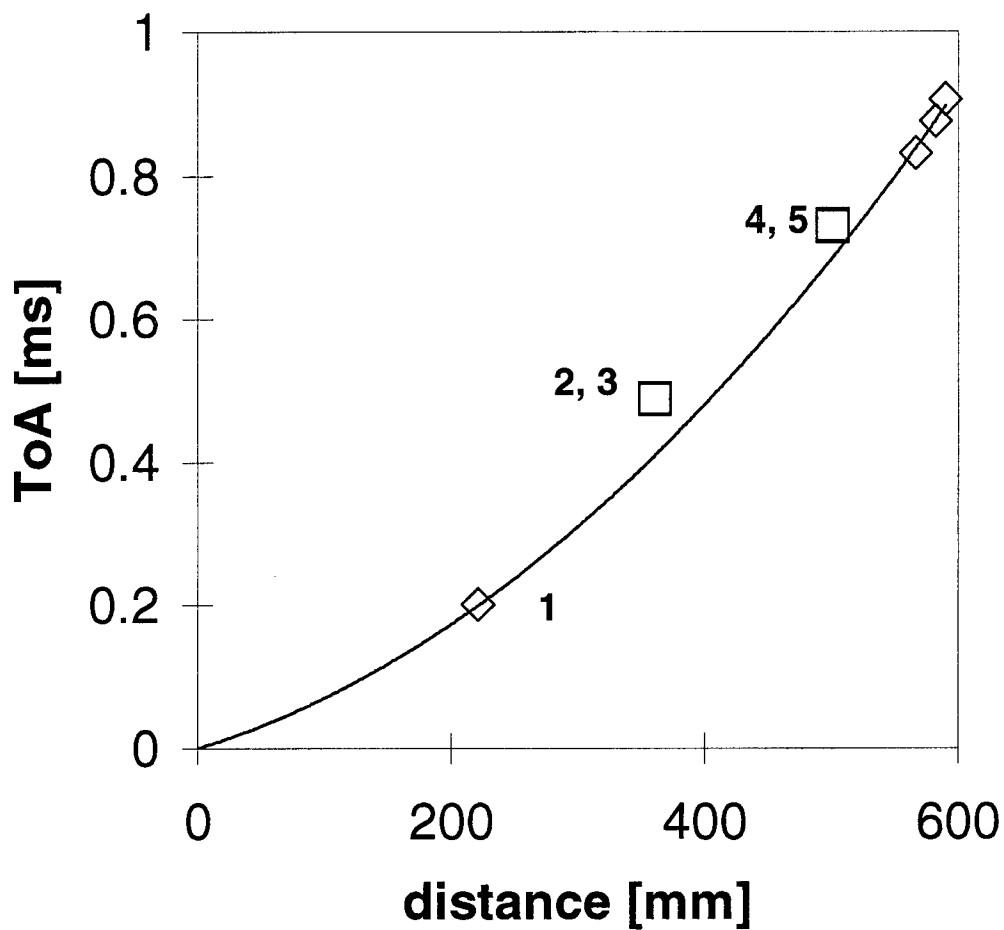


Figure 88. Wave diagram for the multi-chamber system (distance of the gages from the center of detonation in terms of a pathlength along room and corridor axes). Results from tests with different venting holes are overlaid without signifying any relevant influence of the hole onto the incident blast.

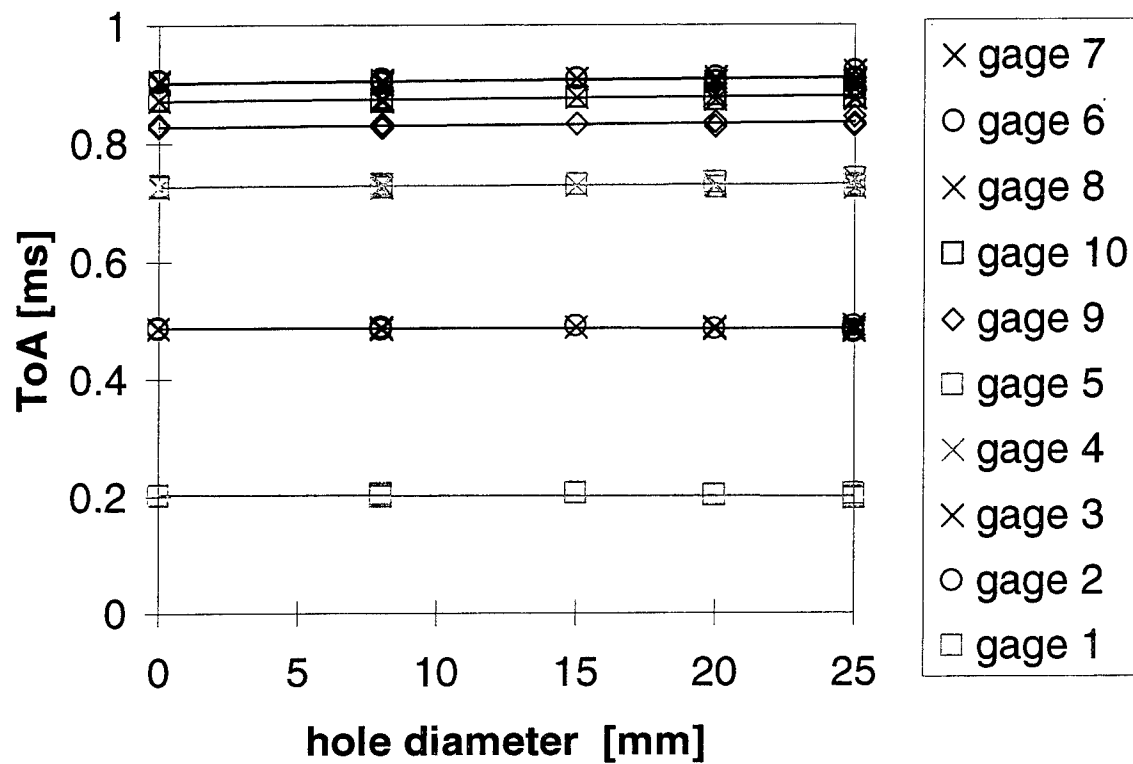


Figure 89. Time-of-arrival values for the incident blast as a function of the venting hole diameter (note that symmetrically positioned gages have nearly identical ToA-values).

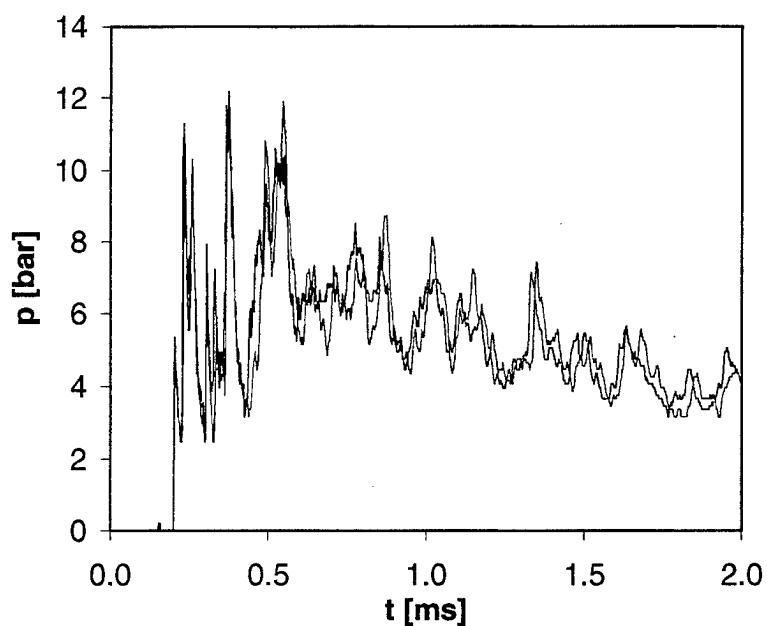
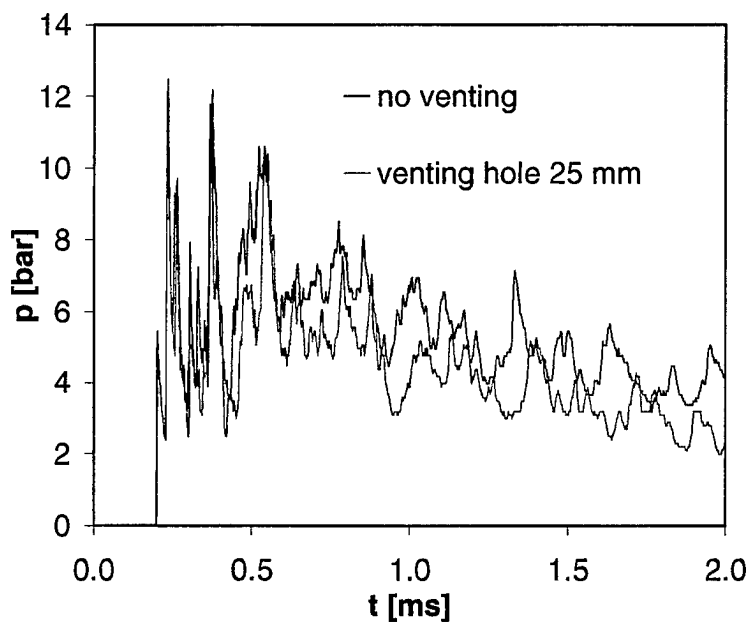
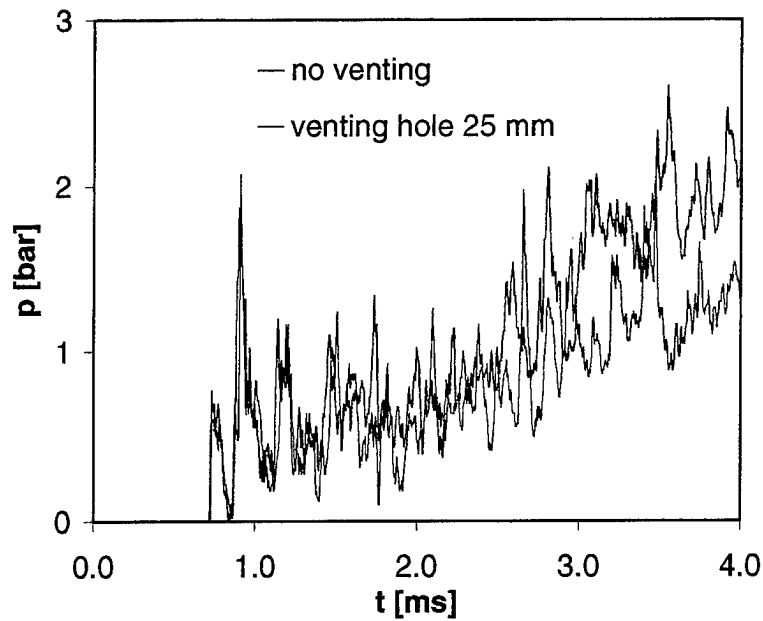


Figure 90. Comparison of two test at gage 1. Both tests in standard configuration without venting hole.

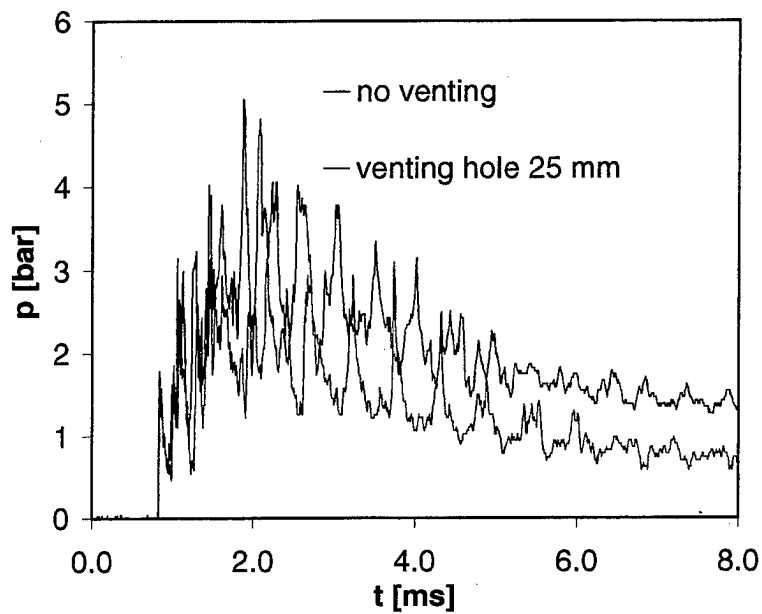


a) Gage 1

Figure 91. Comparison of a test in standard configuration to a test with 25-mm venting hole.

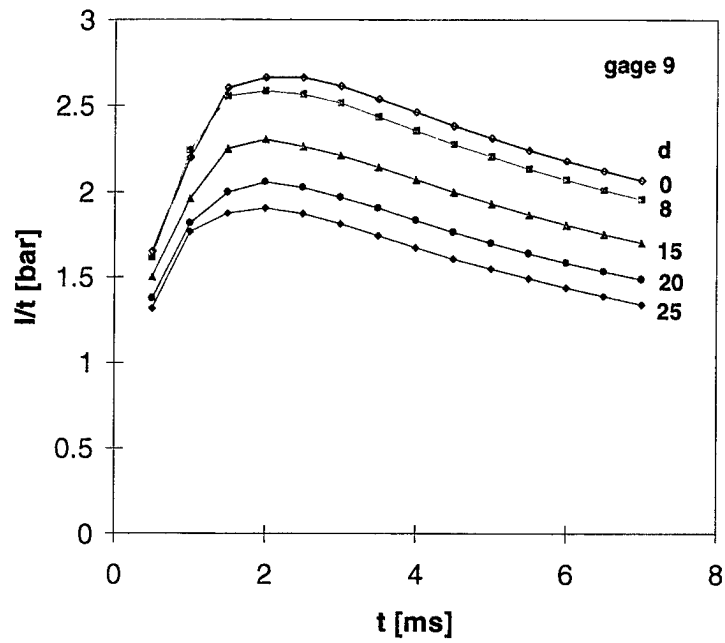


b) Gage 4 (side room branching from the corridor).

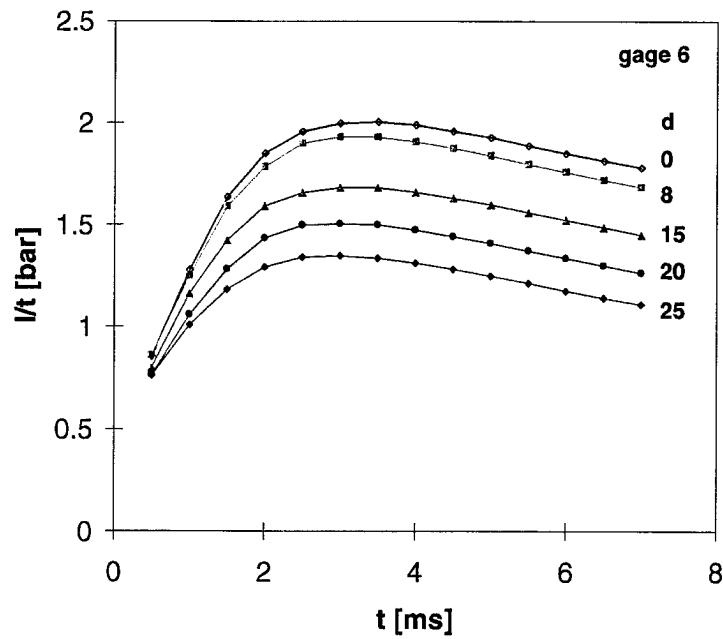


c) Gage 9 (center of the rear wall in the end chamber).

Figure 91. Comparison of a test in standard configuration to a test with 25-mm venting hole. (Continued)

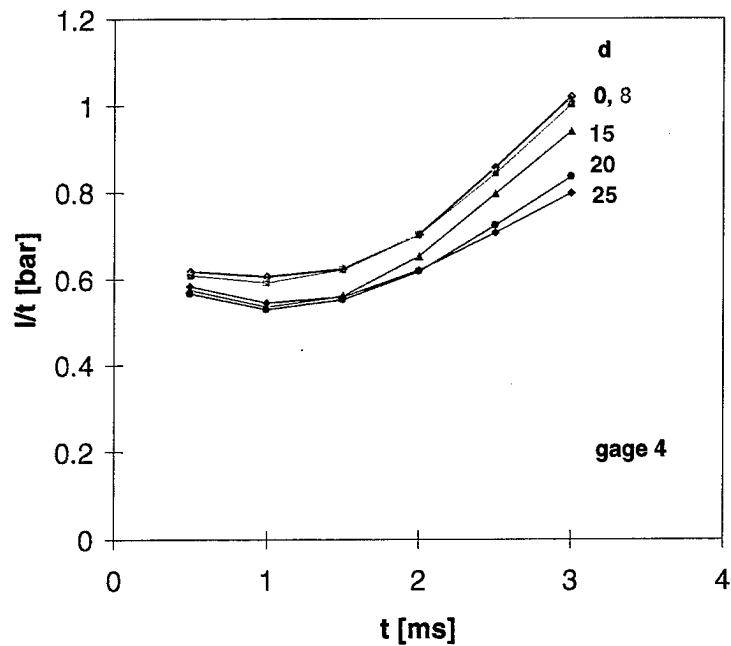


a) Gage 9

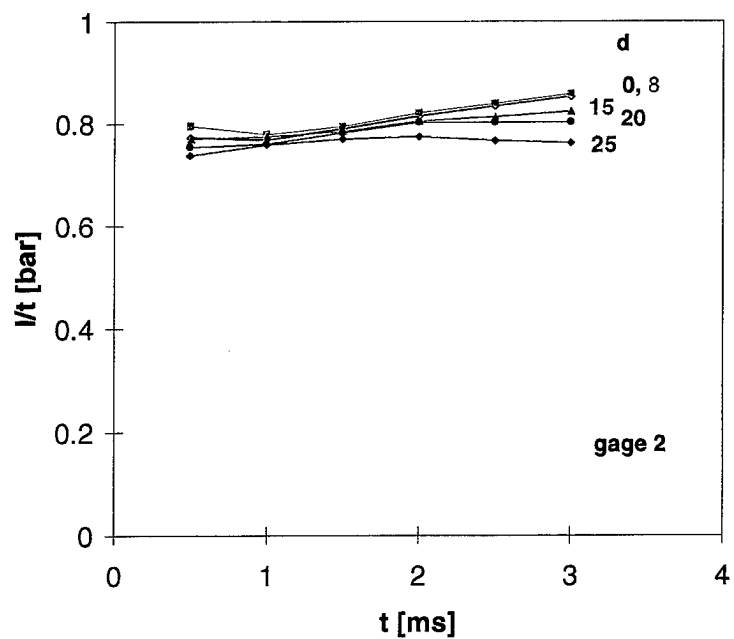


b) Gage 6

Figure 92. Time-averaged overpressure $I(t)/t$. Parameter d : diameter of the venting hole in mm.



c) Gage 4



d) Gage 2

Figure 92. Time-averaged overpressure $I(t)/t$. Parameter d: diameter of the venting hole in mm. (Continued)

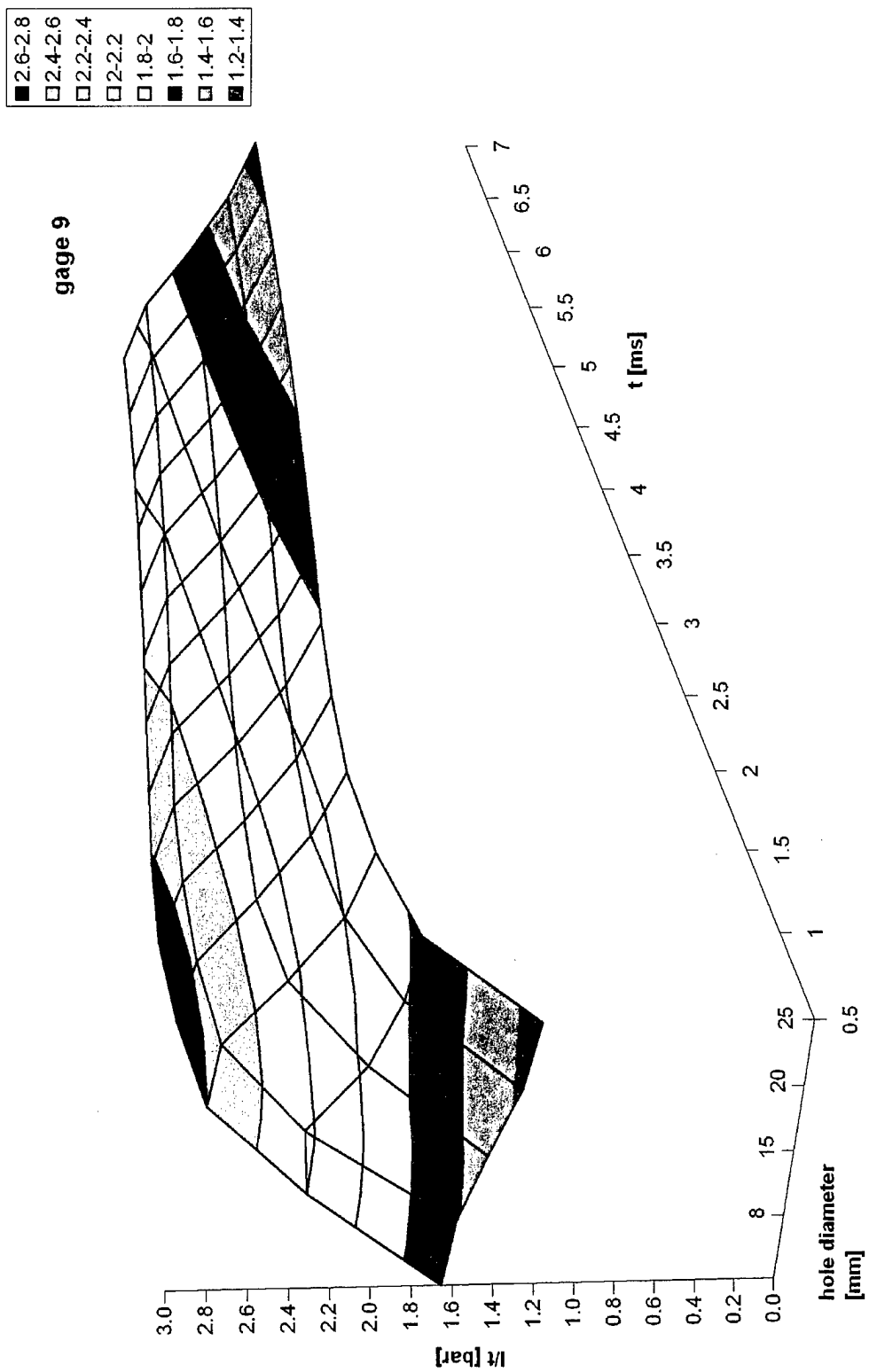
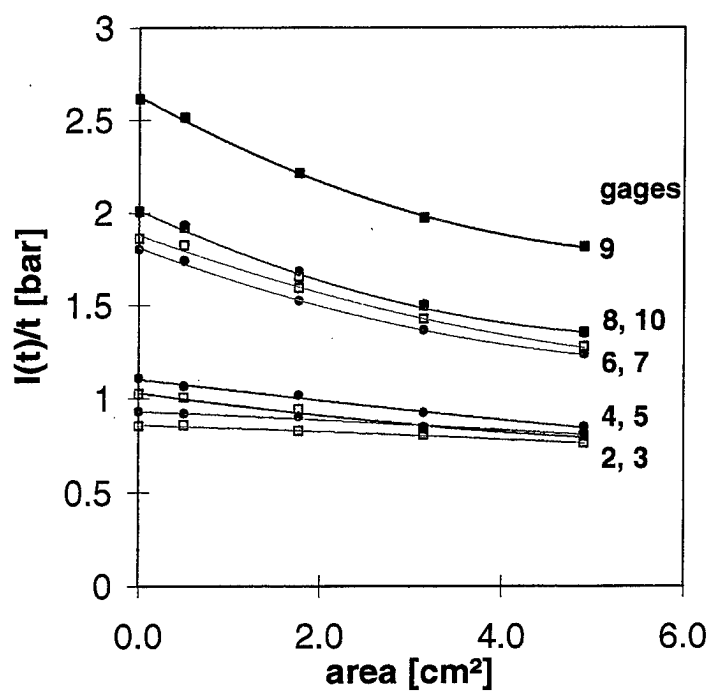
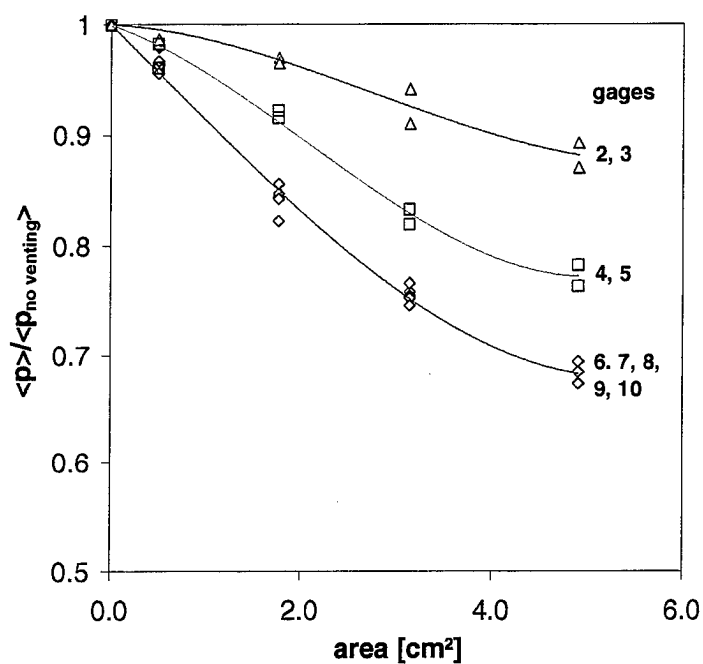


Figure 93. 3-D diagram of the average pressure-time histories at gase 9 for different venting holes.



a) Unscaled values of $I(t)/t$



b) Curves scaled with the values for the non-vented case.

Figure 94. Average pressure load $I(t)/t$ at $t = 3$ ms.

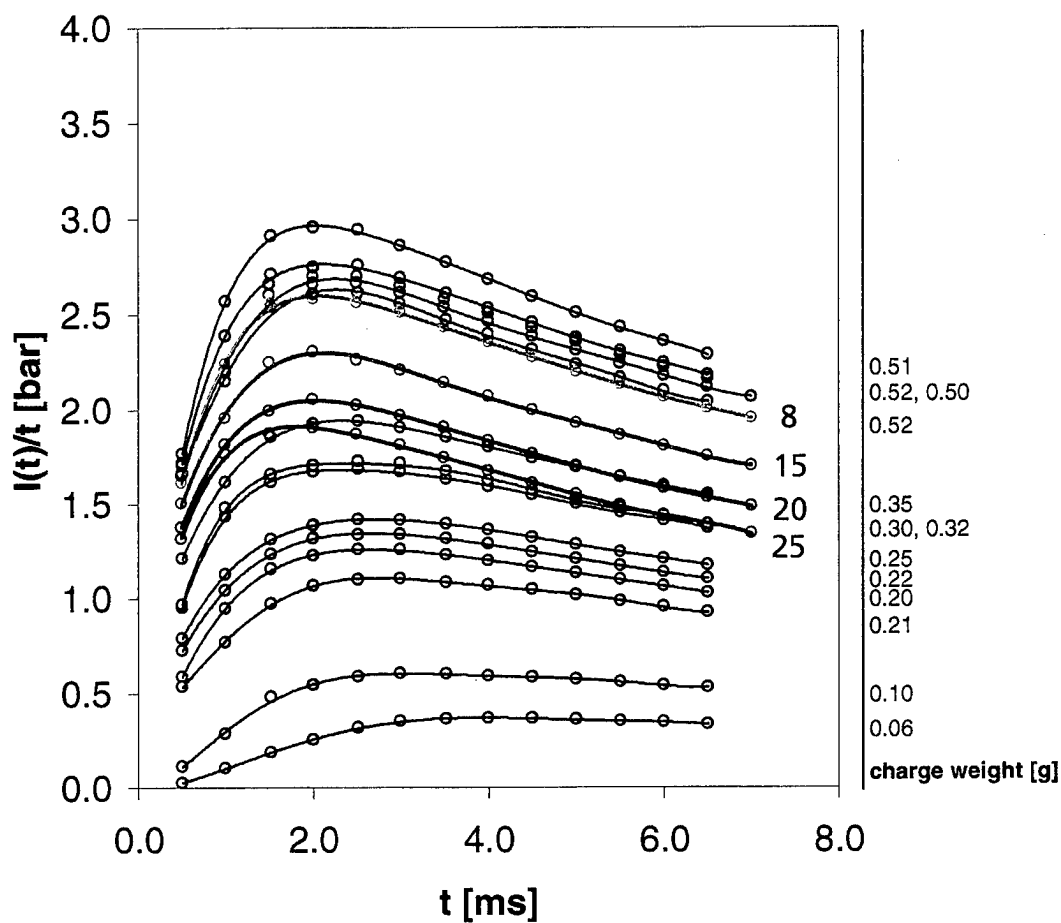
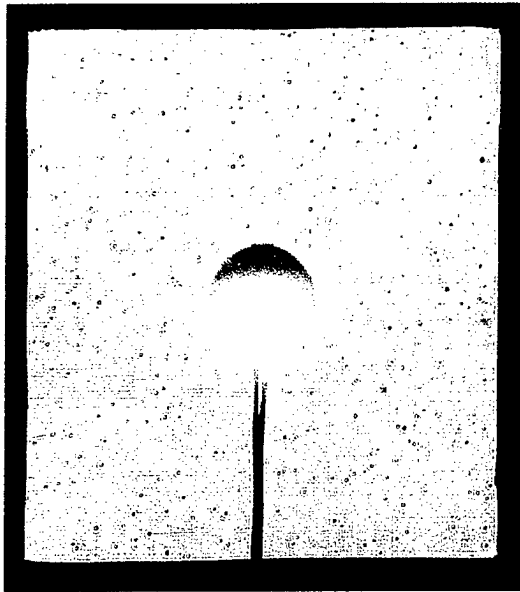
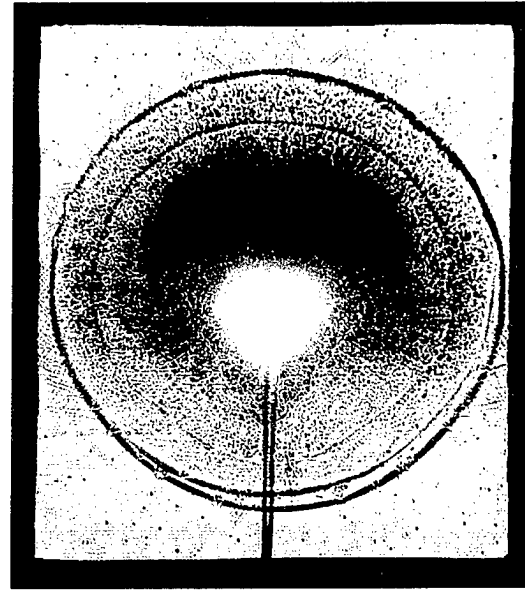


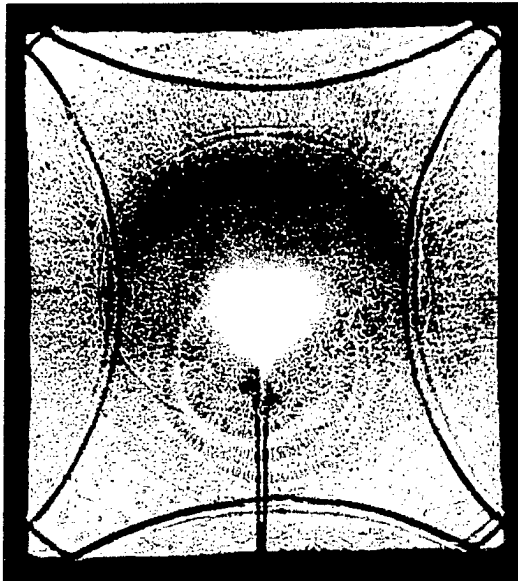
Figure 95. Average pressure loads $I(t)/t$ at gage 9. Comparison of the curves for different charge weights to those with different venting holes and a 0.5-g NP-charge (colored). The parameter labeling the colored curves is the venting hole diameter in mm.



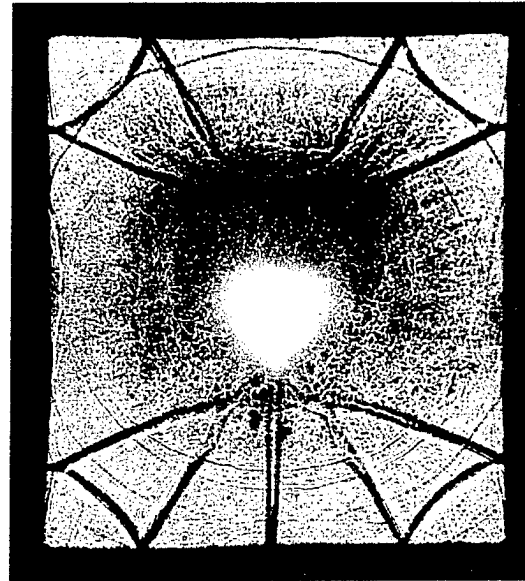
a) $\Delta t = 6.7 \mu s$



b) $\Delta t = 66.7 \mu s$

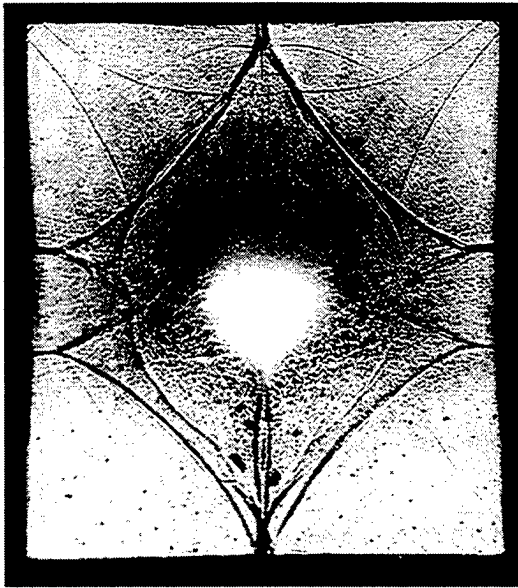


c) $\Delta t = 126.7 \mu s$

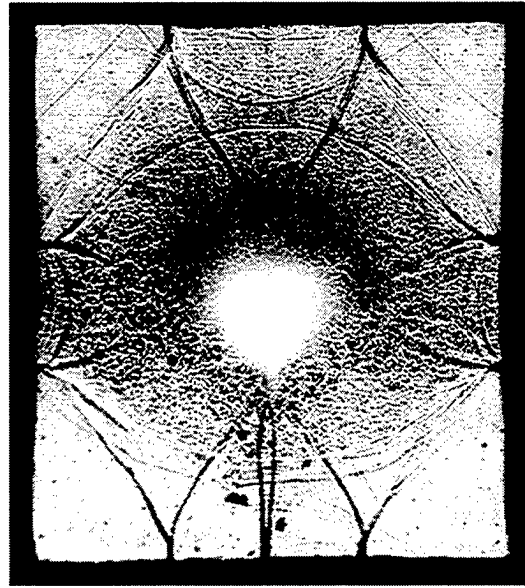


d) $\Delta t = 186.7 \mu s$

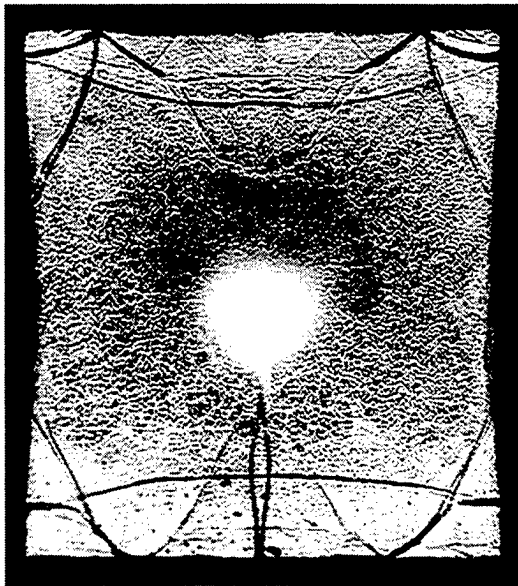
Figure 96. Shadowgraph sequence of a detonation in a closed room.
Charge: HX2 (test: 15459).



e) $\Delta t = 246.7 \mu s$



f) $\Delta t = 306.7 \mu s$

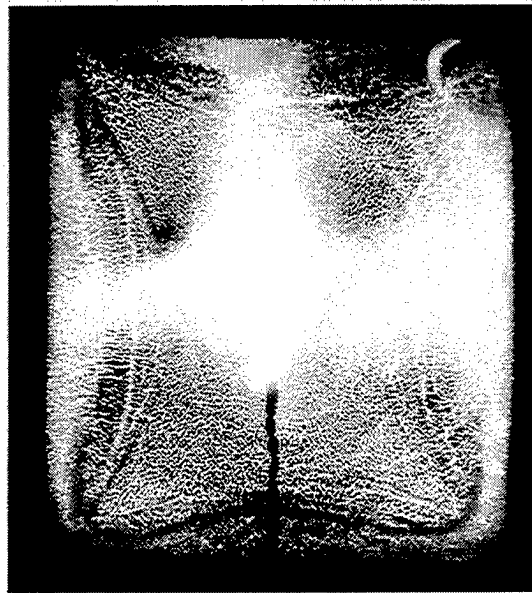


g) $\Delta t = 426.7 \mu s$

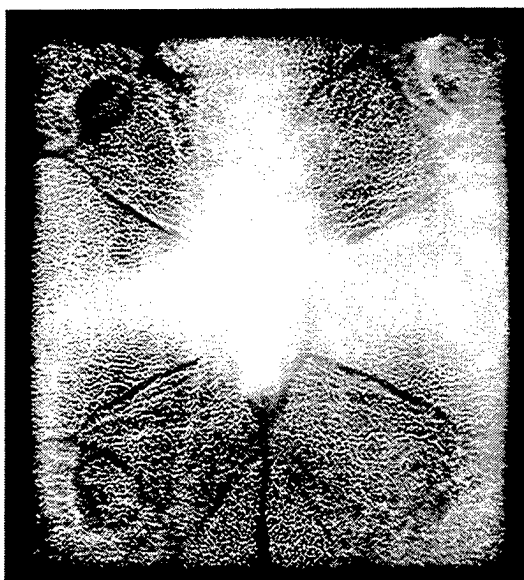
Figure 96. Shadowgraph sequence of a detonation in a closed room.
Charge HX2. (Continued)



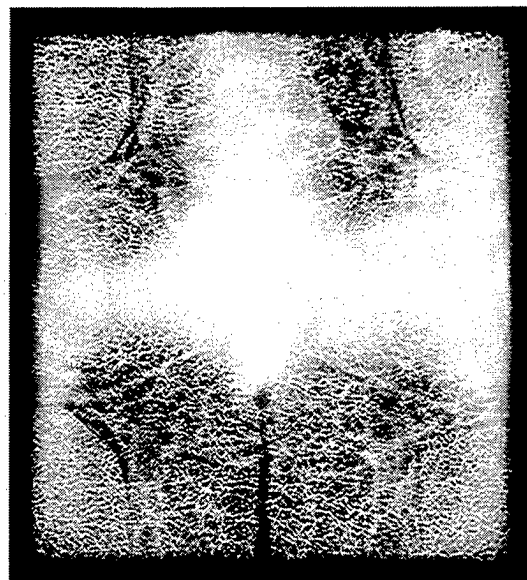
a) $\Delta t = 40.7 \mu s$



b) $\Delta t = 55.7 \mu s$

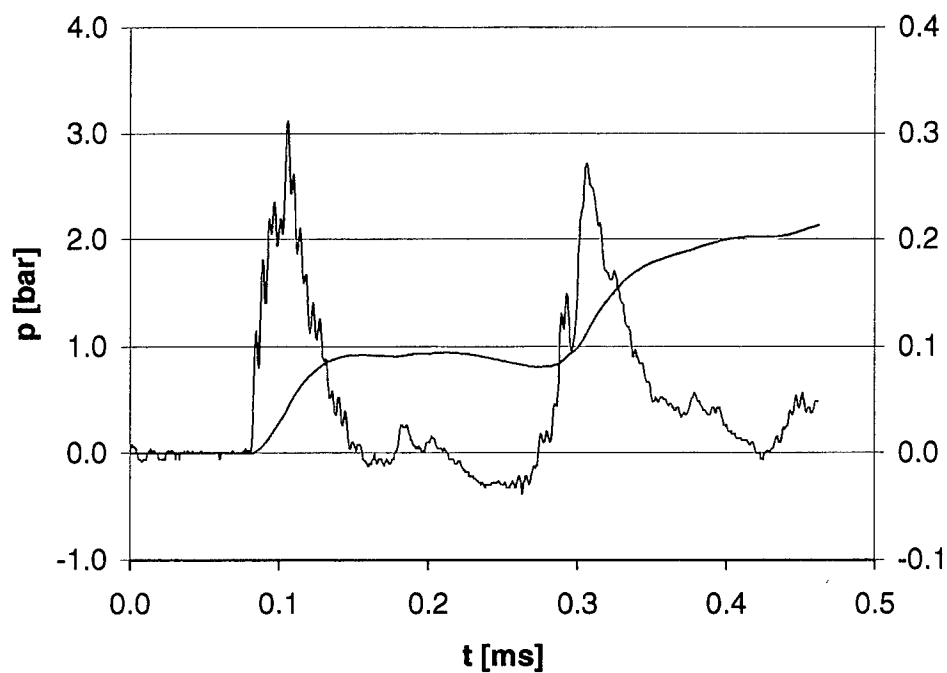


c) $\Delta t = 85.7 \mu s$

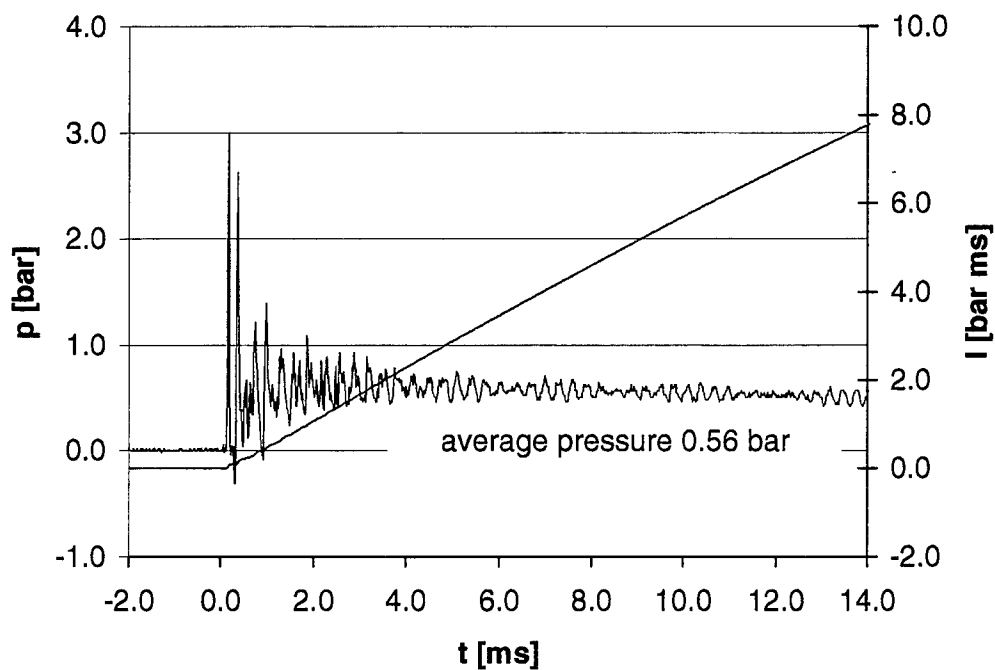


d) $\Delta t = 145.7 \mu s$

Figure 97. Shadowgraph sequence of a detonation in a closed room.
Charge: 0.18-g NP (test: 15460).

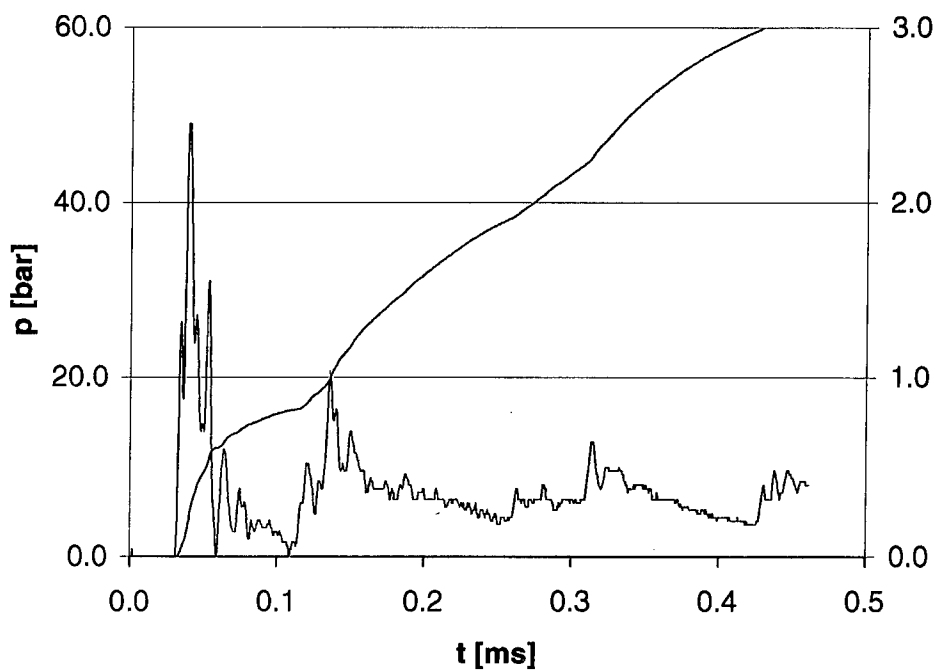


a) The first reflections

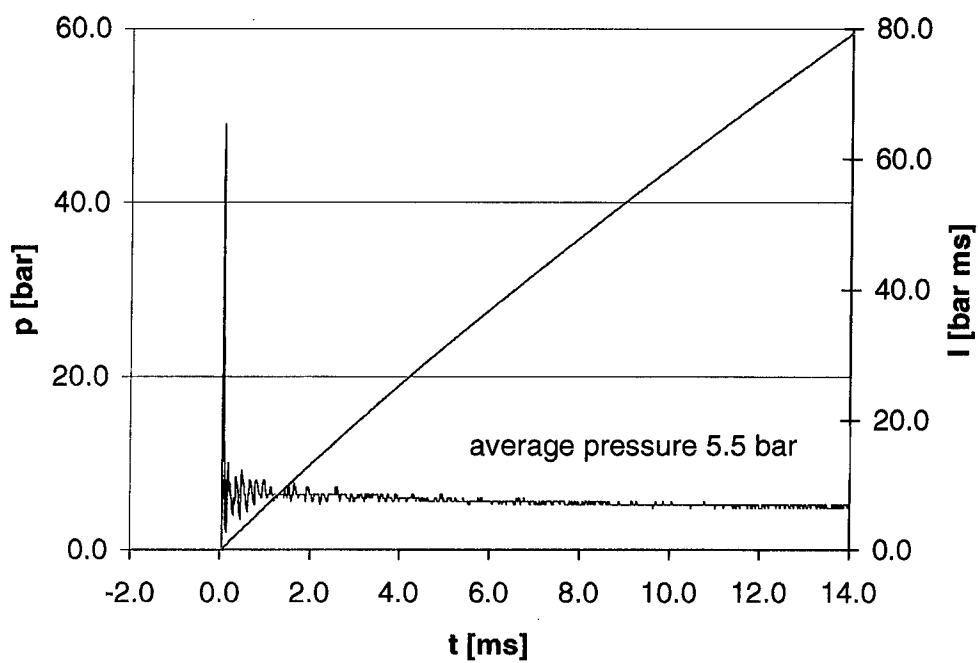


b) The development to quasistatic conditions

Figure 98. Detonation of an HX2-ignitor inside a closed chamber (test 15 459). Overpressure and overpressure impulse versus time.



a) The first reflections



b) The development to quasistatic conditions

Figure 99. Detonation of a 0.18-g NP charge inside a closed chamber (test 15460). Overpressure and overpressure impulse versus time.

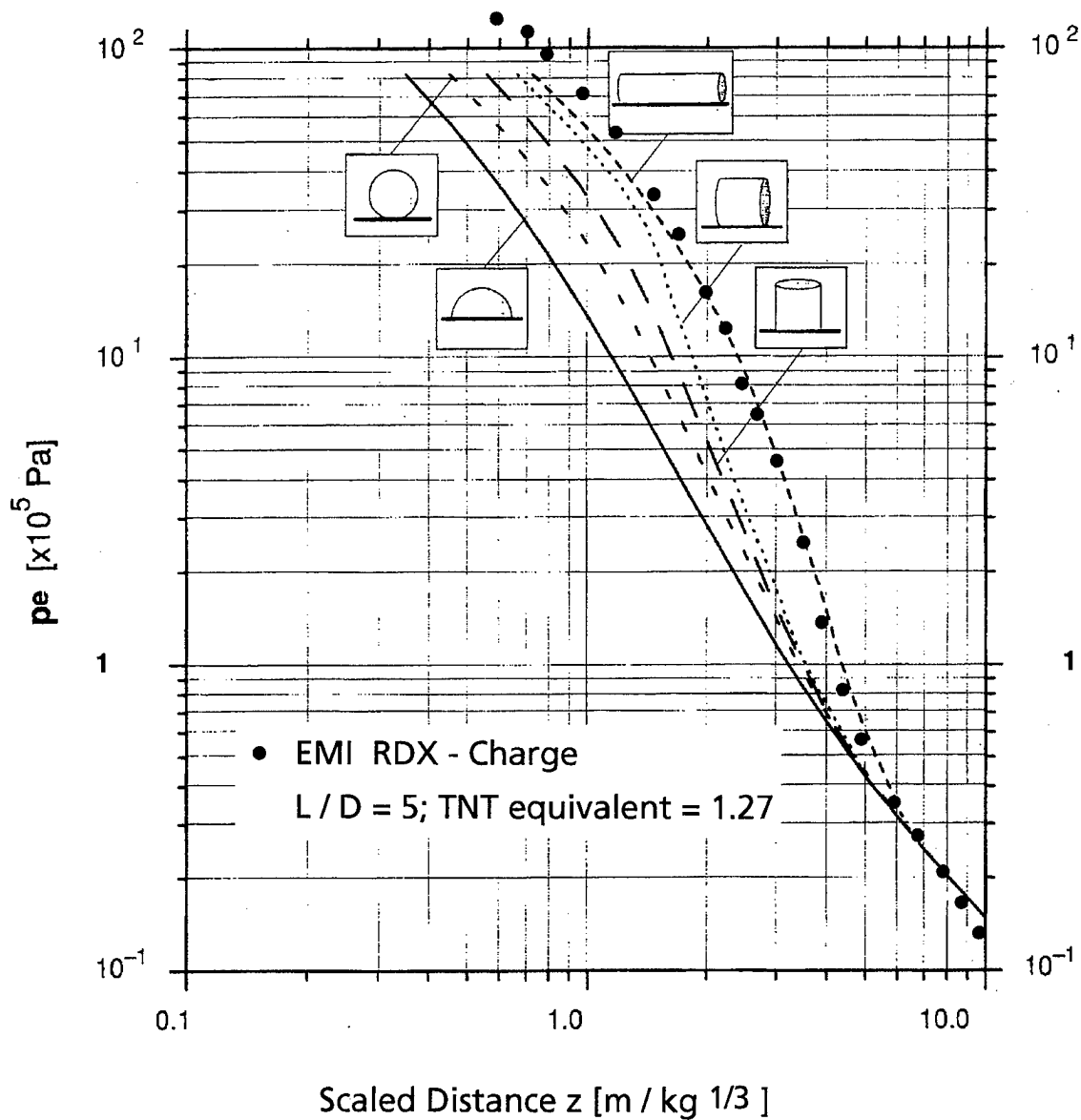


Figure 100. Peak overpressure for a TNT surface burst as a function of the charge geometry. Included are hemispherical, spherical and cylindrical charges, lying ($L/D = 1$; $L/D = 5$) and standing upright ($L/D = 1$ to 3). For cylinders, the data refer to the direction perpendicular to the longitudinal axis. (taken from [12]).

EMI data for a cylindrical RDX-charge ($L/D = 5$) are added as dots. A TNT equivalent factor of 1.27 was used.

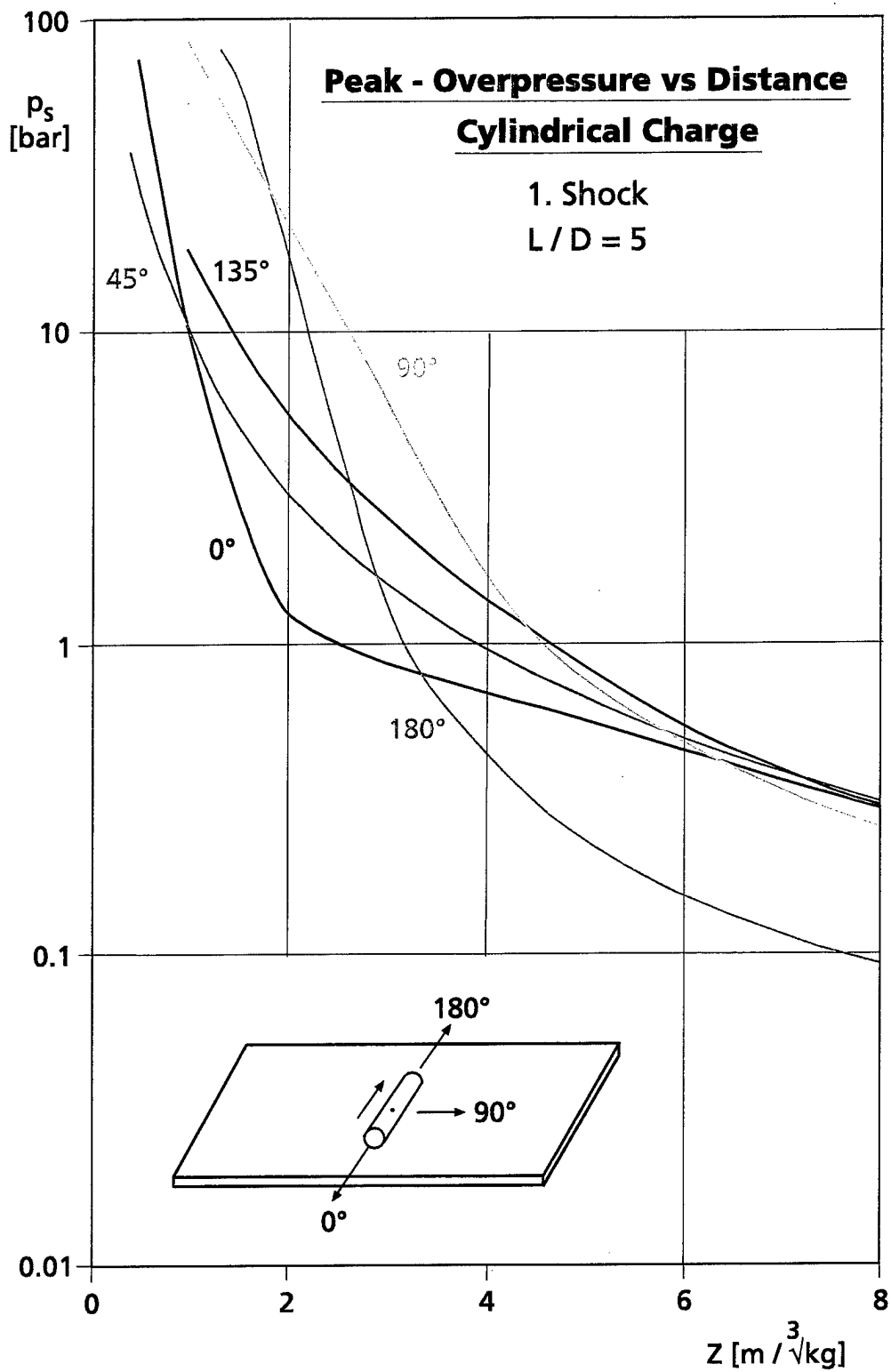


Figure 101. Peak overpressure vs distance for a bare cylindrical charge with $L/D = 5$ at a surface tangent burst.

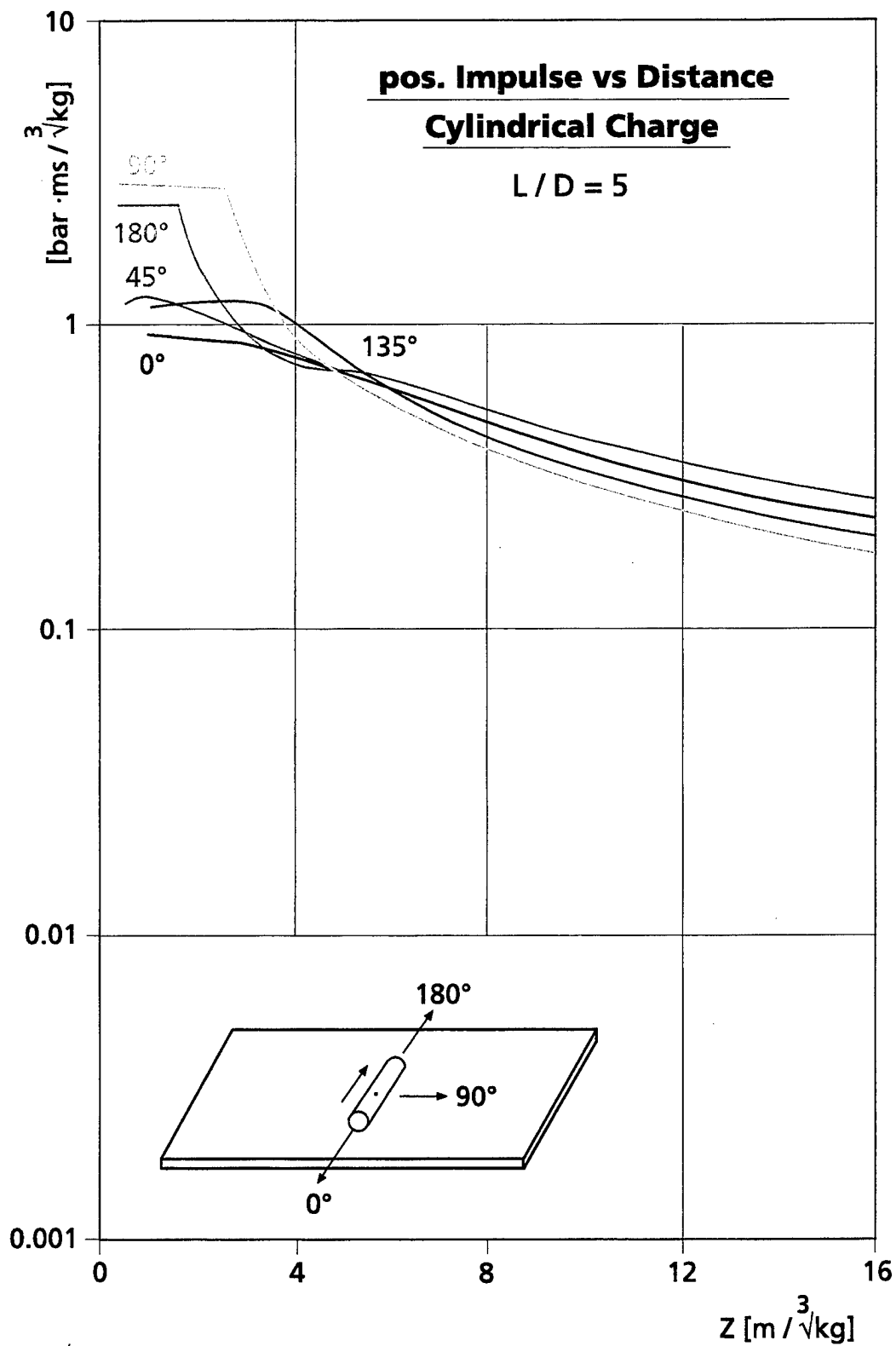


Figure 102. Positive Impulse vs distance for a bare cylindrical charge with $L/D = 5$ at a surface tangent burst.

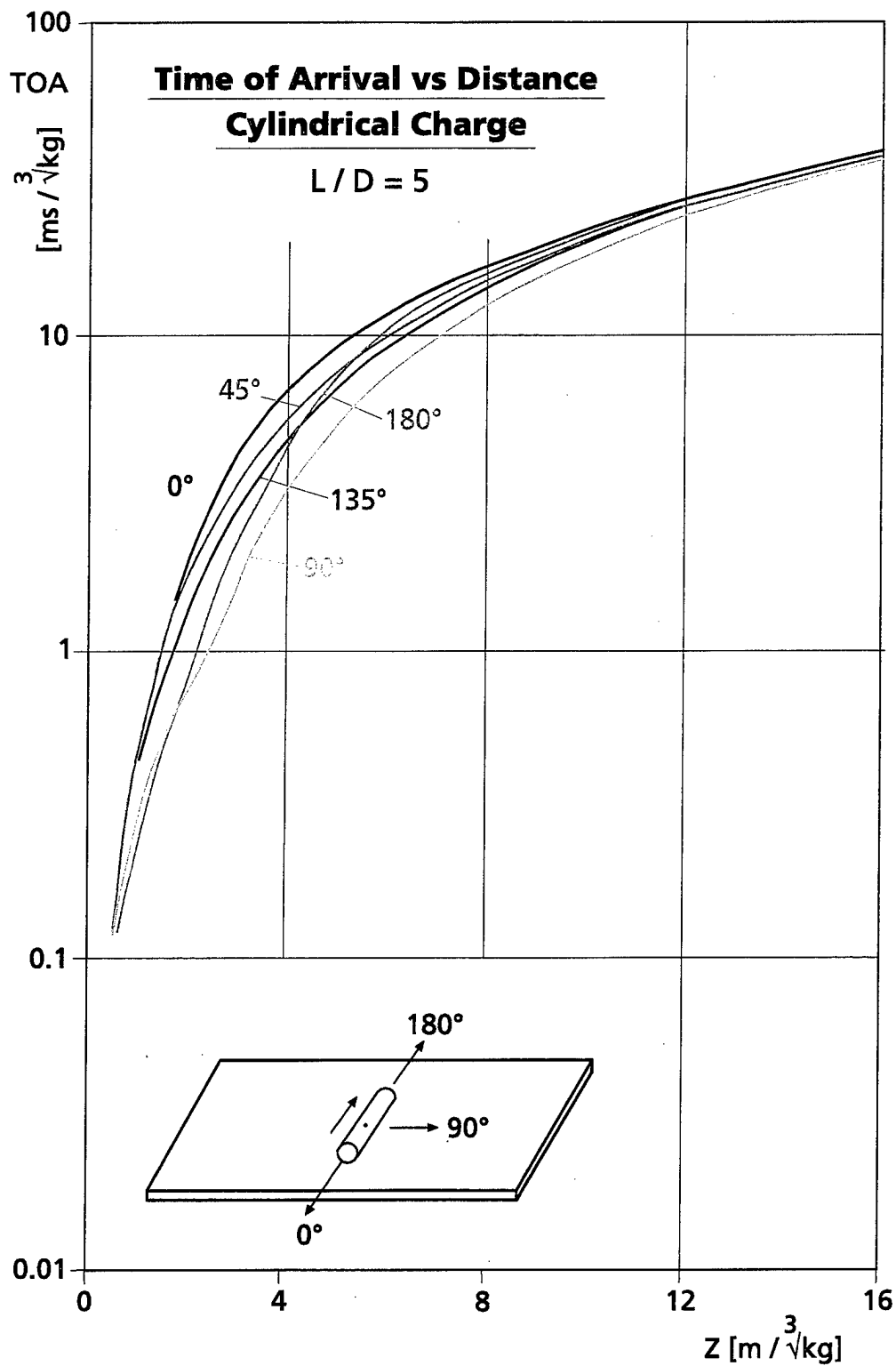


Figure 103. Time of arrival vs distance for a bare cylindrical charge with $L/D = 5$ at a surface tangent burst.

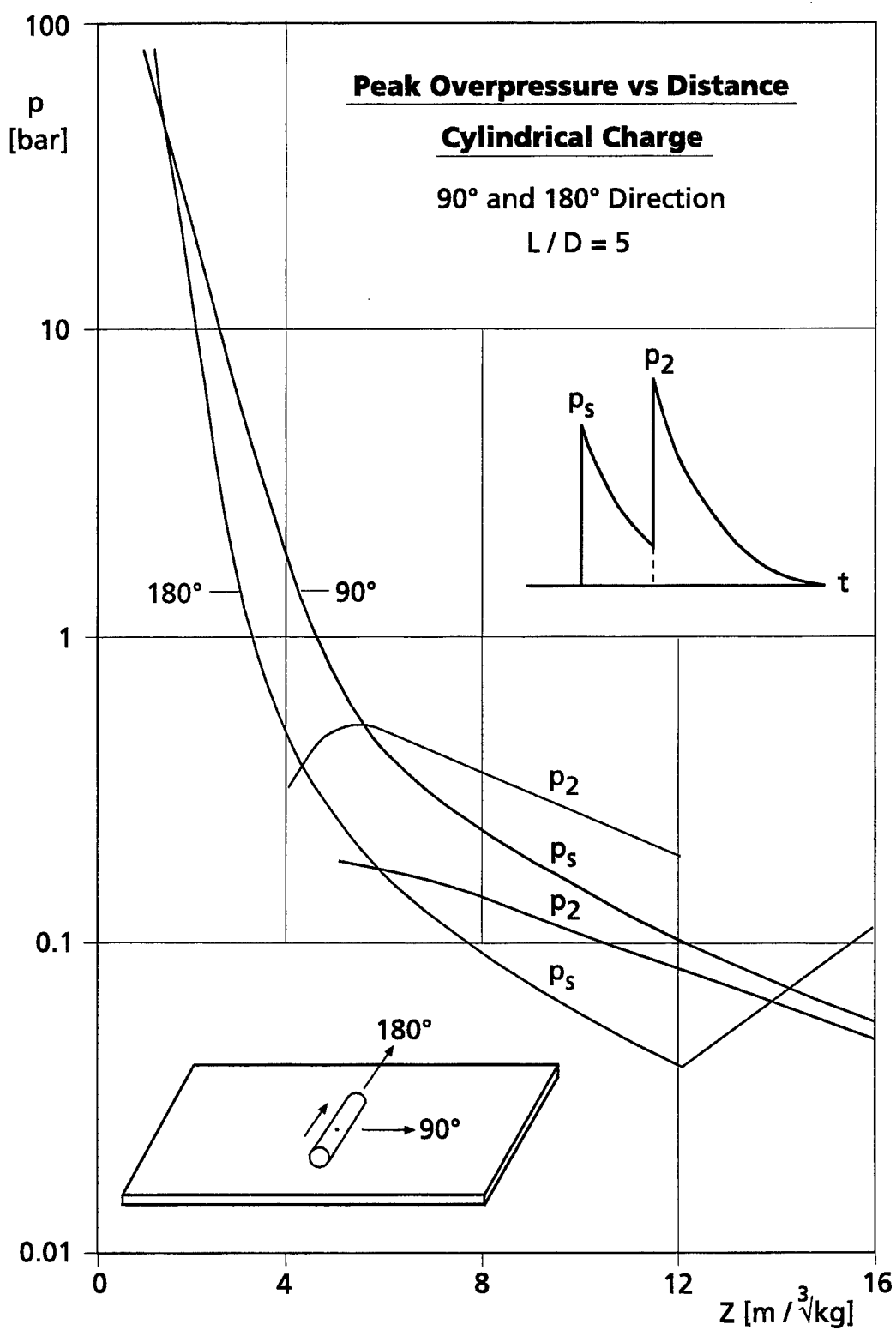


Figure 104. Double peaked blast wave domains for the 90°- and 180°-directions of a bare cylindrical charge with $L/D = 5$.

Peak pressure Isobars

Cylindrical Charge $L/D = 5:1$

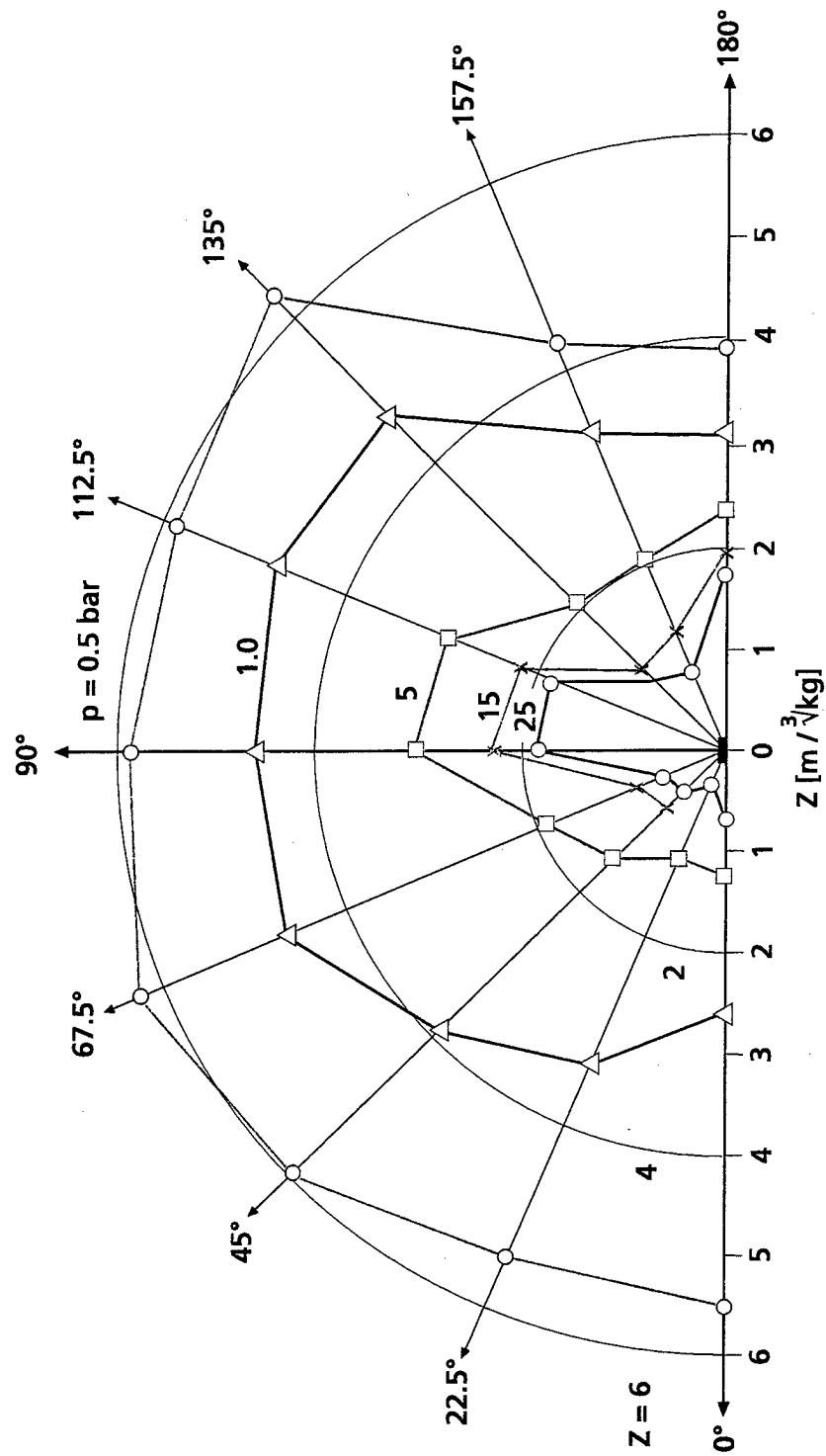


Figure 105. Isobars of a bare cylindrical charge with $L/D = 5$ at a surface tangent burst.

Constant Impulses

Cylindrical Charge $L/D = 5:1$

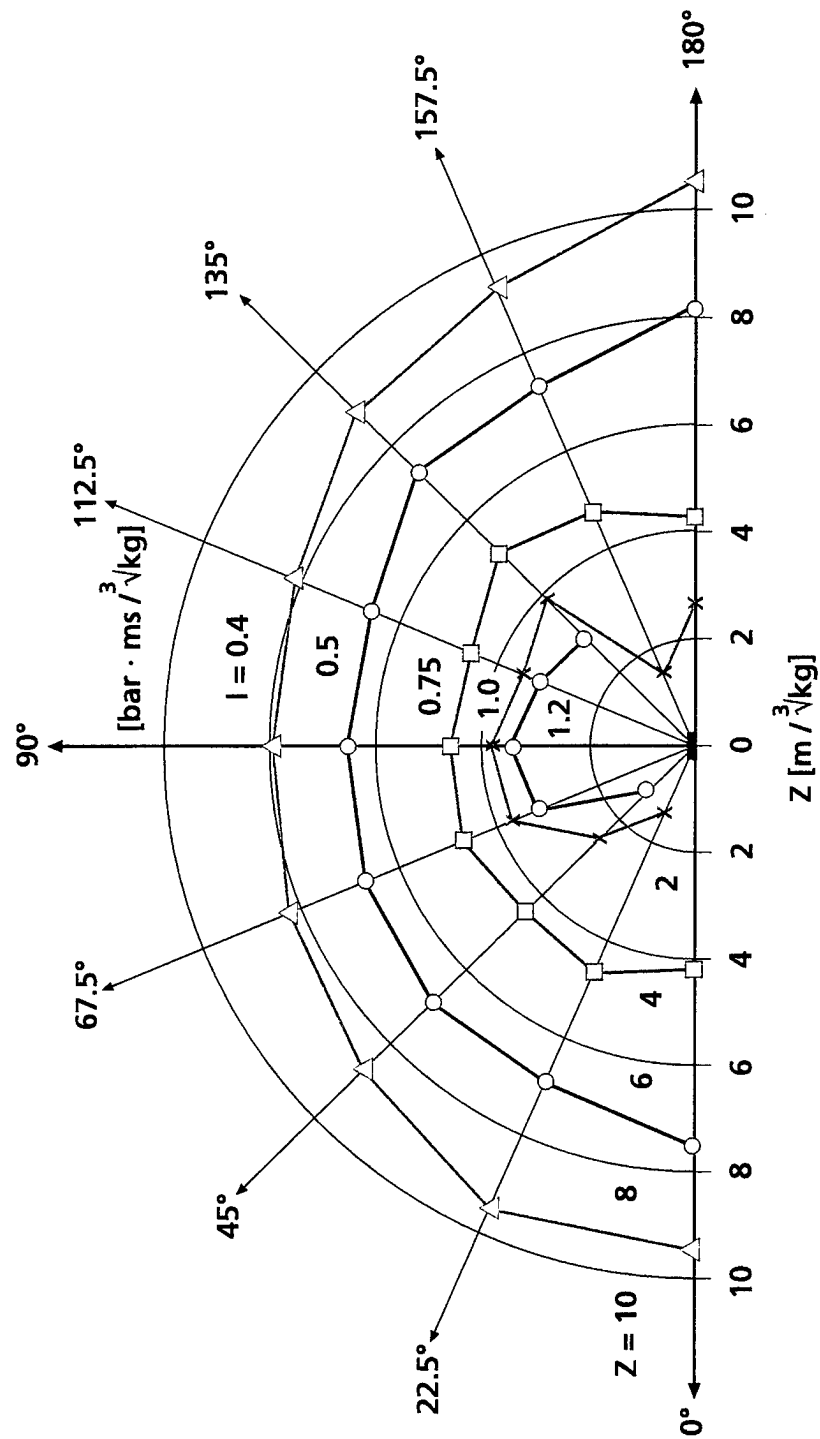


Figure 106. Iso-impulse curves of a bare cylindrical charge with $L/D = 5$.

Constant Arrival Times

Cylindrical Charge $L/D = 5:1$

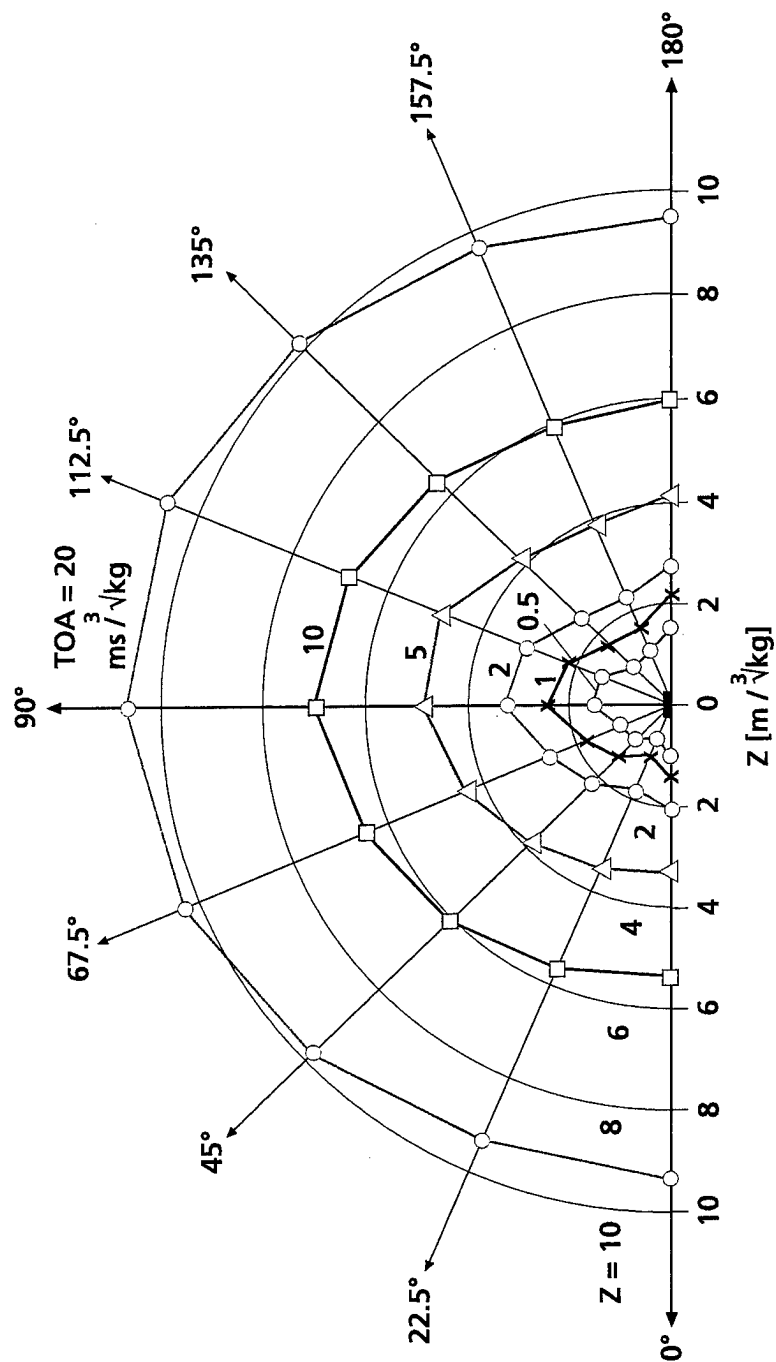
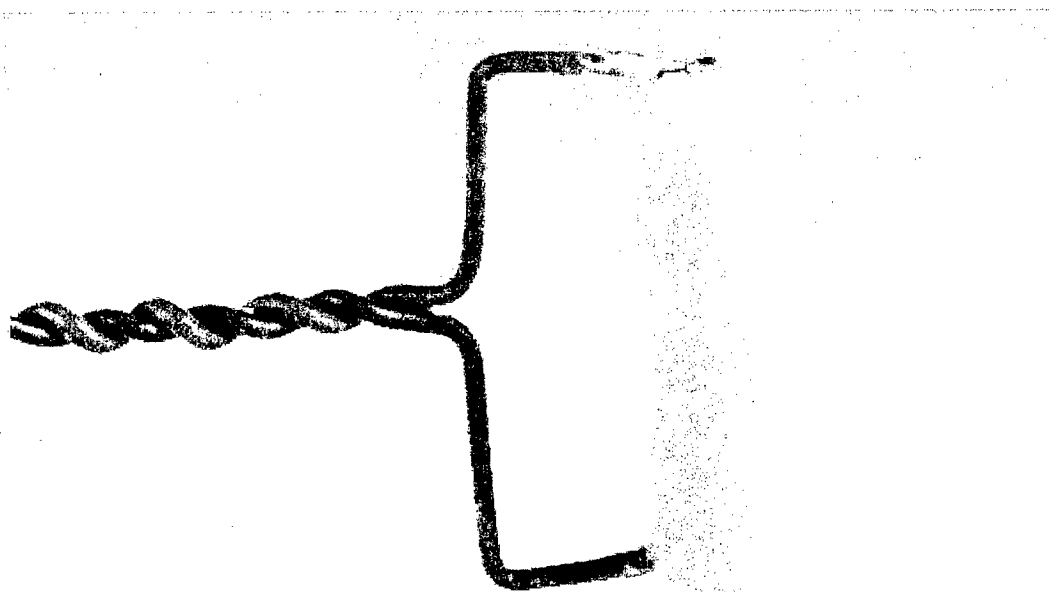
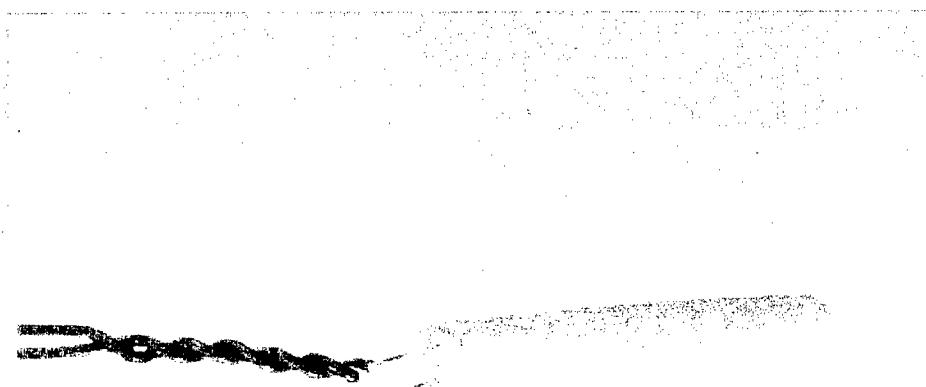


Figure 107. Constant time-of-arrival for a bare cylindrical charge with $L/D = 5$.



30 mm

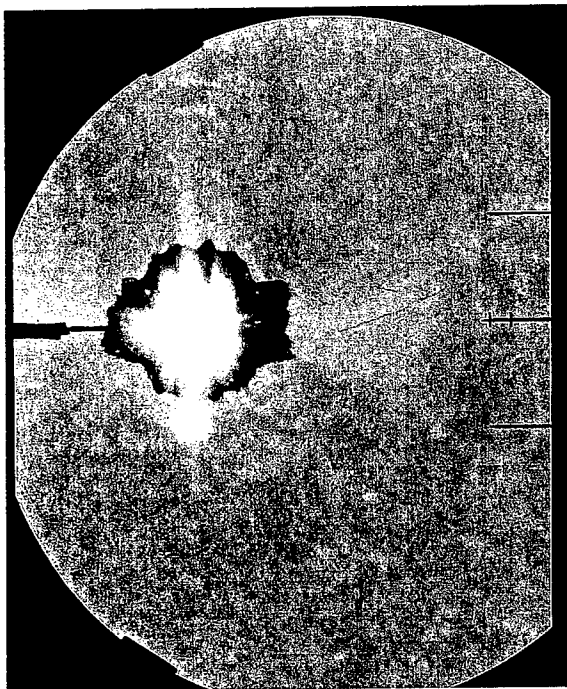
a) Axial Fuse Wire



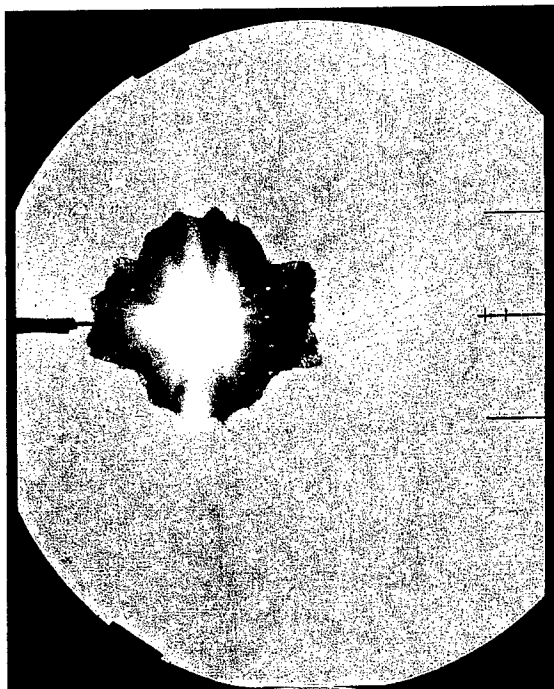
30 mm

b) Face Ignitor

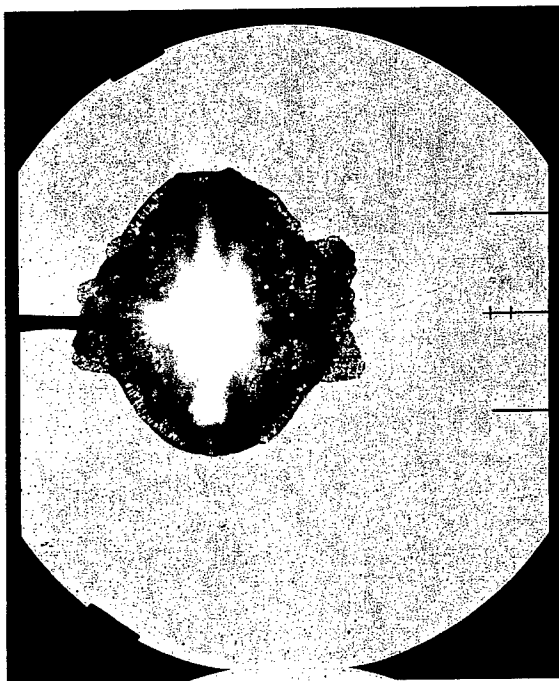
Figure 108.. Different bare cylindrical charges.



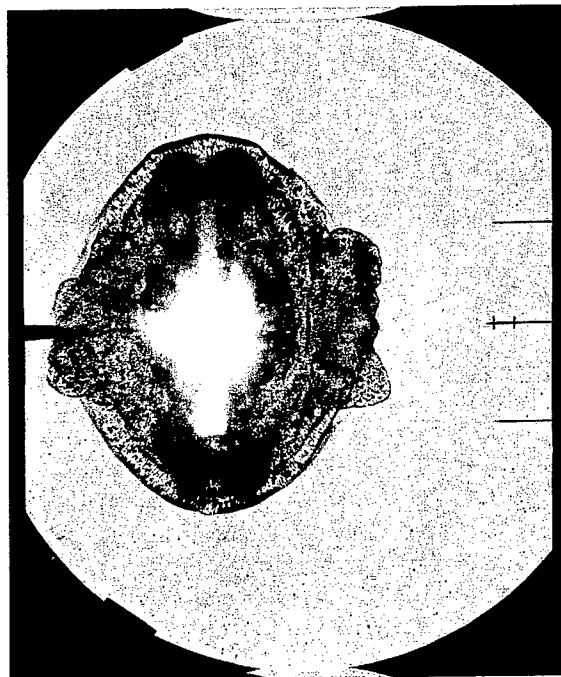
a) $t = 0,0125 \text{ ms}$ (15 558/3)



b) $t = 0,0165 \text{ ms}$ (15 558/4)



c) $t = 0,0245 \text{ ms}$ (15 558/6)

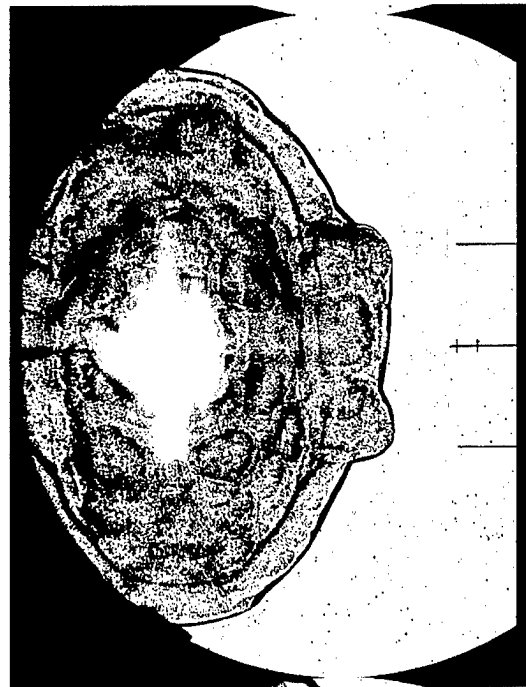


d) $t = 0,0325 \text{ ms}$ (15 558/8)

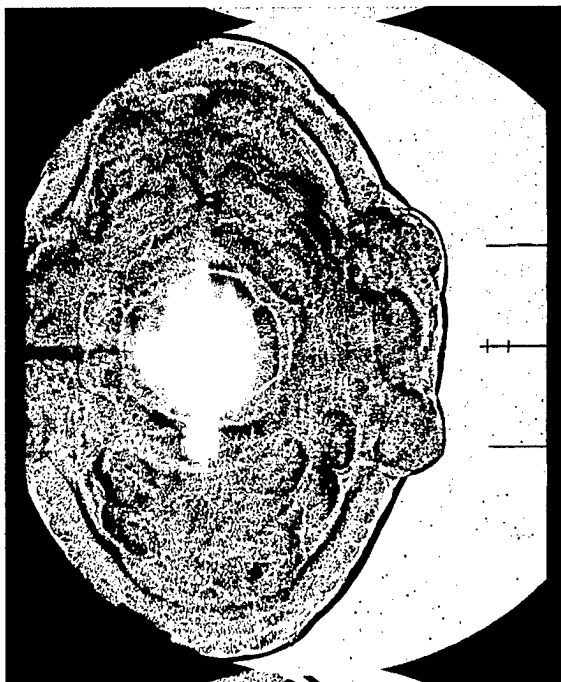
Figure 109. Detonation of an axial ignited bare cylindrical charge in top view.
 $W = 1.29\text{-g}$ Nitropenta; $L = 28 \text{ mm}$; $D = 7 \text{ mm}$;
 $\text{HOB} = 2D$; $t = \text{time after ignition}$, (test 15 558).



e) $t = 0,0405 \text{ ms}$ (15 558/10)



f) $t = 0,0525 \text{ ms}$ (15 558/13)



g) $t = 0,0645 \text{ ms}$ (15 558/16)



h) $t = 0,0965 \text{ ms}$ (15 558/24)

Figure 109. Detonation of an axial ignited bare cylindrical charge in top view.
 $W = 1.29\text{-g}$ Nitropenta; $L = 28 \text{ mm}$; $D = 7 \text{ mm}$;
 $\text{HOB} = 2D$; t = time after ignition, (test 15 558). (Continued)

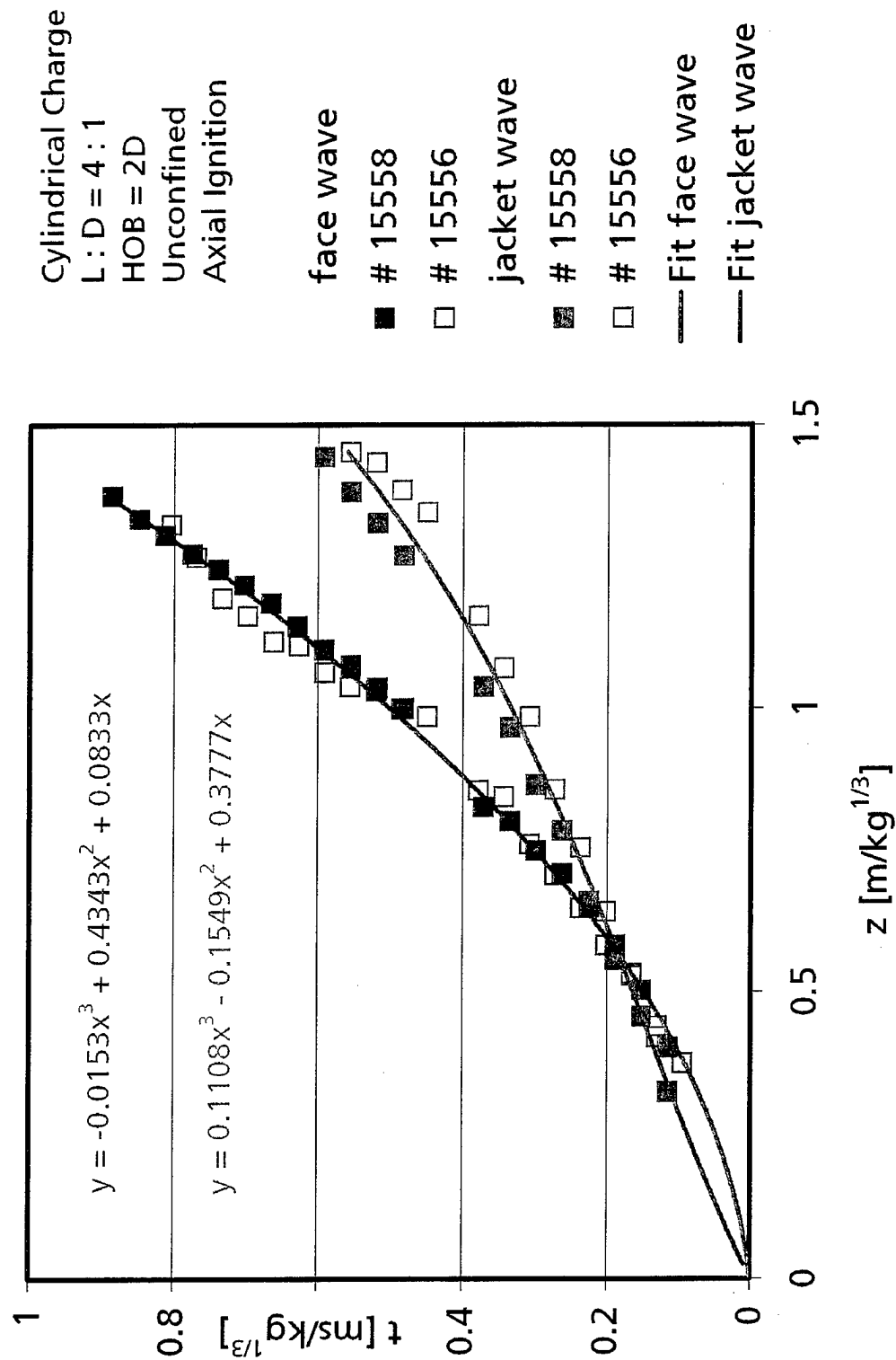


Figure 110. Distance-time curves for face (0°-direction) and jacket wave (90°-direction) of two tests with axial ignited bare cylindrical charges. HOB = 2D; L = 28 mm; D = 7 mm; L:D = 4:1

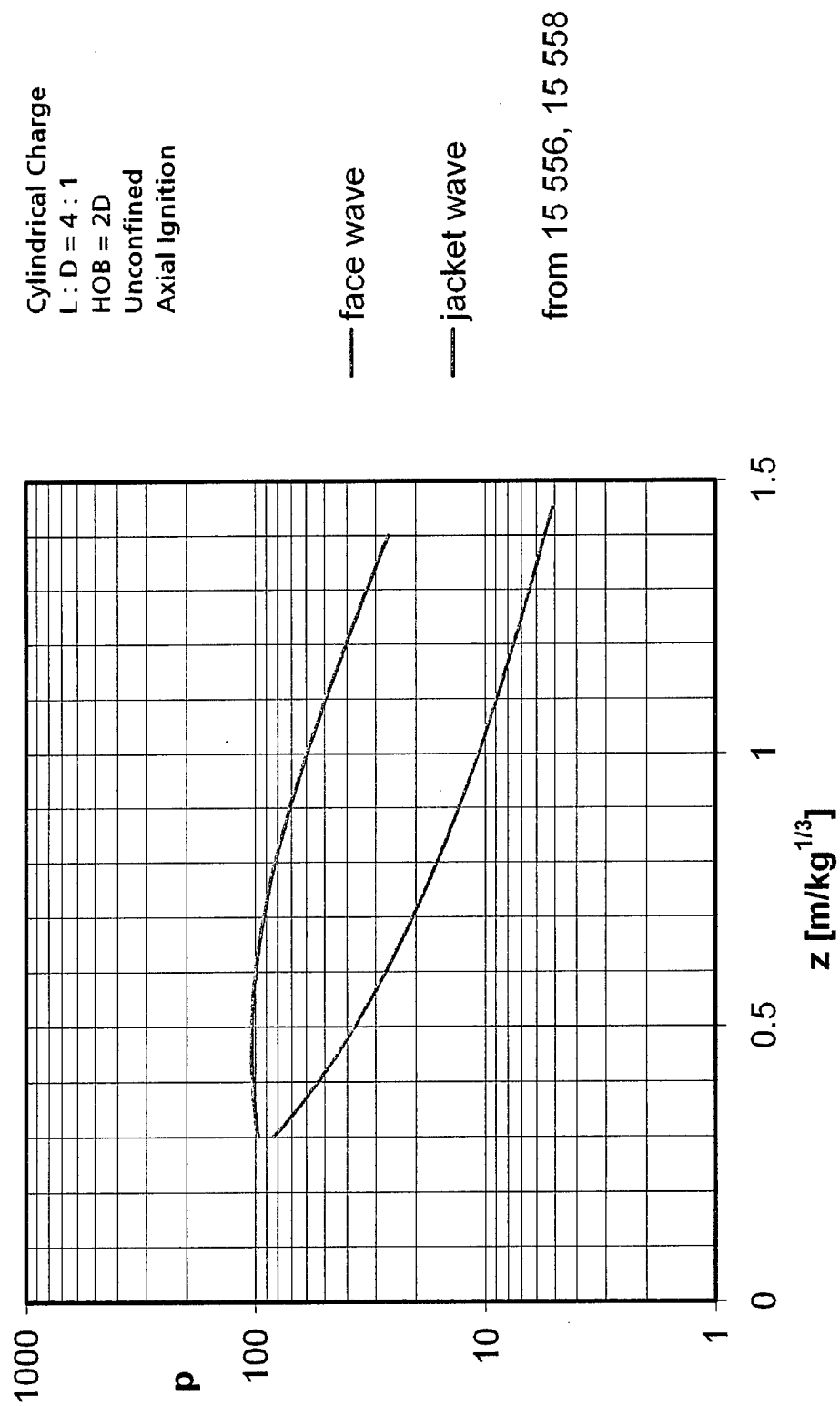
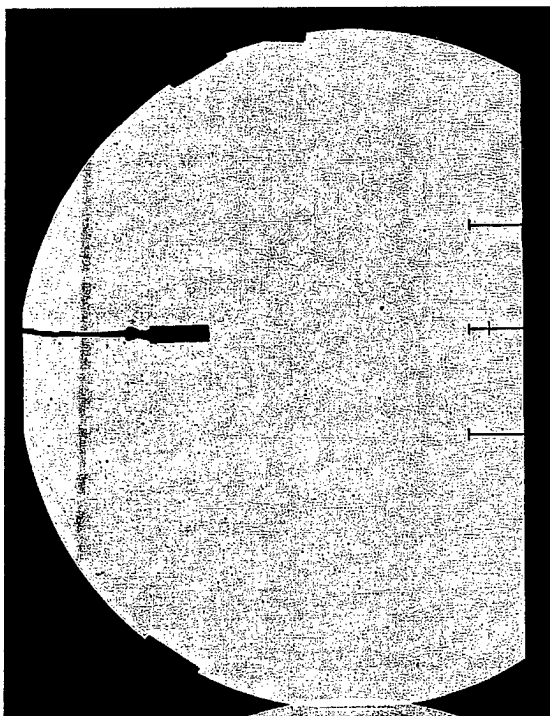
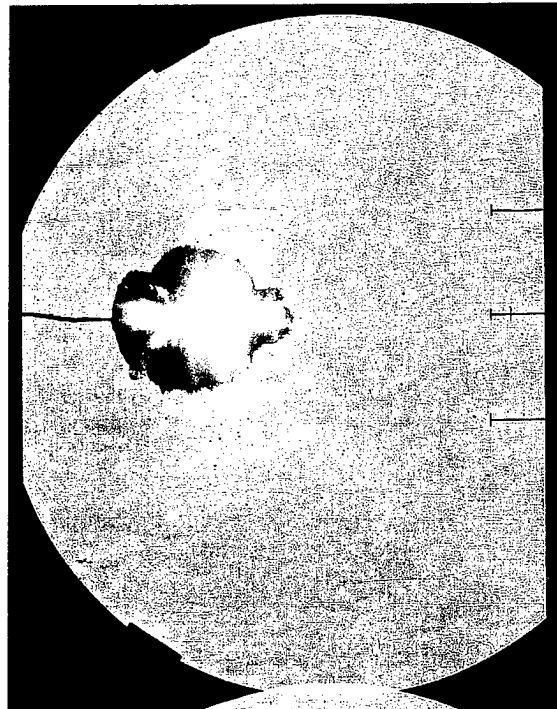


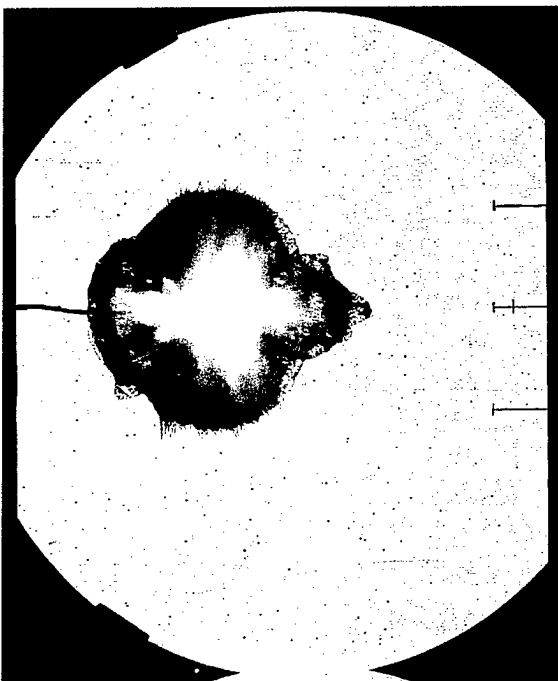
Figure 111. Estimated overpressure-range behavior for face and jacket waves from the fit-functions in Figure 110; (tests 15 556 and 15 558).



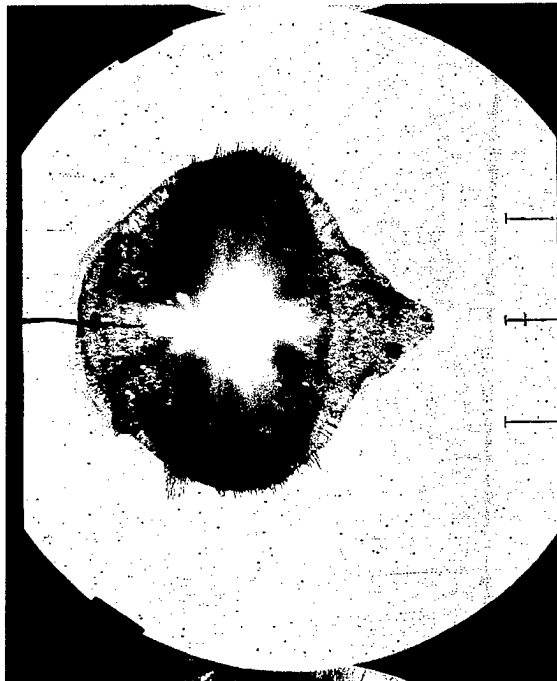
a) Before Ignition



b) $t = 0,0124 \text{ ms (15 559/3)}$



b) $t = 0,0204 \text{ ms (15 559/5)}$



d) $t = 0,0284 \text{ ms (15 559/7)}$

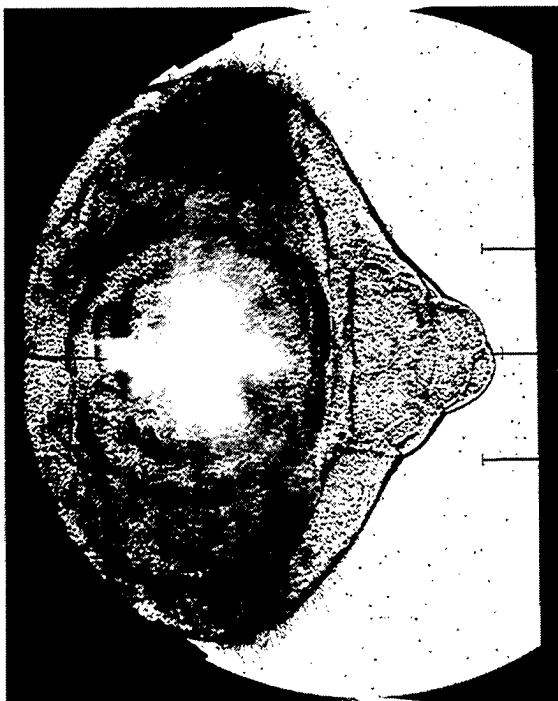
Figure 112. Detonation of a face ignited bare cylindrical charge in top view.
 $W = 1.31\text{-g Nitropenta}$; $L = 28 \text{ mm}$; $D = 7 \text{ mm}$;
 $\text{HOB} = 2D$; $t = \text{time after ignition.}$)



e) $t = 0,0364 \text{ ms}$ (15 559/9)



f) $t = 0,0444 \text{ ms}$ (15 559/11)



f) $t = 0,0524 \text{ ms}$ (15 559/13)



h) $t = 0,0604 \text{ ms}$ (15 559/15)

Figure 112. Detonation of a face ignited bare cylindrical charge in top view.
 $W = 1.31\text{-g}$ Nitropenta; $L = 28 \text{ mm}$; $D = 7 \text{ mm}$;
 $\text{HOB} = 2D$; $t = \text{time after ignition}$. (Continued)



i) $t = 0,0684 \text{ ms}$ (15 559/17)



k) $t = 0,0764 \text{ ms}$ (15 559/19)



l) $t = 0,0844 \text{ ms}$ (15 559/21)



m) $t = 0,0924 \text{ ms}$ (15 559/23)

Figure 112. Detonation of a face ignited bare cylindrical charge in top view.
 $W = 1.31\text{-g}$ Nitropenta; $L = 28 \text{ mm}$; $D = 7 \text{ mm}$;
 $HOB = 2D$; $t = \text{time after ignition}$. (Continued)

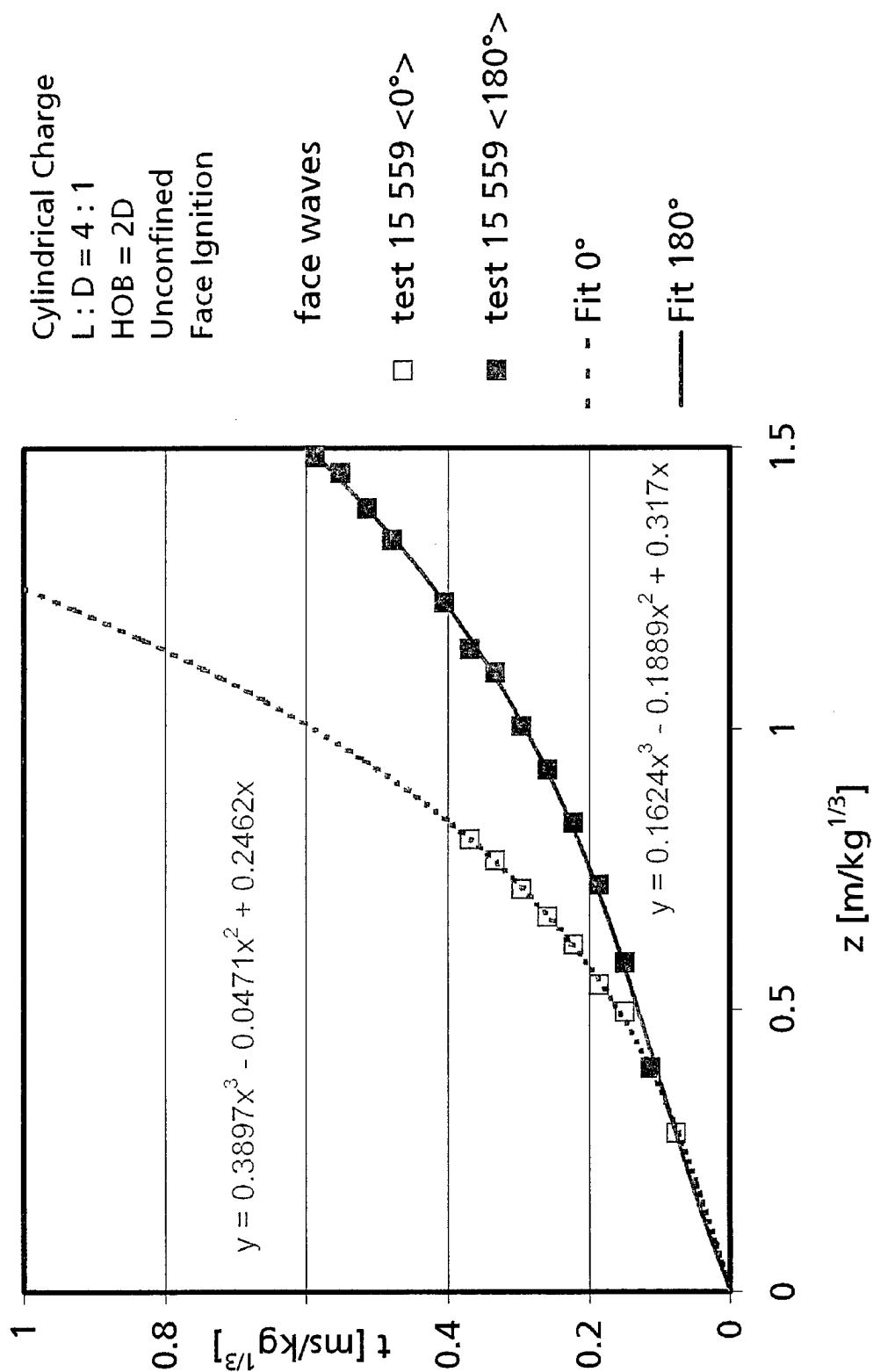


Figure 113. Wave diagrams of the face waves in 0° and 180° direction of a face ignited unconfined cylindrical charge. (test 15 559).

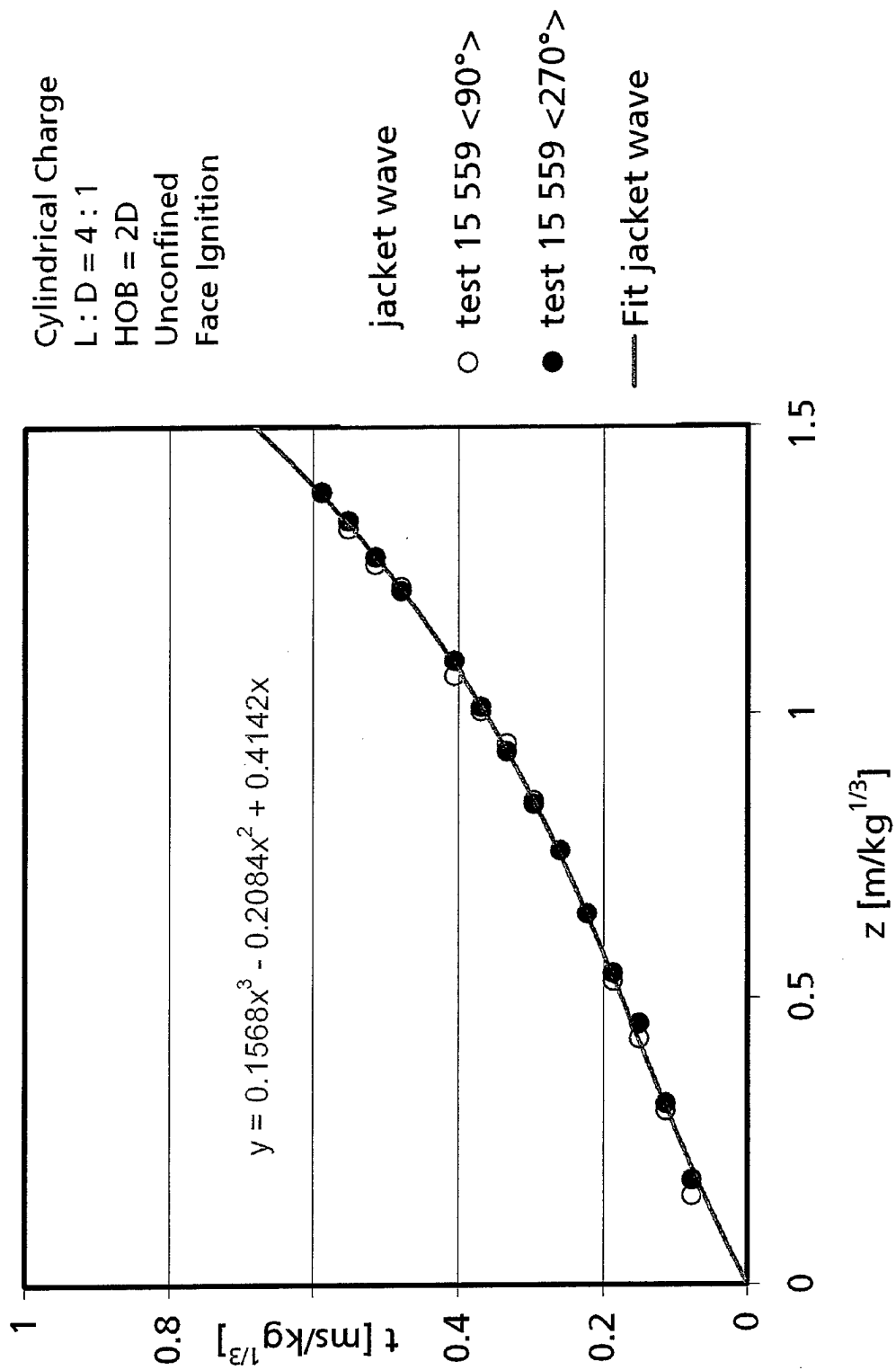


Figure 114. Wave diagrams of the jacket waves in 90° and 270° direction of a face ignited unconfined cylindrical charge. (test 15 559).

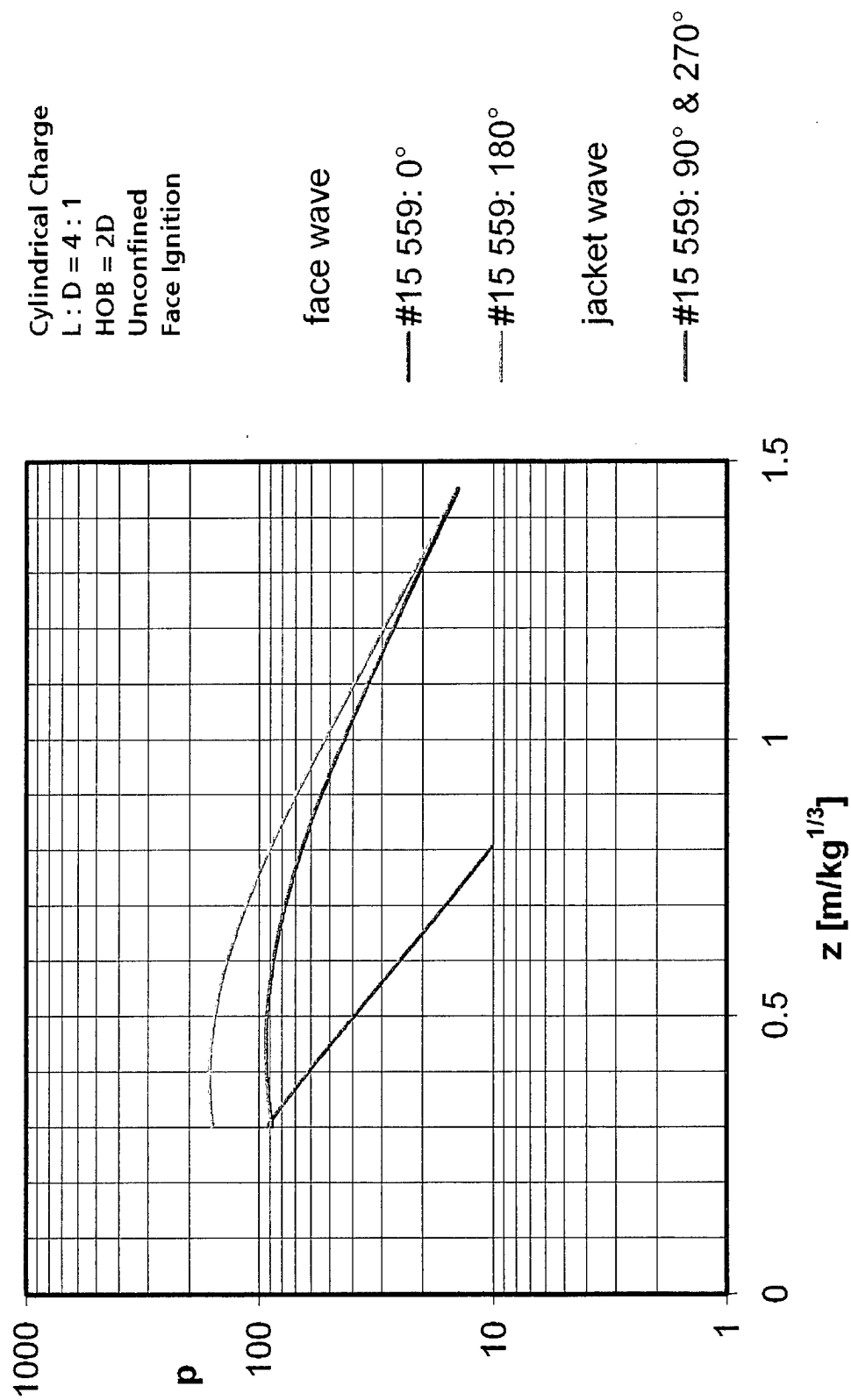


Figure 115. Estimated overpressure-range behavior for face and jacket waves from the fit functions in Figure 113 and 114.

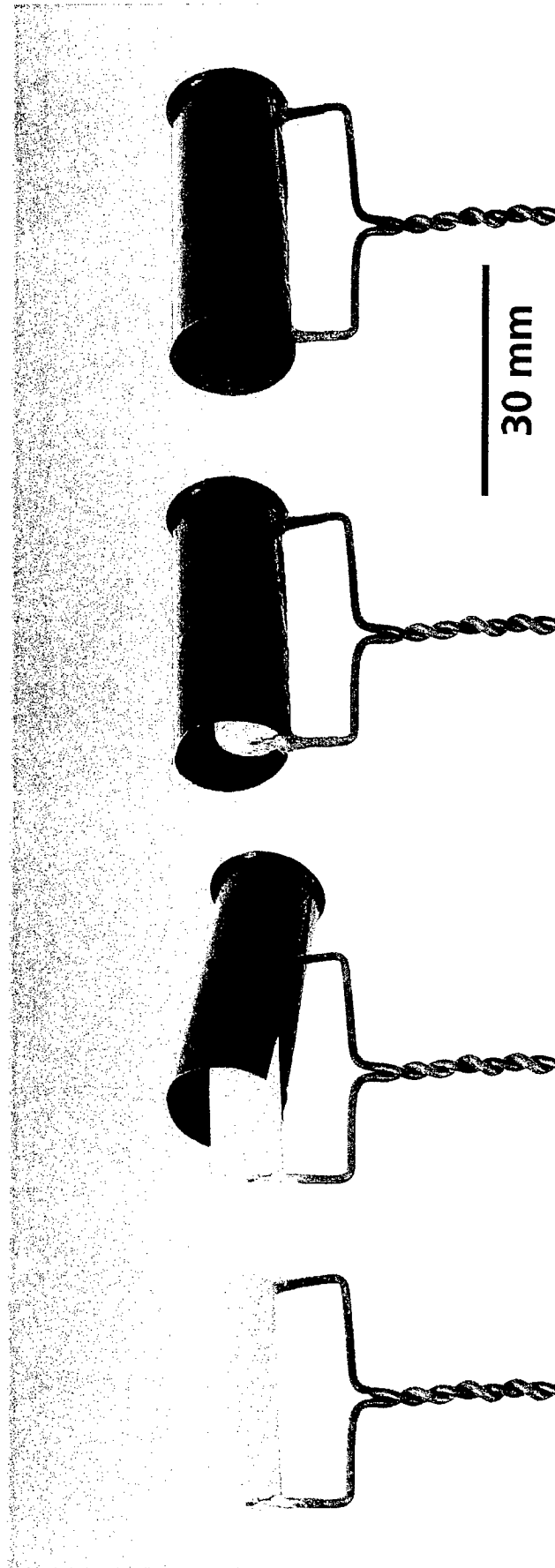
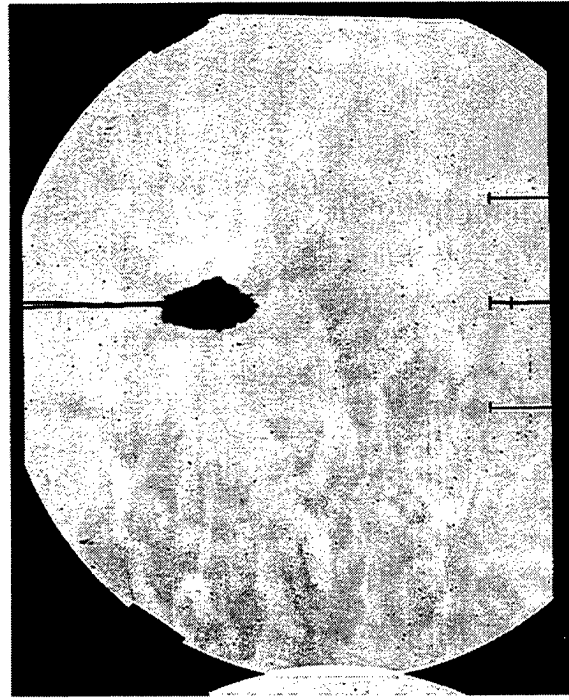


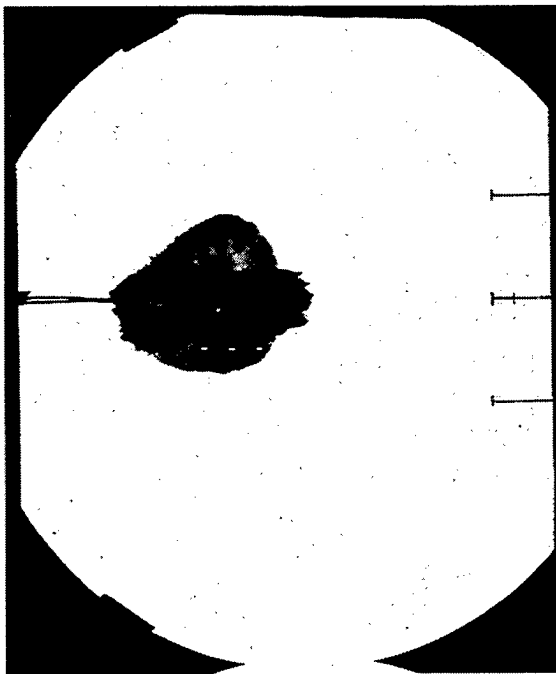
Figure 116. Manufacturing procedure of a blasting composition to simulate the WES experiment. Instead of water the tube is filled with a gelatin solution.



a) $t = \text{before ignition}$ (15 565/1)



b) $t = 0,010 \text{ ms}$ (15 565/3)

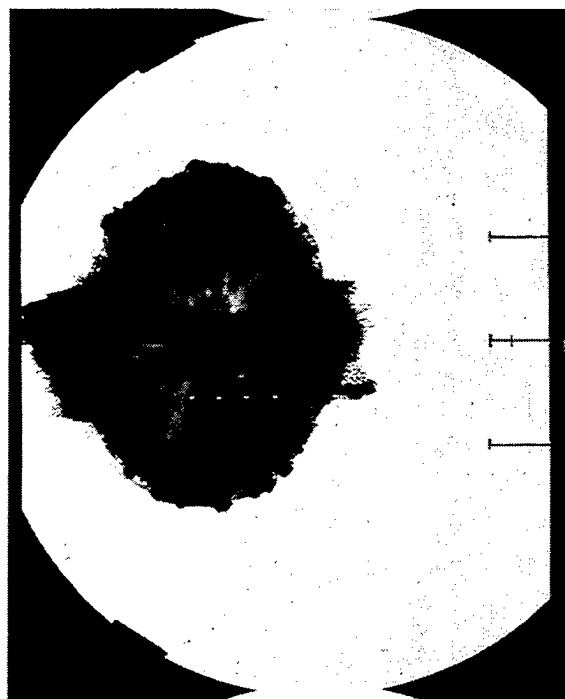


c) $t = 0,018 \text{ ms}$ (15 565/5)

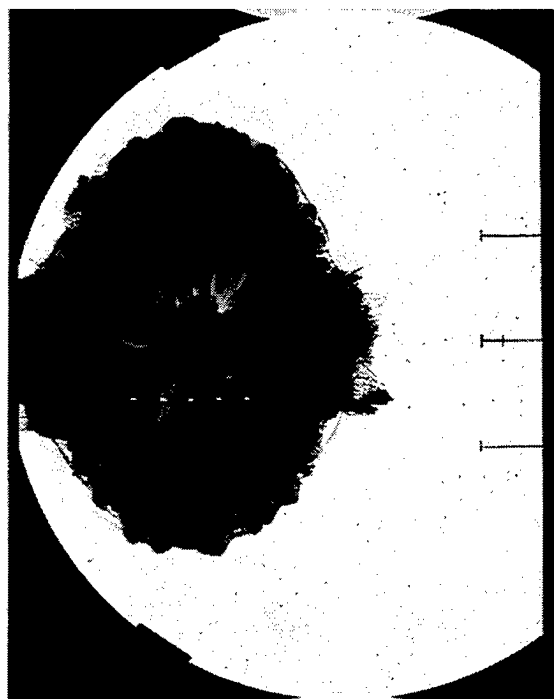


d) $t = 0,026 \text{ ms}$ (15 565/7)

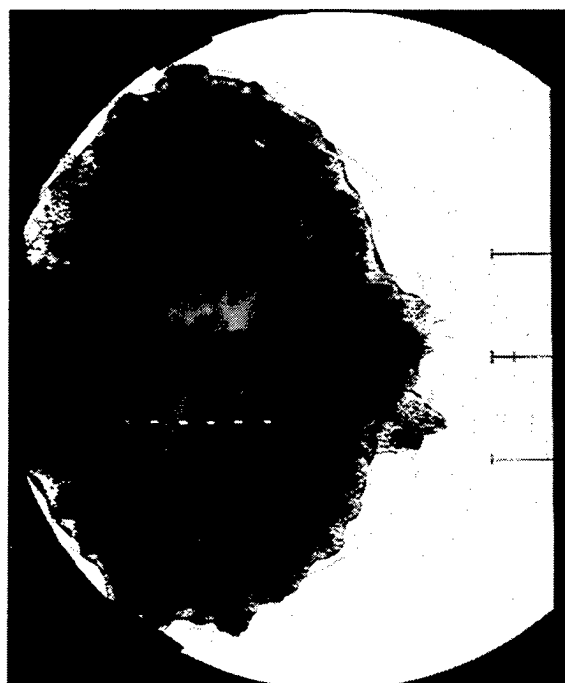
Figure 117. Detonation of an axial ignited confined cylindrical charge in top view.
 $W = 1.28\text{-g}$ Nitropenta, $L = 28 \text{ mm}$, $D = 7 \text{ mm}$,
 tube diameter: $D_t = 11 \text{ mm}$, $\text{HOB} = 2 D_t$, $t = \text{time after ignition}$.



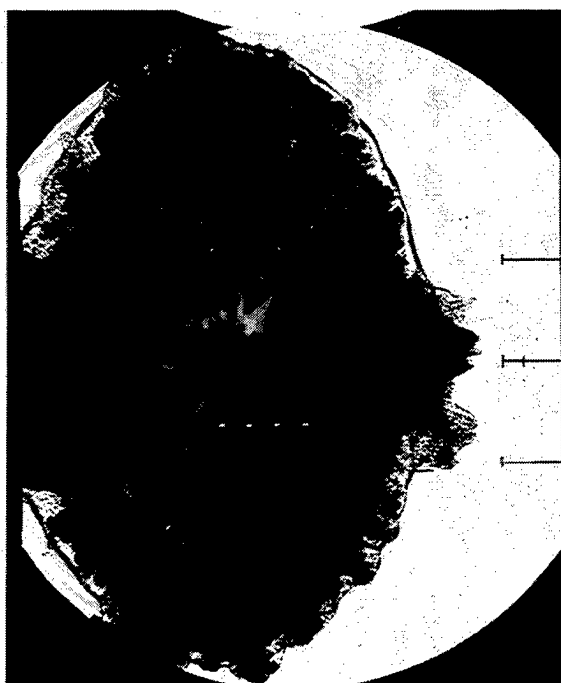
e) $t = 0,034 \text{ ms}$ (15 565/9)



f) $t = 0,042 \text{ ms}$ (15 565/11)

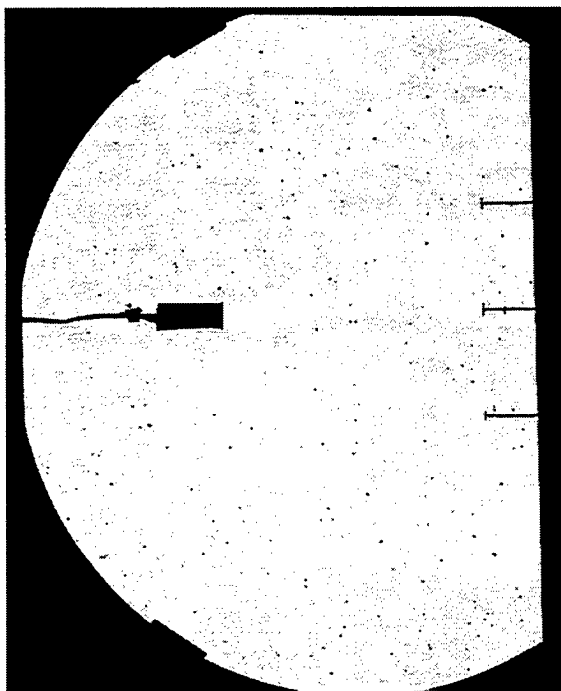


g) $t = 0,058 \text{ ms}$ (15 565/15)

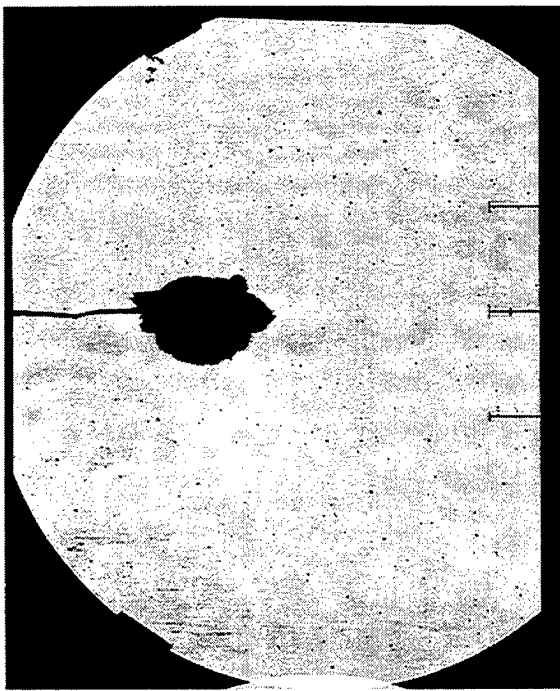


h) $t = 0,070 \text{ ms}$ (15 565/18)

Figure 117. Detonation of an axial ignited confined cylindrical charge in top view.
 $W = 1.28\text{-g}$ Nitropenta, $L = 28 \text{ mm}$, $D = 7 \text{ mm}$,
 tube diameter: $D_t = 11 \text{ mm}$, $\text{HOB} = 2 D_t$, $t = \text{time after ignition}$. (Continued)



a) $t = \text{before ignition}$ (15 561/1)



b) $t = 0,0132 \text{ ms}$ (15 561/3)



c) $t = 0,0212 \text{ ms}$ (15 561/5)



d) $t = 0,0292 \text{ ms}$ (15 561/7)

Figure 118. Detonation of a face ignited confined cylindrical charge in top view.
 $W = 1.32\text{-g}$ Nitropenta, $L = 28 \text{ mm}$, $D = 7 \text{ mm}$,
 Tube diameter $D_t = 11 \text{ mm}$, $\text{HOB} = 2 D_t$, $t = \text{time after ignition}$.



e) $t = 0,0372 \text{ ms}$ (15 561/9)



f) $t = 0,0452 \text{ ms}$ (15 561/11)



g) $t = 0,0532 \text{ ms}$ (15 561/13)



h) $t = 0.0612 \text{ ms}$ (15 561/15)

Figure 118. Detonation of a face ignited confined cylindrical charge in top view.
 $W = 1.32\text{-g}$ Nitropenta, $L = 28 \text{ mm}$, $D = 7 \text{ mm}$,
 Tube diameter $D_t = 11 \text{ mm}$, $HOB = 2 D_t$, $t = \text{time after ignition}$. (Continued)

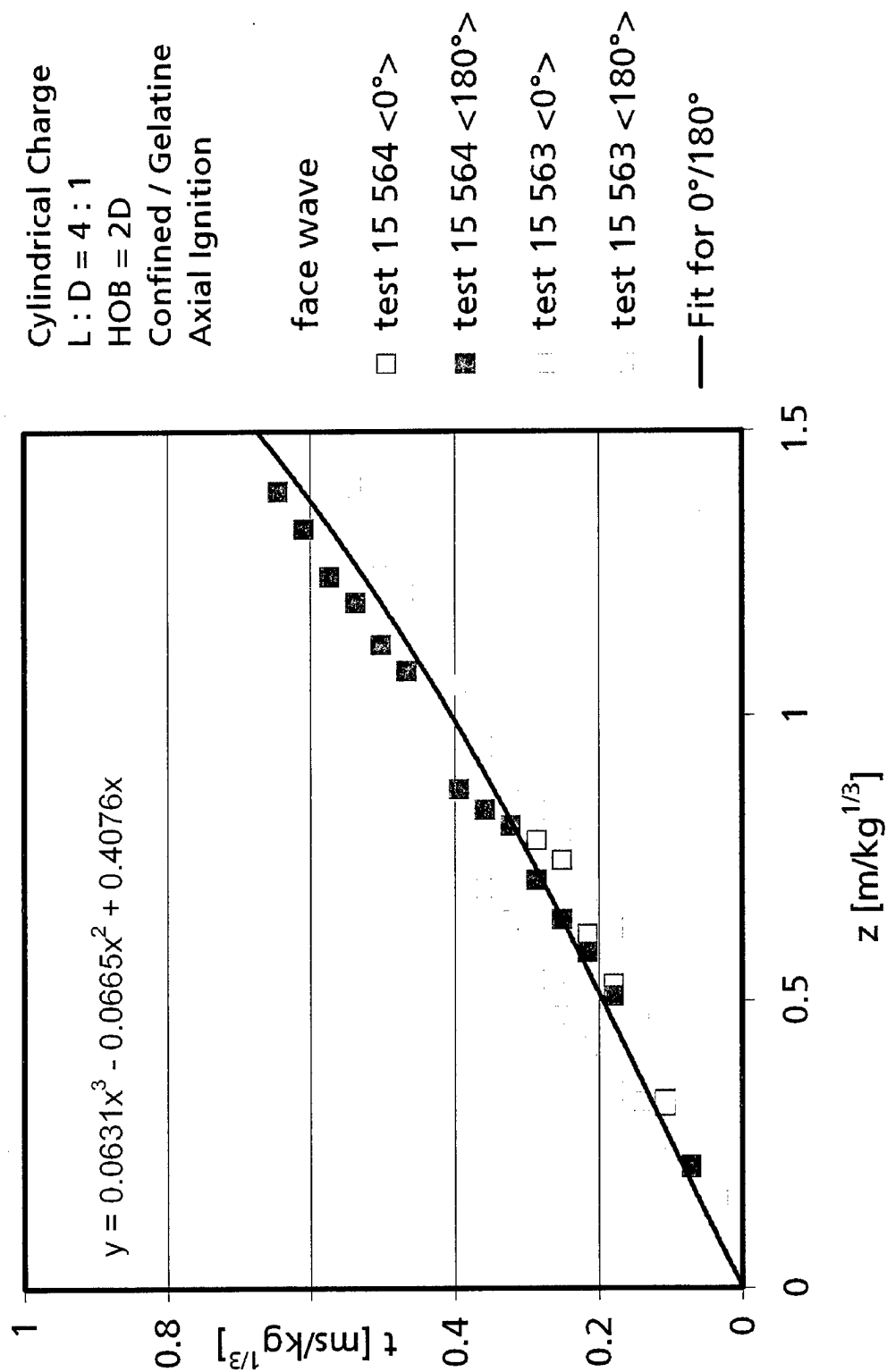


Figure 119. Wave diagrams of the face waves in 0°- and 180°- direction of an axial ignited confined cylindrical charge. (test 15 563 and 15 564)

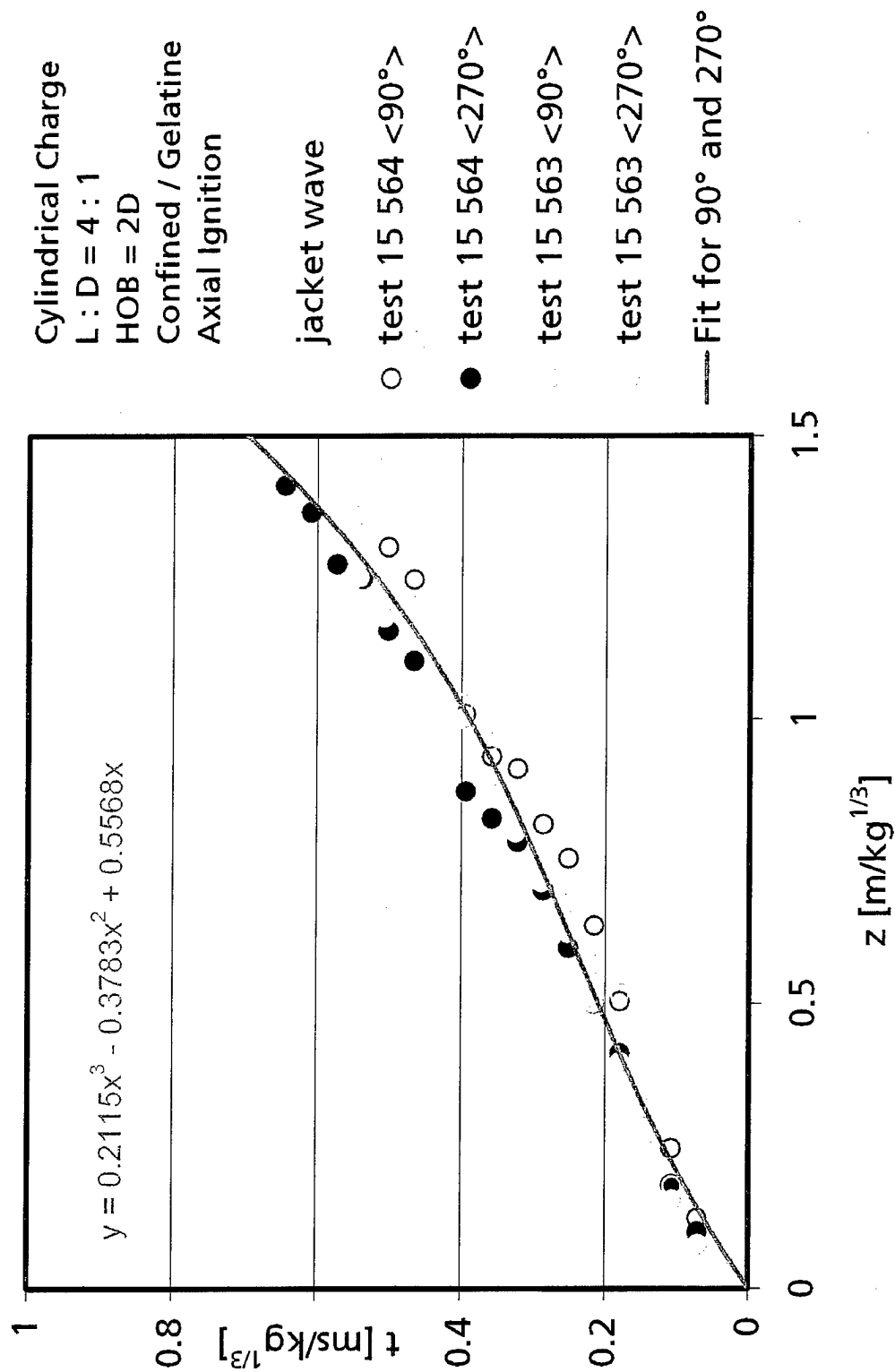


Figure 120. Wave diagrams of the jacket waves in 90° and 270° direction of an axial ignited confined cylindrical charge. (test 15 563 and 15 564)

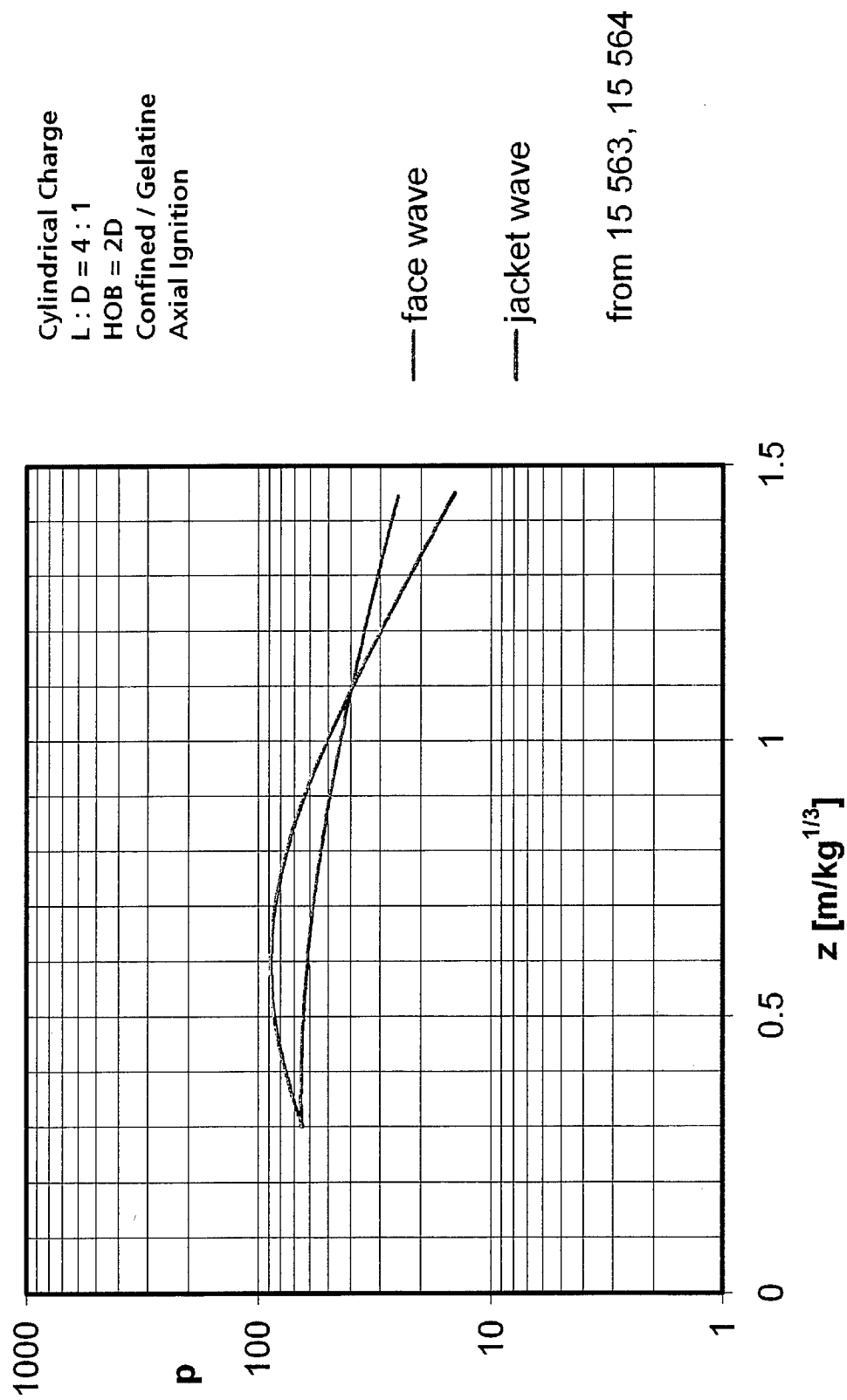


Figure 121. Estimated overpressure-range behavior for face and jacket waves from the fit functions in Figure 119 and 120.

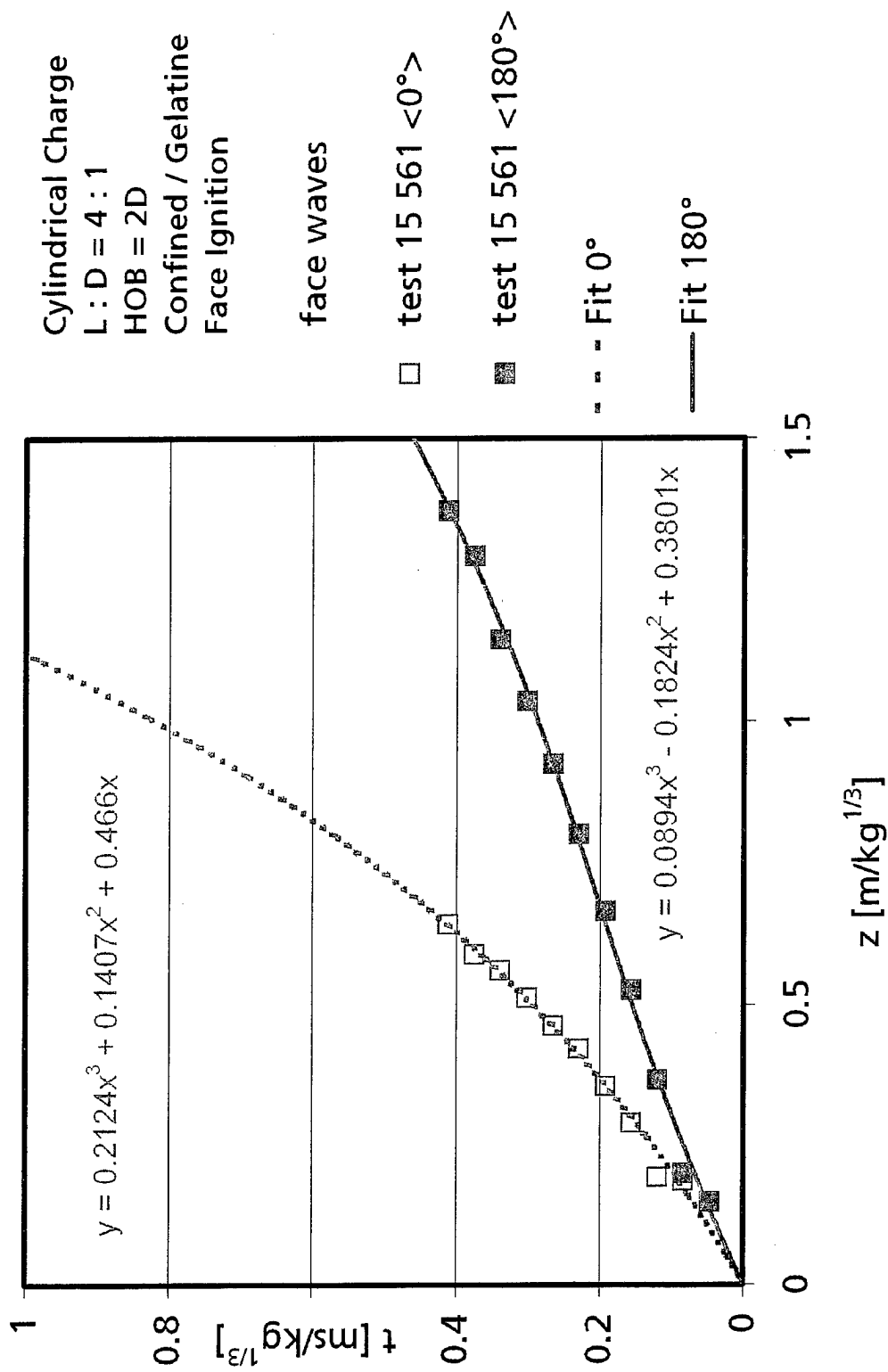


Figure 122. Wave diagrams of the face waves in 0°- and 180°- direction of a face ignited confined cylindrical charge. (test 15 561)

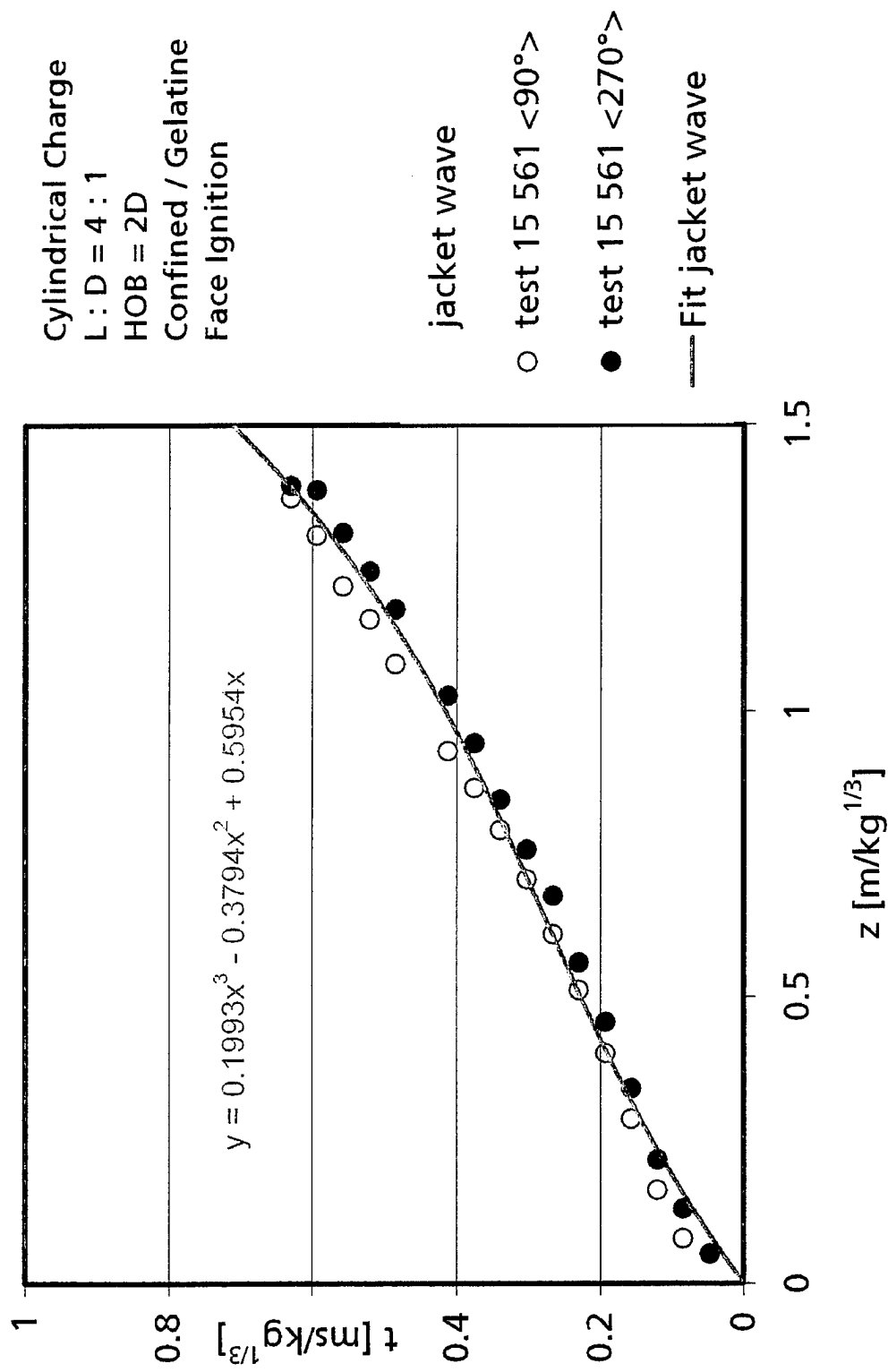


Figure 123. Wave diagrams of the jacket waves in 90° and 270° direction of a face ignited confined cylindrical charge. (test 15 561)

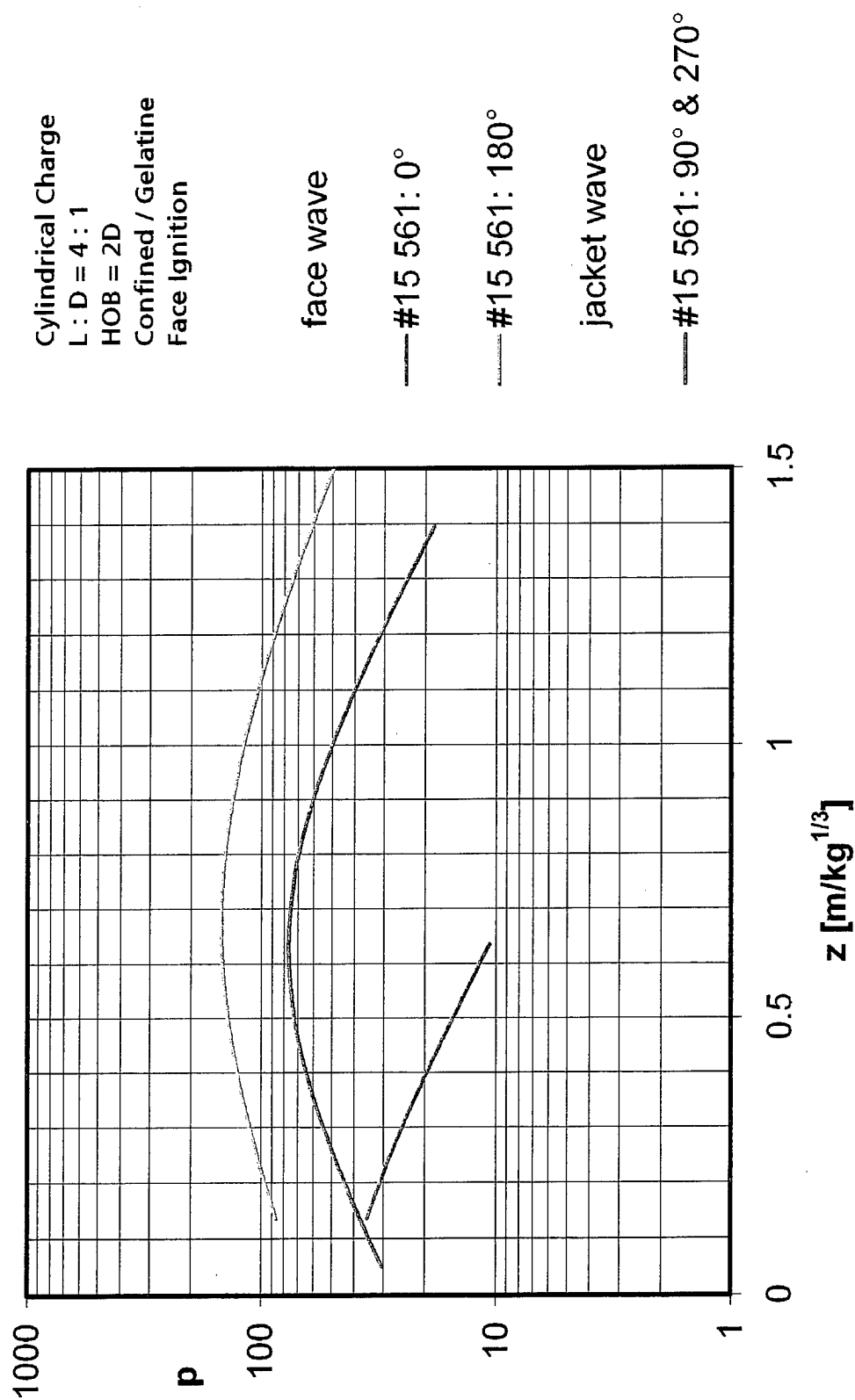


Figure 124. Estimated overpressure-range behavior for face and jacket waves from the fit functions in Figure 122 and 123.

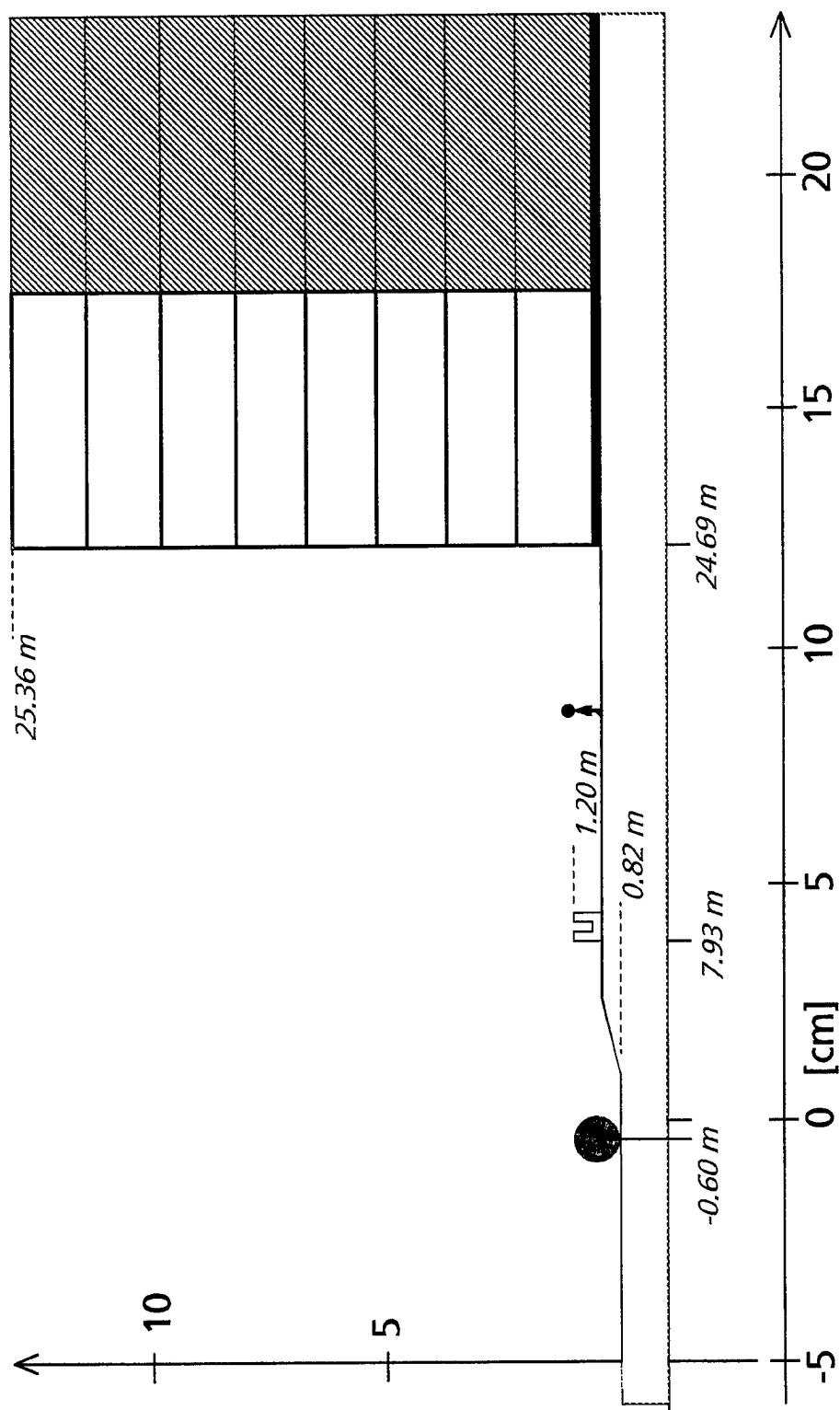


Figure 125. Side view of the Khobar Towers building. The blue Figures correspond to the original dimensions. The measures of the small-scale model are given in black. Charge position is drawn in red.

KHOBAR TOWERS: Schematic scenario

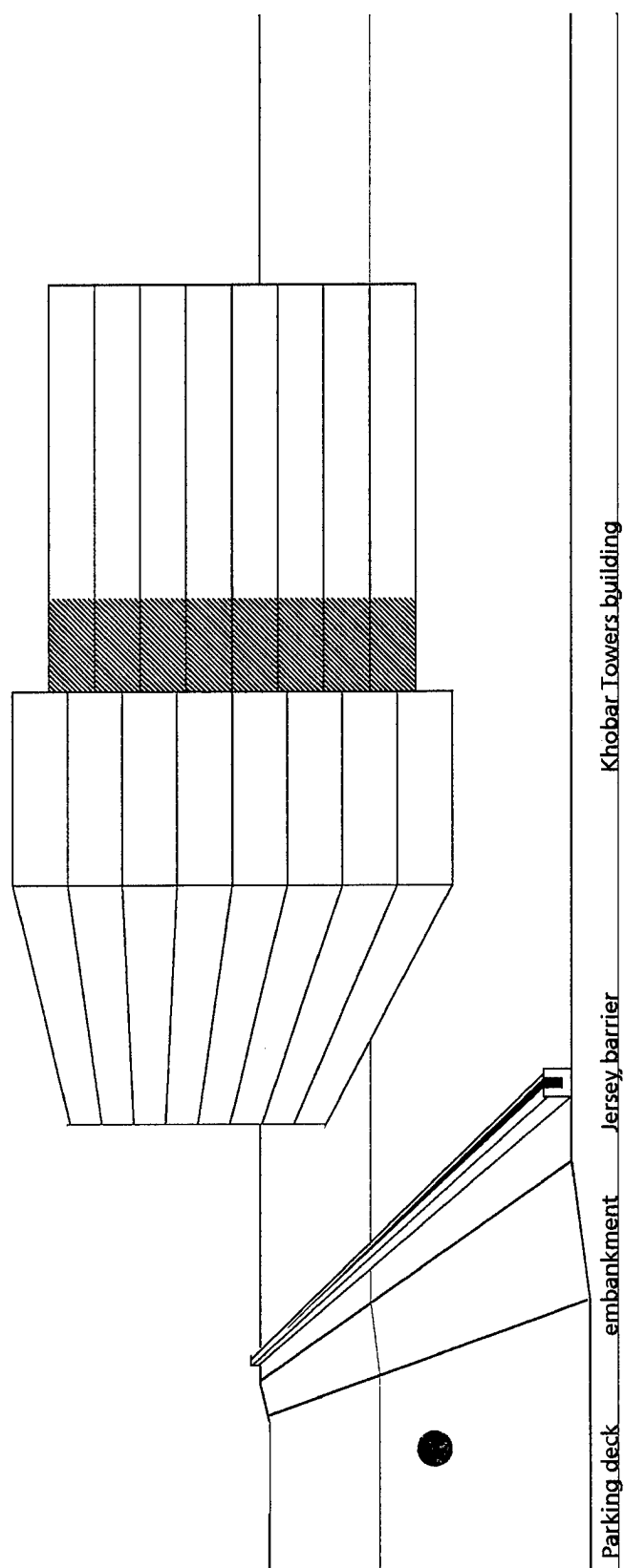


Figure 127. Schematic scenario of the Khobar Towers building.

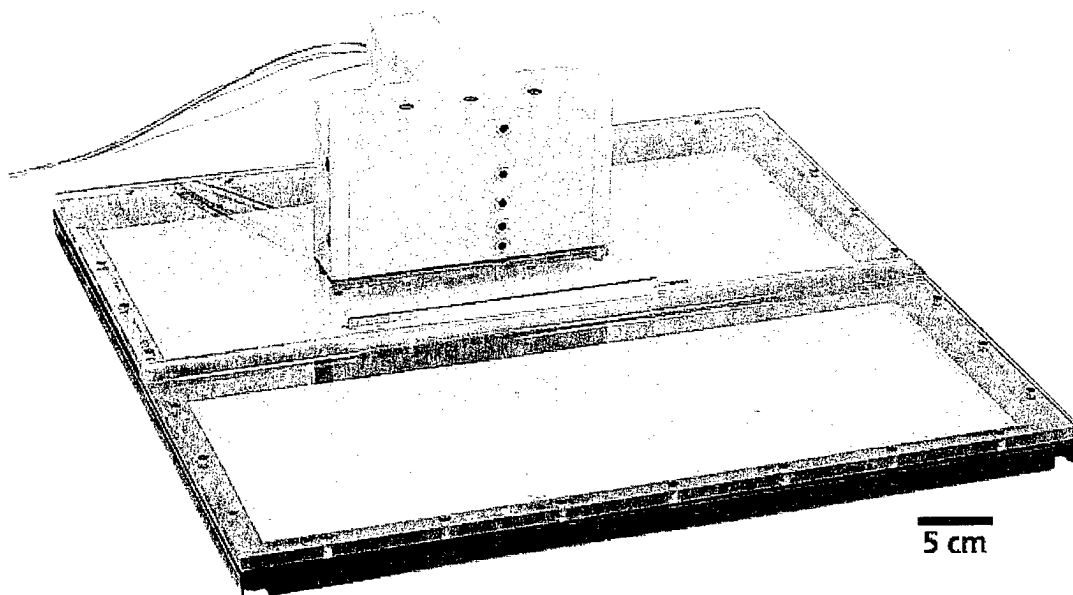


Figure 128. Model of the Khobar Towers building in a scale of 1 : 200. The ground surface is transparent, allowing top view shadow-graphs. Visible are also the position of the pressure gages in the front wall.

2 - D Khobar Towers Model

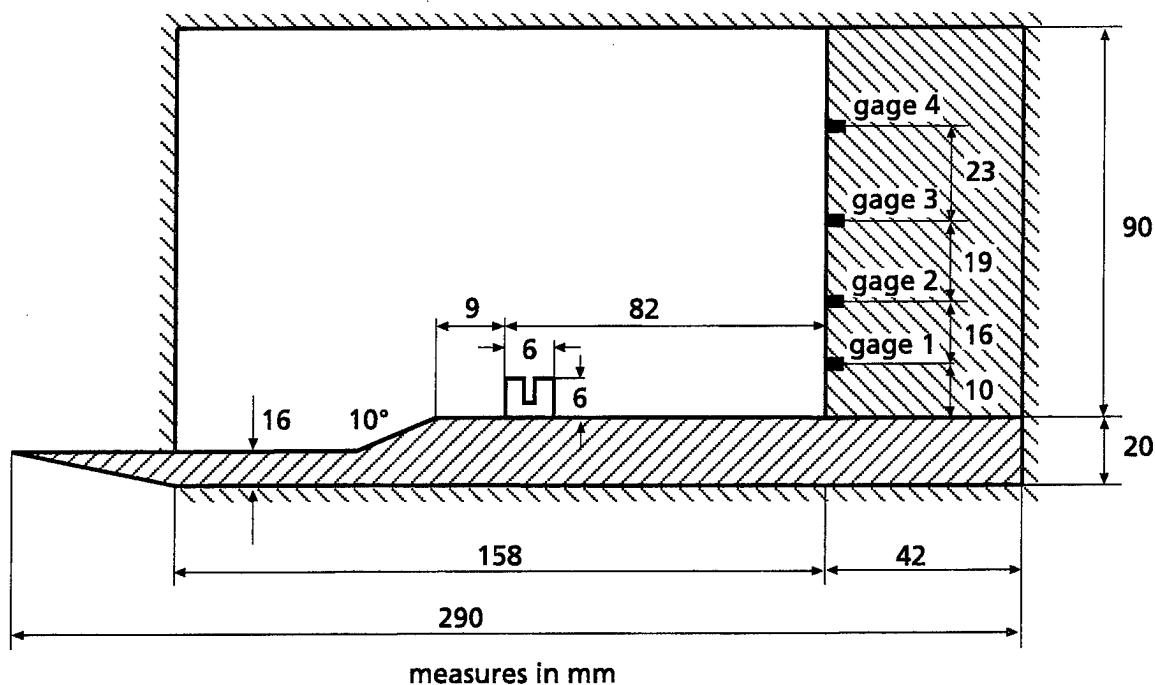
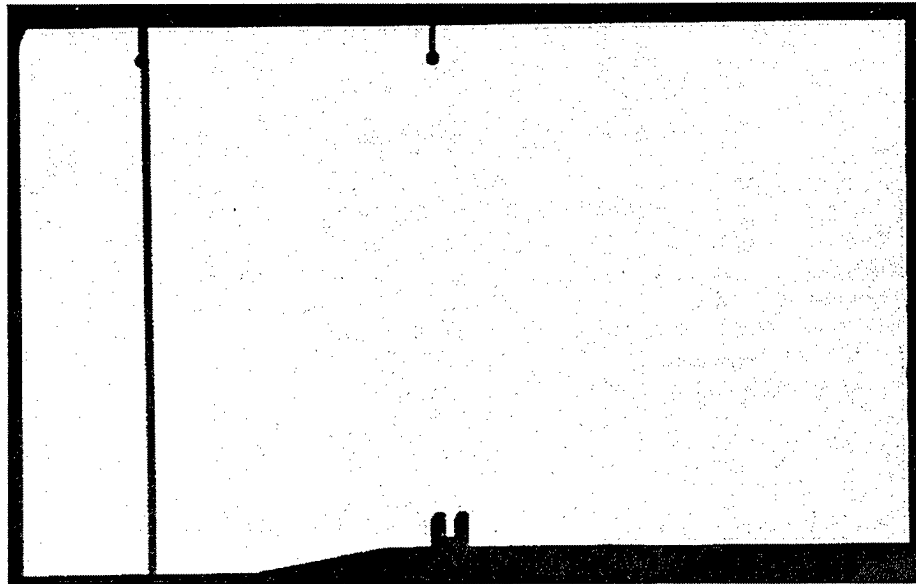
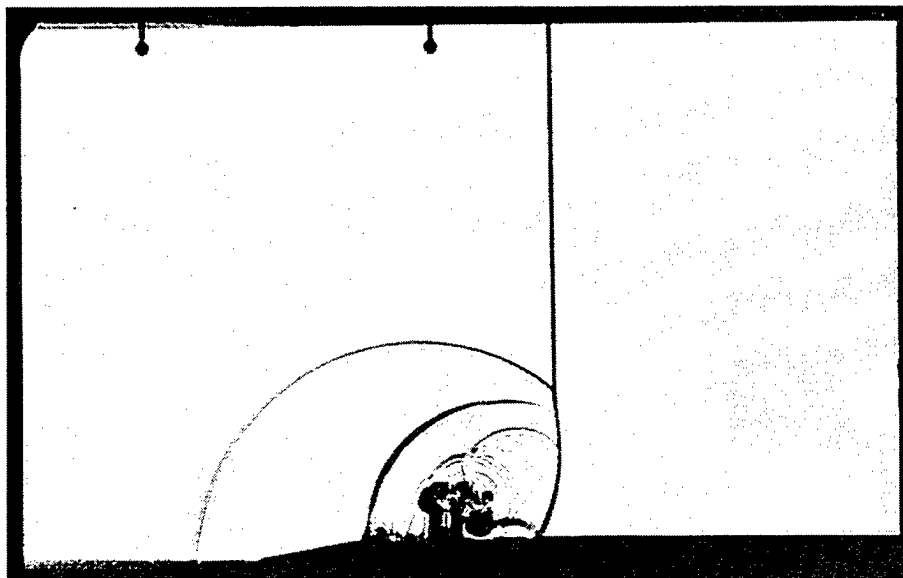


Figure 129. Sketch of the 2-D Khobar Towers model for shock tube tests.



15503/1

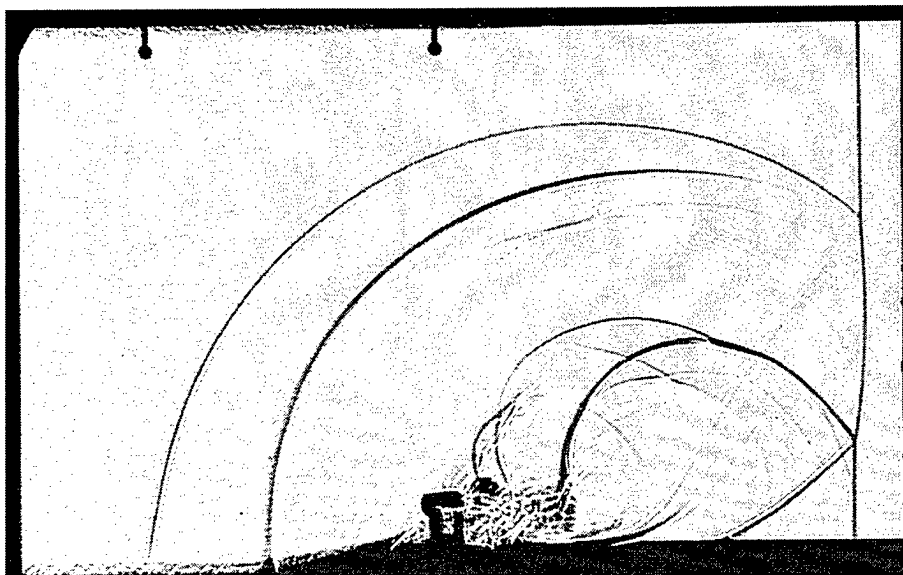
a) $t = 0.000$ ms



15503/5

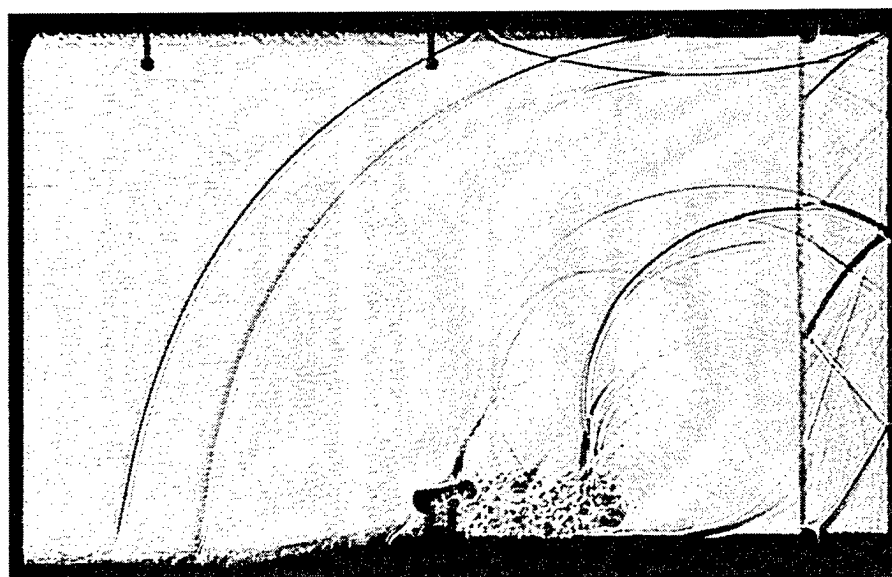
b) $t = 0.120$ ms

Figure 130. Sequence of shadowgraphs. $M_s = 1.7$. (test 15 503)



15503/8

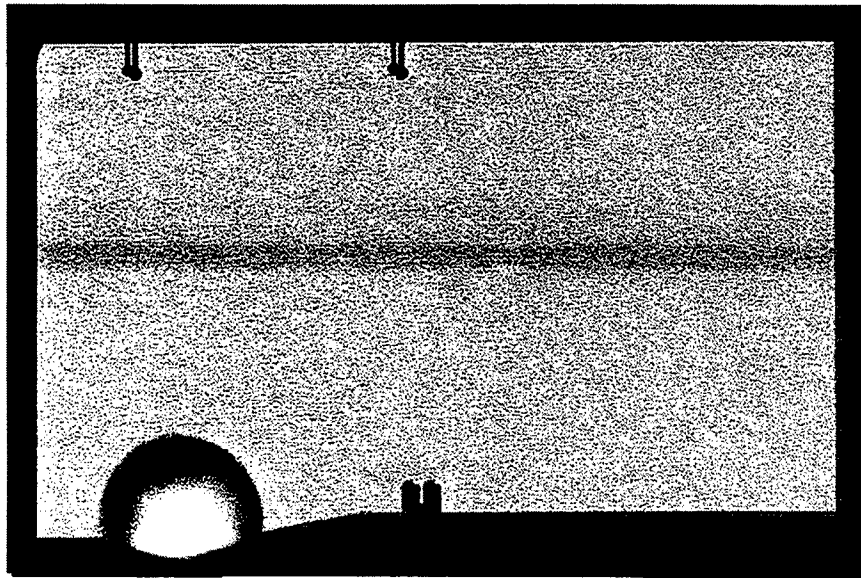
c) $t = 0.210$ ms



15503/10

d) $t = 0.270$ ms

Figure 130. Sequence of shadowgraphs. $M_s = 1.7$. (test 15 503) (Continued)



15517/1

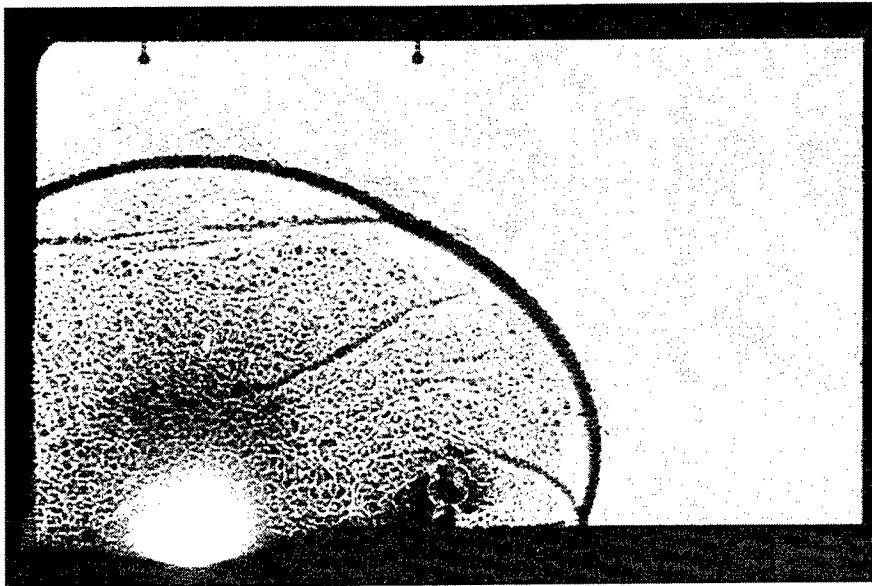
a) $t = 0,010$ ms after ignition



15517/4

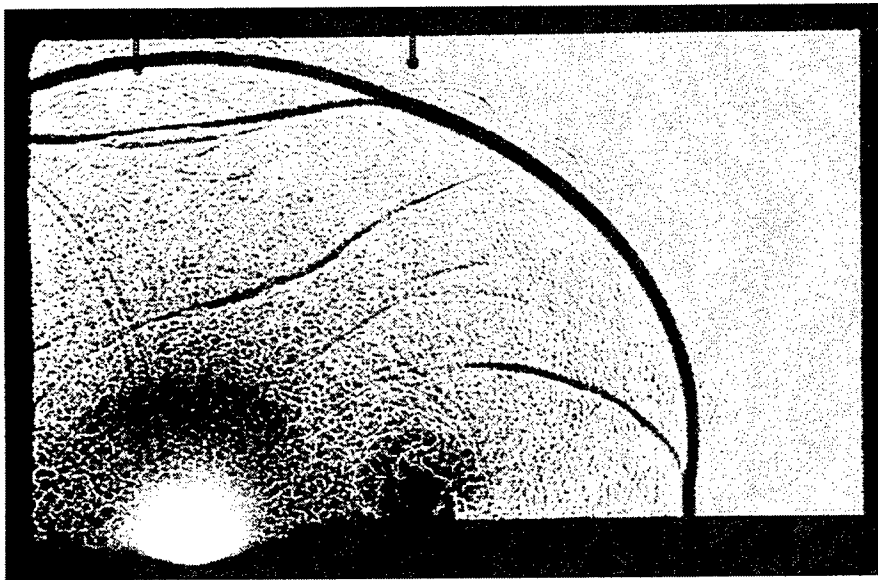
b) $t = 0,055$ ms after ignition

Figure 131. Sequence of shadowgraphs of a detonation test in the shock tube. The windows of the observation chamber were removed. As charge a HX2 igniter was used. (test: 15 517)



15517/7

c) $t = 0,100$ ms after ignition



15517/10

d) $t = ,0145$ ms after ignition

Figure 131. Sequence of shadowgraphs of a detonation test in the shock tube. The windows of the observation chamber were removed. As charge a HX2 igniter was used. (test: 15 517) (Continued)

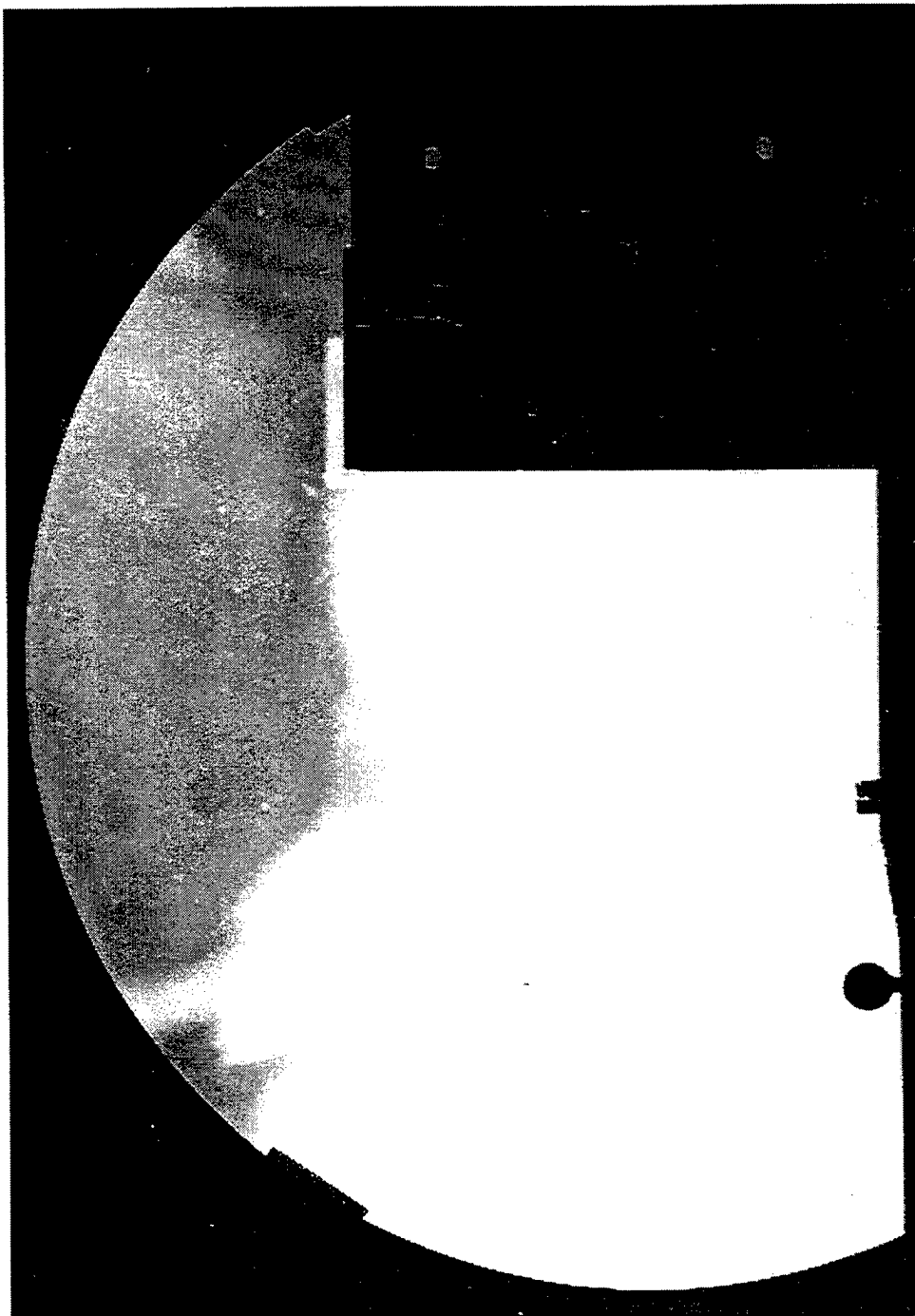
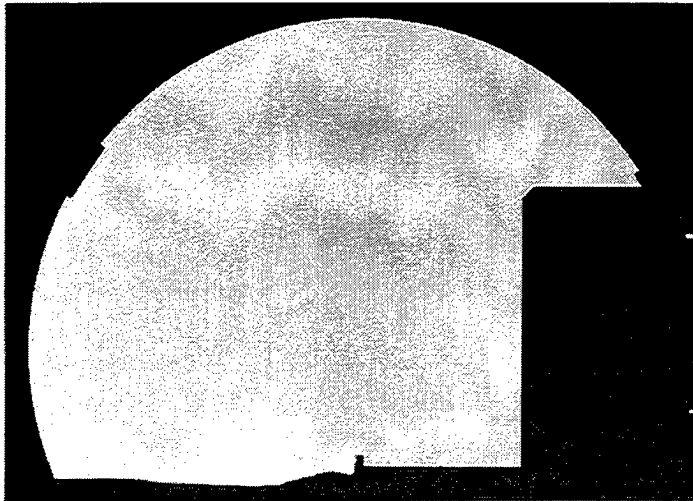
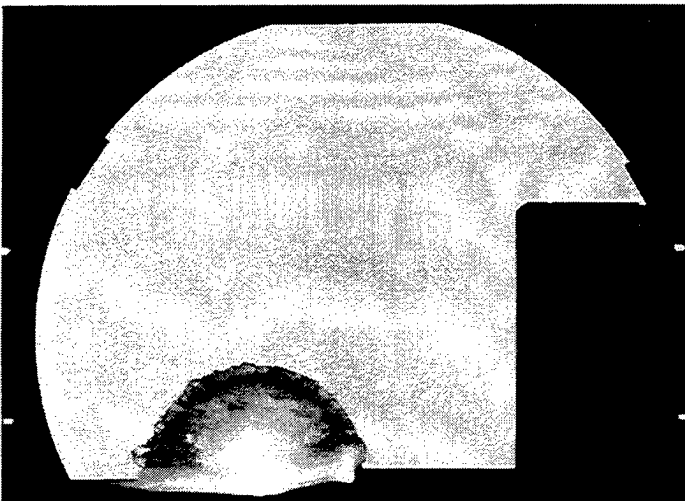


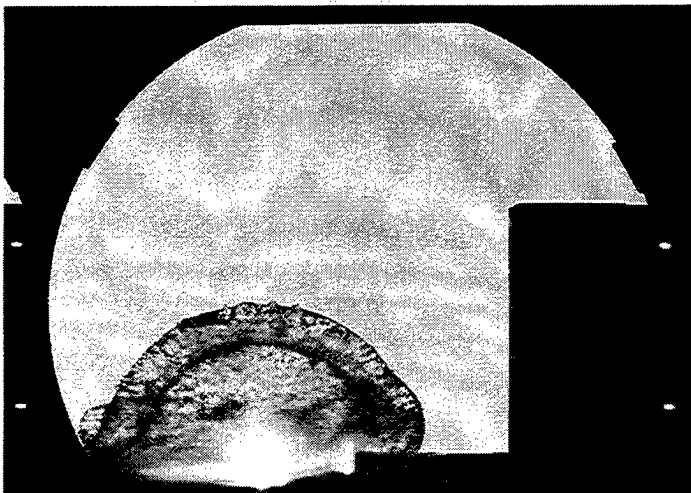
Figure 132. Open-shutter picture of a test with a bare spherical charge of 0.98-g Nitropenta, corresponding in full-scale to 20 700 lb. TNT.
(test 15 545)



a) $t = 0,0026$ ms after
ignition (15 545/1)



b) $t = 0,0176$ ms after
ignition (15 545/2)



c) $t = 0,0326$ ms after
ignition (15 545/3)

Figure 133. Sequence of shadowgraphs in side view of the loading of the Khobar Towers building by the blastwave generated by a bare spherical charge of 0.98-g Nitrophen. (test 15 545)



d) $t = 0,0476$ ms after
ignition (15 545/4)



e) $t = 0,0626$ ms after
ignition (15 545/5)

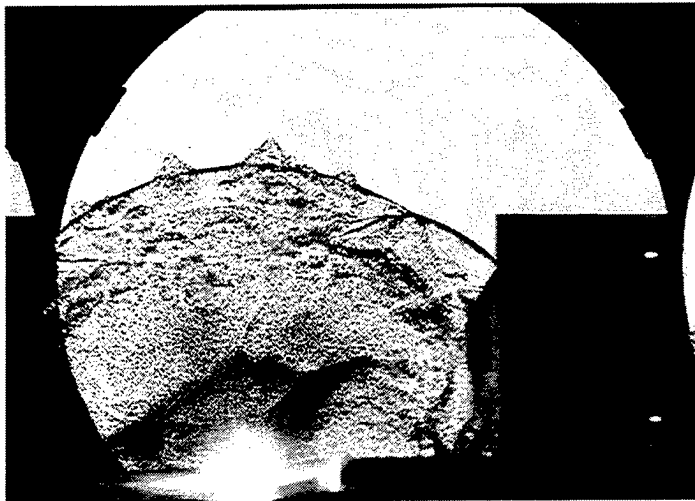


f) $t = 0,0776$ ms after
ignition (15 545/6)

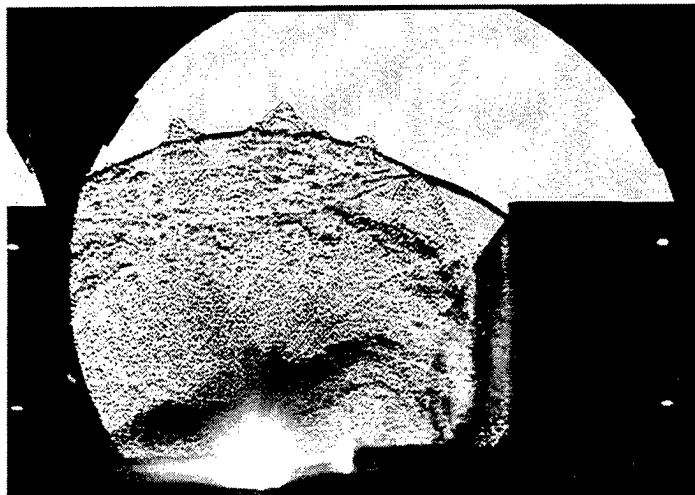
Figure 133. Sequence of shadowgraphs in side view of the loading of the Khobar Towers building by the blastwave generated by a bare spherical charge of 0.98-g Nitrophen. (test 15 545) (Continued)



g) $t = 0,0926$ ms after
ignition (15 545/7)

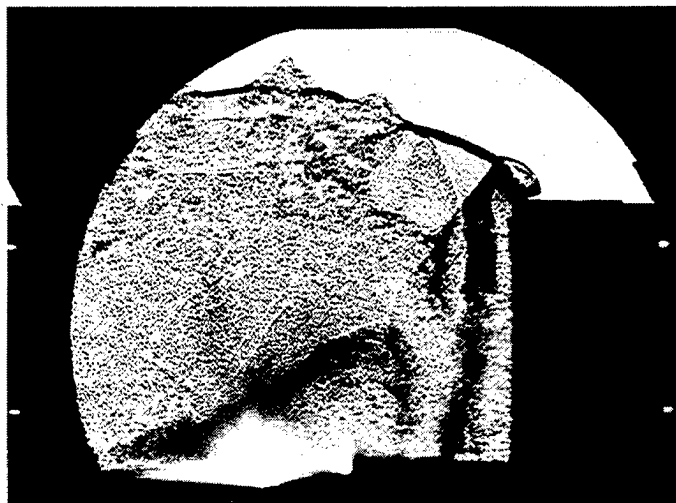


h) $t = 0,1076$ ms after
ignition (15 545/8)



i) $t = 0,2126$ ms after
ignition (15 545/9)

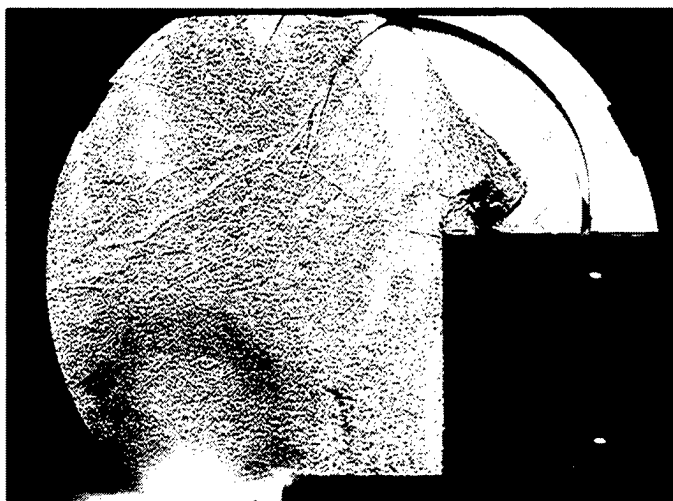
Figure 133. Sequence of shadowgraphs in side view of the loading of the Khobar Towers building by the blastwave generated by a bare spherical charge of 0.98-g Nitrophen. (test 15 545) (Continued)



k) $t = 0,1526$ ms after
ignition (15 545/11)

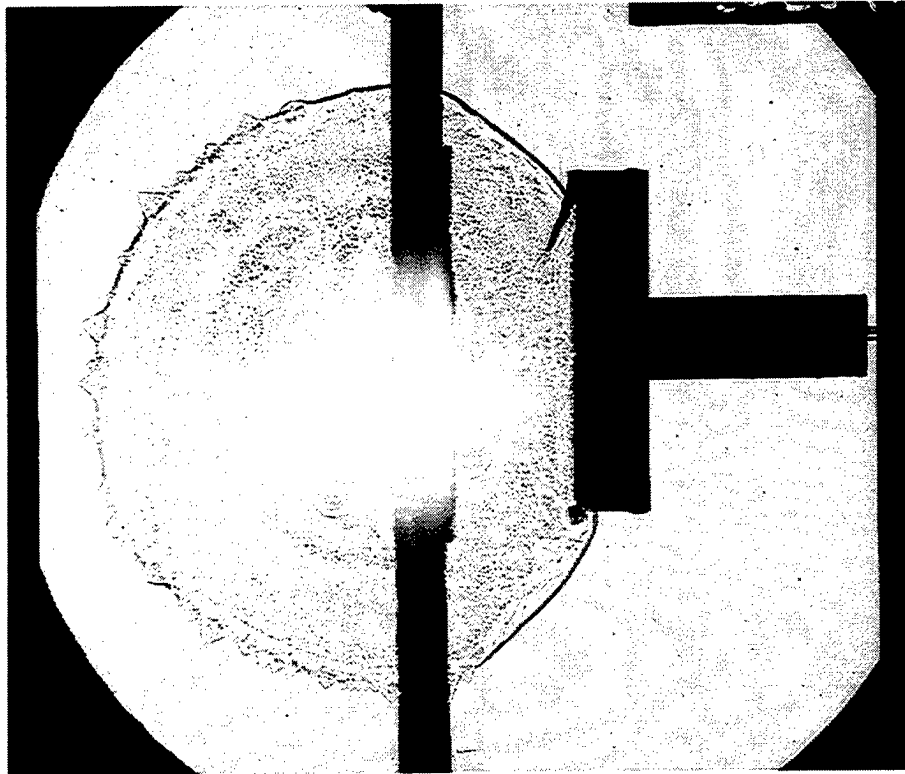


l) $t = 0,1976$ ms after
ignition (15 545/14)

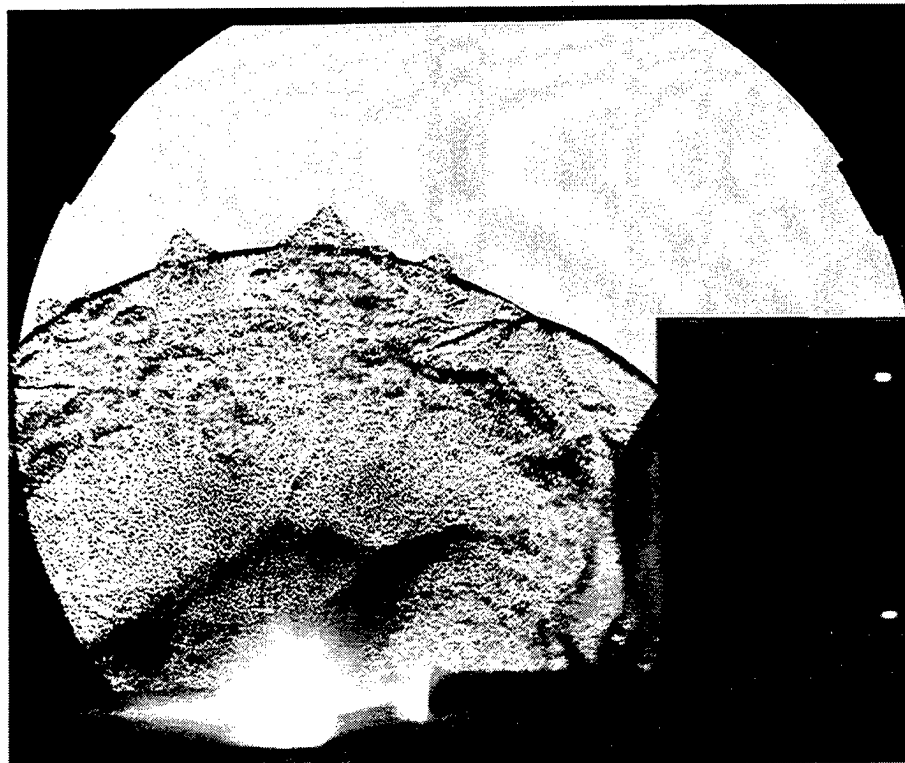


m) $t = 0,2726$ ms after
ignition (15 545/19)

Figure 133. Sequence of shadowgraphs in side view of the loading of the Khobar Towers building by the blastwave generated by a bare spherical charge of 0.98-g Nitrophen. (test 15 545) (Continued)

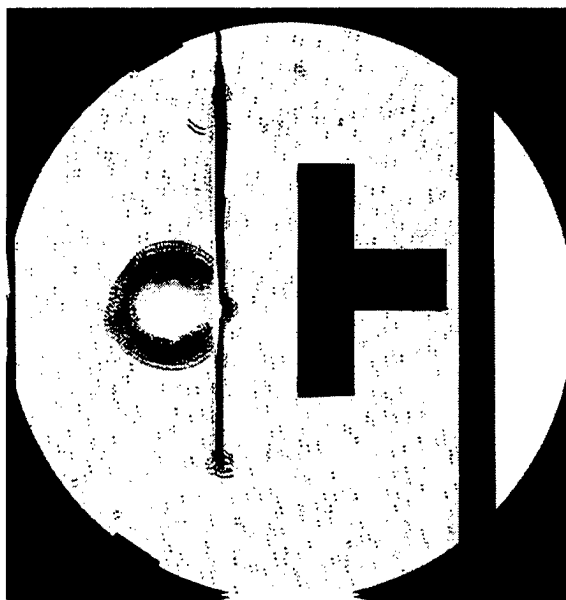


a) Top view. Spherical charge; $W = 1.00\text{-g}$ Nitropenta. Time after Ignition: $t = 0,110\text{ ms.}$ (test 0052 KT)

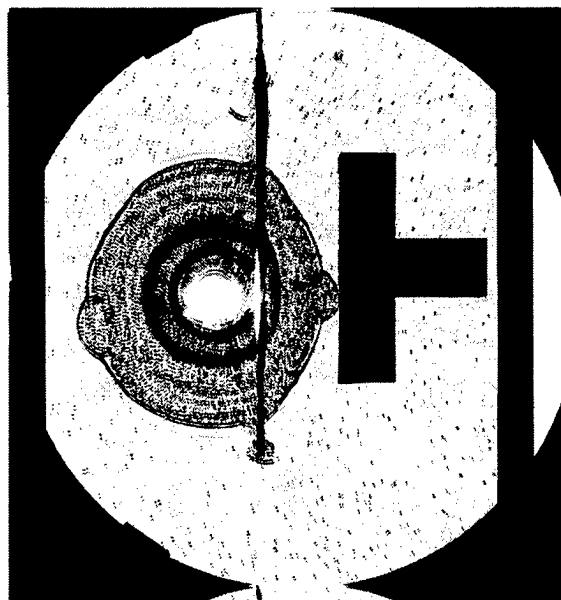


b) Side view. Spherical charge; $W = 0.98\text{-g}$ Nitropenta. Time after Ignition: $t = 0,1076\text{ ms.}$ (test 15 545/8)

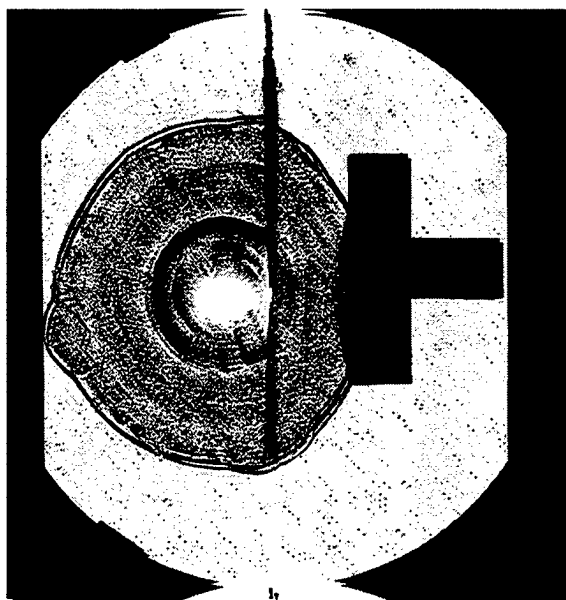
Figure 134. Shadowgraph of the flow field around the building.



a) $t = 0,0079 \text{ ms}$ (15 555/2)



b) $t = 0,0159 \text{ ms}$ (15 555/4)

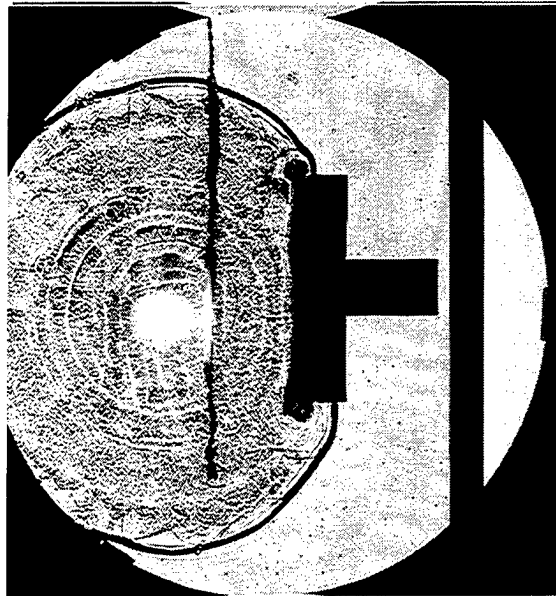


b) $t = 0,0239 \text{ ms}$ (15 555/6)

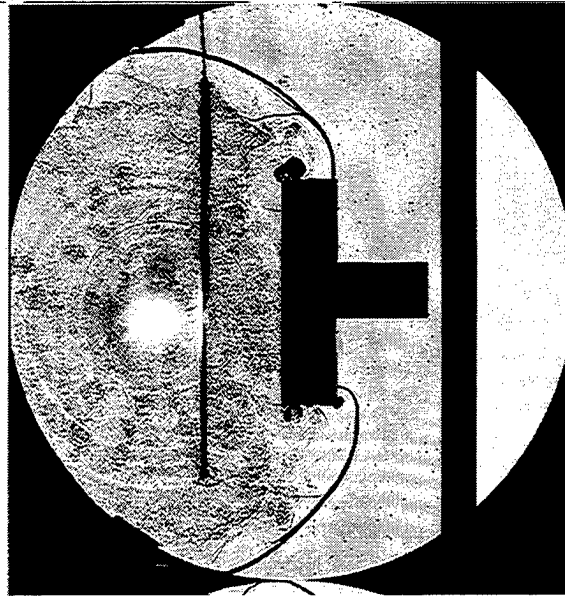


d) $t = 0,0319 \text{ ms}$ (15 555/8)

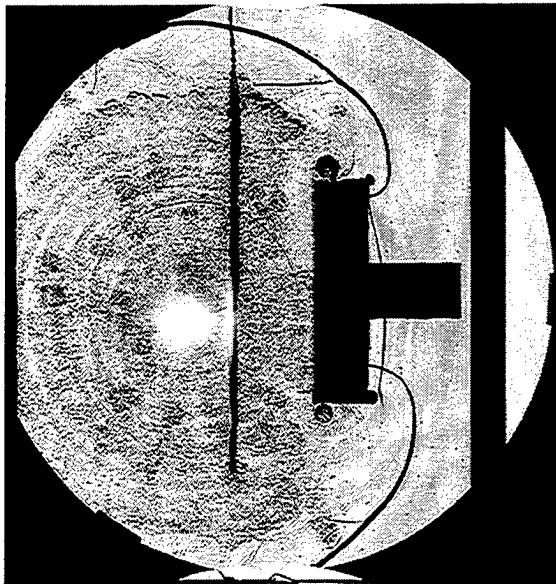
Figure135. Sequence of shadowgraphs in top view of a test with a spherical charge.
Scaling factor of the model is 1 : 350.
Charge weight: $W = 0.19\text{-g}$.



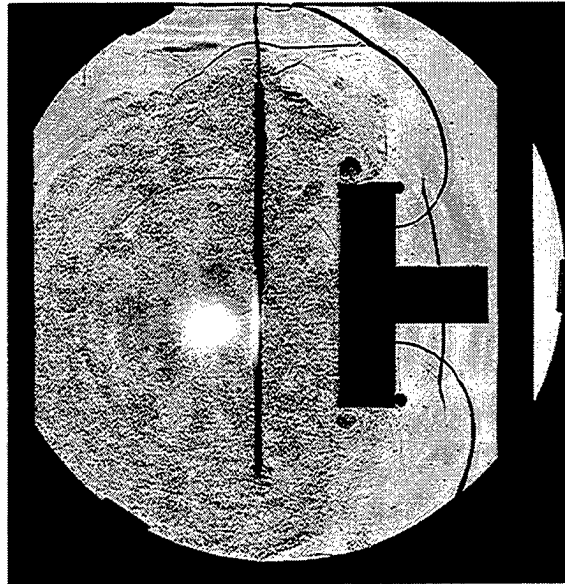
e) $t = 0,0399 \text{ ms}$ (15 555/10)



f) $t = 0,0519 \text{ ms}$ (15 555/13)

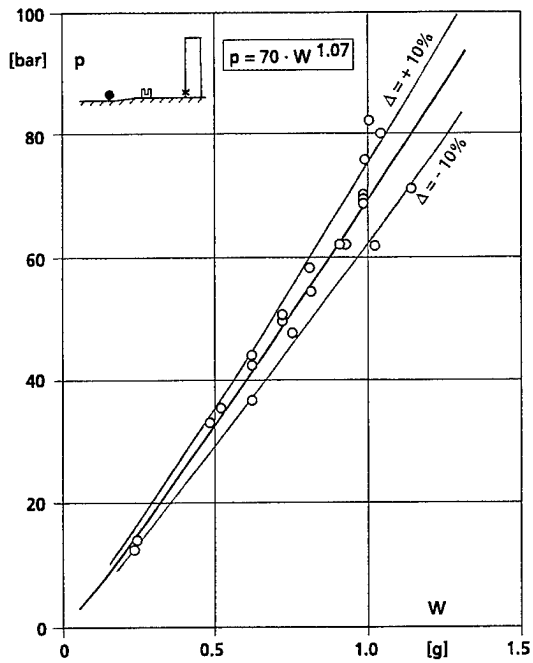


g) $t = 0,0639 \text{ ms}$ (15 555/16)

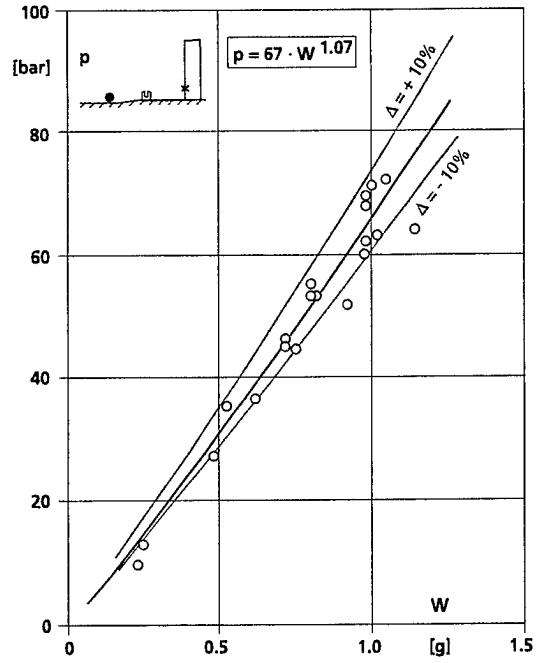


h) $t = 0,0799 \text{ ms}$ (15 555/20)

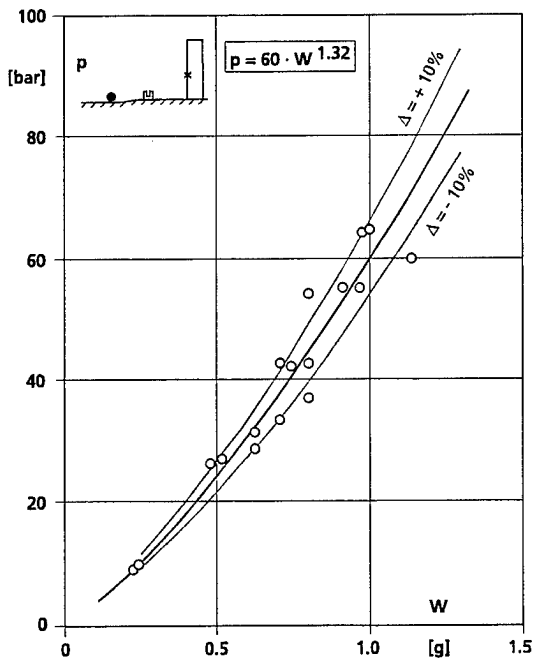
Figure135. Sequence of shadowgraphs in top view of a test with a spherical charge.
Scaling factor of the model is 1 : 350.
Charge weight: $W = 0.19\text{-g}$. (Continued)



a) gage position 1

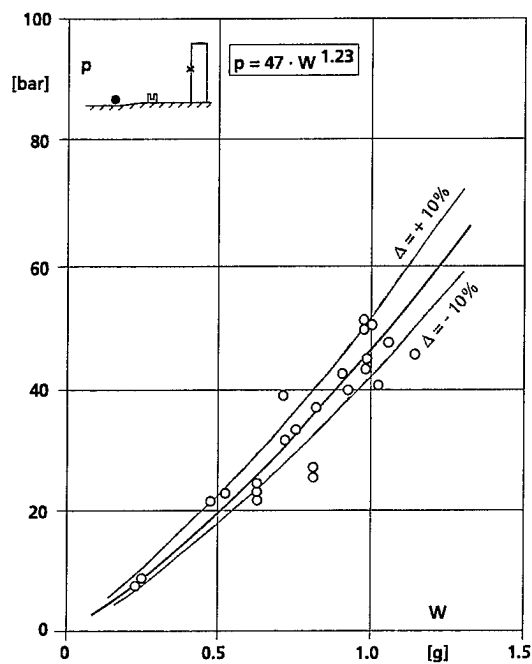


b) gage position 2

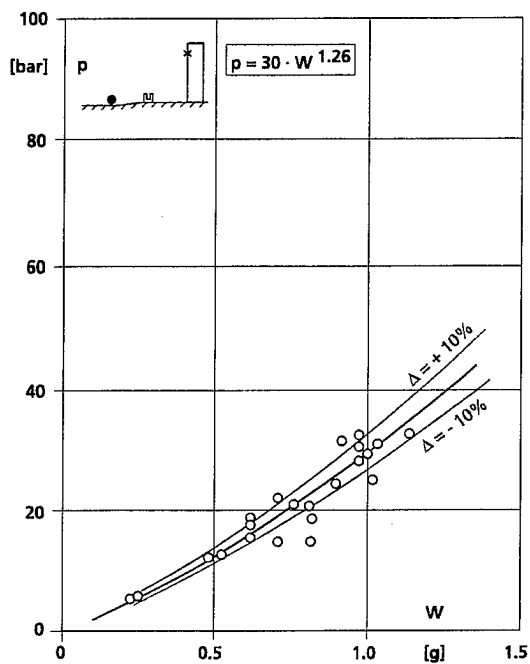


c) gage position 3

Figure 136. Peak overpressure at the front wall vs weight of the spherical charge.

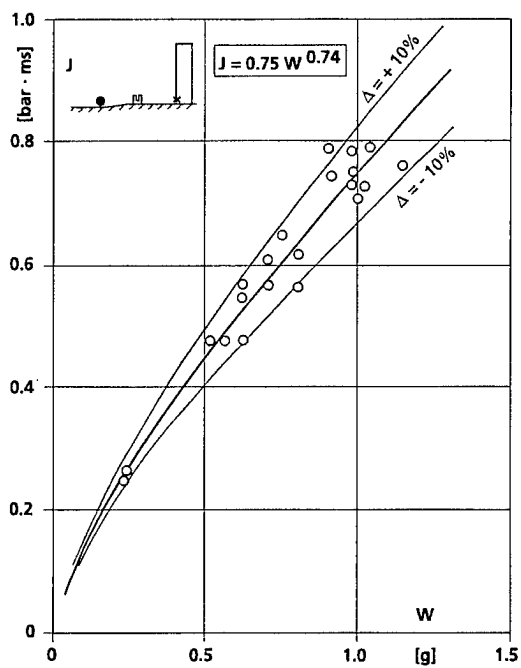


d) gage position 4

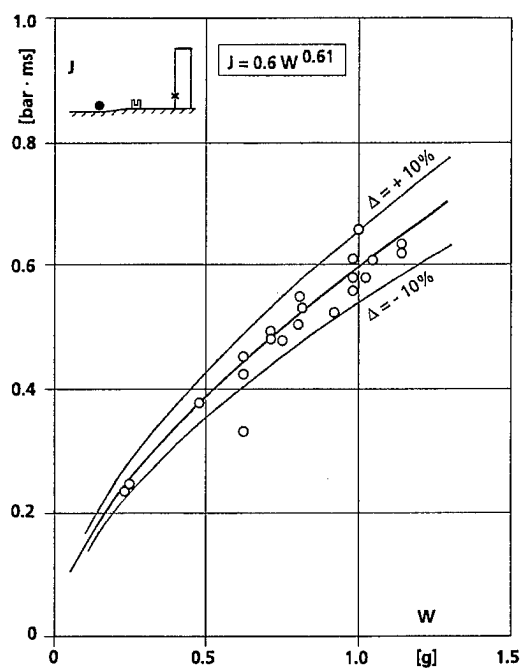


e) gage position 5

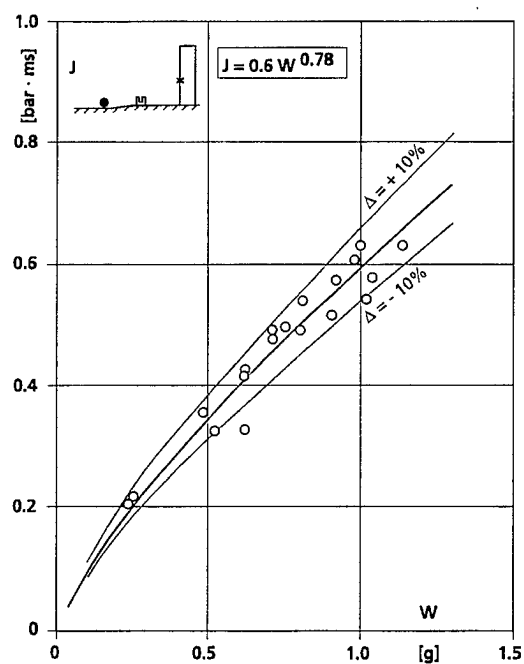
Figure 136. Peak overpressure at the front wall vs weight of the spherical charge. (Continued)



a) gage position 1

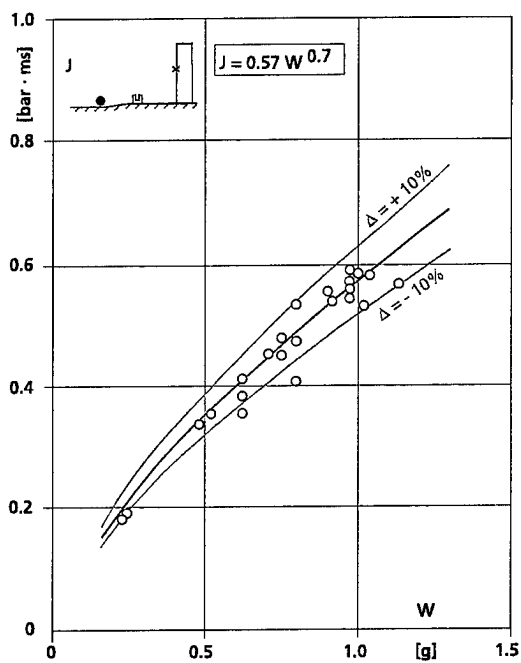


b) gage position 2

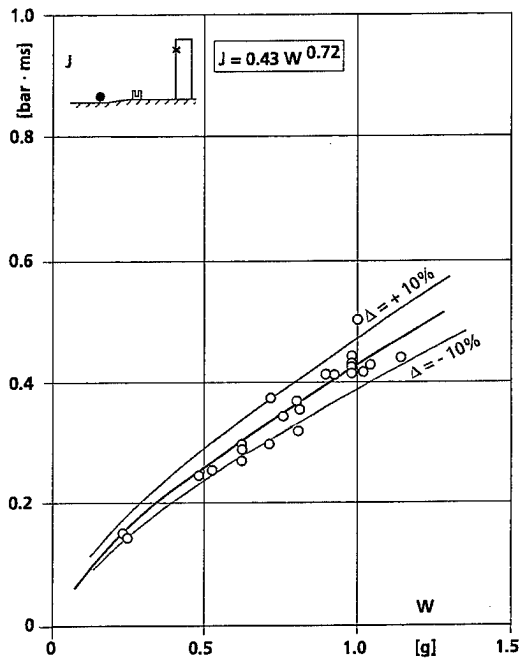


c) gage position 3

Figure 137. Overpressure-impulse at the front wall vs weight of the spherical charge.



d) gage position 4



e) gage position 5

Figure 137. Overpressure-impulse at the front wall vs weight of the spherical charge.
(Continued)

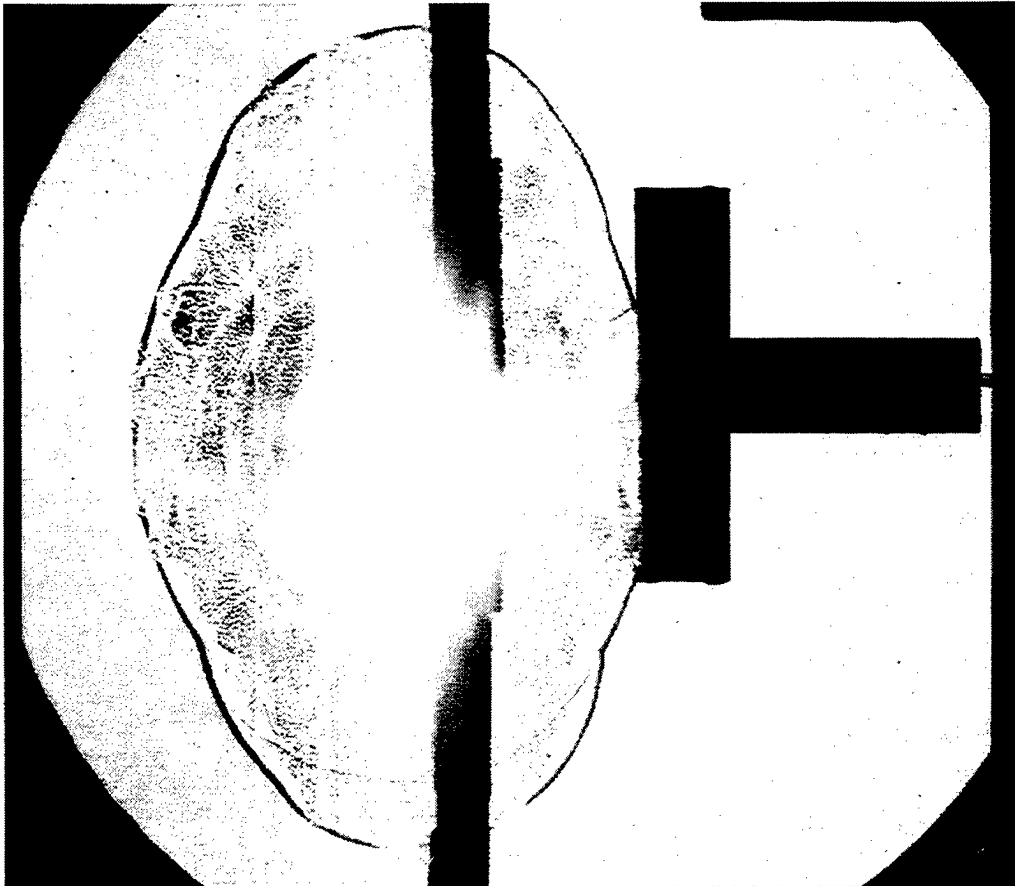


Figure 138. Loading of the Khobar Towers model by an axial ignited unconfined cylindrical charge. Single frame shadowgraph in top view. $HOB = 14 \text{ mm} = 2D$; $L : D = 4 : 1$
time after ignition: $t = 0,110 \text{ ms}$; $W = 1.34\text{-g}$; (Test 0055 KT)

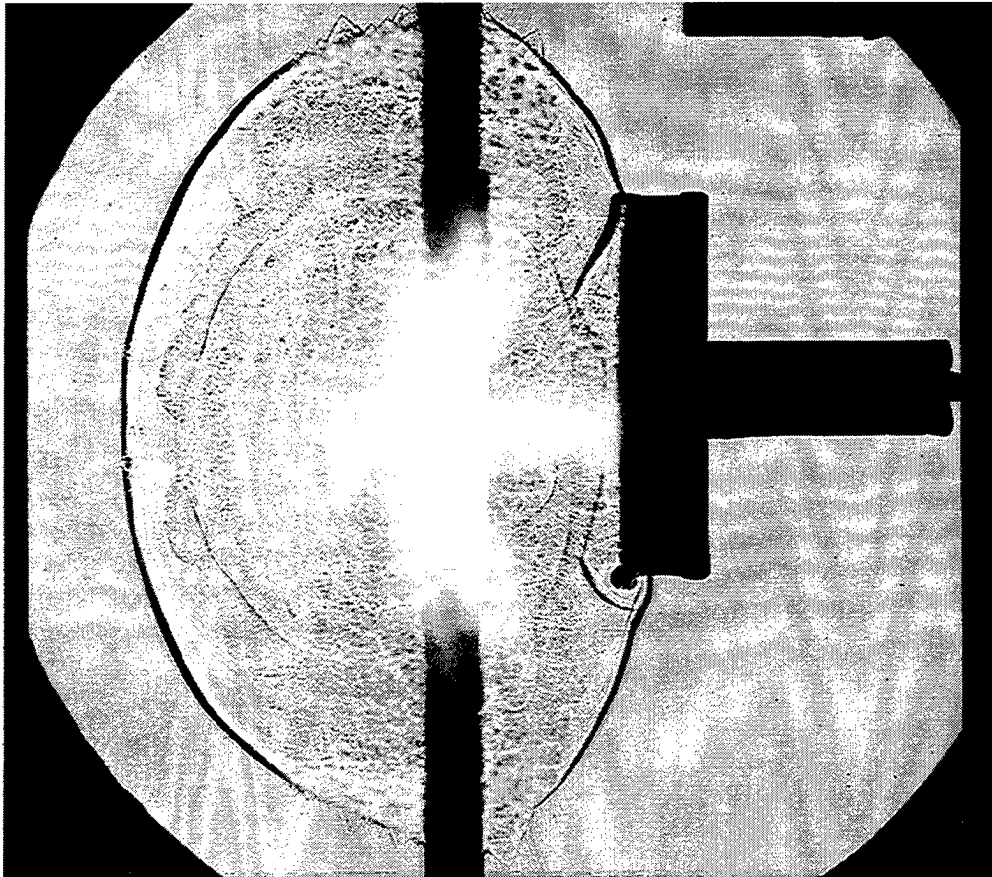
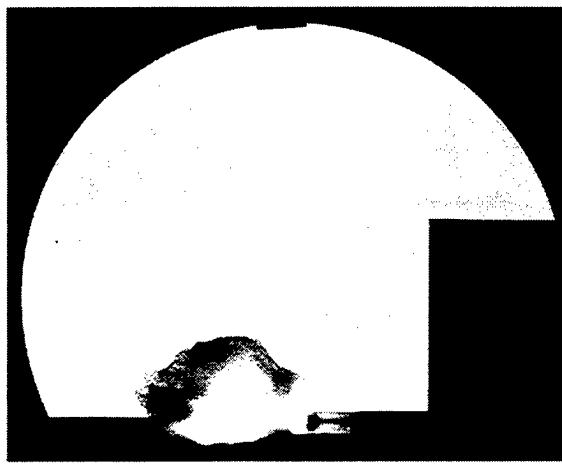
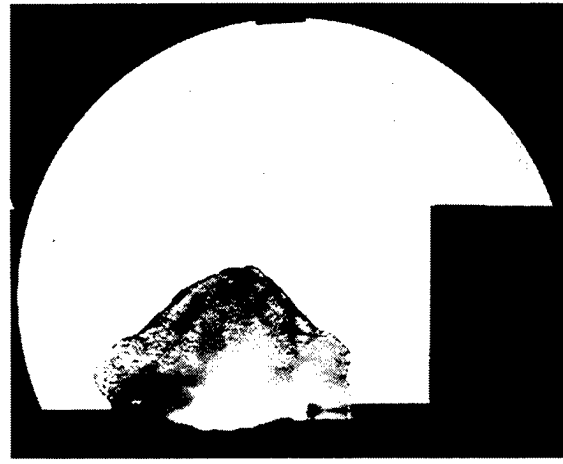


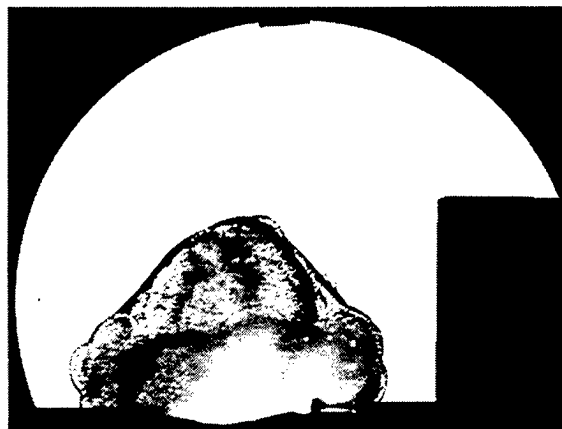
Figure 139. Loading of the Khobar Towers model by a face ignited unconfined cylindrical charge. Single frame shadowgraph in top view. HOB = 14 mm = 2D; L : D = 4
time after ignition: $t = 0,140$ ms; $W = 1.12$ -g; test 0058 KT)



a) $t = 0,020 \text{ ms}$ (15 567/2)



b) $t = 0,035 \text{ ms}$ (15 567/3)

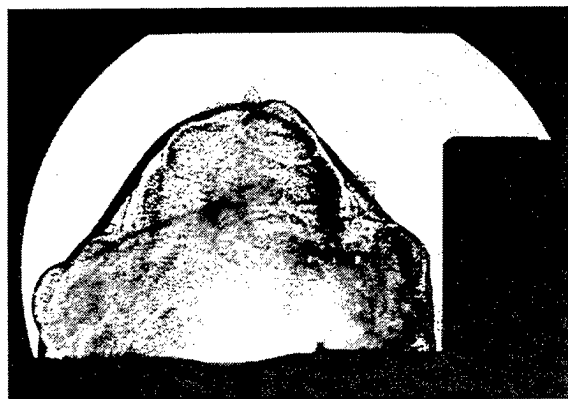


c) $t = 0,050 \text{ ms}$ (15 567/4)

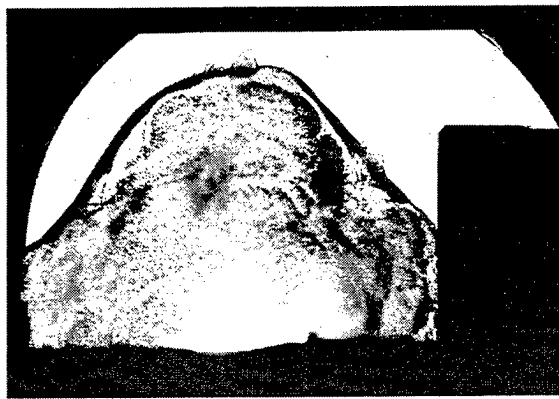


d) $t = 0,065 \text{ ms}$ (15 567/5)

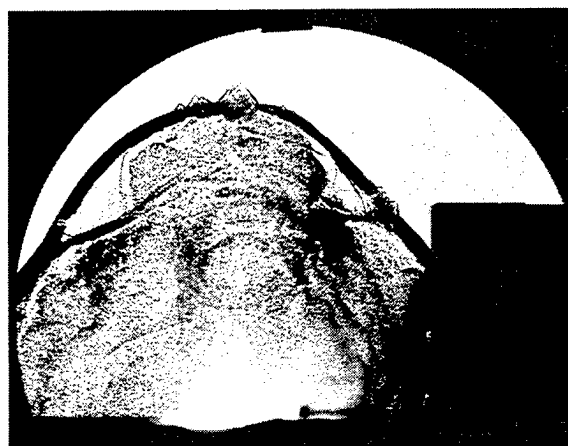
Figure 140. Loading of the Khobar Towers model by an axial ignited unconfined cylindrical charge. Shadowgraph sequence in side view. HOB = 14 mm = 2D; L : D = 4 : 1; W = 1.27-g time after Ignition.



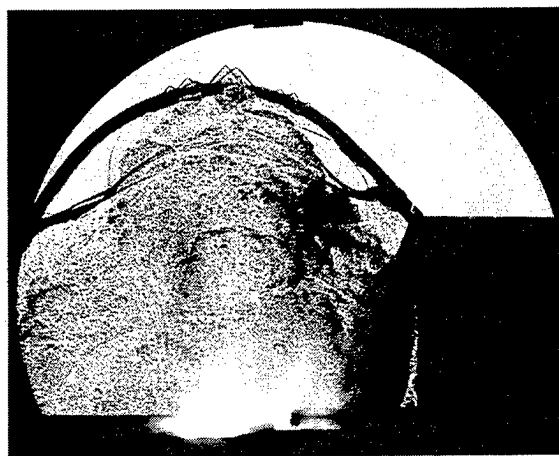
e) $t = 0,080 \text{ ms}$ (15 567/6)



f) $t = 0,095 \text{ ms}$ (15 567/7)

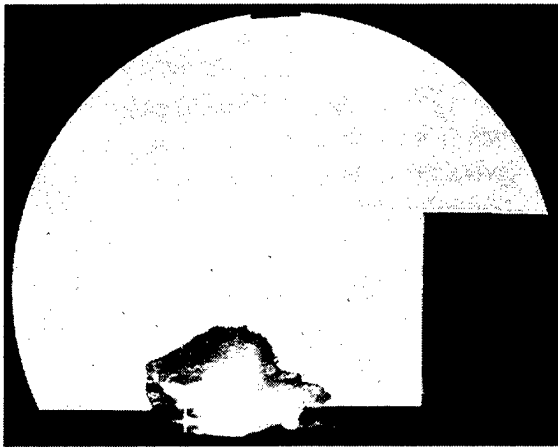


g) $t = 0,125 \text{ ms}$ (15 567/9)

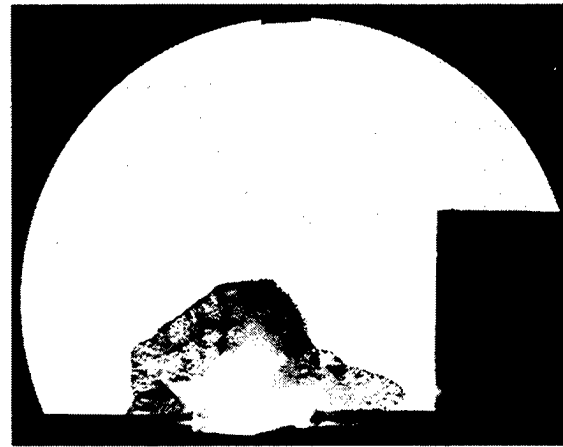


h) $t = 0,155 \text{ ms}$ (15 567/11)

Figure 140. Loading of the Khobar Towers model by an axial ignited unconfined cylindrical charge. Shadowgraph sequence in side view. HOB = 14 mm = 2D; L : D = 4 : 1; W = 1.27-g time after Ignition. (Continued)



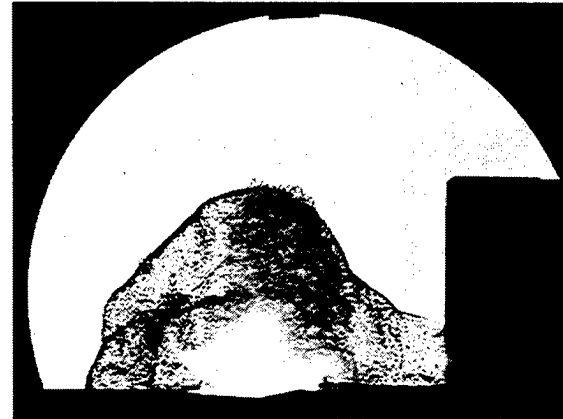
a) $t = 0,0188 \text{ ms}$ (15 574/2)



b) $t = 0,0308 \text{ ms}$ (15 574/3)

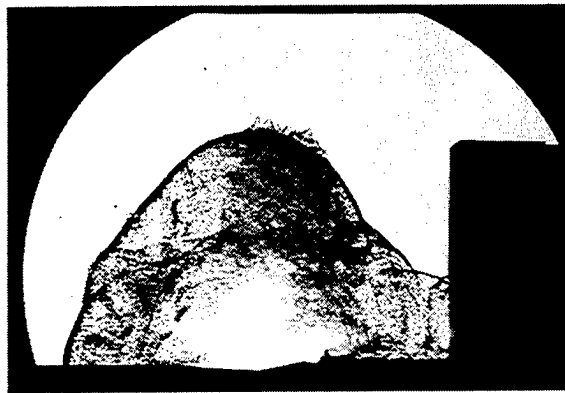


c) $t = 0,0428 \text{ ms}$ (15 574/4)



d) $t = 0,0548 \text{ ms}$ (15 574/5)

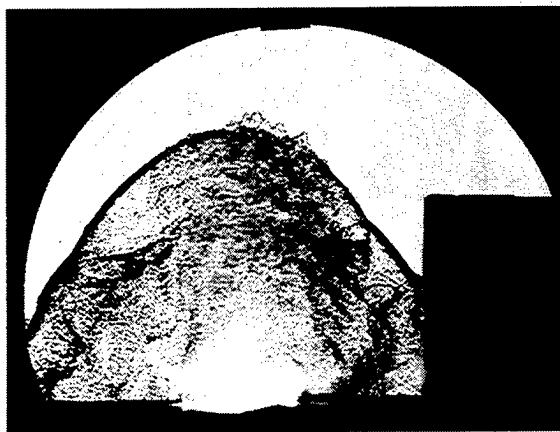
Figure 141. Loading of the Khobar Towers model by a face ignited unconfined cylindrical charge. Shadowgraph sequence in side view. HOB = 14 mm = 2D; L : D = 4 : 1; W = 0.984-g. Time after Ignition, see above.



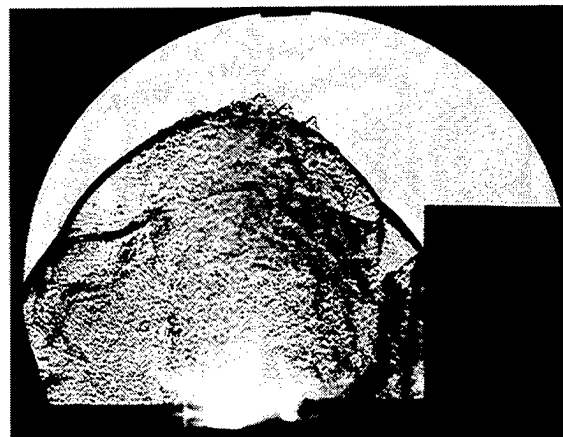
e) $t = 0,0668 \text{ ms}$ (15 574/6)



f) $t = 0,0788 \text{ ms}$ (15 574/7)



g) $t = 0,1028 \text{ ms}$ (15 574/9)



h) $t = 0,1268 \text{ ms}$ (15 574/11)

Figure 141. Loading of the Khobar Towers model by a face ignited unconfined cylindrical charge. Shadowgraph sequence in side view. HOB = 14 mm = 2D; L : D = 4 : 1; W = 0.984-g. Time after Ignition, shown above. (Continued)



Figure 142. Loading of the Khobar Towers model by an axial ignited confined cylindrical charge. Single frame shadowgraph in top view. Time after ignition $t = 0,160$ ms; $W = 1.46$ -g (Test 0061 KT)

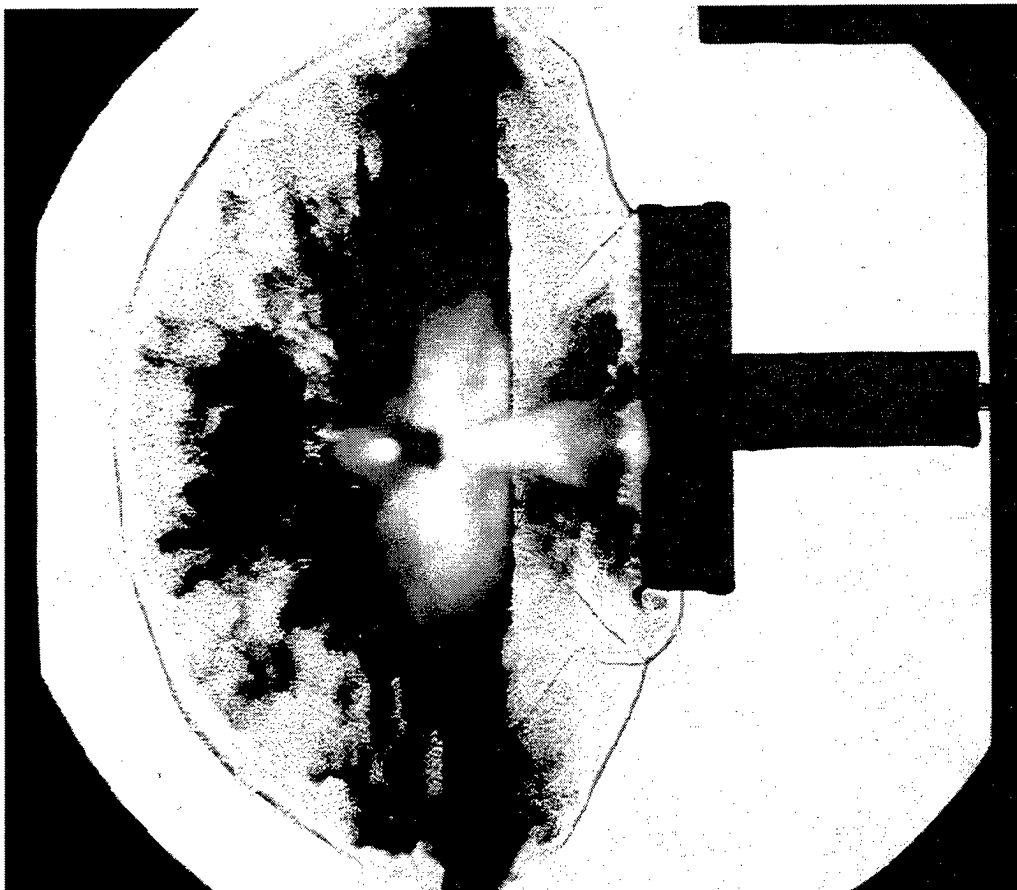
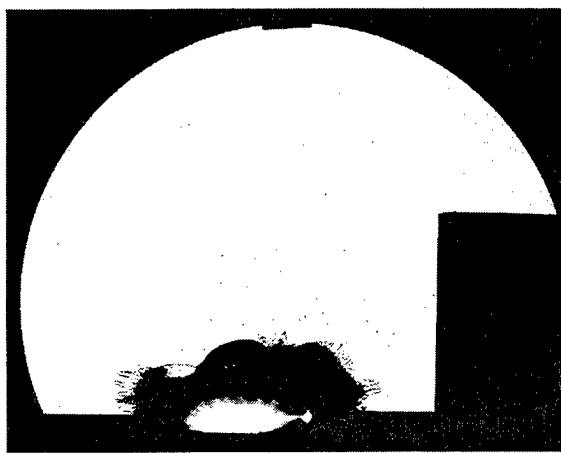


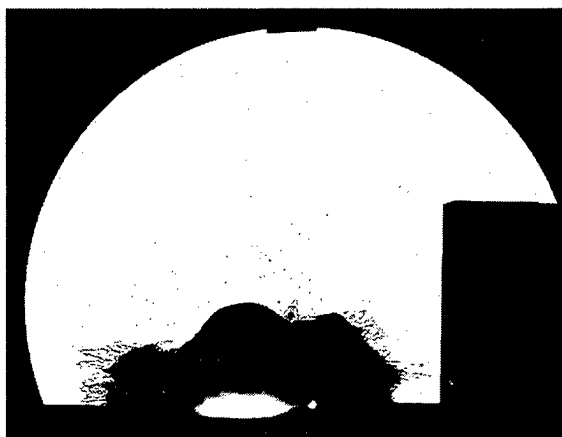
Figure 143. Loading of the Khobar Towers model by a face ignited confined cylindrical charge. Single frame shadowgraph in top view. Time after ignition $t = 0,160$ ms $W = 1.11$ -g (test 0060 KT).



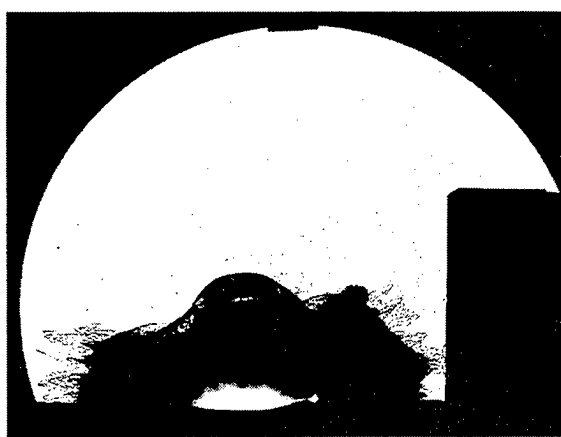
a) $t = 0,0203 \text{ ms}$ (15 598/2)



b) $t = 0,0323 \text{ ms}$ (15 598/3)



c) $t = 0,0443 \text{ ms}$ (15 598/4)



d) $t = 0,0563 \text{ ms}$ (15 598/5)

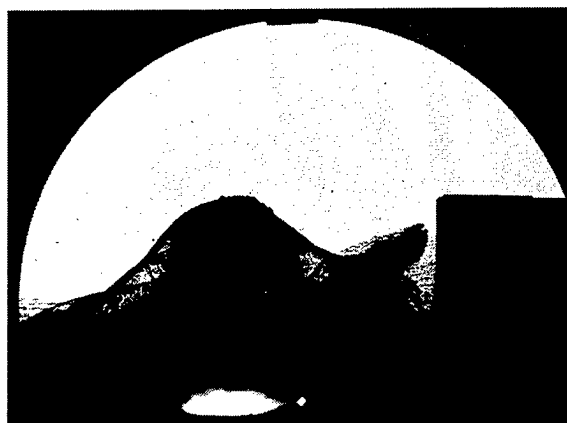
Figure 144. Loading of the Khobar Towers model by an axial ignited confined cylindrical charge. Single frame shadowgraph in side view.
 $W = 1.22\text{-g}$ (test 15 598). Time after ignition, see **above**.



e) $t = 0,0683 \text{ ms}$ (15 598/6)



f) $t = 0,0803 \text{ ms}$ (15 598/7)

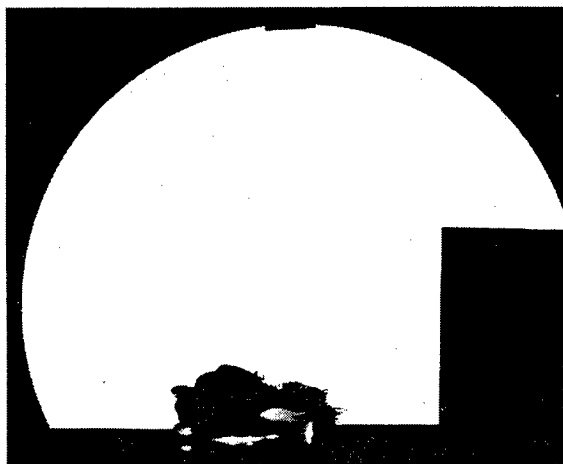


g) $t = 0,1043 \text{ ms}$ (15 598/9)



h) $t = 0,1763 \text{ ms}$ (15 598/15)

Figure 144. Loading of the Khobar Towers model by an axial ignited confined cylindrical charge. Single frame shadowgraph in side view.
 $W = 1.22\text{-g}$ (test 15 598). Time after ignition, see **above**. (Continued)



a) $t = 0,0216 \text{ ms}$ (15 575/2)



b) $t = 0,0336 \text{ ms}$ (15 575/3)



c) $t = 0,0456 \text{ ms}$ (15 575/4)



d) $t = 0,0576 \text{ ms}$ (15 575/5)

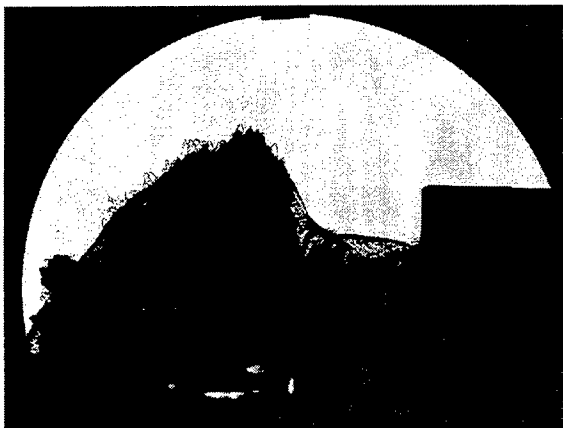
Figure 145. Loading of the Khobar Towers model by a face ignited confined cylindrical charge. Single frame shadowgraph in side view. $W = 1.32\text{-g}$ (test 15 575). Time after Ignition, see above.



e) $t = 0,0696 \text{ ms}$ (15 575/6)



f) $t = 0,0816 \text{ ms}$ (15 575/7)



f) $t = 0,1056 \text{ ms}$ (15 575/9)



h) $t = 0,1296 \text{ ms}$ (15 575/11)

Figure 145. Loading of the Khobar Towers model by a face ignited confined cylindrical charge. Single frame shadowgraph in side view. $W = 1.32\text{-g}$ (test 15 575). Time after Ignition, see above. (Continued)

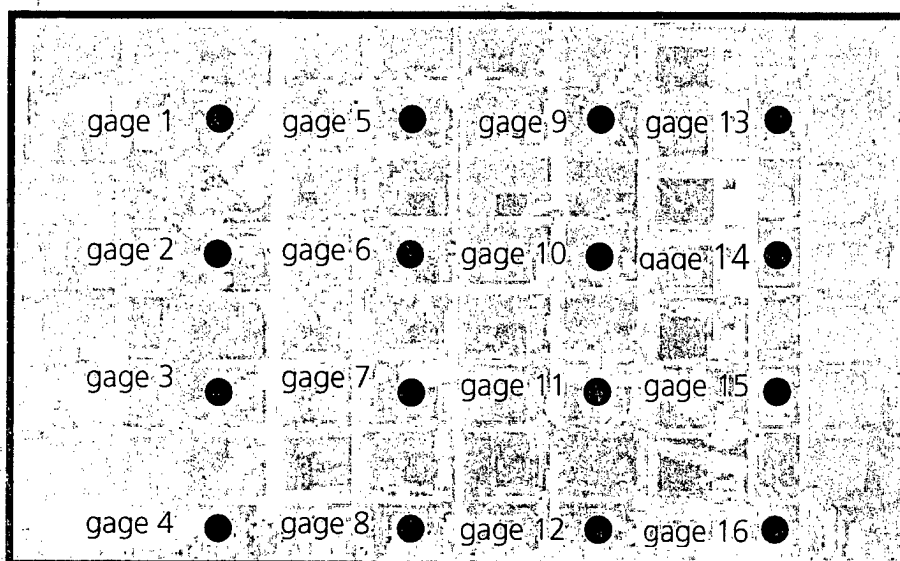
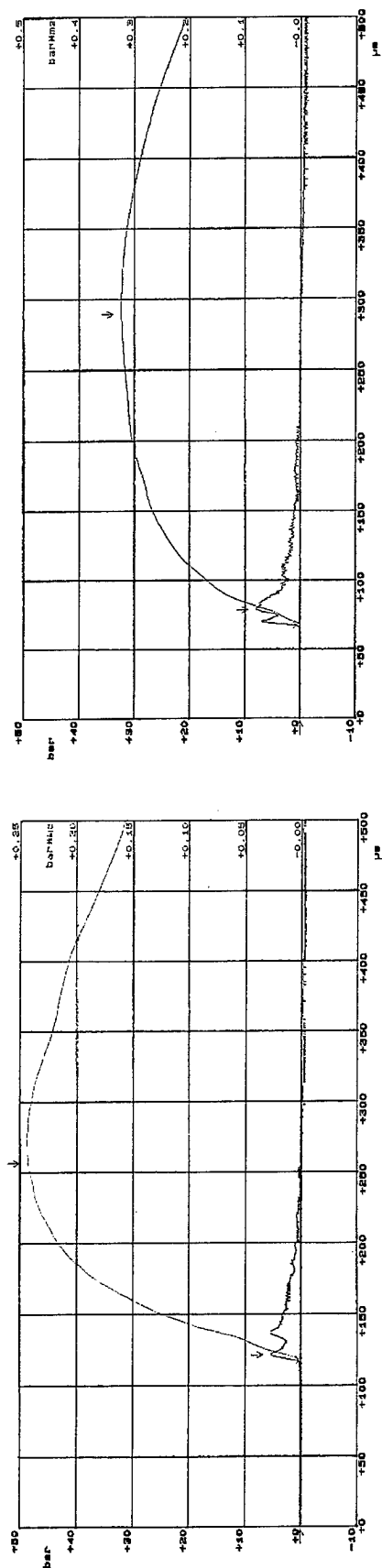
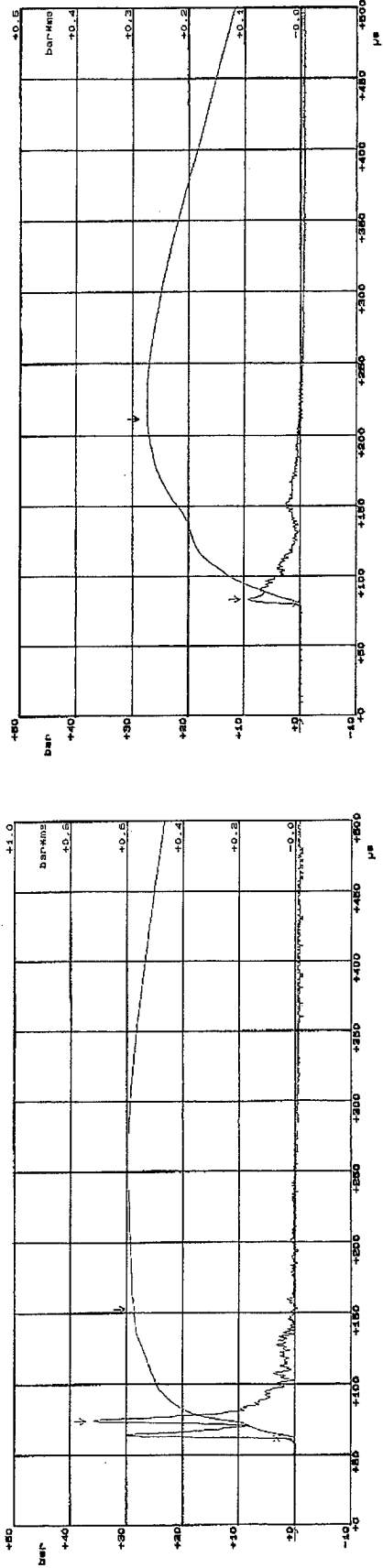


Figure 146. Location of the pressure gages in the front wall of the model. A photograph of the destroyed facade of the original edifice is underlaid.



a) Gage location No. 4

b) Gage location No. 8



c) Gage location No. 12

d) Gage location No. 16

Figure 147. Pressure-time histories at 4 different locations of the front wall. The charge was confined and face ignited. Shadowgraphs of the same test are given in Figure 145. $W = 1.32\text{-g}$; (test 15 575).

Section 6

References

(ALL REFERENCES IN THIS LIST ARE UNCLASSIFIED)

- [1] Reichenbach, H. "Laboratory-Scale Airblast Precursor Experiments - Volume 1: Exploratory Shock Tube Tests", DNA-TR-85-352 and EMI report E 22/85. (UNCLASSIFIED)
- [2] Reichenbach, H. "Laboratory-Scale Airblast Precursor Experiments - Volume 2: Parametric Studies", DNA-TR-85-352V2 and EMI report E 6/87. (UNCLASSIFIED)
- [3] Behrens, K. , Neuwald, P. , Reichenbach, H. , Kuhl, A.L. " Laboratory Experiments of Explosions", DNA-TR- 94-119. (UNCLASSIFIED)
- [4] Neuwald, P. Reichenbach, H. "A New Color Schlieren Setup" EMI report E 27/93. (UNCLASSIFIED)
- [5] Reichenbach, H., Neuwald P. "Fluid-Dynamics of Explosions in Multi-Chamber Systems - Phenomenology Test Program":
 - Quarterly Letter Report No. 1 3. January 1995 (UNCLASSIFIED)
 - Quarterly Letter Report No. 2 30. March 1995 (UNCLASSIFIED)
 - Quarterly Letter Report No. 3 25. July 1995 (UNCLASSIFIED)
 - Quarterly Letter Report No. 4 12. October 1995 (UNCLASSIFIED)
 - Quarterly Letter Report No. 5 31. January 1996 (UNCLASSIFIED)
 - Quarterly Letter Report No. 6 16. April 1996 (UNCLASSIFIED)
 - Quarterly Letter Report No. 7 27. June 1996 (UNCLASSIFIED)
 - Quarterly Letter Report No. 8 16. October 1996 (UNCLASSIFIED)
 - Quarterly Letter Report No. 9 27. January 1997 (UNCLASSIFIED)
 - Quarterly Letter Report No. 10 15. May 1997 (UNCLASSIFIED)
 - Quarterly Letter Report No. 11 23. July 1997 (UNCLASSIFIED)
 - Quarterly Letter Report No. 12 15. October 1997 (UNCLASSIFIED)
- [6] Reichenbach, H. "Small-Scale Airblast Experiments", Workshop on Scaling Aspects of Hardened Structures Tests, 24 - 26 January 1995 Albuquerque, USA. (UNCLASSIFIED)
- [7] Reichenbach, H. "Small-Scale Airblast Experiments - An Excellent tool for Flow Visualization, Parameter and Validation Studies" ,
Proceedings, Specialty Symposium on Structure Response to Impact and Blast.
6 - 10 Oct. Tel Aviv, Israel. (UNCLASSIFIED)

- [8] Neuwald, P., Reichenbach, H. Klein, H. "Unsteady Flows Inside Structures - High Speed Visualization as Tool for Numerical modeling and Code Validation. Proceedings 22nd Intern. Congress on High Speed Photography and Photonics, 27 Oct. -1 Nov. 1996, Santa Fe, N.M. USA. (UNCLASSIFIED)
- [9] Neuwald P.; Reichenbach, H. "Small-Scale Detonations in a Generic Single-Story System – Effect of a Venting Hole on Blast Properties" Proc. 8th International Symposium on Interaction of the Effects of Munitions with Structures, McLean, VA, USA, 22.04 – 25.04.1997. (UNCLASSIFIED)
- [10] Neuwald, P.; Reichenbach, H.; "Small-Scale Detonations in a Generic Single-Story System", 15th International Symposium on the Military Aspects of Blast and Shock (MABS), Banff, Alberta, Canada, 14.09 –19.09.1997. (UNCLASSIFIED)
- [11] Sunshine, D. et al. "Half-Scale Cylindrical Charge Experiments Test Plan", prepared by WES for DSWA, 11 March 1997. (UNCLASSIFIED)
- [12] Anet, B., Binggeli, E. "Airblast Phenomena due to Nuclear and Conventional Explosion", NC-Laboratorium Spiez, Switzerland, 1992. (UNCLASSIFIED)
- [13] Reichenbach, H., Neuwald, P. "Visualization of Complex Blast Waves on Multi-Story Buildings", DSWA Report, Contract No DSWA 01-97-M-0599 (in preparation). (UNCLASSIFIED)

DISTRIBUTION LIST

DEPARTMENT OF DEFENSE

DEFENSE TECHNICAL INFORMATION CENTER
8725 JOHN J KINGMAN RD., SUITE 0944
FORT BELVOIR, VA 22060-6218
ATTN: DTIC/OCF

DEFENSE THREAT REDUCTION AGENCY
6801 TELEGRAPH ROAD
ALEXANDRIA, VA 22310-3398
ATTN: CP, D MYERS
ATTN: CP, MAY AMY EHMANN
ATTN: CPW, MAJ T SMITH
ATTN: CPWCT
ATTN: CPWE, L WITTEWER
ATTN: CPWE, MAJ WELLS
ATTN: CPWS
ATTN: OST, DR C GALLAWAY

DEFENSE THREAT REDUCTION AGENCY
ALBUQUERQUE OPERATIONS
1680 TEXAS ST. SE
KIRTLAND AFB, NM 87117-5669
ATTN: CPT-D G BALADI
ATTN: CPTO

DEPARTMENT OF DEFENSE CONTRACTORS

APPLIED RESEARCH ASSOCIATES, INC.
4300 SAN MATEO BLVD, NE
SUITE A220
ALBUQUERQUE, NM 87110-1260
ATTN: R NEWELL

APTEK, INC.
1257 LAKE PLAZA DRIVE
COLORADO SPRINGS, CO 80906-3578
ATTN: T MEAGHER

CARPENTER RESEARCH CORP.
P O BOX 2490
(FOR CLASSIFIED MAIL)
ROLLING HILLS ESTATES, CA 90274
ATTN: H J CARPENTER

GENERAL ATOMICS, INC
P O BOX 85608
SAN DIEGO, CA 92138
ATTN: CHARLES CHARMAN

INTERNATIONAL DEVELOPMENT & RESOURCES
10560 MAIN STREET, SUITE 515
THE MOSBY BLDG
FAIRFAX, VA 22031
ATTN: H HEAD

ITT INDUSTRIES
ITT SYSTEMS CORPORATION
ATTN: AODTRA/DASIAC
1680 TEXAS ST SE
KIRTLAND AFB, NM 87117-5669
ATTN: DASIAC
ATTN: DASIAC/DARE

ITT SYSTEMS CORP
2560 HUNTINGTON AVENUE
ALEXANDRIA, VA 22303
ATTN: D MOFFETT

ITT SYSTEMS CORP
P O BOX 15012
COLORADO SPRINGS, CO 80935-5012
ATTN: VERN SMITH

JAYCOR
1410 SPRING HILL ROAD
SUITE 300
MCLEAN, VA 22102
ATTN: DR CYRUS P KNOWLES

LOGICON ADVANCED TECHNOLOGY
6053 WEST CENTURY BOULEVARD
LOS ANGELES, CA 90045-6430
ATTN: BINKY LEE
ATTN: LIBRARY

LOGICON RDA
6940 S KINGS HWY
SUITE 202
ALEXANDRIA, VA 22310
ATTN: B WEBSTER
ATTN: T MAZOLLA

LOGICON RDA
P O BOX 9377
ALBUQUERQUE, NM 87119-9377
ATTN: G GANONG

MAXWELL TECHNOLOGIES INC
FEDERAL DIVISION
8888 BALBOA AVENUE
SAN DIEGO, CA 92123-1506
ATTN: J BARTHEL
ATTN: T PIERCE

SCIENCE APPLICATIONS INTL CORP
P O BOX 1303
MCLEAN, VA 22102
ATTN: D BACON
ATTN: J BAUM
ATTN: J MCGAGHAN

SRI INTERNATIONAL
333 RAVENSWOOD AVENUE
MENLO PARK, CA 94025-3434
ATTN: J GRAN

TECH REPS, INC.
5000 MARBLE AVENUE, NE
SUITE 222
PATIO PLAZA OFFICE BLDG
ALBUQUERQUE, NM 87110-6390
ATTN: F MCMULLAN

TITAN CORPORATION (THE)
TITAN RESEARCH & TECHNOLOGY DIVSN
9410 TOPANGO CANYON BLVD
SUITE 104
CHATSWORTH, CA 91311-5771
ATTN: R ENGLAND

TRW S. I. G.
STRATEGIC SYSTEMS DIVISION
P O BOX 1310
SAN BERNARDINO, CA 92402-1310
ATTN: NORMAN LIPNER

WEIDLINGER ASSOC, INC.
4410 EL CAMINO REAL, SUITE 110
LOS ALTOS, CA 94022-1049
ATTN: D TENNANT
ATTN: H LEVINE

WEIDLINGER ASSOCIATES, INC.
375 HUDSON ST., 12TH FLOOR
NEW YORK, NY 10014-3656
ATTN: RAYMOND P DADDAZIO

DEPARTMENT OF ENERGY

UNIVERSITY OF CALIFORNIA
LAWRENCE LIVERMORE NATIONAL LAB
P O BOX 808
LIVERMORE, CA 94551-9900
ATTN: L-030 ALLEN KUHL

DEPARTMENT OF THE AIR FORCE

AIR UNIVERSITY LIBRARY
600 CHENNAULT CIRCLE
BLDG 1405 - ROOM 160
MAXWELL AFB, AL 36112-6424
ATTN: AUL-LSE

DEPARTMENT OF THE ARMY

US ARMY RESEARCH LAB
AMSRL-SL-CS E3331
5101 HOADLEY RD
ABERDEEN PROVING GROUND, MD 21010-5423
ATTN: SLCBR-SS-T (TECH LIB)

US ARMY RESEARCH LABORATORIES
2800 POWDER MILL ROAD
ADELPHI, MD 20783-1197
ATTN: AMSRL-SL-CE

US ARMY RESEARCH & DEVELOPMENT
CENTER
WATERWAYS EXPERIMENT STATION
3909 HALLS FERRY RD.
VICKSBURG, MS 39180-6199
ATTN: SD-R E JACKSON
ATTN: SD-R WELCH
ATTN: SE-R D RICKMAN
ATTN: SS-R F DALLRIVA

DEPARTMENT OF THE NAVY

NAVAL RESEARCH LABORATORY
4555 OVERLOOK AVE, SW
WASHINGTON, DC 20375-5000
ATTN: CODE 5227 RESEARCH REPORT

FOREIGN

ERNST-MACH-INSTITUTE
78 FREIBURG/BR
ECKERSTRASSE 4
REPUBLIC OF GERMANY
ATTN: H REICHENBACH
ATTN: P NEUALD